

NASA Conference Publication 2487

Part 2

Research in Natural Laminar Flow and Laminar-Flow Control

Compiled by
Jerry N. Hefner and Frances E. Sabo
Langley Research Center
Hampton, Virginia

Proceedings of a symposium sponsored
by the National Aeronautics and
Space Administration and held at
Langley Research Center
Hampton, Virginia
March 16-19, 1987



**National Aeronautics
and Space Administration**

**Scientific and Technical
Information Division**

1987

PREFACE

Since the mid 1970's, NASA, industry, and universities have worked together to conduct important research focused at developing laminar-flow technology that could reduce fuel consumption for general aviation, commuter, and transport aircraft by as much as 40 to 50 percent. This research, which was initiated under the NASA Aircraft Energy Efficiency Program and continued through the Research and Technology Base Program, has proved very successful with many significant and impressive results having been obtained.

This symposium was planned in view of the recent accomplishments within the areas of laminar-flow control and natural laminar flow and the potential benefits of laminar-flow technology to the civil and military aircraft communities in the United States. The symposium included technical sessions on advanced theory and design tool development, wind tunnel and flight research, transition measurement and detection techniques, low and high Reynolds number research, and subsonic and supersonic research.

PRECEDING PAGE BLANK NOT FILMED

CONTENTS

PREFACE	iii
ATTENDEES	x

Part 1 *

SESSION 1: OVERVIEWS Chairman: R. V. Harris, Jr.

NASA LAMINAR-FLOW PROGRAM - PAST, PRESENT, FUTURE	1
Roy V. Harris, Jr. and Jerry N. Hefner	
LAMINAR FLOW: CHALLENGE AND POTENTIAL	25
M. E. Kirchner	
LFC - A MATURING CONCEPT	45
John Morris	
LOCKHEED LAMINAR-FLOW CONTROL SYSTEMS DEVELOPMENT AND APPLICATIONS	53
Roy H. Lange	
LAMINAR FLOW - THE CESSNA PERSPECTIVE	79
B. E. Peterman	
LONG-RANGE LFC TRANSPORT	89
W. Pfenninger	

SESSION 2: JETSTAR LEFT PROGRAM Chairman: R. D. Wagner

DEVELOPMENT FLIGHT TESTS OF JETSTAR LFC LEADING-EDGE FLIGHT TEST EXPERIMENT	117
David F. Fisher and Michael C. Fischer	
THE RIGHT WING OF THE L.E.F.T. AIRPLANE	141
Arthur G. Powell	
PERFORMANCE OF LAMINAR-FLOW LEADING-EDGE TEST ARTICLES IN CLOUD ENCOUNTERS	163
Richard E. Davis, Dal V. Maddalon, and Richard D. Wagner	
SIMULATED AIRLINE SERVICE EXPERIENCE WITH LAMINAR-FLOW CONTROL LEADING-EDGE SYSTEMS	195
Dal V. Maddalon, David F. Fisher, Lisa A. Jennett, and Michael C. Fischer	

*Part 1 is presented under separate cover.

SESSION 3: ADVANCED STABILITY THEORY AND ITS APPLICATION

Chairman: D. M. Bushnell

STABILITY THEORY APPLICATIONS TO LAMINAR-FLOW CONTROL	219
Mujeeb R. Malik	
NONPARALLEL STABILITY OF BOUNDARY LAYERS	245
Ali H. Nayfeh	
INTERACTION OF TOLLMIE-SCHLICHTING WAVES AND GÖRTLER VORTICES	261
P. Hall	
BOUNDARY-LAYER RECEPTIVITY AND LAMINAR-FLOW AIRFOIL DESIGN	273
E. J. Kerschen	
GÖRTLER INSTABILITY ON AN AIRFOIL	289
Vijay Kalburgi, S. M. Mangalam, J. R. Dagenhart, and S. N. Tiwari	
EFFECT OF ROUGHNESS ON THE STABILITY OF BOUNDARY LAYERS	301
Ali H. Nayfeh, Saad A. Ragab, and Ayman Al-Maaitah	

Part 2

SESSION 4: BASIC WIND TUNNEL RESEARCH/TECHNIQUES

Chairman: W. D. Harvey

ADVANCED MEASUREMENT TECHNIQUES - PART I	317
Bruce J. Holmes, Debra L. Carraway, Gregory S. Manuel, and Cynthia C. Croom	
ADVANCED MEASUREMENT TECHNIQUES - PART II	341
INTRODUCTION	
Charles B. Johnson	342
FLOW QUALITY MEASUREMENTS IN COMPRESSIBLE SUBSONIC FLOWS	
P. C. Stainback and C. B. Johnson	345
HOT-FILM SYSTEM FOR TRANSITION DETECTION IN CRYOGENIC WIND TUNNELS	
C. B. Johnson, D. L. Carraway, P. C. Stainback, and M. F. Fancher	358
PREDICTED AND HOT-FILM MEASURED TOLLMIE-SCHLICHTING WAVE CHARACTERISTICS	
John P. Stack, Robert B. Yeaton, and J. R. Dagenhart	377
REMOTE DETECTION OF BOUNDARY-LAYER TRANSITION BY AN OPTICAL SYSTEM	
Robert M. Hall, Medhat Azzazy, and Dariush Modarress	381
THREE-COMPONENT LASER DOPPLER VELOCIMETER MEASUREMENTS IN A JUNCTURE FLOW	
L. R. Kubendran and J. F. Meyers	389
BASIC AERODYNAMIC RESEARCH FACILITY FOR COMPARATIVE STUDIES OF FLOW DIAGNOSTIC TECHNIQUES	
Gregory S. Jones, Luther R. Gartrell, and P. Calvin Stainback	401

RECENT TESTS AT LANGLEY WITH A UNIVERSITY OF TENNESSEE SPACE INSTITUTE (UTSI) SKIN FRICTION BALANCE Pierce L. Lawing, A. D. Vakili, and J. M. Wu	407
RECENT FLOW VISUALIZATION STUDIES IN THE 0.3-m TCT Walter L. Snow, Alpheus W. Burner, and William K. Goad	412
EXPERIMENTAL STUDIES ON GÖRTLER VORTICES	421
S. M. Mangalam, J. R. Dagenhart, and J. F. Meyers	
AN EXPERIMENTAL EVALUATION OF SLOTS VERSUS POROUS STRIPS FOR LAMINAR-FLOW APPLICATIONS	435
Kenneth C. Cornelius	
RESULTS OF LFC EXPERIMENT ON SLOTTED SWEEP SUPERCRITICAL AIRFOIL IN LANGLEY'S 8-FOOT TRANSONIC PRESSURE TUNNEL	453
C. W. Brooks, Jr. and C. D. Harris	
BOUNDARY-LAYER STABILITY ANALYSIS OF LARC 8-FOOT LFC EXPERIMENTAL DATA	471
Scott Berry, J. R. Dagenhart, C. W. Brooks, and C. D. Harris	
SESSION 5: COMPUTATIONAL TRANSITIONAL RESEARCH	
Chairman: P. J. Bobbitt	
SENSITIVITY OF LFC TECHNIQUES IN THE NON-LINEAR REGIME	491
D. M. Bushnell, M. Y. Hussaini, and T. A. Zang	
NUMERICAL SOLUTIONS OF THE COMPRESSIBLE 3-D BOUNDARY-LAYER EQUATIONS FOR AEROSPACE CONFIGURATIONS WITH EMPHASIS ON LFC	517
Julius E. Harris, Venkit Iyer, and Samir Radwan	
THEORETICAL METHODS AND DESIGN STUDIES FOR NLF AND HLFC SWEEP WINGS AT SUBSONIC AND SUPERSONIC SPEEDS	547
Suresh H. Goradia and Harry L. Morgan, Jr.	
NUMERICAL EXPERIMENTS ON TRANSITION CONTROL IN WALL-BOUNDED SHEAR FLOWS	577
S. Biringen and M. J. Caruso	
APPLICATION OF SOUND AND TEMPERATURE TO CONTROL BOUNDARY-LAYER TRANSITION	593
L. Maestrello, P. Parikh, A. Rayliss, L. S. Huang, and T. D. Bryant	
NEAR-FIELD NOISE PREDICTIONS OF AN AIRCRAFT IN CRUISE	617
John W. Rawls, Jr.	

Part 3*

SESSION 6: ADVANCED AIRFOIL DEVELOPMENT

Chairman: J. W. Stickle

DESIGN OF THE LOW-SPEED NLF(1)-0414F AND THE HIGH-SPEED HSNLF(1)-0213 AIRFOILS WITH HIGH-LIFT SYSTEMS	637
J. K. Viken, S. A. Viken, W. Pfenninger, H. L. Morgan, Jr., and R. L. Campbell	
WIND TUNNEL RESULTS OF THE LOW-SPEED NLF(1)-0414F AIRFOIL	673
Daniel G. Murri, Robert J. McGhee, Frank L. Jordan, Jr., Patrick J. Davis, and Jeffrey K. Viken	
WIND TUNNEL RESULTS OF THE HIGH-SPEED NLF(1)-0213 AIRFOIL	697
William G. Sewall, Robert J. McGhee, David E. Hahne, and Frank L. Jordan, Jr.	
DESIGN AND TEST OF A NATURAL LAMINAR FLOW/LARGE REYNOLDS NUMBER AIRFOIL WITH A HIGH DESIGN CRUISE LIFT COEFFICIENT	727
C. E. Kolesar	
DESIGN AND TEST OF AN NLF WING GLOVE FOR THE VARIABLE-SWEEP TRANSITION FLIGHT EXPERIMENT	753
E. G. Waggoner, R. L. Campbell, P. S. Phillips, and J. B. Hallissy	
THE DESIGN OF AN AIRFOIL FOR A HIGH-ALTITUDE, LONG-ENDURANCE REMOTELY PILOTED VEHICLE	777
Mark D. Maughmer and Dan M. Somers	

SESSION 7: FLIGHT RESEARCH EXPERIMENTS

Chairmen: T. G. Ayers and B. J. Holmes

757 NLF GLOVE FLIGHT TEST RESULTS	795
L. J. Runyan, G. W. Bielak, R. Behbehani, A. W. Chen, and R. A. Rozendaal	
F-14 VSTFE AND RESULTS OF THE CLEANUP FLIGHT TEST PROGRAM	819
Robert R. Meyer, Bianca M. Trujillo, and Dennis W. Bartlett	
VARIABLE-SWEEP TRANSITION FLIGHT EXPERIMENT (VSTFE) - STABILITY CODE DEVELOPMENT AND CLEAN-UP GLOVE DATA ANALYSIS	845
R. A. Rozendaal	
EXPERIMENTAL AND NUMERICAL ANALYSES OF LAMINAR BOUNDARY-LAYER FLOW STABILITY OVER AN AIRCRAFT FUSELAGE FOREBODY	861
Paul M. H. W. Vijgen and Bruce J. Holmes	

*Part 3 is presented under separate cover.

STATUS REPORT ON A NATURAL LAMINAR-FLOW NACELLE FLIGHT EXPERIMENT	887
SUMMARY.....	888
Earl C. Hastings, Jr.	
NACELLE DESIGN.....	891
G. K. Faust and P. Mungur	
NACELLE AERODYNAMIC PERFORMANCE.....	908
Clifford J. Obara and S. S. Dodbele	
EFFECTS OF ACOUSTIC SOURCES.....	914
James A. Schoenster and Michael G. Jones	

SESSION 8: SUPERSONIC TRANSITION/LFC RESEARCH
Chairman: R. W. Barnwell

SUPERSONIC LAMINAR-FLOW CONTROL	923
D. M. Bushnell and M. R. Malik	
DESIGN AND FABRICATION REQUIREMENTS FOR LOW NOISE SUPERSONIC/HYPERSONIC WIND TUNNELS	947
I. E. Beckwith, F.-J. Chen, and M. R. Malik	
THE EFFECTS OF WALL SURFACE DEFECTS ON BOUNDARY-LAYER TRANSITION IN QUIET AND NOISY SUPERSONIC FLOW	965
E. L. Morrisette and T. R. Creel, Jr.	
EXPERIMENTAL AND THEORETICAL INVESTIGATION OF BOUNDARY-LAYER INSTABILITY MECHANISMS ON A SWEPT LEADING EDGE AT MACH 3.5	981
T. R. Creel, Jr., M. R. Malik, and I. E. Beckwith	
SUPERSONIC BOUNDARY-LAYER TRANSITION ON THE LaRC F-106 AND THE DFRF F-15 AIRCRAFT	997
PART I: TRANSITION MEASUREMENTS AND STABILITY ANALYSIS	
F. S. Collier, Jr. and J. B. Johnson	998
PART II: AERODYNAMIC PREDICTIONS	
O. J. Rose and D. S. Miller	1015

ATTENDEES

WILLIAM J. ALFORD, Jr.
DEI

TED AYERS
NASA-DPRF

JENNIFER L. BAER-RIEDHART
NASA-DPRF

WAYNE BALDWIN
AFWAL/FIMG

MARK J. BERGEZ
LOCKHEED-CALIFORNIA COMPANY

SCOTT BERRY
ESC

MARK EUGENE BEYER
OMAC

S. BIRINGEN
UNIVERSITY OF COLORADO

JOHN BLASCOVICH
GRUMMAN CORPORATION

MICHAEL D. BONDY
NASA-DPRF

ALAN B. CAIN
McDONNELL DOUGLAS

GARY D. CARLSON
NASA-DPRF

FANG-JENG CHEN
HIGH TECHNOLOGY CORPORATION

RODNEY L. CLARK
AFWAL/FIMM

FAYETTE S. COLLIER
HIGH TECHNOLOGY CORPORATION

KENNETH C. CORNELIUS
LOCKHEED-GEORGIA CO.

EDWIN G. CHAPLIN
OMAC, INC.

S. DODBELE
VIGYAN

R. O. DODSON
BOEING

CO DONALDSON
TITAN ASSOCIATES

CORNELIUS DRIVER
EAGLE ENGINEERING, INC.

NABIL M. EL-HADY
ODU

DAVE ELLIS
CESSNA

JEANNE EVANS
TELEDYNE RYAN AERONAUTICAL

G. K. FAUST
GENERAL ELECTRIC

DAVID F. FISHER
NASA-AMES-DRYDEN

EDWARD A. GABRIEL
FAA

HEINZ A. GERHARDT
NORTHROP CORPORATION

DR. GERALD GREGOREK
OHIO STATE UNIVERSITY

SURESH GORADIA
VIRA

GLENN J. GRUBER
PRATT & WHITNEY

M. HUSSAINI
ICASE

DOUG HALL
NADC

PHIL HALL
ICASE

THORWALD HERBERT
VPI&SU

MICHAEL L. HINSON
GATES LEARJET CORP.

VENKIT S. IYER
VIGYAN RESEARCH ASSOC., INC.

LISA A. JENNETT
NASA-DRYDEN

JOSEPH B. JOHNSON
NASA-DRYDEN

M. JONES
PRC-KENTRON

CHANTAL JOUBERT
McDONNELL DOUGLAS CORP.

VIJAY KALBURGI
ODU

OSAMA KANDIL
ODU

ABRAHAM KAREN
LEADING SYSTEMS, INC.

K. KAUPS
DOUGLAS AIRCRAFT CO.

EDWARD J. KERSCHEN
UNIVERSITY OF ARIZONA

MARK E. KIRCHNER
BOEING COMM. AIRPLANE CO.

MAX KLOTZCHE
DOUGLAS AIRCRAFT

MARTIN A. KNUTSON
NASA-DRYDEN

THOMAS R. LACEY
McDONNELL AIRCRAFT CO.

ROY H. LANGE
LOCKHEED-GEORGIA CO.

SPIRO LEROUDIS
OFFICE OF NAVAL RESEARCH

JOHN O. LINDGREN
DOUGLAS AIRCRAFT CO.

GARY L. LINK
BOEING

T. M. LIU
ROHR INDUSTRIES, INC.

LAURENCE K. LOFTIN, JR.
SELF

W. K. LONDENBERG
GDS/FT. WORTH DIV.

WESLEY K. LORD
PRATT & WHITNEY

LESLIE M. MACK
JET PROPULSION LABORATORY

DR. MUJEEB MALIK
HIGH TECHNOLOGY CORPORATION

DONALD L. MALLICK
NASA-DRYDEN

SIVA M. MANGALAM
AS&M, INC.

MARK D. MAUGHMER
PENN STATE UNIVERSITY

FRED W. MAY
BOEING MILITARY AIRPLANE CO.

WILLIAM D. McCAULEY
TRW

BARNES W. McCORMICK
PENN STATE UNIVERSITY

DAVID E. MCNAY
DOUGLAS AIRCRAFT COMPANY

ROBERT R. MEYER
NASA-DRYDEN

LAWRENCE C. MONTROYA
NASA-DPRF

MARK V. MORKOVIN
ILLINOIS INSTITUTE OF TECH.

DR. THOMAS J. MUELLER
UNIVERSITY OF NOTRE DAME

PARMA MUNGUR
GENERAL ELECTRIC

JOHN W. MURDOCK
THE AEROSPACE CORPORATION

WILLIAM R. MURPHY
GULFSTREAM AEROSPACE CORP.

DEL NAGEL
BOEING

A. NAYFEH
VPI&SU

RON NEAL
BEECH AIRCRAFT

ORAN NICKS
TEXAS A&M

CLIFF OBARA
PRC-KENTRON

ARNOLD OTCHIN
TELEDYNE RYAN AERONAUTICAL

WILLIAM M. OTTO
OTTO LABORATORIES, INC.

PARESH PARIKH
VIRA, INC.

WILFRED E. PEARCE
DOUGLAS AIRCRAFT COMPANY

BRUCE PETERMAN
CESSNA

WERNER PFENNINGER
AS&M

DAVID PICKETT
BOEING MILITARY AIRPLANE CO.

DR. ARTHUR G. POWELL
DOUGLAS AIRCRAFT CO.

JOHN W. RAWLS, JR.
PRC-KENTRON

KENNETH H. ROGERS
DOUGLAS AIRCRAFT COMPANY

OLLIE J. ROSE
PRC-KENTRON

ROGER A. ROZENDAAL
BOEING COMM. AIRPLANE CO.

JIM RUNYAN
BOEING COMM. AIRPLANE CO.

DALLAS M. RYLE
LOCKHEED-GEORGIA COMPANY

F. CHRIS SAUTTER
PENN STATE UNIVERSITY

PAUL SHANG
NAVAL SHIP R&D CENTER

A. J. SMITH
SELF

GREGORY E. SMITH
DYNAMIC ENGINEERING, INC.

NORBERT F. SMITH
McDONNELL DOUGLAS

ROBERT J. STEWART
GULFSTREAM

DENNIS M. STRAUSSFOGEL
PENNSYLVANIA STATE UNIV.

G. TEMANSON
PRC-KENTRON

BIANCA M. TRUJILLO
NASA-DRYDEN

CHANDRA S. VEMURU
AS&M, INC.

PAUL VIJGEN
UNIVERSITY OF KANSAS

**SALLY WATSON-VIKEN
COMPLERE**

**GIUSEPPE VOLPE
GRUMMAN CORP. RES. CTR.**

**KENNETH B. WALKLEY
DYNAMIC ENGINEERING, INC.**

**RICHARD T. WHITCOMB
SELF**

**MICHAEL WUSK
ODU**

LANGLEY RESEARCH CENTER ATTENDEES

RICHARD BARNWELL
HSAD

DENNIS BARTLETT
LSAD

DR. H. LEE BEACH
D/AERO

WILLIAM D. BEASLEY
TAD

IVAN E. BECKWITH
HSAD

PERCY J. BOBBITT
TAD

ALBERT L. BRASLOW
SELF

CUYLER W. BROOKS, JR.
TAD

DENNIS M. BUSHNELL
HSAD

RICHARD L. CAMPBELL
TAD

DEBRA CARRAWAY
IRD

A. M. CARY, JR.
HSAD

WILLIAM CORLETT
HSAD

THEODORE R. CREEL
HSAD

CINDY CROOM
LSAD

RAY DAGENHART
TAD

PAMELA DAVIS
SDD

RICHARD E. DAVIS
FED

DANIEL J. DICARLO
LSAD

SAM DOLLYHIGH
AVD

DOUGLAS DWOYER
HSAD

JAMES FERRIS
TAD

TOM FOUGHNER
TAD

DAVID HAHNE
LSAD

ROBERT HALL
TAD

JAMES HALLISSY
TAD

CHARLES D. HARRIS
TAK

JULIUS E. HARRIS
HSAD

ROY V. HARRIS, JR.
D/AERO

WILLIAM D. HARVEY
TAD

EARL C. HASTINGS
LSAD

JERRY N. HEFNER
AVD

ORIGINAL PAGE IS
OF POOR QUALITY

TODD HODGES
MD

BRUCE HOLMES
LSAD

CHARLES JOHNSON
TAD

JOSEPH L. JOHNSON
LSAD

ROBERT A. JONES
HSAD

FRANK JORDAN
LSAD

PIERCE L. LAWING
TRAD

DAL V. MADDALON
LSAD

LUCIO MAESTRELLO
TAD

JACK MOLLOY
OFFICE OF D/AERO

GREGORY S. MANUEL
LSAD

ROBERT J. MCGHEE
TAD

JIM MEYERS
IRD

HARRY MORGAN
LSAD

C. E. K. MORRIS, JR.
AVD

SHELBY J. MORRIS
AVD

LEON MORRISETTE
HSAD

DAN MURRI
LSAD

RICHARD H. PETERSEN
DIRECTOR

PAM PHILLIPS
TAD

JAMES L. PITTMAN
HSAD

LAWRENCE E. PUTNAM
TAD

JAMES A. SCHOENSTER
AcoD

WILLIAM SEWALL
TAD

DAN SOMERS
TAD

JERRY SOUTH
OFFICE OF DIRECTOR

JOHN P. STACK
TAD

P. CALVIN STAINBACK
TAD

DAVID STEPHENS
AD

ERIC C. STEWART
LSAD

JOSEPH W. STICKLE
LSAD

H. PAUL STOUGH III
LSAD

HARRY A. VERSTYNEN, JR.
FAA

NICHOLAS G. VRETAKIS
AFSC LIAISON OFFICE

ED WAGGONER
TAD

RICHARD D. WAGNER
LSAD

BETTY S. WALKER
TAD

RALPH WATSON
HSAD

JOHN WHITCOMB
MD

RICHARD WOOD
HSAD

LONG YIP
LSAD

JAMES YOUNGBLOOD
SSD

TOM ZANG
HSAD

N90-12520

ADVANCED MEASUREMENT TECHNIQUES - PART I

**Bruce J. Holmes,
Debra L. Carraway,
Gregory S. Manuel, and
Cynthia C. Croom
NASA Langley Research Center
Hampton, Virginia**

TRANSITION PHYSICS RESEARCH

In modern laminar flow flight and wind tunnel research, it is important to understand the specific cause(s) of laminar to turbulent boundary-layer transition. Such information is crucial to the exploration of the limits of practical application of laminar flow for drag reduction on aircraft. The process of transition involves both the possible modes of disturbance growth, and the environmental conditioning of the instabilities by free-stream or surface conditions (see fig. 1). The possible modes of disturbance growth include viscous (e.g. Tollmien-Schlichting), inviscid (e.g. crossflow), and modes which may bypass these "natural" ones. Theory provides information on the possible modes of disturbance amplification, but experiment must be relied upon to determine which of those modes actually dominates the transition process in a given environment. This presentation covers the results to date of research on advanced devices and methods used for the study of transition phenomena in the subsonic and transonic flight and wind tunnel environments.

$$\text{Cause(s) of transition} = \left[\begin{array}{c} \text{Mode(s) of} \\ \text{disturbance growth} \end{array} \right] \times \left[\begin{array}{c} \text{Environmentally conditioned} \\ \text{instabilities} \end{array} \right]$$

Viscous	Turbulence
Inviscid	Vorticity
Bypasses	Thermal
	Acoustics
	Vibration

Figure 1

TRANSITION IN THE FLIGHT ENVIRONMENT

Different experimental environments can produce different transition modes. In the subsonic flight environment, the instabilities of practical interest include the Tollmien-Schlichting instability in two-dimensional boundary layers, laminar separation-induced inflectional instability, crossflow instability in three-dimensional boundary layers, and instabilities which may bypass these "natural" modes, caused by surface imperfections or acoustics for example (fig. 2). Very few flight transition experiments have attempted to document the mode of disturbance growth or cause of transition (ref. 1). The data published in nearly all past experiments focus on the transition locations without exploring the dominant instability(ies) responsible for initiating the transition process. Ultimately it is very important that transition studies be conducted at the speeds and altitudes at which the laminar-flow technology is intended to be applied. This is important because on laminar airframe surfaces which are practical to build and maintain, the transition process will be influenced by unit Reynolds number as well as length Reynolds number. The simultaneous scaling of both of these parameters is not possible; large-scale flight conditions are required for complete understanding of transition behavior.

- Tollmien-Schlichting instability
 - 2-D boundary layers/unswept wings
- Laminar separation
- Crossflow instability
 - 3-D boundary layers/swept wings
- Bypasses
 - Manufacturing tolerances
 - Engine/airframe noise
 - Insect contamination

Figure 2

TRANSITION MEASUREMENT TECHNIQUES

Laminar, transitional, and turbulent flows exhibit a variety of changes in fluid properties which provide the means to detect the state of the flow. Such property changes include skin friction, boundary-layer thickness, local turbulence, heat transfer, mass transfer, local flow direction, and others. Past research has made extensive use of a wide variety of transition measurement methods which rely on the flow properties mentioned. Such methods include sublimating chemical, oil flow, China clay, acoustic sensors, total surface tubes, liquid films, hot films sensors, and liquid crystals. Each technique has advantages and disadvantages. Hot films, for example, are extremely useful for continuous recording of point-measurements of transition during continuously changing test conditions. In the past, however, hot-film transition sensors were not widely used to detect the spatial or temporal mode behavior of the transition process (e.g. for laminar separation-induced transition behavior). Some of the available transition visualization methods such as sublimating chemicals have the advantage that they can provide for post-flight observations of transition details (ref 2). However, flow visualization of transition using sublimating chemicals was not practical at flight altitudes much above 20,000 feet. This presentation concentrates on recent research on arrayed hot-film sensors for use in transition mode measurements and on the development of the liquid-crystal method for flow visualization (fig. 3).

- Sublimating chemicals
- Oil flow
- China clay
- Hot films
- Acoustic detection
- Total pressure surface tubes
- Liquid film
- Liquid crystals

Figure 3

ARRAYED HOT-FILM DEVICES FOR MEASUREMENT OF TRANSITION LOCATION AND MODE

Applications of thin hot-film devices to measure transition location began in the early 1930's, and their use since then has been principally limited to single-point measurements of transition location. Thus, except for a few experiments where Tollmien-Schlichting wave frequencies were measured with hot-films, these devices have not been used to detect transition mode. Three arrayed hot-film device concepts have recently been developed for detection of transition modes, the multi-element hot-film transition sensor, the laminar separation bubble sensor, and the laminar crossflow vorticity sensor (ref 3). While these arrayed hot-film concepts can apply to either wind tunnel or flight research, the present discussion focuses on flight applications. For many flight research applications, through-the-surface types of sensor installation are not practical. For such situations, the mounting of the sensors and associated signal leads must be done on the exterior surface. The problems associated with surface-mounted sensors are addressed by these arrayed hot-film devices. The multi-element transition sensor and the laminar separation sensor were evaluated in flight. The laminar separation sensor has been evaluated in wind tunnel tests, and the prototype crossflow sensor has not been tested (fig. 4).

- Multi-element hot-film transition sensor
- Laminar separation bubble sensor
- Laminar crossflow vorticity sensor

Figure 4

GATES LEARJET MODEL 28/29 AIRCRAFT

The flight evaluations of the advanced measurement techniques discussed in this presentation were conducted on a NASA-operated Lear Model 28/29 business jet airplane used at Langley for viscous drag reduction flight research (see figure 5). The airplane provides a flight envelope including Mach numbers up to 0.805, maximum unit Reynolds numbers up to 2.65 million per foot, and maximum altitudes up to 51,000 feet. The wing on this airplane incorporates a non-production, modified airfoil section. Both the wing and the winglet on this airplane have very smooth surfaces on which to conduct laminar-flow research.



Figure 5

ORIGINAL PAGE
BLACK AND WHITE PHOTOGRAPH

~~ORIGINAL PAGE IS~~
~~OF POOR QUALITY~~

MULTI-ELEMENT HOT-FILM TRANSITION SENSOR

For many research efforts, it is important to study the growth of disturbances as nearly along streamlines as possible. Behavior along streamlines is of particular concern in three-dimensional flows, for example on swept wings and on three-dimensional bodies such as fuselages and engine nacelles. For these kinds of investigations, the multi-element hot-film sensor overcomes the disadvantages of the individual ("postage stamp") sensors often used in the past. The disadvantages of the individual surface-mounted hot-film sensors concern installation and signal interpretation. With individual hot-film sensors, downstream contamination of a sensor by an upstream neighboring sensor creates the requirement for staggering of the devices. This staggering of the sensors provides information on transition behavior along different streamwise stations for each sensor. In three-dimensional flows, staggering of the individual sensors may not provide useful transition behavior information. Other examples where the multi-element arrayed sensor may be useful include investigations of laminar-flow behavior in propeller slipstreams, during flight through clouds, or in the presence of acoustic disturbances where noise radiation patterns may not be uniform. The sensor is fabricated by imbedding the required number and spatial distribution of hot-film elements and signal leads between two layers of polyimide film. Figure 6 presents the geometric detail of a 25-element sensor design.

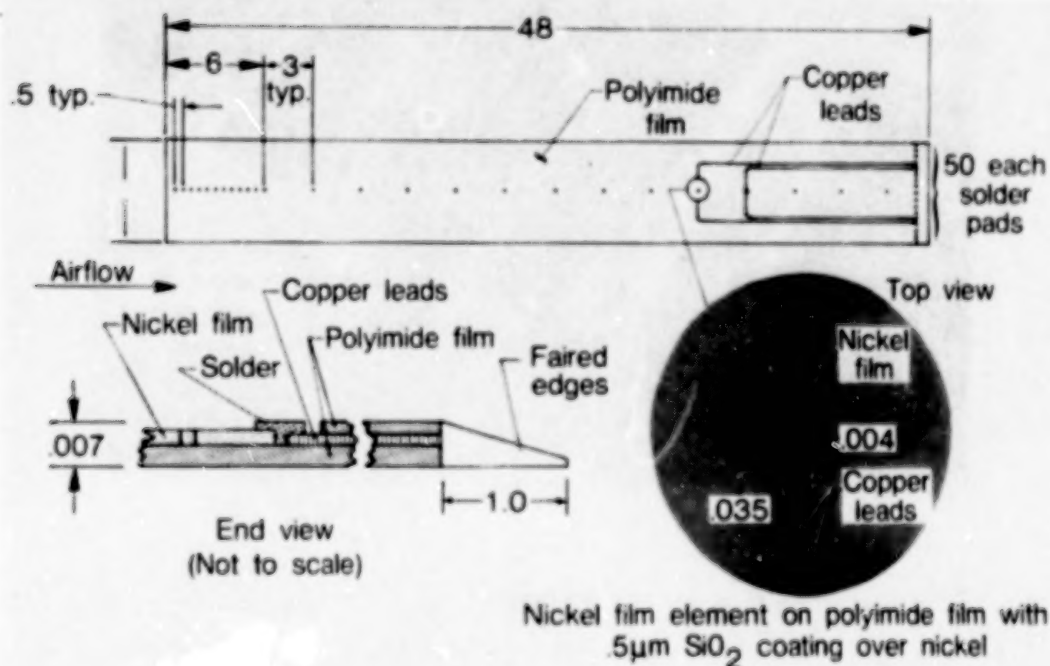


Figure 6

LEAR 28/29 HOT-FILM ANEMOMETRY INSTALLATION

Figure 7 depicts the arrangement of sensors on the left wing upper surface on the Lear 28/29. The figure shows the location of the multi-element sensor and the laminar separation sensors which were flown. Transition data acquisition with the multi-element sensor was accomplished using an electronic switching system which allows rapid switching of all sensor elements through six anemometers on board the airplane. Thus at any instant, six of the 25 sensor elements could be recorded simultaneously. Prior to operation of the multi-element sensor for transition investigation, the sensor and surrounding wing surface regions were sprayed with sublimating chemicals to ensure that the imperfect surface of the sensor did not cause transition. The results of these tests showed that for altitudes above about 29,000 feet where the cruise unit Reynolds number was below about 2.1 million per foot, the sensor roughness did not affect transition behavior.

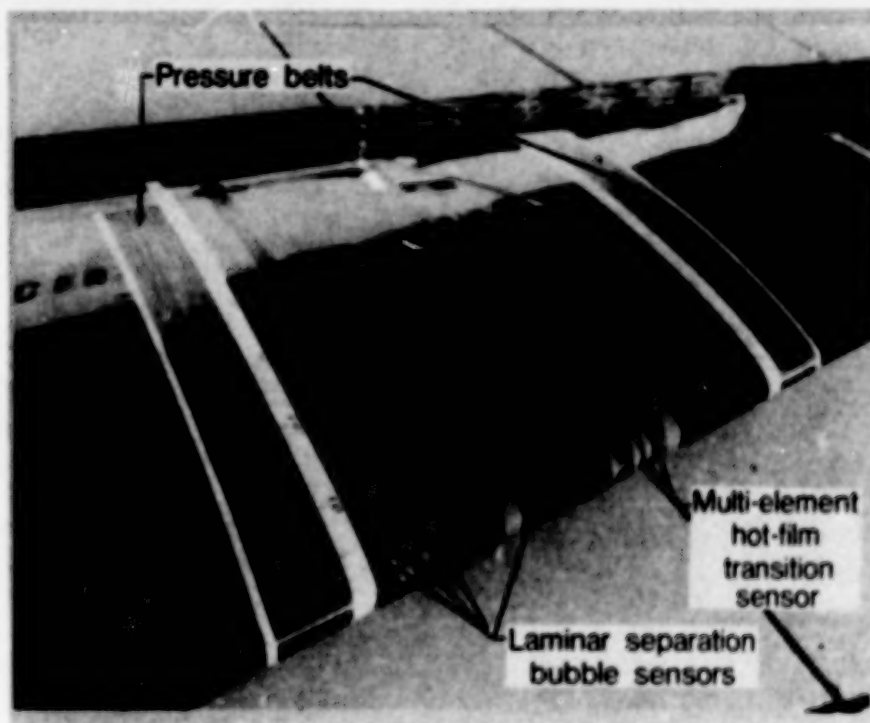


Figure 7

ORIGINAL PAGE
BLACK AND WHITE PHOTOGRAPH

~~ORIGINAL PAGE IS
OF POOR QUALITY~~

LEAR 28/29 FLIGHT-MEASURED TRANSITION AND PRESSURE DISTRIBUTION

Figure 8a) illustrates typical transition data which can be acquired with the multi-element transition sensor; the pressure distribution (figure 8b) was measured with the pressure belts previously illustrated in figure 7. Transition onset is located at 41% chord where the first turbulent spikes are observed in the hot-film traces. The transitional boundary layer produces larger amplitude fluctuations in the signal traces, and at the end of the transitional region, the fully developed turbulent boundary layer produces the large amplitude uniformly fluctuating hot-film signal seen at the 52% chord element. The total length of the transition region extends over about eight percent of the chord. This transition region length and the character of the hot-film signal are indicative of Tollmien-Schlichting (T-S) initiated transition. To assure that this transition mechanism is active, analytical predictions of disturbance growth rates (n -factors) and most amplified T-S frequencies are compared to amplified hot-film signal data.

FLIGHT-MEASURED TRANSITION USING MULTI-ELEMENT SENSOR

$M = 0.77$, $h_p = 39,000$ R, $R_c = 8.8 \times 10^6$

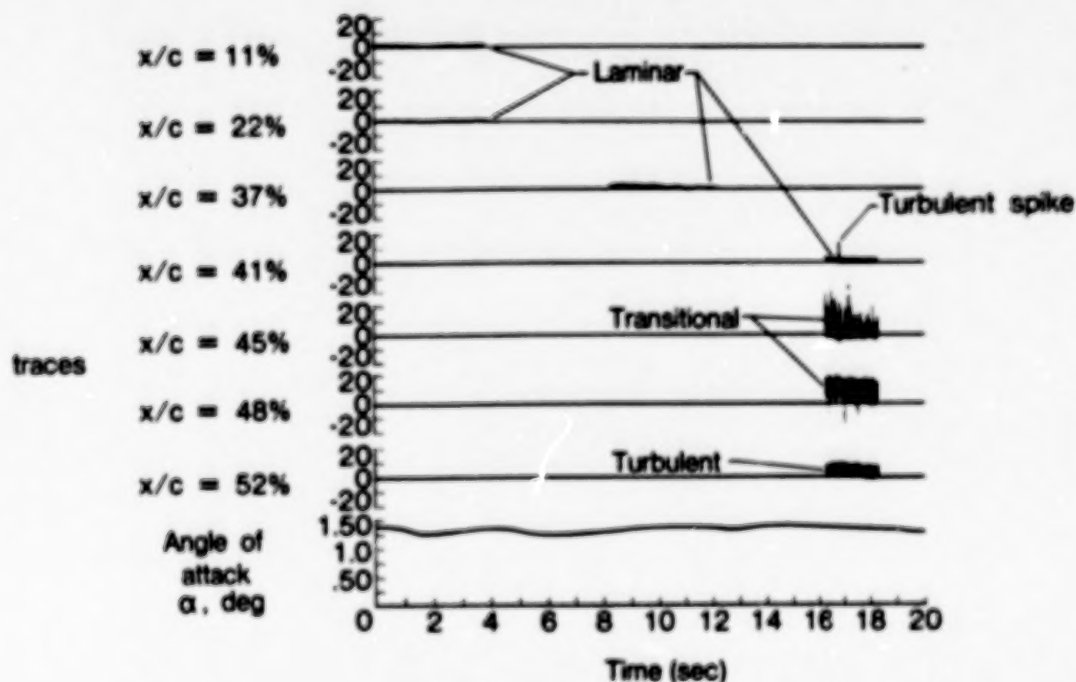


Figure 8a

LEAR 28/29 PRESSURE DISTRIBUTION

$M = 0.80$, $h = 40427$ ft, $R' = 1.51 \times 10^6$ ft⁻¹, $\eta = .362$

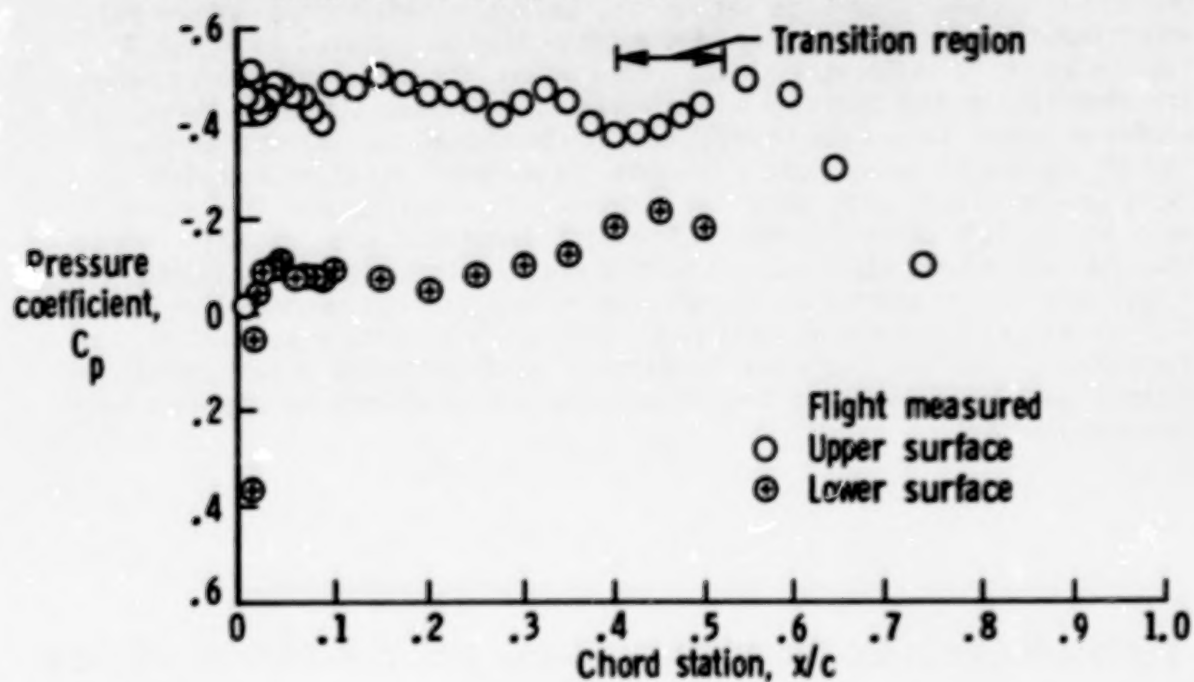


Figure 8b

TOLLMIEIN-SCHLICHTING INSTABILITY DETECTION FROM HOT-FILMS

The identification of the Tollmien-Schlichting disturbance frequencies associated with transition is important for validation of laminar stability theory, and for ruling out possible bypass-induced initiators of transition not related to "natural" T-S amplification. Figure 9 shows a hot-film signal trace from an individual hot-film sensor on the Lear 28/29 wing. With typical signal conditioning, hot-film records such as previously shown in figure 8 cannot be used to measure T-S frequencies; the hot-film signal must be amplified in order to detect these disturbances. The full-scale voltage of the laminar hot-film signal in figure 9 is of the same amplitude as the turbulent signals shown in figure 8. To provide the necessary sensitivity to detect T-S frequencies, the hot-film anemometry was operated with as large an overheat ratio as could be achieved without melting the sensor element, and the signal was given a high external gain prior to recording. Figure 9 shows 0.005 seconds of the data on an expanded time scale, revealing the periodic T-S oscillations. Spectral analysis of these signals can provide information on the most amplified frequencies for correlation with theory.

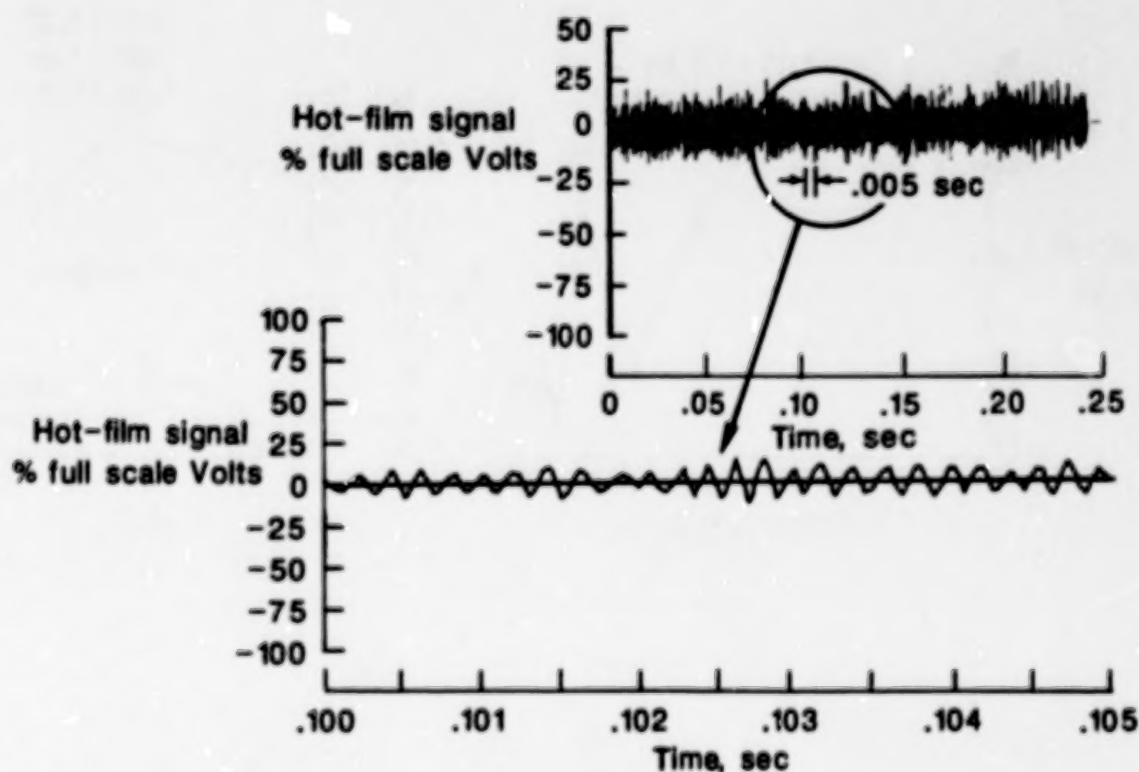


Figure 9

PREDICTED AND MEASURED TOLLMIEN-SCHLICHTING WAVE CHARACTERISTICS

The identification of the Tollmien-Schlichting frequencies associated with transition is important for validation of laminar stability theory and for ruling out possible bypass-induced initiators of transition not related to "natural" T-S amplification. Figure 10 illustrates the power spectral density (PSD) analysis of the T-S frequencies near transition measured in flight on the Lear 28/29 wing. The spectral analysis of the hot-film signal at transition onset shows that the most amplified frequencies occur near 4800 Hz. This frequency is in close agreement with theory. The hot-film spectrum can also show subharmonic or superharmonic frequencies, whereas the linear theory used only accounts for the growth of the fundamental frequency.

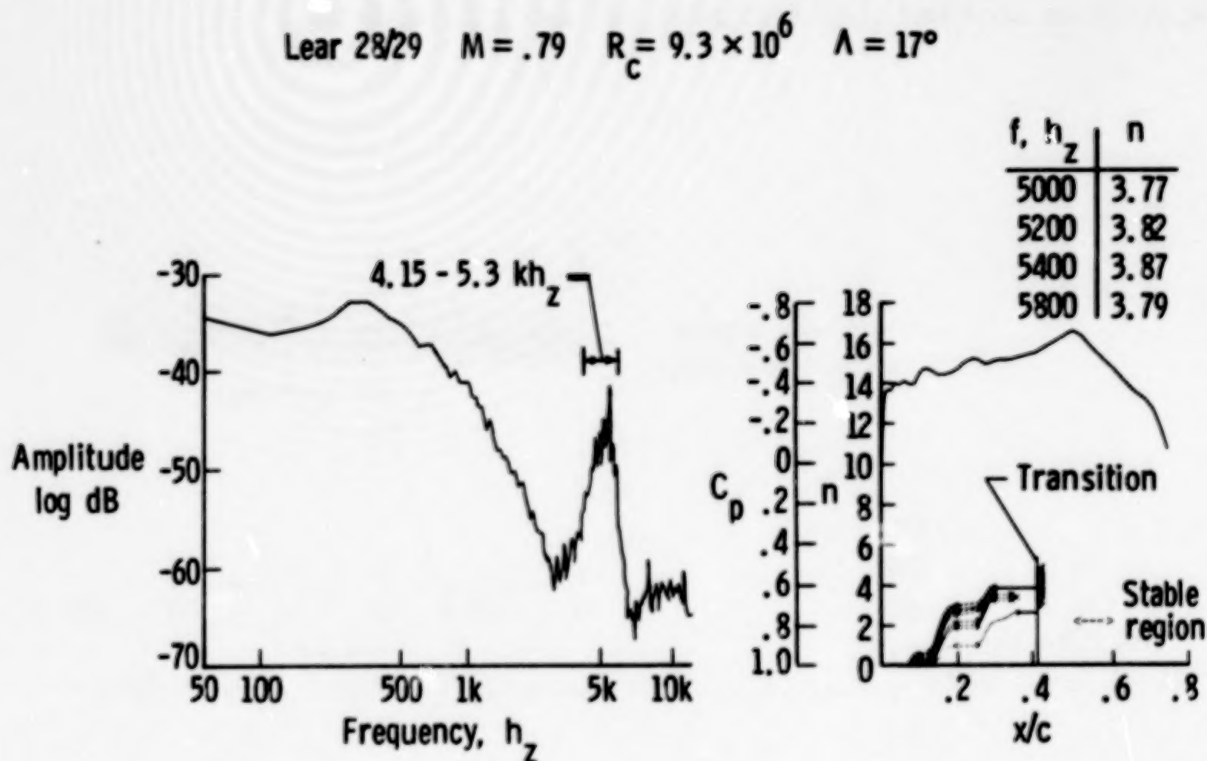


Figure 10

CONCEPTUAL OPERATING PRINCIPLE OF THE LAMINAR SEPARATION SENSOR

For many practical flight conditions of interest, boundary-layer transition may occur at the location of laminar separation, in a pressure recovery far downstream from the airfoil leading edge. This is most likely to occur in dominantly two-dimensional flows at moderate Reynolds numbers, but can occur in three-dimensional flows as well, for example on swept wings at lower Reynolds numbers. It is particularly important to identify the presence of laminar separation and the associated transition for calibration of laminar stability theory. Without such knowledge, it can be misleading to correlate predicted linear amplification ratios (n -factors) with experimental transition locations for the purpose of theory calibration for use in transition prediction. The laminar separation sensor conceptually illustrated in figure 11 provides a simple means for the detection of the presence of laminar separation and the associated transition. The sensor consists of an array of hot-films (three in the illustration) aligned in the direction of the local freestream. The center film is electronically heated by a constant temperature anemometer (CTA). The remaining two films, upstream and downstream of the center element, are incorporated into two legs of a bridge circuit to operate as resistance thermometers in a flow reversal meter (FRM) circuit. Thus, flow direction is detected when the heat from the center element is transported upstream or downstream.

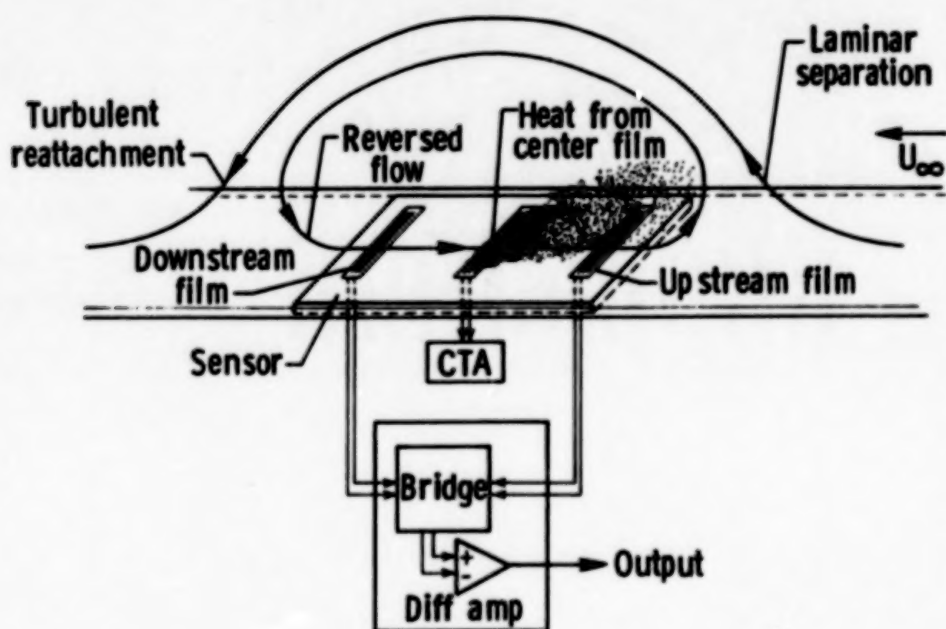


Figure 11

MULTI-ELEMENT LAMINAR SEPARATION ARRAYED HOT-FILM SENSOR

For detailed studies of laminar separation and transition behavior it is desirable to simultaneously measure the locations of separation of the laminar boundary-layer, transition on the bubble, and turbulent reattachment. These measurements have been accomplished using the array of hot-film elements shown in figure 12. With this configuration, the elements were operated in sets of three (sub-arrays) at a time. By switching the sub-arrays sequentially from the front of the sensor to the rear, the details of the laminar separation bubble can be measured.

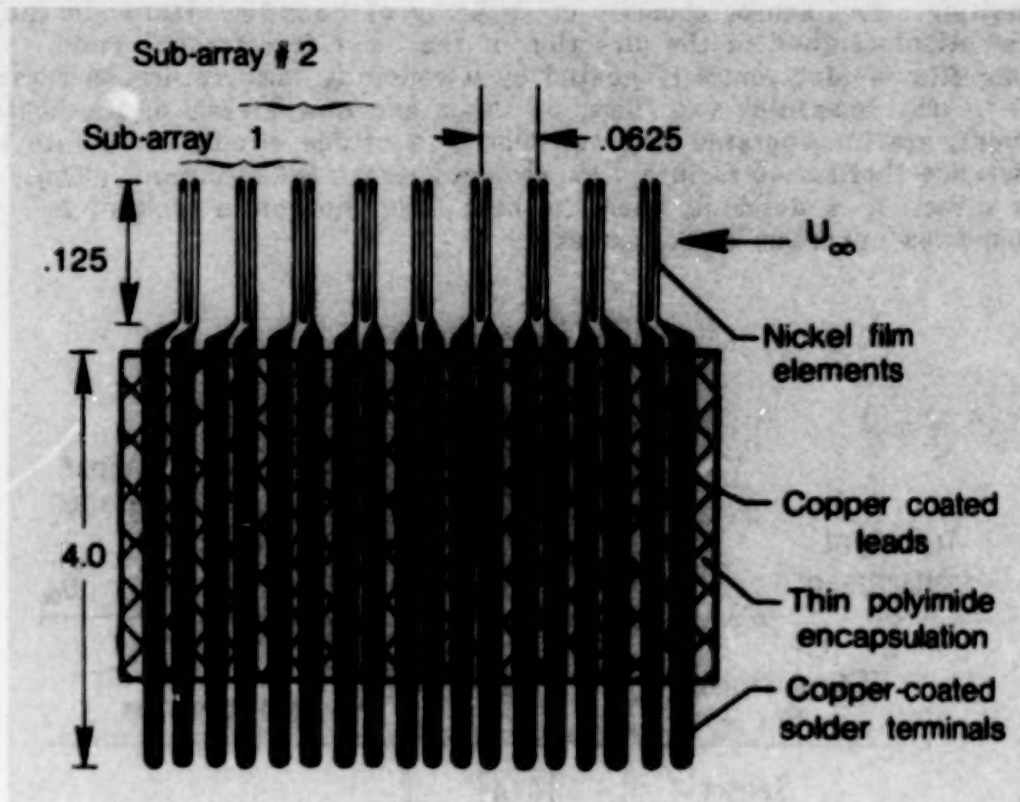


Figure 12

~~ORIGINAL PAGE IS
OF POOR QUALITY~~

LAMINAR SEPARATION SENSOR WIND-TUNNEL EXPERIMENT

In figure 13, the experimental setup is shown of the laminar separation sensor installed on an airfoil model in the Langley 14x22-Foot Wind Tunnel. The arrangement includes the multi-element array with 48 elements at 1/16 inches spacing in the streamwise direction. The sensor is mounted on the upper surface of a 6-inch chord Wortmann airfoil. The model was designed and built at Notre Dame University for research on laminar bubble behavior planned by Dr. T. Mueller. This cooperative research effort also includes planned flight measurements of laminar bubble behavior on the same model to be conducted on a sailplane at Texas A&M University by Dr. S. Miley. The purpose of the Langley wind tunnel experiment shown in the figure was to evaluate the operation of the multi-element laminar separation bubble sensor prior to the planned flight experiments.

~~ORIGINAL PAGE IS~~
~~OF POOR QUALITY~~

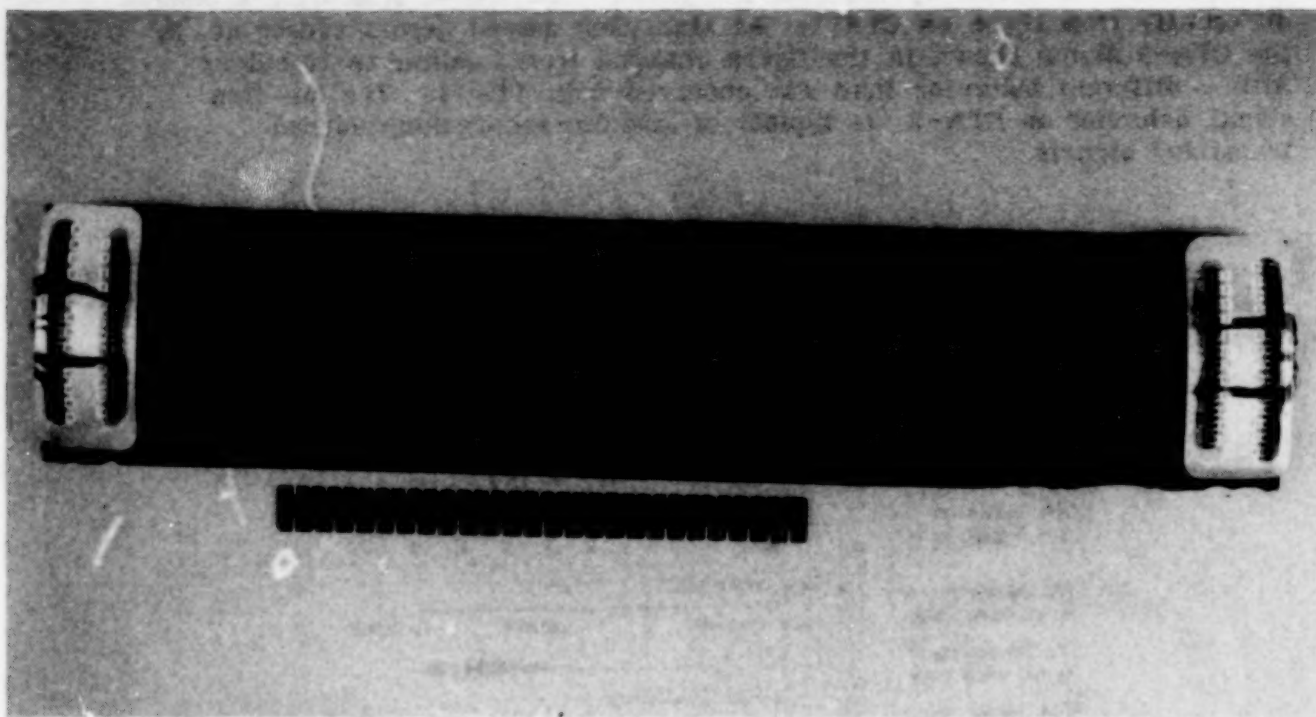


Figure 13

ORIGINAL PAGE
BLACK AND WHITE PHOTOGRAPH

LAMINAR SEPARATION SENSOR DATA SAMPLE

An example of transition and flow direction data from the laminar separation sensor is shown in figure 14. The figure presents oscillograph signals, both from the center elements (CTA's) of each sensor, and from the flow reversal meters (FRM's) monitoring the temperature differences between the outer two elements of each sensor. The data run began at a high angle of attack with transition occurring upstream of the forward-most sensor (no. 1). As shown in the figure, the center element in sensor no. 1 (CTA-1) indicated a turbulent boundary-layer state at the higher angle of attack, with transition moving across the element as angle of attack was reduced, until the element indicated a laminar state. The corresponding data from FRM-1 for this sensor showed that no flow reversal occurs. Thus, transition initiated by T-S amplification had occurred at location no. 1 for these conditions. The same data for sensor no. 3 (located in the middle of the bubble at zero degrees angle of attack) showed that this sensor experienced laminar separation. As angle of attack decreases, the passage of transition is indicated by CTA-2, and flow reversal is shown by the FRM-2 signals. The traces from CTA-2 behave differently from those on CTA-1. As transition moved across sensor no. 2, the CTA-2 signal shown in the figure changed from laminar to turbulent with a different behavior than was observed from CTA-1. The hot-film signal behavior on CTA-2 is typical of laminar-separation-induced transition signals.

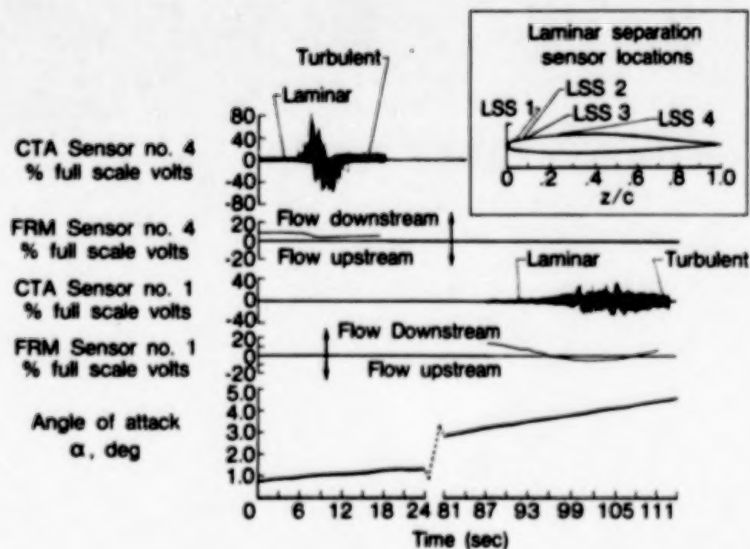


Figure 14

CONCEPTUAL OPERATING PRINCIPLE OF THE CROSSFLOW VORTICITY SENSOR

Near the leading edge of a swept wing, or on a body with non-axisymmetric pressure gradients, longitudinal vortices can develop in the laminar boundary layer, and can cause transition. Locally, these vortices cause spatial variations in heat transfer. As illustrated in figure 15, these variations in heat transfer can provide the source for detecting the wavelength (vortex spacing) and, if nonstationary, the most amplified frequencies of crossflow vorticity. A prototype crossflow vorticity sensor is illustrated in the figure. The spacing of the individual hot-film elements in the sensor is selected to provide accurate wavelength determination. Wind tunnel and flight experiments are planned to evaluate the performance of this sensor concept.

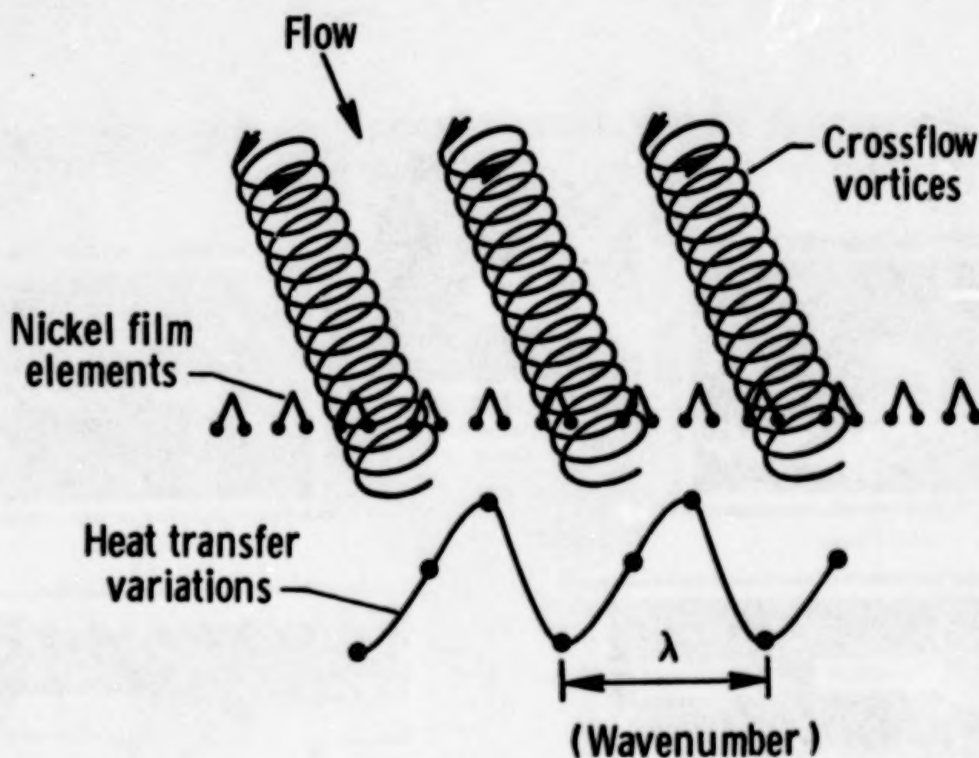


Figure 15

SUBLIMATING CHEMICALS FOR BOUNDARY-LAYER TRANSITION VISUALIZATION

In the past, several methods for in-flight and for wind tunnel visualization of transition have been productively used. One most useful in recent work has been the sublimating chemical method, illustrated in figure 16. It has the advantage of providing, in many situations, data which can be recorded on the ground after the flight or after the wind tunnel is shut down. Unfortunately, sublimating chemicals have two significant disadvantages also. First, only one data point (transition measurement) can be obtained with a coating of chemicals; second, for altitudes above about 20,000 feet, sublimating chemicals or oil flows are impractical to use. For practical purposes, no means have been available in the past for transition visualization at the cruise altitudes of modern aircraft. Results will be presented here to illustrate the use of liquid crystals to overcome some of the shortcomings of prior means for transition visualization. (Fig 17.)

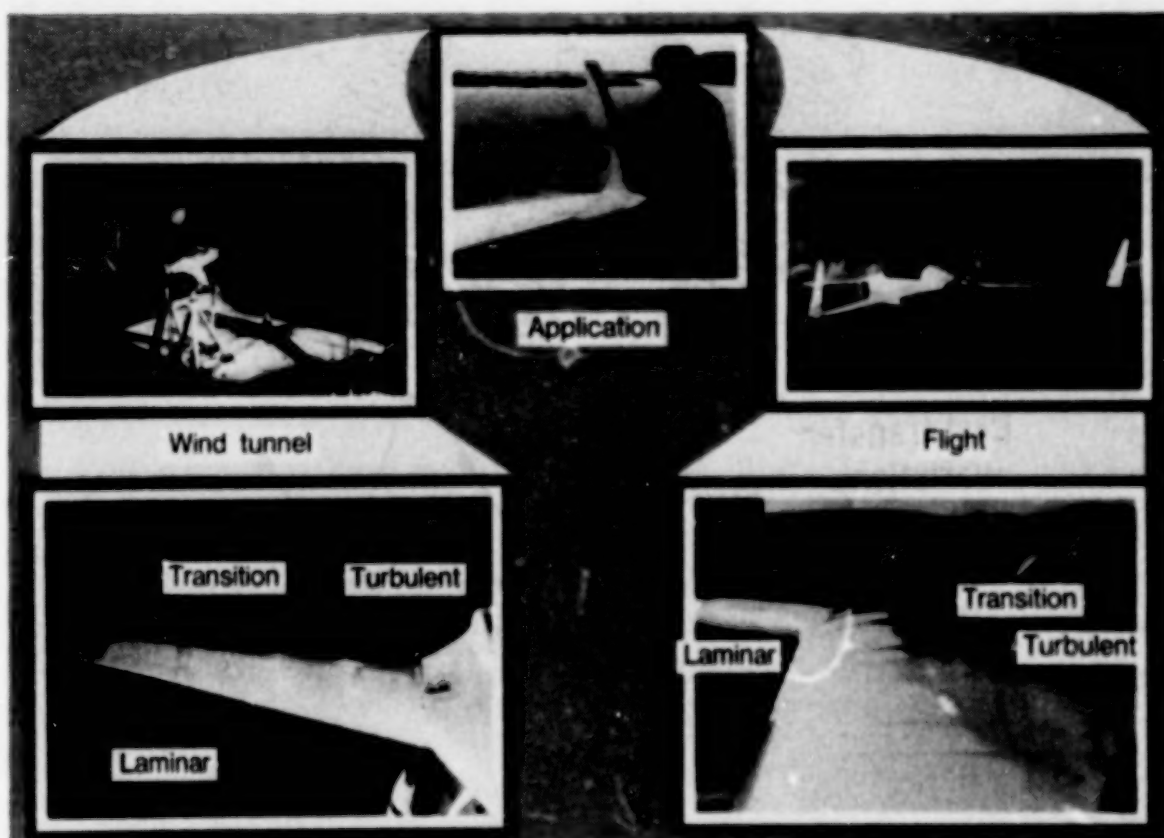


Figure 16

~~ORIGINAL PAGE IS
OF POOR QUALITY~~

HOW LIQUID CRYSTALS INDICATE BOUNDARY-LAYER TRANSITION

Liquid crystals are a peculiar state of matter between solid and liquid. Although they appear as oily liquids, they have certain mechanical properties which are similar to solid crystals. In particular, liquid crystals scatter light very selectively. Within a liquid crystal film, the axis of alignment of molecules is rotated in a helical fashion. The pitch length of the helix is within the range of visible light, and when subjected to certain physical influences, the helix pitch changes and the wavelength of the reflected light changes accordingly. In this fashion liquid crystal coatings change colors in response to changes in shear stress, temperature, pressure, ferromagnetism, and certain chemical vapors. References 4, 5, and 6 describe recent development and applications of the liquid crystal flow visualization method. (Fig 17.)

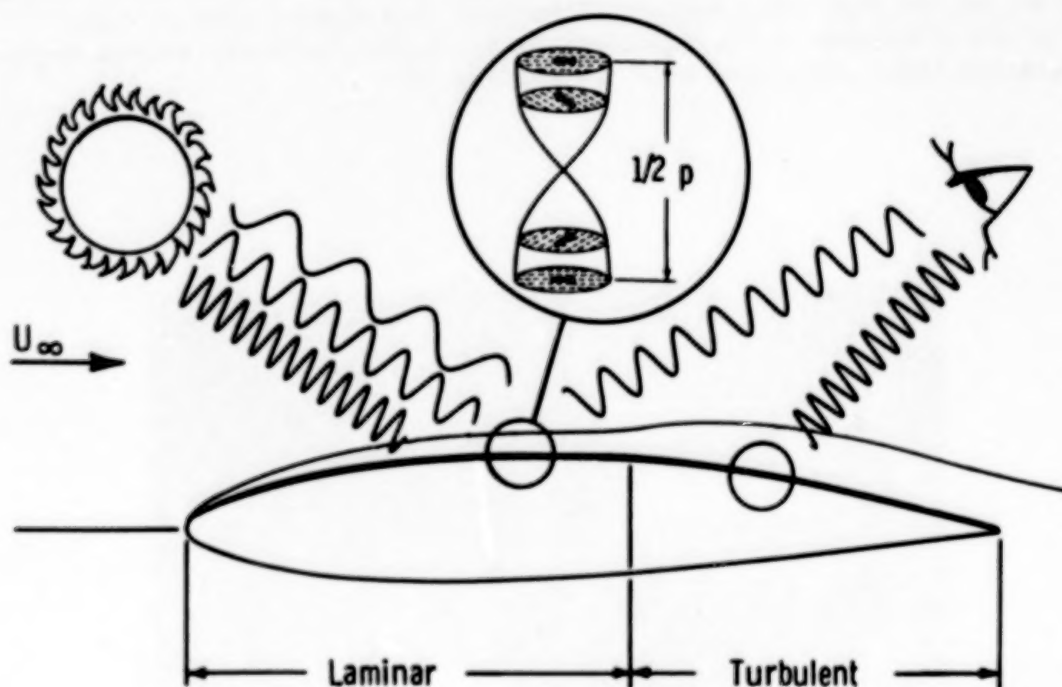


Figure 17

TRANSITION VISUALIZATION IN THE LEAR 28/29 WING USING LIQUID CRYSTALS

Exploratory flight experiments were conducted using many liquid crystal formulations on the wing and winglet of the Lear 28/29. Figure 18 shows the right wing of the airplane. The surface was prepared for testing by spraying on a deep matte flat black paint. A liquid crystal mixture is then formulated for the range of surface temperatures anticipated during the experiment. The mixture is formulated to have the color-play bandwidth (temperature range over which colors will appear) which will be most useful for the particular test needs. Narrower bandwidths (about 5 to 10 degrees Fahrenheit) have proven very useful for providing detailed resolution of transition location. Wider bandwidths (as much as 50 or more degrees Fahrenheit) have been useful for tests which experience wider temperature fluctuations. The liquid crystal material can be either brushed on neat, or thinned about 8 to 1 with solvent and sprayed on. By either technique, the objective is to obtain a very thin liquid crystal film. When applied with the proper film thickness, the liquid crystal coating will neither run, nor collect lint and other debris. The figure shows transition near the 30- to 35-percent chord location at Mach number of .8 at 48,000 feet. The regions of laminar flow appear blue in color, and no color appears in the turbulent areas; a few turbulent wedges appear emanating from tape edges near the leading edge.

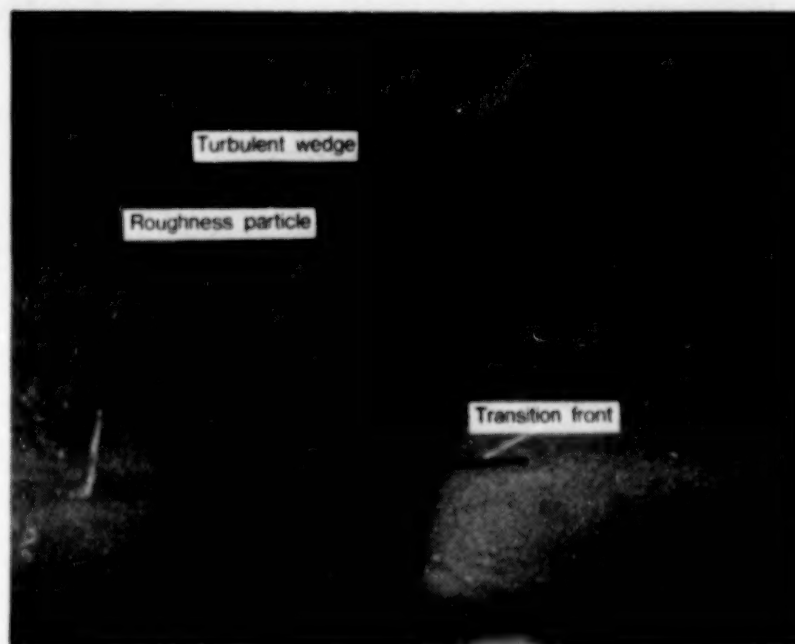
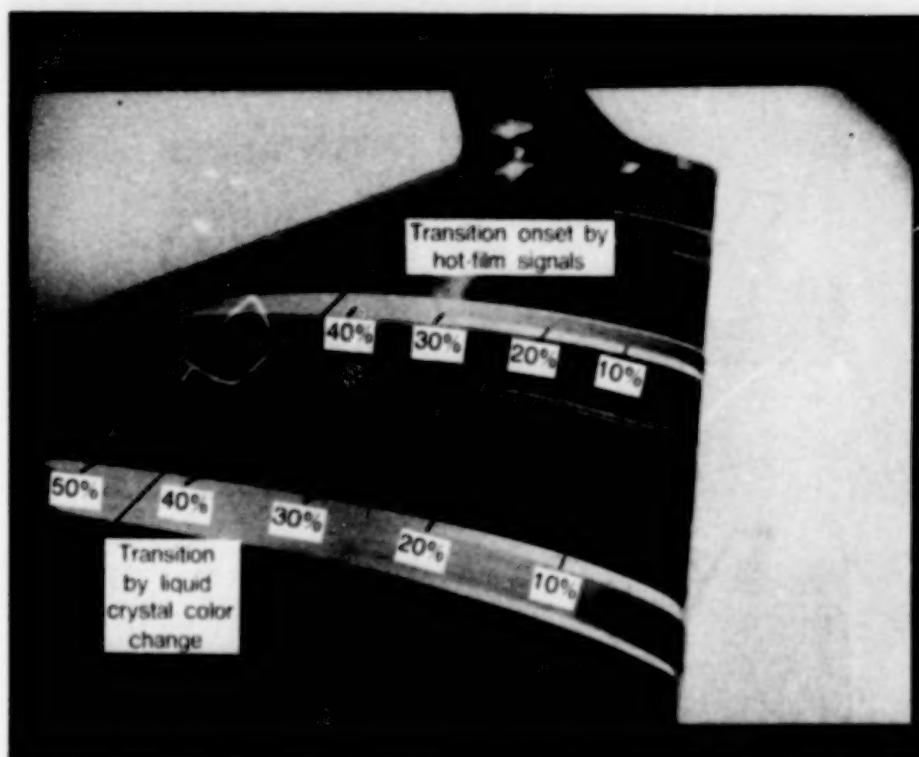


Figure 18

~~ORIGINAL PAGE IS
OF POOR QUALITY~~

CORRELATION BETWEEN LIQUID CRYSTALS AND HOT-FILM TRANSITION INDICATIONS

In order to correlate the transition indications of the liquid crystals with another transition method, a liquid crystal coating was applied to the region on the left wing of the Learjet, where the multi-element hot-film sensor was installed. Figure 19 shows the transition as indicated by the liquid crystal coating at Mach = 0.8 at 48,000 feet. On-board real time observations of the hot-film signals on the oscilloscopes showed that the color change in the liquid crystal coating correlated with the first appearance of turbulent spots in the hot-films. Thus, with transition by Tollmien-Schlichting amplification, the liquid crystals show the onset of the transition region. This differs from the response of sublimating chemicals, which show the end of the transition region.



$M = .8, h = 48,000 \text{ ft}$

Figure 19

ORIGINAL PAGE
BLACK AND WHITE PHOTOGRAPH

~~ORIGINAL PAGE IS
OF POOR QUALITY~~

DYNAMIC RESPONSE OF LIQUID CRYSTAL COLOR CHANGES TO TRANSITION MOTION

An additional objective of the liquid crystal flight experiments on the Lear 28/29 was to qualitatively evaluate the time response of liquid crystal coatings to changes in transition location. Figure 20 shows elapsed time photographs taken from video record of the transition front motions on the winglet. Liquid crystals were brushed on the left winglet and flown at an altitude of 17,150 feet at Mach = 0.525. During this flight the airplane was oscillated to sideslip angles of +3.9 and -3.5 degrees with a period of 0.56 seconds. The resulting maneuver provided variations in local angles of attack and pressure distributions on the winglet, causing transition to move from near the leading edge to near the 70 percent chord location. On this particular airfoil, pressure recovery at small angles of attack begins at about 65 percent chord. The observed movement of transition was in phase with the sideslip oscillation, indicating very rapid time response of the coating.

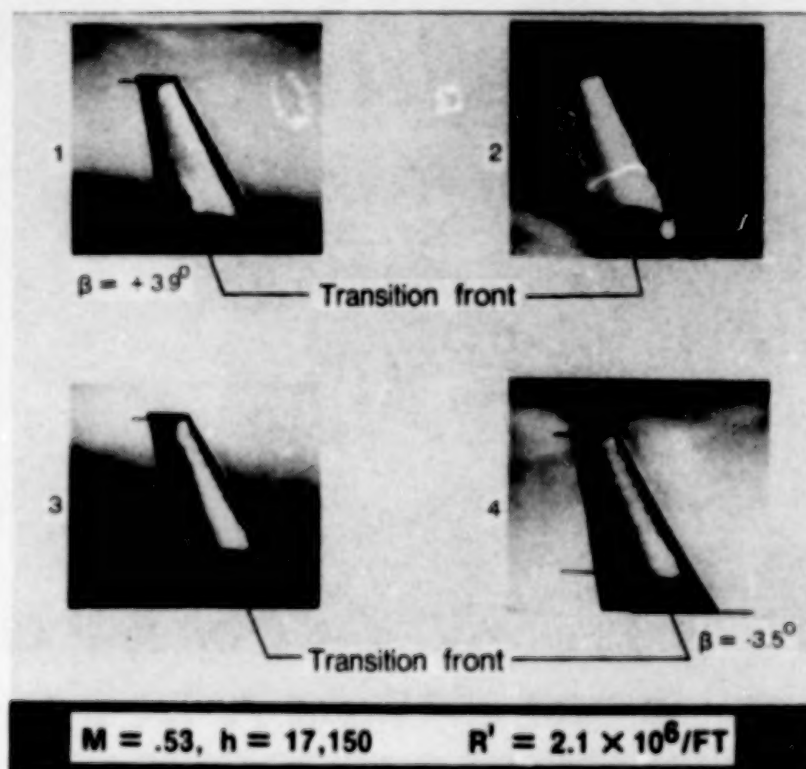


Figure 20

~~ORIGINAL PAGE IS
OF POOR QUALITY~~

LIQUID CRYSTAL TRANSITION VISUALIZATION

The use of liquid crystal coatings in future transition research can provide data which is very difficult to acquire by other means. Such applications include the study of transition mode phenomena which are affected by changes in freestream disturbance states (e.g. acoustics) or by changes in geometry (e.g. sweep). The method overcomes one of the limitations of sublimating chemicals by providing continuous (reversible) indications of transition locations for flight conditions which are difficult to stabilize, such as at high angles of attack or sideslip. Liquid crystals have been used for visualization of shock and shock-induced separation in wind-tunnel testing, and for visualization of transition in underwater testing (ref 7). Further evaluations are planned of encapsulated liquid crystal coatings which may be useful in applications where the thermal response to transition at compressible speeds may be sufficiently strong to provide needed information. Examples include tests on rotating surfaces (high-speed propellers) where the use of neat materials would not be practical. (Fig. 21.)

● Advantages

- Reversible
- Rapid time response
- Non-toxic
- Low cost

● Applications

- Transient test conditions
- Variable wing sweep
- Variable acoustic disturbances
- High altitudes

Figure 21

CONCLUDING REMARKS

Historically, as applications for laminar technology have been pushed to higher speeds, the necessary research tools have developed in parallel. With the progress in use of arrayed hot-film transition mode sensor technology and high-altitude liquid-crystal transition visualization methods, we see this trend in tool development continuing. Applications for laminar flow throughout future aircraft flight envelopes will require detailed knowledge of transition behavior. Transition mode behavior must be understood at the flight conditions of interest (i.e. real Mach numbers and altitudes) if passive and active laminar flow control applications are to be optimized.

REFERENCES

1. Holmes, B.J.: Flight Experiences with Natural Laminar Flow. Natural Laminar Flow Aircraft Certification Workshop. NASA CP 2413, 1986.
2. Obara, C.J.: Boundary-Layer Flow Visualization for Flight Testing. Natural Laminar Flow Aircraft Certification Workshop. NASA CP 2413, 1986.
3. Holmes, B.J.; Croom, C.C.; Gall, P.D.; Manuel, G.S.; and Carraway, D.L.: Advanced Transition Measurement Methods for Flight Applications. AIAA Paper No. 86-9786.
4. Holmes, B.J.; Gall, P.D.; Croom, C.C.; Manuel, G.S.; and Kelliher, W.H.: A New Method for Laminar Boundary Layer Transition Visualization in Flight - Color Changes in Liquid Crystal Coatings. NASA TM 87666, 1986.
5. Holmes, B.J.; Croom, C.C.; Gall, P.D.; Manuel, G.S.; and Carraway, D.: Advanced Boundary Layer Transition Measurement Methods For Flight Applications. AIAA Paper No. 86-9786, presented at Third AIAA Flight Testing Conference, April 2-4, 1986.
6. Gall, P.D.; and Holmes, B.J.: Liquid Crystals for High-Altitude In-Flight Boundary Layer Flow Visualization. AIAA Paper No. 86-2592, 1986.
7. Besch, P.K.; Jones, T.B.; and Sikora, J.P.: Evaluation of Liquid Crystals, Dot Fluids, and Compliant Coatings for Hydrodynamic Flow Visualization on Surfaces. David W. Taylor NSRDC-86/046, 1986.

ADVANCED MEASUREMENT TECHNIQUES-PART II

Introduction
Charles B. Johnson

Flow Quality Measurements
in Compressible Subsonic Flows
P. C. Stainback and C. B. Johnson

Hot-Film System for Transition Detection
in Cryogenic Wind Tunnels
C. B. Johnson, D. L. Carraway, P. C. Stainback,
and M. F. Fancher

Predicted and Hot-Film Measured
Tollmien-Schlichting Wave Characteristics
John P. Stack, Robert B. Yeaton, and J. R. Dagenhart

Remote Detection of Boundary-Layer Transition
by an Optical System
Robert M. Hall, Medhat Azzazy, and Dariush Modarress

Three-Component Laser Doppler Velocimeter
Measurements in a Junction Flow
L. R. Kubendran and J. F. Meyers

Basic Aerodynamic Research Facility
for Comparative Studies
of Flow Diagnostic Techniques
Gregory S. Jones, Luther R. Gartrell, and P. Calvin Stainback

Recent Tests at Langley With a
University of Tennessee Space Institute (UTSI)
Skin Friction Balance
Pierce L. Lawing, A. D. Vakili, and J. M. Wu

Recent Flow Visualization Studies
in the 0.3-m TCT
Walter L. Snow, Alpheus W. Burner, and William K. Goad

INTRODUCTION

Charles B. Johnson
Langley Research Center
Hampton, Virginia

In recent years a number of measurement techniques have been developed and refined for use in fluid mechanic flow diagnostics. These diagnostic tools have been primarily used in wind tunnels and, in several instances, have been extended for use in flight. The purpose of this paper is to present a brief review of some of the advanced techniques that have been developed by eight groups of researchers. The eight specific advanced techniques encompass five basic areas of measurements (fig. 1).

The first section describes the basic measurement of flow quality by a recently developed technique which uses a three-wire hot-wire probe to obtain velocity, density, and total temperature fluctuation in subsonic compressible flow. The three-wire-hot wire probe technique was primarily developed for use in the determination of wind tunnel disturbance levels, but, as indicated in this paper, it has also been used in flight (refs. 1, 2, 3, and 4).

The second section describes the basic type of measurement of boundary-layer transition detection by two somewhat different hot-film methods and by an optical method. The segment including the first hot-film method discusses the recent developments with a specialized hot-film system for on-line transition detection in cryogenic wind tunnels such as the U.S. National Transonic Facility (refs. 4, 5, 6, 7, 8, and 9). The segment describing the second hot-film technique discusses the measurement and theoretical validation of the existence of Tollmien-Schlichting waves that were obtained with a different hot-film system (ref. 10). The third transition detection technique discussed involves a recently developed nonintrusive optical system which uses a high-resolution interferometer coupled with electronic data acquisition system that senses changes in density fluctuation in the boundary layer to indicate the transition region (ref. 11).

The third type of basic measurement encompasses the general area of flow diagnostics (i.e., flow quality) made with two types of three component laser velocimeter (LV) systems. The first LV system discussed is a single-axis five-beam system which indicates excellent resolution with the longitudinal and vertical (u and v) components of velocity but poor resolution with the spanwise component (w) of velocity due to a high degree of nonorthogonality between the laser beam and w component of velocity (refs. 12, 13, and 14). The second LV system discussed utilizes three orthogonal beams (and fringe patterns) for use in a "Basic Aerodynamic Research Facility" (ref. 15) which has test section side walls and ceiling made of glass to accommodate the "orthogonal LV" technique.

The fourth type of basic measurement is skin friction. This section describes a unique moving belt balance which was developed for the direct measurement of the wall shear stress (refs. 16, 17, and 18). Measurements with the moving belt balance made on the test section side walls of the two Langley facilities are presented.

The fifth basic type of measurement is flow visualization as applied to cryogenic wind tunnels. This section describes various background shadowgraph measurements made at different pressures and temperatures in a cryogenic tunnel (ref. 19). The modifications to the "test section optical access" that were required for an interference free background shadowgraph are discussed.

BASIC AREAS OF MEASUREMENTS

- Flow quality: three-wire hot-wire probe
- Transition detection: two hot-film techniques and an optical technique
- Flow diagnostics: two LV systems
- Skin friction measurements: moving belt balance
- Flow visualization: shadowgraphs in cryogenic tunnels

Figure 1

N90-12521

**FLOW QUALITY MEASUREMENTS
IN COMPRESSIBLE SUBSONIC FLOWS**

**P. C. Stainback and C. B. Johnson
Langley Research Center
Hampton, Virginia**

MEASUREMENTS USING THREE-WIRE PROBE TECHNIQUE

Until recently, very few hot-wire measurements were reported for subsonic compressible, transonic, and low supersonic flows. There are several reasons for this. First, for a given probe, the heat transfer from a heated wire oriented normal to the flow is a function of the three fluid variables: velocity, density, and total temperature. This makes the calibration of the hot-wire probe very time consuming. Also, since the heat transfer from the hot wire is a function of the combined effect of these three fluid variables, it is difficult to separate the individual effects of these variables. Finally, the dynamic pressures in these speed ranges are high and wire breakage can be excessive due to aerodynamic loads and, of course, any particles in the flow can cause wire failure.

Before the development of the three-wire hot-wire probe (fig. 1, refs. 1 and 2), the application of hot-wire anemometry to compressible subsonic and transonic flow was similar to that existing in high supersonic flow. In this earlier application, the heat transfer from hot wires was considered to be a function of mass flow and total temperature (i.e., two-parameter method) rather than the individual quantities of velocity, density, and total temperature. The results using a two-parameter method made the calibration of hot-wire probes and data reduction somewhat less complex, and fluctuating quantities using this technique have been reported for compressible subsonic, transonic, and low supersonic flows. The two-parameter method represented an advance in hot-wire anemometry and renewed interest in the problems encountered in making such measurements in these flow regimes. However, the two-parameter method requires several restrictive assumptions and required additional measurements to obtain quantitative flow quality results. In contrast, the three-wire hot-wire probe technique requires only the assumption usually made for hot-wires anemometry with small perturbations (refs. 1, 2, 20, and 21).

The purpose of this paper (fig. 1) is to: (1) re-examine the heat transfer from a hot-wire probe in the compressible subsonic flow regime, (2) describe the three-wire hot-wire probe calibration and data reduction technique used to measure the velocity, density, and total temperature fluctuations, and (3) present flow quality results obtained in the Langley 0.3-Meter Transonic Cryogenic Tunnel (0.3-m TCT) and in flight with the NASA JETSTAR from the same three-wire hot-wire probe.

- Compare wind tunnel and flight measurements with same probe and data reduction technique
- Langley 0.3-meter transonic cryogenic tunnel flow quality (8 by 24-in. test section)
- Jet Star flights at Dryden to obtain atmospheric turbulence (over Mojave Desert)
- Three-wire hot-wire probe method:
 - No restrictive assumptions — such as used with the single wire technique
 - Data reduction technique separates velocity, density and total temperature fluctuations

GENERAL HOT-WIRE EQUATIONS

The mean voltage measured across a given hot wire, oriented normal to the flow, is a function of velocity, density, total temperature, and wire temperature. The total change in the mean voltage due to a change in the independent variables can be obtained from the calculus. If a constant temperature hot-wire anemometer is used, $dT_w = 0$ within the limits of the ability of the feedback amplifier to hold the temperature of the wire constant. The equation for the fluctuating quantities and the definitions of the three sensitivity coefficients are given in figure 2. Attempts usually are made to solve this equation by using the mean square values of e' . However, this method results in an equation with six unknowns. The squared equation can, in principle, be solved by operating a single wire at six overheats and solving a system of six equations for the six unknowns. However, when this was tried, difficulties were encountered inverting the 6×6 matrix.

$$E = f(u, \rho, T_t, T_w)$$

$$\left(\frac{e'}{E}\right) = S_{\bar{u}}\left(\frac{u'}{\bar{u}}\right) + S_{\bar{\rho}}\left(\frac{\rho'}{\bar{\rho}}\right) + S_{\bar{T}_t}\left(\frac{T_t'}{\bar{T}_t}\right)$$

$$S_{\bar{u}} = \left(\frac{\partial \log E}{\partial \log \bar{u}}\right)_{\bar{\rho}, \bar{T}_t, T_w}$$

$$S_{\bar{\rho}} = \left(\frac{\partial \log E}{\partial \log \bar{\rho}}\right)_{\bar{u}, \bar{T}_t, T_w}$$

$$S_{\bar{T}_t} = \left(\frac{\partial \log E}{\partial \log \bar{T}_t}\right)_{\bar{u}, \bar{\rho}, T_w}$$

Figure 2

EQUATIONS FOR THREE-WIRE HOT-WIRE PROBE

The form of the general hot-wire equation in figure 2 suggests that the instantaneous values of u' , ρ' , and T_t can be obtained from the solution of an equation with three unknowns. The means used for obtaining a solution for the three instantaneous quantities was to fabricate a single probe with three hot wires normal to the flow, with each wire operated at a slightly different overheat. Then an equation can be written for each of the three wires as shown in figure 3 and the set of three equations can then be solved for the three unknowns, u' , ρ' , and T_t , as a function of time. Prior to the solution of the sets of equations, the sensitivity coefficients must be determined from a calibration which uses the measured values of E , u , ρ , and T_t (ref. 2). Once the fluctuating quantities are obtained conventional statistical techniques can be used to obtain mean and root mean square (RMS) values, auto correlations, cross products, spectra, etc.

In principle, the ability to obtain fluctuating quantities using the three-wire hot-wire probe technique can be extended into the transonic and low supersonic flow regimes without difficulty except those typically associated with lengthy calibration and possible wire breakage.

$$\left(\frac{e'}{E}\right)_i = S_{\bar{u},i} \left(\frac{u'}{\bar{u}}\right) + S_{\bar{\rho},i} \left(\frac{\rho'}{\bar{\rho}}\right) + S_{\bar{T}_t,i} \left(\frac{T'_t}{\bar{T}_t}\right) \quad i \text{ (hot wires)} = 1, 2, 3$$

$$u', \rho', T'_t, \dot{m}' \quad (\text{instantaneous values})$$

$$\overline{u'\rho'}, \overline{u'T'_t}, \overline{\rho'T'_t} \quad (\text{mean of cross product terms})$$

From instantaneous values statistical values are determined

$$\tilde{u}, \tilde{\rho}, \tilde{T}_t, \tilde{m}, \text{ etc}$$

Figure 3

THREE-WIRE HOT-WIRE PROBE

The hot-wire probe which was used to obtain flow quality data in the 0.3-m TCT and in flight with NASA JETSTAR is shown in figure 4. The probe was fabricated with six "needles" made from piano wires which were used to mount the three hot wires normal to the flow. The needles, which were about 1 inch long, were glued into a section of six-hole ceramic tubing. The ceramic tubing, with the needles and lead wires, was glued into a section of 0.250-inch stainless-steel tubing. Platinum-coated tungsten wire having a diameter of 0.0004 inch was mounted between the tips of the needles with about 1/4 circle slack in each wire. The wires were about 0.10 inch long and about 0.040 inch apart. Each of the three wires on the probe was operated with its own constant temperature hot-wire anemometer and signal condition system.

For the wind tunnel test, the hot-wire probe was mounted in the 8- by 24-inch test section of the 0.3-m TCT, (both floor and ceiling 5 percent open), in a mounting position normally used for the drag rake. The sensing elements were located midway between the centerline of the tunnel and the ceiling at an axial position approximately at the center of turntables which were usually used to hold two-dimensional models. A shorting probe with three low resistance wires attached to pairs of needles was positioned below and rearward of the active probe. The shorting probe with leads going to the anemometer was used to balance out any lead resistance changes which occurred due to changes in ambient temperature. The resistances of the shorting probe and leads were matched to those of the active probe and both sets of leads followed the same path from the tunnel test section to the anemometers in order to ensure that each set of leads was subjected to the same temperature environment. The shorting probe was used to balance out any lead resistance changes which occurred due to changes in temperature during the test program. This procedure was followed during the wind tunnel (ref. 2) and flight tests.

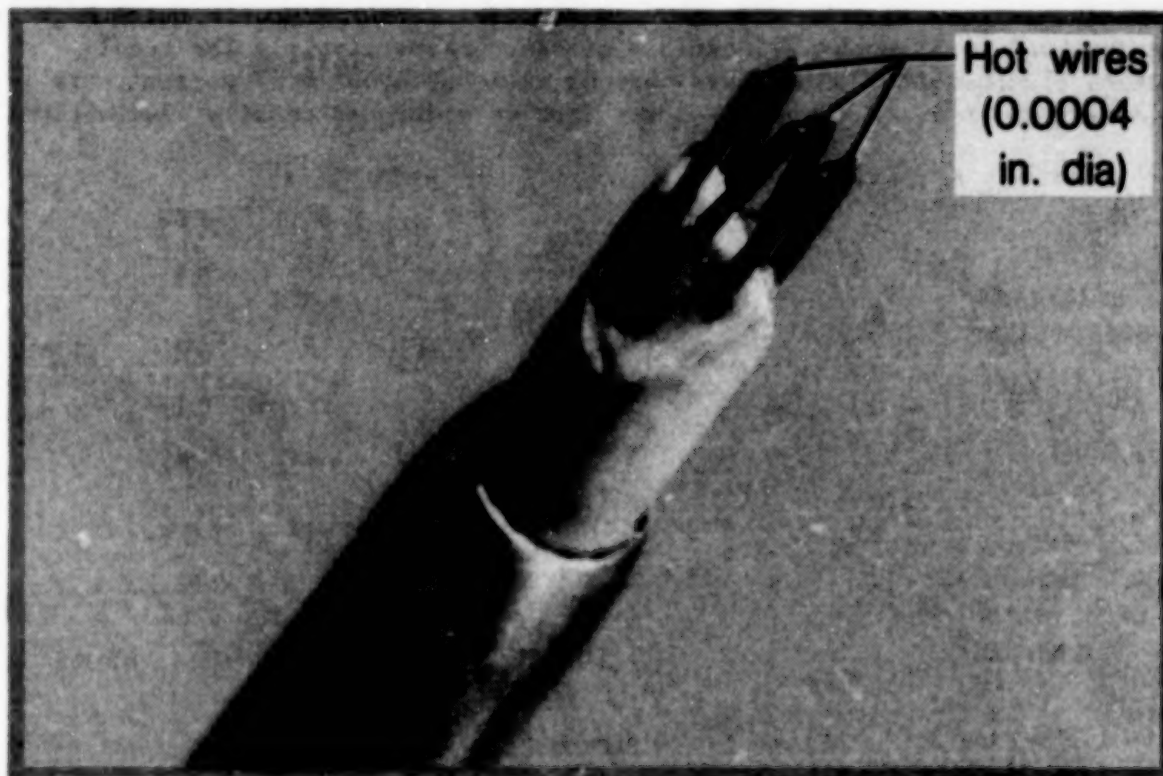


Figure 4

VELOCITY, DENSITY, AND TOTAL TEMPERATURE FLUCTUATIONS FROM 0.3-M TCT USING THREE-WIRE HOT-WIRE PROBE

The RMS values of the velocity, density and total temperature, normalized by their respective mean values (fig. 5) were calculated from the large amount of detailed data taken during the calibration of the three-wire hot-wire probe. The calibration of the three hot wires (ref. 2) (to obtain wire sensitivity coefficient indicated in figs. 2 and 3) was started at a condition of maximum dynamic pressure ($V_\infty = 747$ ft/sec, $p_t = 48$ psia, and $T_t = 504^\circ\text{R}$). The three wires were operated at overheat ratios of 1.6, 1.8, and 2.0). A square wave signal was used to set approximately equal time constants for the three wires. The upper frequency response of the hot-wire anemometry system was about 20 kHz. During the calibration, the velocity was varied from 747 to 220 ft/sec in five even increments with the mean and fluctuating voltages recorded on line at each velocity. In addition, the fluctuating voltages were recorded on odd-numbered tracks of a seven-track tape recorder. As the velocity was reduced, the total pressure was decreased to maintain a constant density at this fixed total temperature condition. The density was reduced in three steps with a similar velocity variation for each of the density steps. The same procedure with varying velocities at constant density was repeated for total temperatures of 522°R and 540°R .

This constant parameter method of calibration, which is a cumbersome procedure, is not required if the multiple linear regression technique is used to obtain the sensitivity coefficients. However, the constant parameter method is useful for determining the form of the correlation equation to be used for the multiple regression method (refs. 2, 20, and 21).

The three sets of fluctuating quantities (fig. 5) were obtained from the simultaneous solution of the hot-wire equation in figure 3 for the three hot wires. The data indicate a significant increase in \tilde{u} , \tilde{p} , and \tilde{T}_t with increasing unit Reynolds number for a given Mach number and also indicate an increase with increasing Mach number. In general, the velocity and density fluctuations are quite high and have maximum values of about 7.5 and 8.4 percent, respectively. The total temperature fluctuations, which have maximum value of about 0.57 percent, are approximately an order of magnitude lower than velocity and density fluctuations.

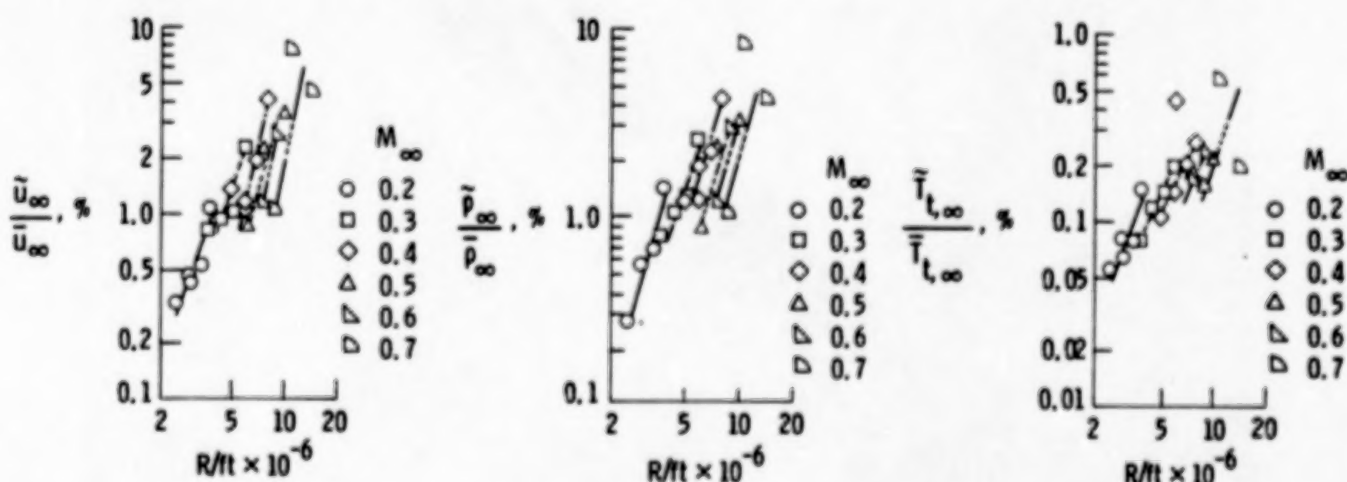


Figure 5

MASS FLOW FLUCTUATIONS FROM THREE-WIRE HOT-WIRE PROBE DATA

In the past, mass flow fluctuations were often used to infer wind tunnel disturbance levels in a manner similar to the way velocity fluctuations (as shown in fig. 5) were used to quantify wind tunnel disturbance levels. However, the mass flow fluctuations are about an order of magnitude lower than velocity fluctuations at the higher Mach numbers and Reynolds numbers. An example of this can be seen from the calculation of the normalized mass flow fluctuations (fig. 6) from the same three-wire hot-wire probe data that were used to determine the velocity and density fluctuations in figure 5. The mass flow RMS fluctuations were calculated from the sum of the instantaneous velocity and density values. The maximum value of the mass flow fluctuations is about 0.78 percent compared to a maximum value of 7.5 percent for the velocity fluctuations at the same conditions. The reduction in the mass flow fluctuations is predominately due to the fact that at high subsonic Mach numbers the major disturbances in the test section were due to upstream propagation of sound from the diffuser. For these conditions, the velocity and density fluctuations are anti-correlated, with a correlation coefficient nearly equal to -1.0, thereby resulting in a lower value for the mass flow fluctuations (refs. 2 and 4).

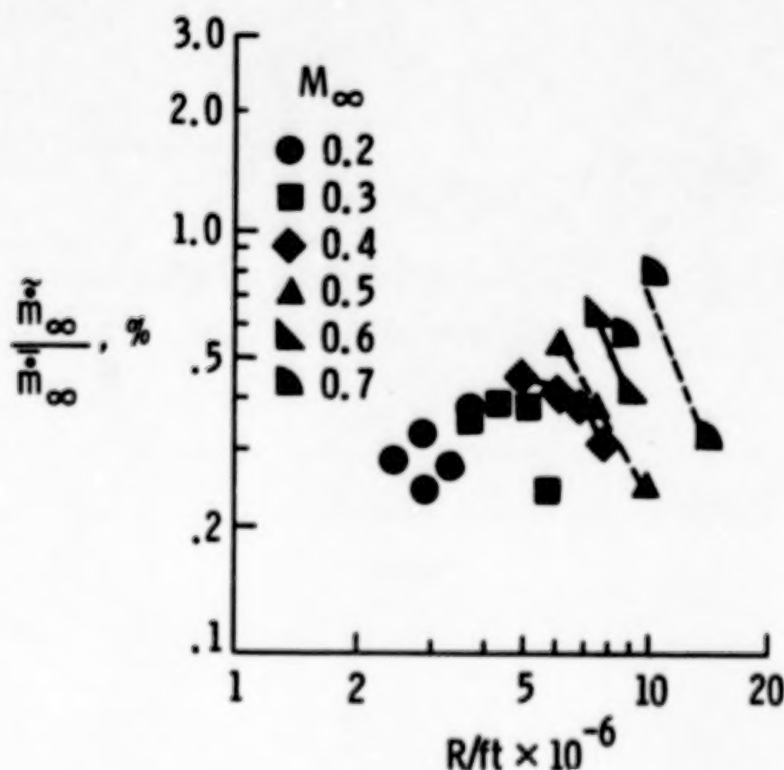


Figure 6

NASA JETSTAR WITH THREE-WIRE PROBES MOUNTED ON WING

Flight tests, which were conducted at the Dryden Flight Research Facility, using the Lockheed JETSTAR were made with the same three-wire hot-wire probe used in the 0.3-m TCT tests (figs. 4, 5, and 6). A photograph of the NASA JETSTAR (fig. 7) indicates the location of the hot-wire probes on the leading edge on the left-hand portion of the wing.



Figure 7

~~ORIGINAL PAGE IS
OF POOR QUALITY~~

CLOSE VIEW OF THREE-WIRE PROBES MOUNTED ON LEADING EDGE OF JETSTAR WING

A closeup view of the probes (fig. 8) indicates the type of installation used to mount the three-wire hot-wire probe holders on the leading edge of the wing. The dummy probe was mounted nearer to the fuel tanks where possible flow interferences could occur. The active probe was mounted in a more outboard position, in what was considered to be a more interference-free flow field. Note that when this photograph was taken, the leading-edge flap was lowered to facilitate the installation of the two probes on the leading edge of the wing.

The dummy probe, or shorting probe, contained three low resistance wires across the three pairs of needles. This probe was used to balance out any change in lead resistance due to ambient temperature changes, in the aircraft. A similar procedure with a dummy probe was used during the flow quality test in the 0.3-m TCT (fig. 5 and ref. 2).

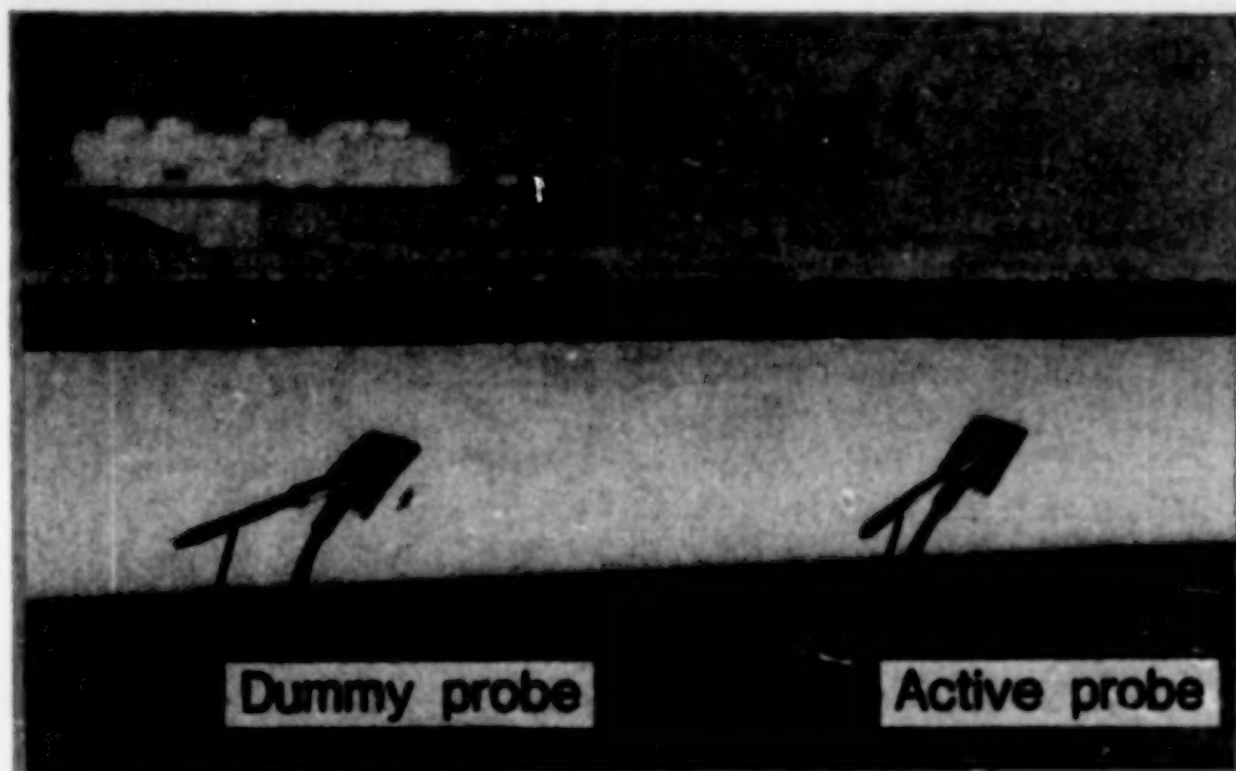


Figure 8

ORIGINAL PAGE
BLACK AND WHITE PHOTOGRAPH

THREE-WIRE PROBE DATA ACQUISITION EQUIPMENT IN JETSTAR

A photograph of the three-wire hot-wire probe anemometry data acquisition system mounted in the NASA JETSTAR (fig. 9) was essentially the same acquisition system used in the flow quality test in the 0.3-m TCT (ref. 2). Three commercially available, constant temperature anemometers (CTAs) (DISA 55N system with 55M10CTA standard bridge) were used in both the wind tunnel and flight tests. The mean and RMS voltages were recorded by hand from the respective instruments during the flight. The signal conditioner was used to bandpass the signal (1.0 Hz lower frequency cutoff and 20 kHz upper frequency cutoff) and amplify the signal as required. The fluctuating and mean voltages were also recorded on a 28-track tape recorder used specifically for the flight test. The anemometers were operated by batteries in an effort to eliminate 60 Hz electrical noise present in the JETSTAR.

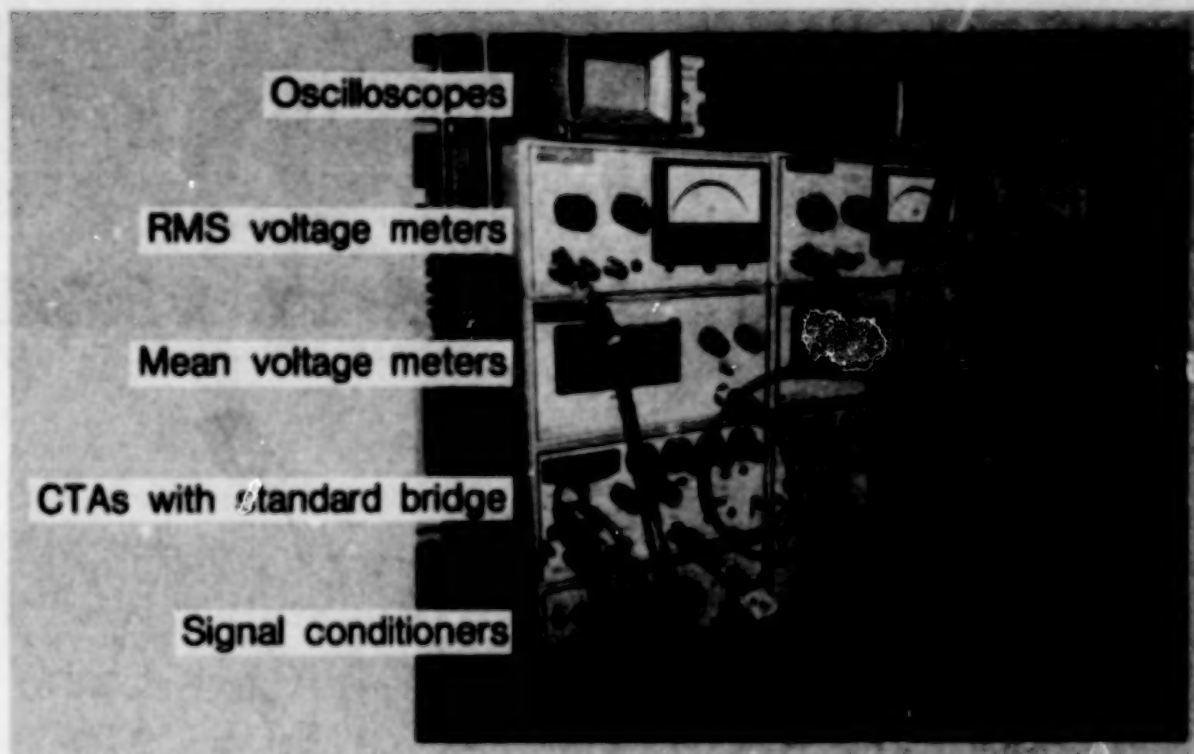


Figure 9

ORIGINAL PAGE
BLACK AND WHITE PHOTOGRAPH

ORIGINAL PAGE IS
OF POOR QUALITY

ATMOSPHERIC TURBULENCE FLIGHT DATA FROM THREE-WIRE PROBE

The RMS values of velocity, density, and total temperature, normalized by their respective free-stream quantities (fig. 10), were obtained with the three-wire hot-wire probe in a flight with the NASA JETSTAR in January 1982. The data were obtained at an altitude of 5000 feet over the Mojave Desert at Mach numbers of 0.2, 0.3, 0.4, and 0.5. The floor of the desert, relative to sea level, ranges from about 2200 to 2400 feet, which meant the flight altitude was about 2700 feet relative to the ground. The proximity of the desert floor, coupled with the high winds that generally prevail during the time of year of the flight, accounted for the rather high level of atmospheric turbulence (i.e., normalized RMS velocity fluctuation). The turbulence level and the extremely rough "ride quality" would put these measurements in the classification of "clear air turbulence."

Previous measurements of atmospheric turbulence (refs. 22 and 23), in terms of normalized RMS mass flow fluctuations, which were made at altitudes of 12, 29, and 39 thousand feet and Mach numbers from 0.28 to 0.80, indicated levels an order of magnitude less than those obtained with the three-wire probe (fig. 10). The density fluctuations (fig. 10) were somewhat lower than the velocity fluctuations, and the total temperature fluctuations were even lower. A comparison of the flight data in figure 10 with the wind tunnel data in figure 5 (from the identical hot wire probe) indicates that all three fluctuating quantities from the flight data are of at least an order of magnitude lower than the wind tunnel data.

M_∞	$R/ft \times 10^{-6}$	$\frac{\tilde{u}_\infty}{\bar{u}_\infty}, \%$	$\frac{\tilde{\rho}_\infty}{\bar{\rho}_\infty}, \%$	$\frac{\tilde{T}_{t,\infty}}{\bar{T}_{t,\infty}}, \%$
0.2	1.24	0.6203	0.2029	0.07037
0.3	1.85	0.7014	0.2620	0.10630
0.4	2.47	0.4366	0.1339	0.08333
0.5	3.09	0.4503	0.1329	0.07231

Figure 10

SPECTRA OF VELOCITY, DENSITY, AND TOTAL TEMPERATURE FLUCTUATIONS FROM FLIGHT MEASUREMENTS OF ATMOSPHERIC TURBULENCE

Spectra were obtained from the flight measurements using the three-wire hot-wire probe at an altitude of 5000 feet for a Mach number of 0.5 and a Reynolds number about 3 million per foot (fig. 11). The slopes of the spectra for the velocity, density, and total temperature fluctuations appear to follow the expected $-5/3$ slope for a region of equilibrium turbulence. In this region, referred to as the inertial subrange, there is no production or dissipation and the spectra will have a $-5/3$ slope. The 60-Hz noise and its harmonics are present to some extent up to the limit of the spectra.

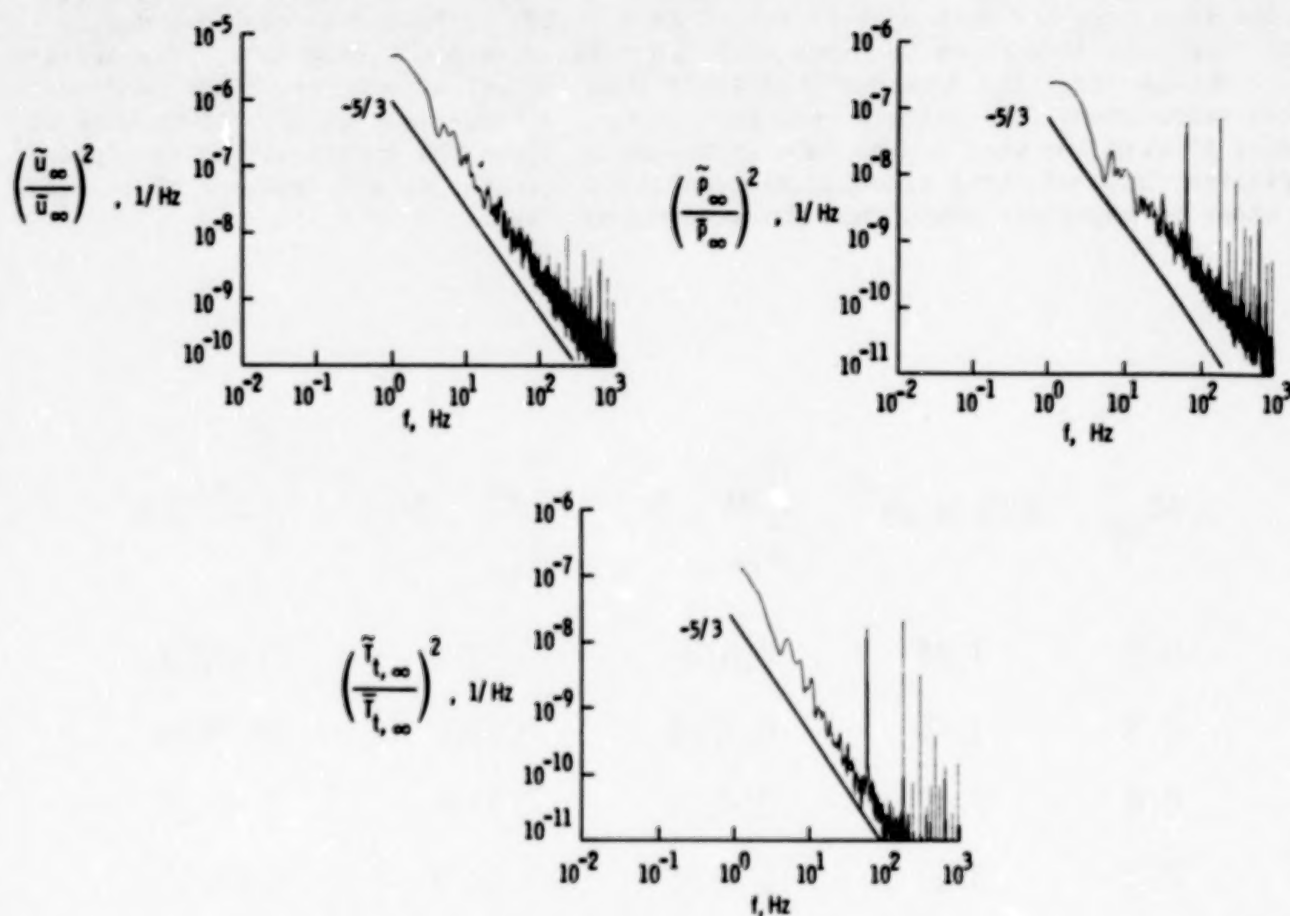


Figure 11

COMPARISON OF SEVERAL MEASUREMENTS OF ATMOSPHERIC TURBULENCE

The atmospheric turbulence measurements made with the three-wire hot-wire probe are compared with other atmospheric flight measurements (fig. 12) which include high and low altitude clear air turbulence, cumulus turbulence, and thunderstorm turbulence (ref. 24). The comparison, which is made in terms of the power spectral density versus reduced frequency, indicates good agreement between the three wire probe data and the other clear air turbulence data. All the data shown indicate a $-5/3$ slope over the entire range of reduced frequencies. The high and low altitude clear air turbulence data (ref. 24) was measured with sensors that had a low pass frequency cutoff of 16 Hz. In contrast, three-wire hot-wire probe data had a low pass frequency cutoff of 2500 Hz and thus extended out to reduced frequencies that were about two orders of magnitude higher than the other clear air turbulence data. It is interesting to note that the three wire data and the high and low altitude clear air turbulence data fall into a nearly linear band. The fact that the three sets of data "line up" is believed to be somewhat fortuitous.

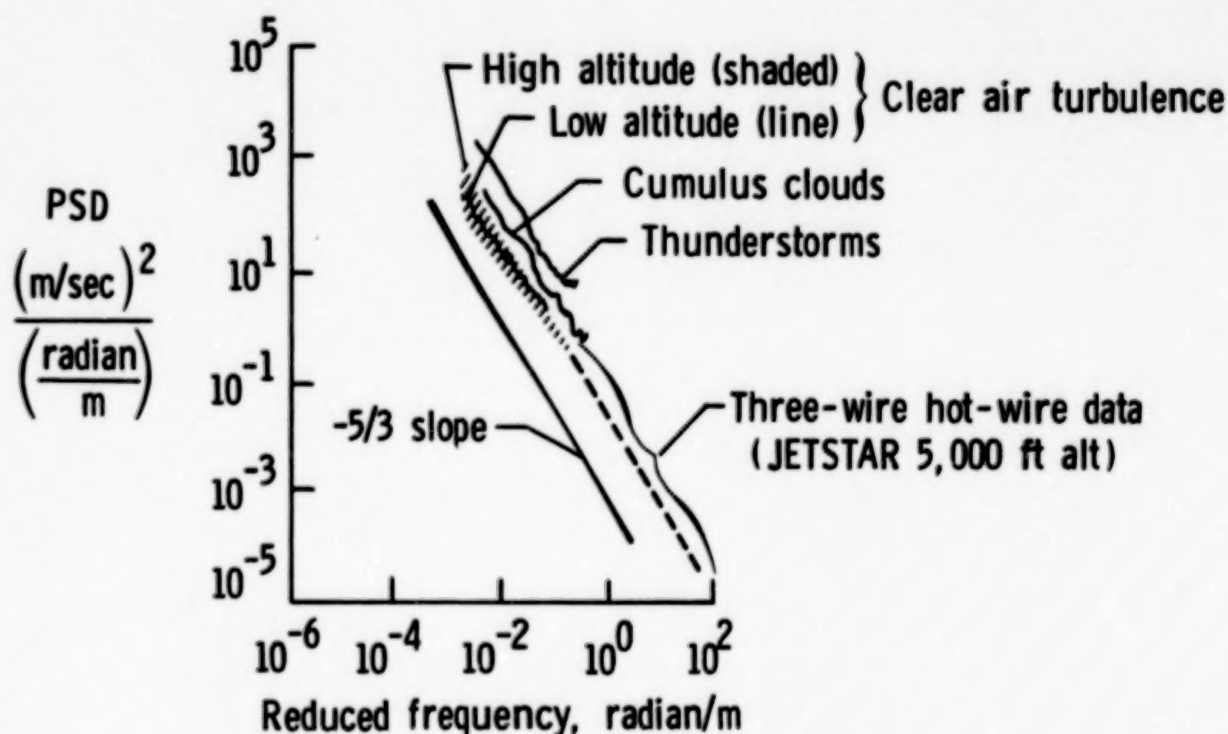


Figure 12

HOT-FILM SYSTEM FOR TRANSITION DETECTION IN CRYOGENIC WIND TUNNELS

C. B. Johnson, D. L. Carraway, and P. C. Stainback
Langley Research Center
Hampton, Virginia

M. F. Fancher
Douglas Aircraft Company
Long Beach, California

INTRODUCTION TO HOT-FILM SYSTEMS FOR CRYOGENIC WIND TUNNELS

It is well known that the determination of the location of boundary-layer transition is necessary for the correct interpretation of aerodynamic data in transonic wind tunnels such as the U.S. National Transonic Facility (NTF) and the Langley 0.3-Meter Transonic Cryogenic Tunnel (0.3-m TCT) (refs. 5 and 22). In the past, hot-film gauges (hot films) have proved to be one of the best devices for detecting the beginning and end of boundary-layer transition on models in conventional (near-ambient temperature and pressure) wind tunnels (ref. 7). However, the types of hot films used in the conventional wind tunnels are unsuitable for use in cryogenic wind tunnels, such as the NTF, because of the large range of temperatures (cryogenic to ambient) and because of the high Reynolds numbers encountered in testing (refs. 8 and 9) (fig. 1). In addition, the wing of a typical NTF model of a transport aircraft, with a wing span of 4 to 5 feet, would require as many as 100 hot films to adequately locate transition over the wide range of test conditions encountered in a typical force and moment test. Furthermore, the hot films would have to be located on the surface of 3-D shapes such as leading edges of wings and winglets.

In the late 1970's the Douglas Aircraft Company (DAC) developed a vapor deposition hot-film system for transition detection in cryogenic wind tunnels (refs. 23 and 24). The ability of the DAC hot-film system to detect transition was first validated in an ambient temperature test (ref. 6) and later validated in a cryogenic test in the 0.3-m TCT (ref. 8). Although a significant amount of transition data was obtained with the DAC hot-film system in the 0.3-m TCT, the original goal of on-line detection of transition was not achieved. Since the tests in the TCT, Langley has developed an improved deposition technique for cryogenic hot films. The new technique includes a new dielectric and a new process for the buildup of the hot-film substrate. Tests of the new hot films in a low-speed tunnel demonstrated the ability to obtain on-line transition data with an enhanced simultaneous hot-film data acquisition system.

Langley is also developing a large-scale vapor deposition system which will include two large (5-foot diameter) chambers that will be used to put hot films on large NTF models.

● Special requirements

- Operate from ambient to cryogenic condition
 - Nonintrusive (less than critical roughness height)
 - Large number of films and realistic models (i.e., 3-D shapes)
 - Obtain transition on line as adjunct to primary force and moment test
- A cryo hot film system was developed by Fancher of DAC
- Validated system in ambient temperature and cryogenic tunnels
- Since validation tests, Langley has been developing:
- A new hot film and substrate deposition technique
 - Two new on-line data acquisition systems
 - A system for transition detection of NTF models

Figure 1

MODEL USED IN CRYOGENIC TRANSITION DETECTION STUDY: 0.3-M TCT

The 2-D airfoil used in the boundary layer transition detection study in the 0.3-m TCT (ref. 8), with 38 hot films on the upper surface, is shown mounted between the two test section turntables (fig. 2). With a technique they had developed (refs. 6, 23, and 24), DAC vapor deposited the hot films and their respective 76 gold leads on a dielectric substrate that was uniformly applied to the entire flow surface of the airfoil. The surface installation of the vapor deposited hot films and gold leads was 4 to 8 microinches thick, well below the critical roughness height required to trip the thinnest adiabatic laminar boundary layer that was encountered during the tests.

The 9-inch chord model, made of beryllium copper, was an advanced-technology supercritical airfoil, designed by NASA, designated the NASA SC(3)-0712. The model was fabricated with 16 internal liquid nitrogen (LN_2) cooling passages and 7 thermocouples, 0.050 below the surface, to monitor the model wall temperature. The ability to cool the model to wall temperatures as low as $169^{\circ}R$ demonstrated the ability of the cryogenic hot-film system to operate at cryogenic conditions.

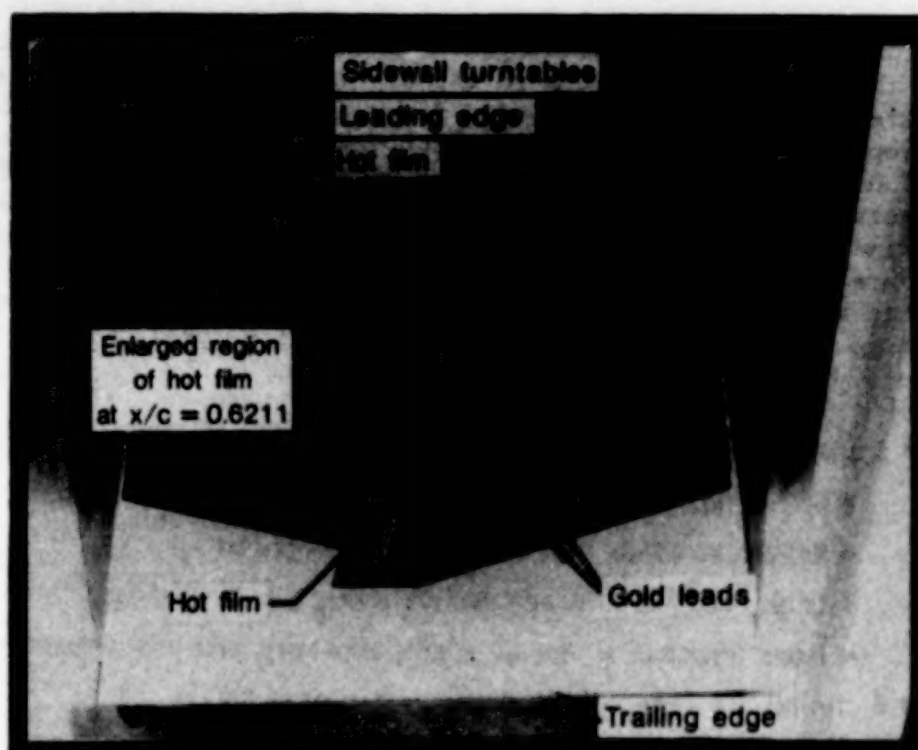


Figure 2

ORIGINAL PAGE
BLACK AND WHITE PHOTOGRAPH

~~ORIGINAL PAGE IS~~
~~OF POOR QUALITY~~

ENLARGED VIEW OF HOT-FILM AND GOLD LEADS

The hot films, which are extremely small and barely visible in figure 2 can easily be distinguished in an enlarged photograph of the hot-film at an x/c of 0.6211 (fig. 3). The photograph, which has a magnification of about 12, clearly indicates the hot-film located between the two gold leads. The gold leads are so thin that a portion of the metallic hot films (i.e., the end pads) can be seen through the leads.

The DAC procedure used to deposit an array of specialized cryogenic hot films on the surface of a model (refs. 6, 23, and 24) consisted of first applying a coating of dielectric substrate on the model, in this case an epoxy paint, and then polishing the substrate to a smooth finish of a uniform thickness of about 0.001 in. (0.0254 mm). Next, a pattern of hot films was applied to the surface by a vapor deposition technique. Each end of the hot film was then connected to a copper wire contact (i.e., model surface penetration) by a set of vapor deposited gold leads.

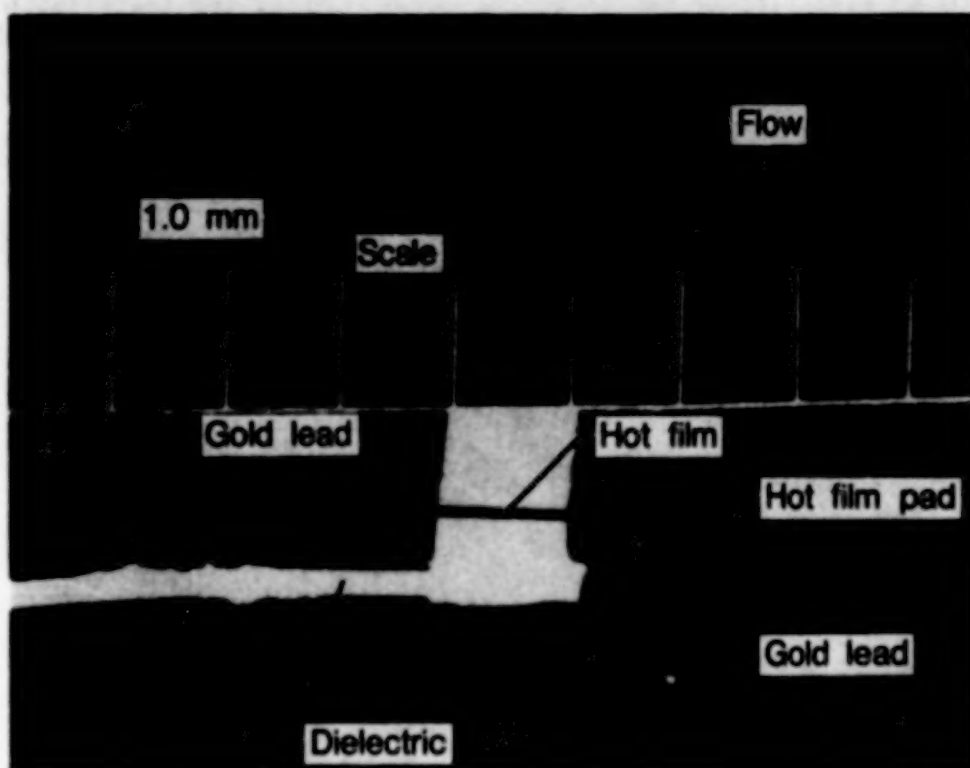


Figure 3

~~ORIGINAL PAGE IS
OF POOR QUALITY~~

ENLARGED VIEW OF WIRE PENETRATION CONTACT FOR HOT-FILM LEADS

An important component of the vapor deposited cryogenic hot-film system is the model wire penetrations which are flush to the model surface and serve to carry the hot-film signal from the vapor deposited electrical leads, through insulated wires in the model, to lead wires outside the model. For 2-D airfoils (refs. 6, 8, and 9), the wires run from the sides of the model at the point where the vapor deposited lead connects to the wire penetrations. This connection which is a vital link in the hot-film system must have a constant, low resistance electrical connection.

For the transition detection study in the 0.3-m TCT (ref. 8), the wire penetration was accomplished by cutting 76 slots (38 in each side) in the upper surface of the model and 20 slots in the lower surface to provide lead wires for 38 upper surface hot films and 10 lower surface hot films (fig. 4). The wire penetration contact points for the hot-film leads protrude above the surface of the airfoil about 0.001 in (0.0254 mm) in order to be flush with the surface dielectric coating, which is also about 0.001 in thick. The penetration wires were bonded into the slots with an electrically nonconducting epoxy. After the installation, each wire was checked to ensure that it was isolated from the model. (The 7 tubes on the side of the model (fig. 4) are part of the liquid nitrogen cooling system.)

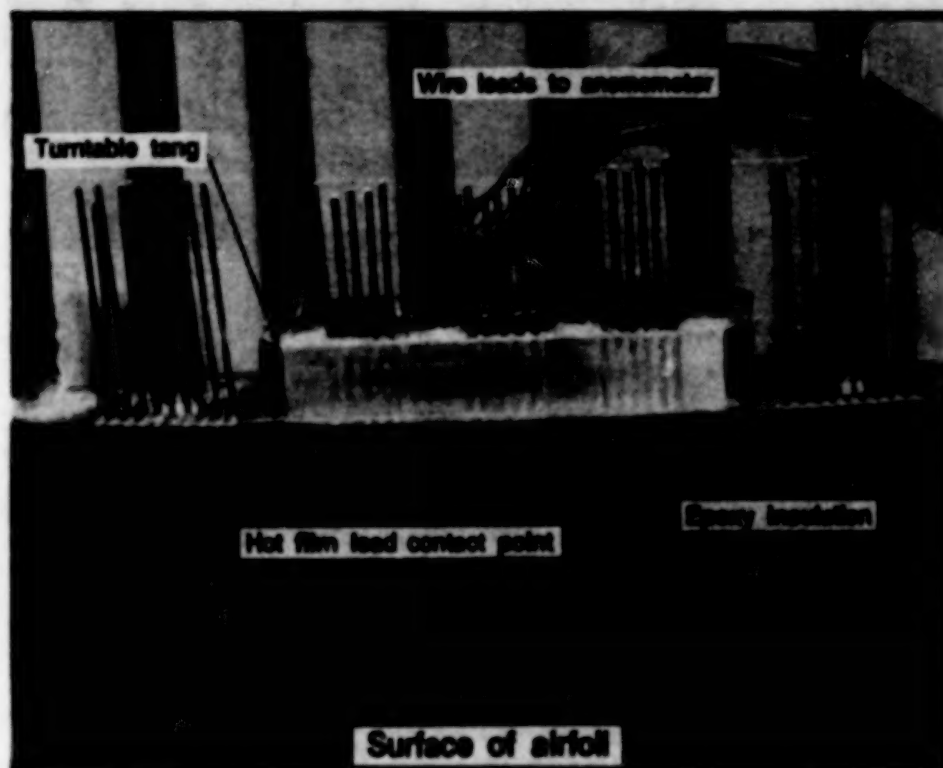


Figure 4

ORIGINAL PAGE
BLACK AND WHITE PHOTOGRAPH

ORIGINAL PAGE IS
OF POOR QUALITY

INITIAL APPROACH TO METALIZATION FOR CRYOGENIC HOT-FILM SYSTEM

For a number of years prior to the hot-film tests in the 0.3-m TCT (refs. 8 and 9), Langley had been evaluating various dielectric substates that would be considerably thinner than the epoxy paint used in the DAC method and that could be applied by a vapor deposition process that would ensure a uniformly thick substrate over 3-D shapes. Finally, a vapor deposited polymer called Parylene C was selected as the potential dielectric for use on a 3-D model to be tested in the NTF. The initial approach was to coat a number of polished aluminum coupons (about 4 in by 4 in) with various thicknesses of Parylene C (about 0.001 in to 0.003 in) and then deposit a chrome/nickel metal coating over the Parylene. It appeared at first the approach of depositing Parylene C as a dielectric on a model surface and then depositing the hot films on top of the Parylene C in a manner similar to the DAC hot-film method (refs. 6, 8, 9, 26, and 27) would be a satisfactory technique for 3-D model hot-film application. However, when a metallic coupon with an array of hot films vapor deposited by this technique were checked for uniformity of resistance, it was discovered that there was a wide variation in the level of resistance. In addition, when these same films were powered with a moderately low level of current by an anemometer, there was a significant number of hot-film failures. When the metalization of a chrome/nickel strip deposited on top of a coating of Parylene C was examined under a microscope (ref. 9), a number of cracks were discovered in the metals (fig. 5). It was soon realized the reason for the cracks was due to the flexible nature of the Parylene C dielectric substrate. The Parylene C has the capability to accommodate different linear coefficients of expansion. However, when hot films, which have intrinsic stresses, were deposited on the Parylene surface, fractures resulted in the metal film (fig. 5).



Figure 5

ORIGINAL PAGE IS
OF POOR QUALITY

ORIGINAL PAGE
BLACK AND WHITE PHOTOGRAPH

LANGLEY-DEVELOPED METALIZATION FOR CRYOGENIC HOT-FILM DEPOSITION

The problem of the fractures in the metalization procedure, indicated in figure 5, was solved after several months of intensive research and development. The solution to the fractures in the metalization was to coat the Parylene dielectric substrate with a thin layer of fused silica (SiO_2) (ref. 9). When this Langley-developed technique was examined in the microscope, there were no fractures (i.e., failures) in the metal film (fig. 6). This addition of the SiO_2 "buffer" layer enabled the Parylene C to act as a strain isolation pad between the model surface and the layer of SiO_2 . With the addition of a layer of SiO_2 , a dielectric substrate was produced that was thermally, chemically, and mechanically stable enough to prevent the cracking failure of the hot films at both ambient and cryogenic conditions (ref. 9).



Figure 6

ORIGINAL PAGE
BLACK AND WHITE PHOTOGRAPH

~~ORIGINAL PAGE IS~~
~~DE ROOR CHATTV~~

**AIRFOIL WITH LANGLEY-DEVELOPED CRYOGENIC HOT-FILM
ON UPPER SURFACE INSERT**

**ORIGINAL PAGE IS
OF POOR QUALITY**

Throughout the transition detection studies in the 0.3-m TCT with the DAC cryogenic hot-film system (ref. 8), the on-line voltage output from various hot-film anemometers versus time traces on oscillographs and oscilloscopes showed a clear distinction between laminar, transitional, or turbulent boundary-layer states. However, on-line plots of the RMS voltages versus chordwise location (for an array of hot films) could not be obtained in real time due to numerous problems with the hot films and the data acquisition system. The results from a posttest analysis, which required the use of digitized data obtained from the FM tape recordings made during the test, clearly validated the ability of this type of system to detect boundary-layer transition at cryogenic conditions. However, it was also apparent from the tests that if this type of cryogenic hot-film system was to be used for the on-line detection of boundary-layer transition in the NTF, significant advances had to be made: (1) in the hot-film metalization process, (2) in the on-line data acquisition systems, and (3) in the type of dielectric that was used on the wings of large NTF models.

Since the transition detection study in the 0.3-m TCT (ref. 8), Langley has developed a new technique for a cryogenic hot-film metalization process, which includes a new type of dielectric substrate (ref. 9 and fig. 6). In addition, the simultaneous hot-film data acquisition system used in the 0.3-m TCT test was significantly enhanced (ref. 9). In order to evaluate both the new Langley hot-film deposition technique and the enhanced data acquisition system a low speed wind tunnel test was conducted with a model of the NACA 0012 airfoil. One surface of the 12 inch chord (12 inch span) had a chordwise array of 30 of the Langley hot films (fig. 7). The model also had a chordwise installation of 23 pressure orifices on the surface that also contained the 30 hot films.

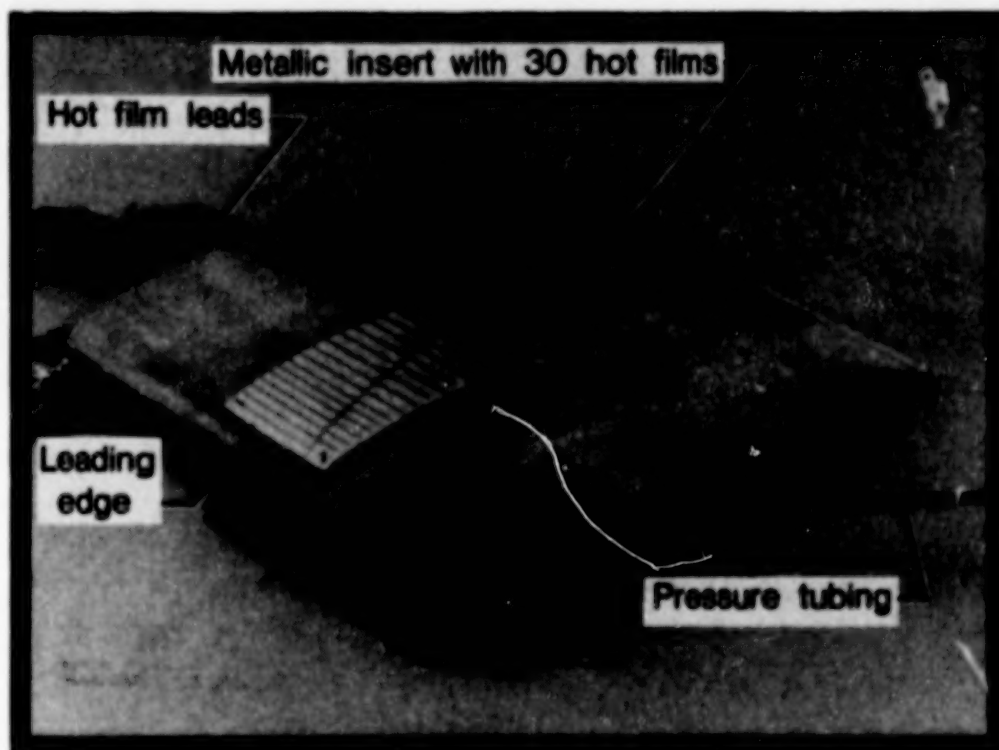


Figure 7

METALLIC INSERT USED IN AIRFOIL TEST OF CRYOGENIC HOT-FILM SYSTEM

The model used for the low-speed tests of the Langley cryogenic hot-film system, shown in figure 7, was fabricated with an internal core of high strength, closed-cell foam insulation and an outer shell of reinforced fiberglass. The stainless steel pressure tubing (0.20 in. i.d. and 0.30 o.d.) was routed through the internal core and was hand sanded to be flush to the fiberglass surface of the airfoil. A slot was cut in the upper surface of the airfoil for a 3 in. by 10 in. aluminum insert with a thickness of 0.125 in. on which 30 of the Langley developed cryogenic hot films were deposited.

The 3 by 10 inch aluminum insert (fig. 8) was closely fitted to the slot (i.e., no gaps) in the upper surface of the model and worked to conform to the design contour of the airfoil. Screws which fit into four countersunk holes in the corners of the insert held the insert in place so that the entire upper surface of the airfoil had the correct airfoil contour. There were 31 contact points (i.e., wire penetrations) on each side of the insert flush to the insert's outer surface.

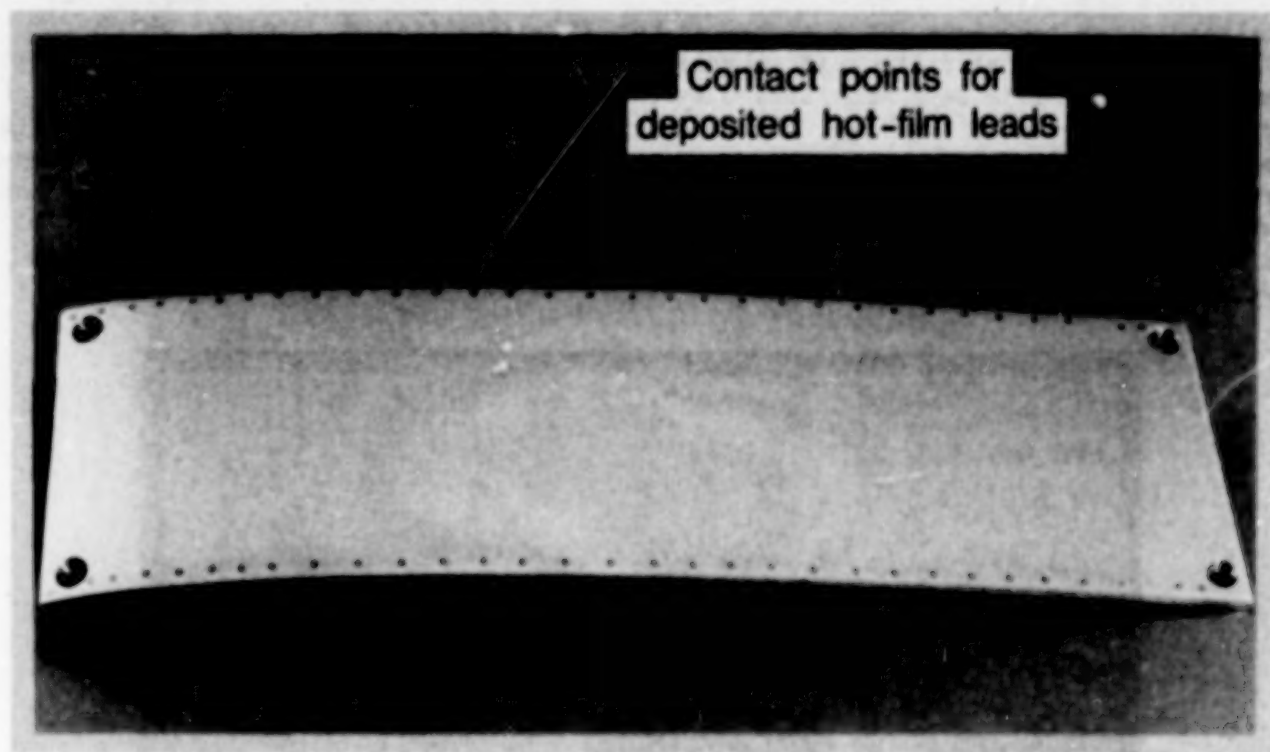


Figure 8

ORIGINAL PAGE IS
OF POOR QUALITY

ORIGINAL PAGE
BLACK AND WHITE PHOTOGRAPH

BACKSIDE OF METALLIC INSERT USED FOR CRYOGENIC HOT-FILM INSTALLATION

The surface electrical wire penetrations (sometimes referred to as pin connections in 3-D model installations), shown in figures 4 and 7, must be installed in a manner that does not introduce a surface roughness which could trip the laminar boundary layer in a localized area. The backside of the aluminum insert (fig. 5), used for the 30 hot films, shows the epoxy compound used to bond the individual copper wire to the backside of the insert to ensure the wire penetrations remain flush to the surface of the insert. For the low speed tests (ref. 9), which were made at a constant ambient temperature, dissimilar metal for the model insert and wire penetrations (i.e., aluminum and copper) were used and presented no problem because of the near isothermal condition of the model during the test. However, for the wire surface penetrations used for cryogenic testing, the wires (or pins) must be of the same material to avoid a differential growth between the model and the pins when the model temperature varies from ambient condition to cryogenic condition.



Figure 9

ORIGINAL PAGE
BLACK AND WHITE PHOTOGRAPH

ORIGINAL PAGE IS
OF POOR QUALITY

**METALLIC INSERT WITH CRYOGENIC SENSORS INSTALLED
FOR LOW SPEED WIND TUNNEL TEST**

Once the aluminum insert shown in figures 8 and 9 had been coated with Parylene C and SiO_2 , the contact points were cleared of any material that would impede the necessary secure electrical connection without exposing any of the surface of the aluminum insert to the vapor deposited aluminum leads. Next, the array of 30 hot films was vapor deposited on the insert by using a mask fabricated by a photolithographic technique. The array of 30 hot films and the 60 surface contact points were then connected by vapor deposited aluminum electrical leads (fig. 10).

The hot films were deposited in two swept arrays (skewed 15° from the model chord line), with 23 films in the array near the leading edge and the remaining 7 hot films in the downstream array. The 15° skew reduces the concentration of energy into the boundary layer along a given chord line that an unskewed array of films would produce. In addition, the skew reduces the downstream influence that a spurious turbulent wedge from a given hot film might have on the array of hot films. There is a shorted lead at the downstream end of the insert which is used to balance out any variation in lead resistance due to temperature changes, which will be an important consideration in testing in a cryogenic wind tunnel.

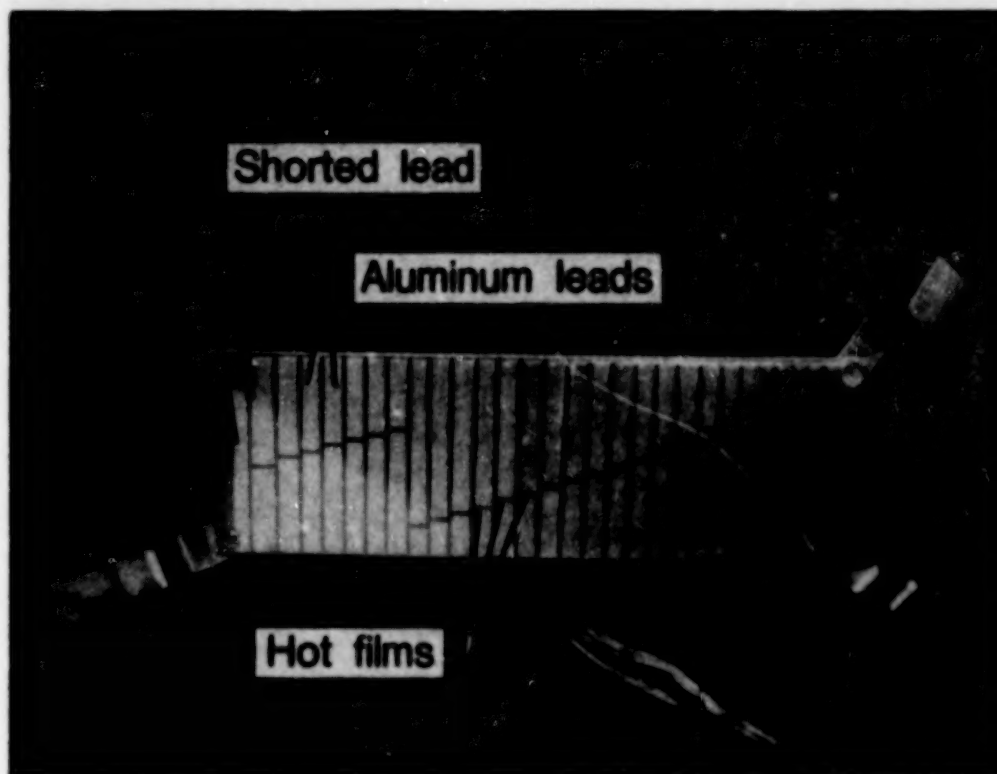


Figure 10

ORIGINAL PAGE
BLACK AND WHITE PHOTOGRAPH

CLOSEUP OF HOT-FILM INSERT INSTALLED IN AIRFOIL

An enlarged view of the forward portion of the NACA 0012 airfoil shows the upstream end of the hot-film insert installed in the upper surface (fig. 11). The hot films can be seen between the aluminum leads, and the electrical contact points can be seen at the chordwise edges of the insert. In addition, several of the pressure orifices can be seen in the lower right hand portion of the photograph.

The upstream end of the 10 in. long hot-film insert was located 0.4 in. from the leading edge of the airfoil, as measured along the chord line of the symmetrical airfoil. The chordwise centerline of the metallic insert was 5.5 in. from the right side of the model. The row of pressure orifices was 7.6 in. from the right side of the model. The model coordinates were within ± 0.001 in. of the design coordinate of the NACA 0012 airfoil.

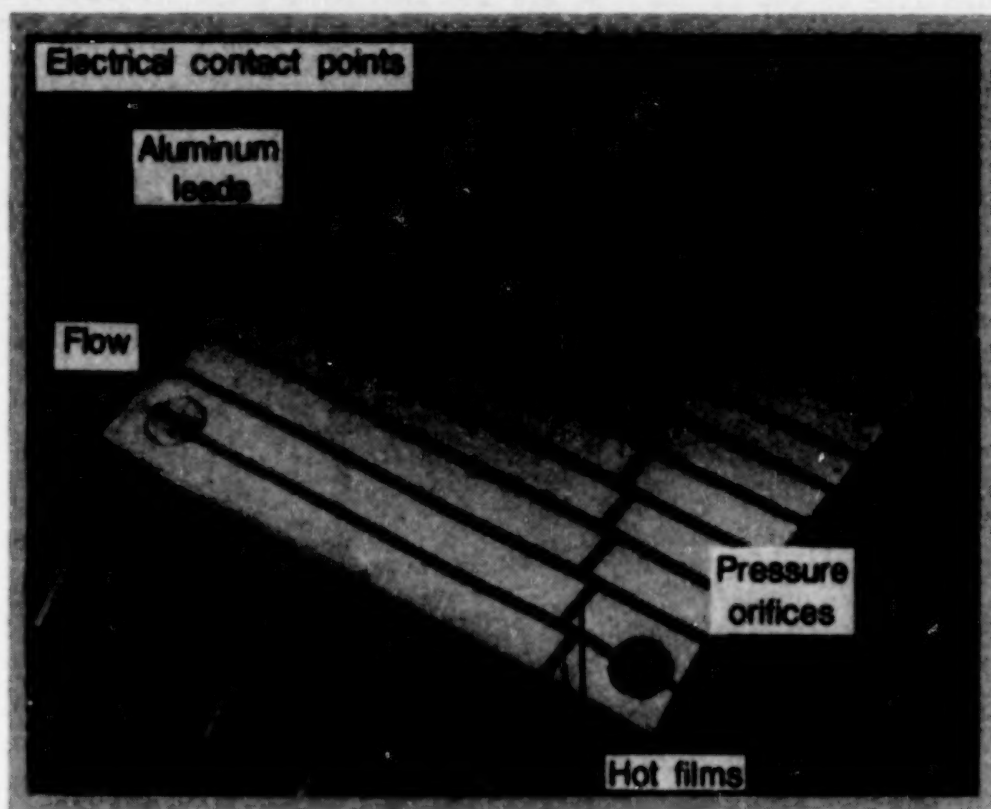


Figure 11

~~ORIGINAL PAGE IS
OF POOR QUALITY~~

ORIGINAL PAGE
BLACK AND WHITE PHOTOGRAPH

INSTRUMENTED AIRFOIL MOUNTED IN LANGLEY SMALL CALIBRATION FACILITY

The instrumented NACA 0012 airfoil was tested in Langley's Instrument Research Division (IRD) small calibration facility (ref. 9). The facility is an open-circuit tunnel that takes in room temperature air, at ambient pressure, from within the building where the facility is located and exhausts the air in the same area of the building. The tunnel operates over a test section speed range from very low subsonic to a Mach number of about 0.25 and is driven by a 50 hp motor that operates a squirrel cage blower at either 885 revolutions per min (RPM) or 1780 RPM. At a given fan RPM, the tunnel speed is set by regulating 12 radial damper vanes which are located at the downstream end of the diffuser.

The airfoil was tested in a vertical position in the 17 in. by 12 in. test section with a chord line (at $\alpha = 0^\circ$) at the center of the floor and ceiling (fig. 12). The 12-in. span model was secured between two turntables located in the longitudinal center of the test section floor and ceiling. The angle of attack was set by the alignment of a finely marked circular scale on the top turntable to a finely scribed line on top of the test section that marked the longitudinal flow axis. The model was tested at angles of attack of -2° , 0° , and $+2^\circ$; at Mach numbers of 0.092, 0.122, and 0.247; and at chord Reynolds numbers of 0.65×10^6 , 0.86×10^6 , and 1.70×10^6 .

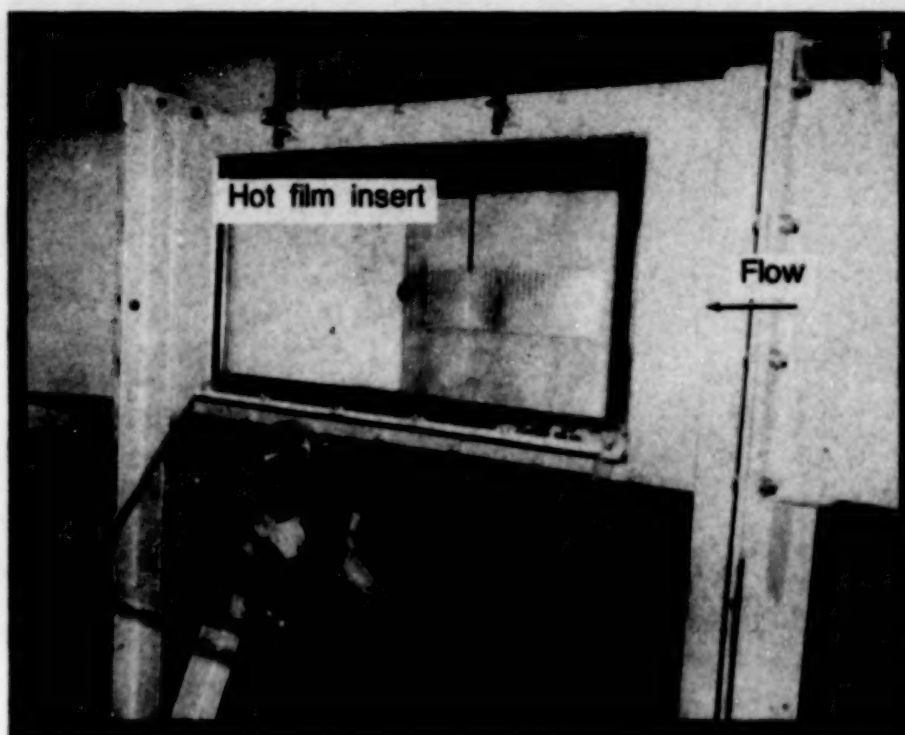


Figure 12

ORIGINAL PAGE
BLACK AND WHITE PHOTOGRAPH

~~ORIGINAL PAGE IS~~
~~OF POOR QUALITY~~

ON-LINE CHORDWISE FLUCTUATING VOLTAGES FOR VARIOUS ANGLES OF ATTACK

One of the goals of the low-speed wind tunnel tests, with the hot-film instrumented NACA 0012 airfoil described with figure 12, was to demonstrate an on-line capability to obtain the location of the beginning and end of transition with a "specialized" cryogenic hot-film system (ref. 9). On-line transition data, presented as the ratio of the RMS voltage to the mean voltage across the anemometer bridge, were obtained for the chordwise array of hot films at a Mach number of 0.122 and chord Reynolds number of 0.86×10^6 at angles of attack of 0° and $\pm 2^\circ$ (fig. 13). The data indicate three distinct regions where the boundary layer is first laminar, then transitional, and finally fully turbulent. The transitional region is between the beginning and end of transition. The sudden rise in the normalized voltage indicates the beginning of transition. In the transition region the normalized voltage reaches a peak value and then rapidly decreases to a point where the voltage has a nearly constant value which indicates the end of transition. The normalized voltage for the laminar boundary layer upstream of the beginning of transition has a value slightly less than 0.1 while the normalized voltage for the fully turbulent boundary layer downstream of the end transition has a value between about 0.5 and 0.8. As the angle of attack increases from -2° to 0° to $+2^\circ$, the location of the beginning of transition correspondingly moves forward from 51 to 43 to 24 percent of chord. This forward movement of the beginning of transition is expected based on the type of pressure gradients noted in the pressure distribution which were obtained during the test program (ref. 9).

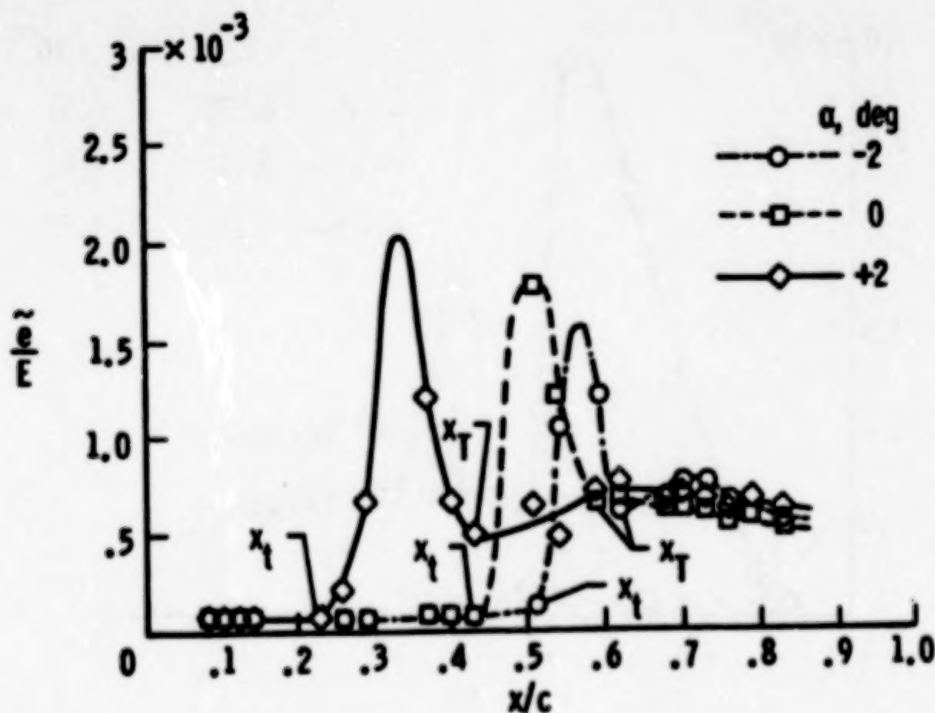


Figure 13

ON-LINE CHORDWISE FLUCTUATING VOLTAGES FOR VARIOUS MACH NUMBERS

On-line normalized fluctuating voltages, which indicated the beginning and end of transition, were also obtained from the chordwise array of hot films for Mach numbers of 0.092, 0.122, and 0.247 at an angle of attack of 0° (fig. 14). The RMS fluctuating voltages for the three Mach numbers again indicate the beginning and end of transition based on the sharp increase and rapid decrease of normalized voltages in the region where the boundary layer is transitional. When the Mach number increased from 0.092 to 0.122, there was a slight forward movement in the voltage distribution that defined the transitional region, but a clear difference in the beginning and end of transition could not be distinguished because of variations in the spacing of the operational films in the array. For the two lowest Mach numbers the beginning and end of transition appears to be 43 and 59 percent, respectively. When the Mach number was increased to 0.247, there was a significant upstream movement in the location of the beginning of transition to about 10 percent of chord. In addition, the chordwise extent of the transition region more than doubled and the level of the normalized voltage for the fully turbulent boundary in was 60 to 70 percent higher than the normalized voltage for the two lower Mach numbers.

Thus, fluctuating voltage obtained in a real-time mode from a closely spaced chordwise array of hot films (figs. 13 and 14) will give a clear indication of the beginning and end of transition with the new Langley hot films and an enhanced simultaneous data acquisition system.

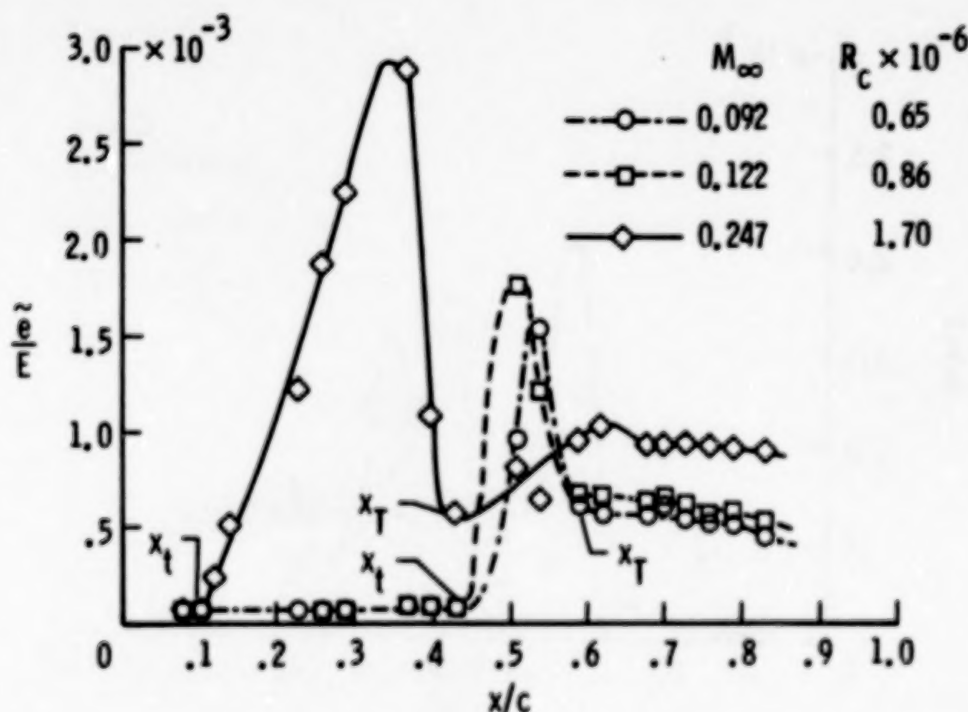


Figure 14

FLUCTUATING CHORDWISE VOLTAGES AND CORRESPONDING VOLTAGE VERSUS TIME TRACES

The fluctuating voltage output from the hot films, which was recorded on FM tape with a 28 track tape recorder (ref. 9), was examined on oscilloscopes both during (i.e., on-line) and after the tests. From the posttest examinations, selected voltage-versus-time traces, that correspond to RMS voltages in figures 13 and 14, were obtained with a digital storage oscilloscope and were then plotted directly on an analog x-y plotter (ref. 9). The voltage-versus-time traces (fig. 15), which correspond to specific values of RMS voltage, at an angle of attack of 0° , a Mach number of 0.122, and a chord Reynolds number of 0.86×10^6 , clearly indicate the waveform for a laminar boundary layer associated with the low RMS voltages upstream of the beginning of transition. Downstream of the end of transition the waveform is that of a fully developed turbulent boundary with the associated elevated level of RMS voltage. The transition region, between the beginning and end of transition, indicates the expected positive voltage spikes caused by turbulent bursts in the area where the RMS voltage is increasing and also indicates the negative voltage spikes associated with "laminar intervals" in the area where the RMS voltage is decreasing. The voltage versus time traces (fig. 15) are typical of those from tests with similar cryogenic hot films systems (ref. 9) and from tests with conventional hot films systems (ref. 3).

The data acquisition system which enabled the realization of on-line transition detection consisted of 30 channels of hot-film anemometry, a computer-controlled switching network, scanner, digital multimeter, filter, and true RMS meter. All components in the system were calibrated very carefully to ensure that each channel of hot-film anemometry would have a nearly uniform sensitivity and frequency response. Measurements were directly taken with the digital multimeter and assimilated in the desktop computer. They were then displayed as a plot of e/E vs x/c .

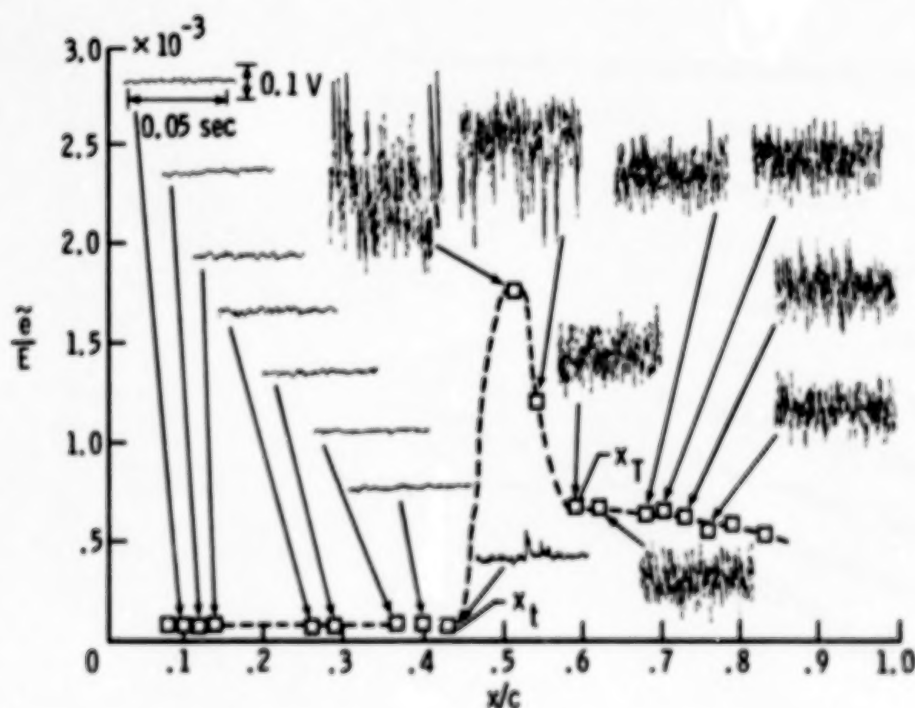


Figure 15

**TEST OF CRYOGENIC HOT-FILM DIELECTRIC WITH AIRFOIL
MOUNTED ON TEST SECTION SIDEWALL OF NTF**

Two test entries were made in the NTF to evaluate the durability and survivability of the Parylene C dielectric substrate over a wide range of Mach numbers, Reynolds numbers, and total temperatures. Each facility entry was about 2 weeks in duration and remained in the test section during the entire "primary" test program. The two qualitative evaluation tests were made with an 8-in. span, 5.575-in. chord, 20-percent thick symmetrical airfoil and were mounted on the side wall of the test section of the NTF (fig. 16). Two separate, but identical, airfoil sections with a 0.0003-in. thick coating of Parylene C were used in each of the tunnel entries. The airfoil sections were mounted on the right side wall of the test section well downstream of the primary force and moment model. During both tests, a minimum of 4 inches of the outboard portion of the coated airfoil was in the freestream flow of the test section, and at highest Reynolds numbers as much as 7 inches of the airfoil span were in the free stream. During the first entry, the NTF was operated in the air mode at Mach numbers from 0.2 to 0.9, a total temperature of 100°F, and a total pressure of about 1 atm. A posttest examination of the Parylene C coating indicated no mechanical failure and an electrical check indicated the coating would be an excellent dielectric substrate for the hot-film system. During the second tunnel entry, a second airfoil, also coated with 0.0003 in. of Parylene C, was tested in the cryogenic mode. During the tests, the Mach number varied from low subsonic to 1.15, and the total temperature was as low as -247°F (118 K), with a dynamic pressure as high as 3600 PSF. These test conditions represented a severe set of test conditions for the Parylene C dielectric. The results of a posttest examination again indicated no mechanical failure of the dielectric substrate at the high dynamic pressure - cryogenic condition. An electrical check again indicated the Parylene C would serve as an excellent dielectric substrate for the cryogenic hot-films system.



Figure 16

DAC - NTF PATHFINDER I WING WITH PROVISIONS FOR THE INSTALLATION OF CRYOGENIC HOT FILMS

The application of the cryogenic hot-film system to three-dimensional models is the next step in the development of this measurement technique. It is well known that future test programs of airplane configurations in the NTF all have the general user requirement of a boundary-layer transition detection capability, preferably on-line. At this time, the only cryogenically validated transition detection system is the vapor deposited hot-film system as discussed in this section of the publication. Currently there are NTF models, in the general class of transport aircraft, that contain the necessary surface pin penetrations on the surface to accommodate the installation of the Langley cryogenic hot films. One of these NTF models is the Douglas Aircraft Company's (DAC) Pathfinder I wing (fig. 17) which has 44 surface penetrations pins installed at 4 spanwise stations (i.e., four chordwise arrays of hot films) on the upper surface of the right hand span of the wing. The installation technique that DAC has developed for hot-film pin penetration produces an extremely smooth surface at the point of penetration. The pins for the hot-film leads are electrically isolated from the model and are attached to lead wires that connect to the hot-film data acquisition system.

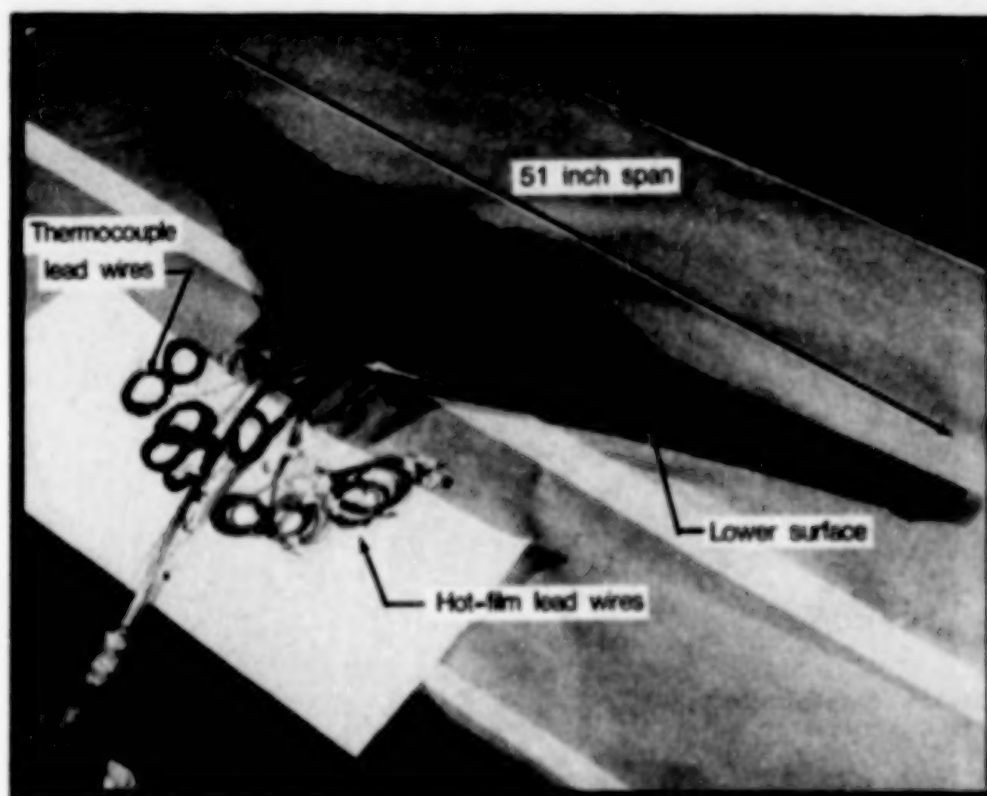


Figure 17

ORIGINAL PAGE IS
OF POOR QUALITY

VACUUM CHAMBERS AT LANGLEY FOR DEPOSITION OF CRYOGENIC HOT FILMS ON LARGE MODELS

Since there has been a requirement for transition detection on NASA models to be tested in the NTF for a number of years, coupled with the DAC requirement that a cryogenic hot-film system be vapor deposited on the 51-inch span wing, shown in figure 17, Langley has been developing a large-scale deposition system. The large scale system will consist of two large vacuum chambers (5 ft i.d.) and the required large capacity vacuum system to go with both chambers (fig. 18). The two large chambers were obtained from surplus equipment and are being refurbished for use as large vacuum chambers.

One of the large chambers (fig. 18) will be used to deposit the Parylene C dielectric substrate on the large wings of NTF models and will have a Parylene C system similar to Langley's small scale system (ref. 9). The other large chamber (fig. 18), for the metalization/ deposition process, is made from stainless steel and will require a much lower vacuum than the chamber used for the dielectric. The system for the large metalization/deposition chamber will be similar to Langley's small scale system (ref. 9). In addition, two large 30 horse power mechanical vacuum pumps with a pumping capacity of 730 CFM were also obtained from surplus. One of the mechanical pumps will provide a sufficiently low vacuum for the chamber used for dielectric deposition. The other vacuum pump will serve as the roughing pump for the large metalization/deposition chamber which requires a much lower pressure (i.e., 10^{-5} to 10^{-6} mm of mercury). A diffusion pump will be used in the vacuum system for this chamber to obtain the necessary high vacuum required for metalization/ deposition.

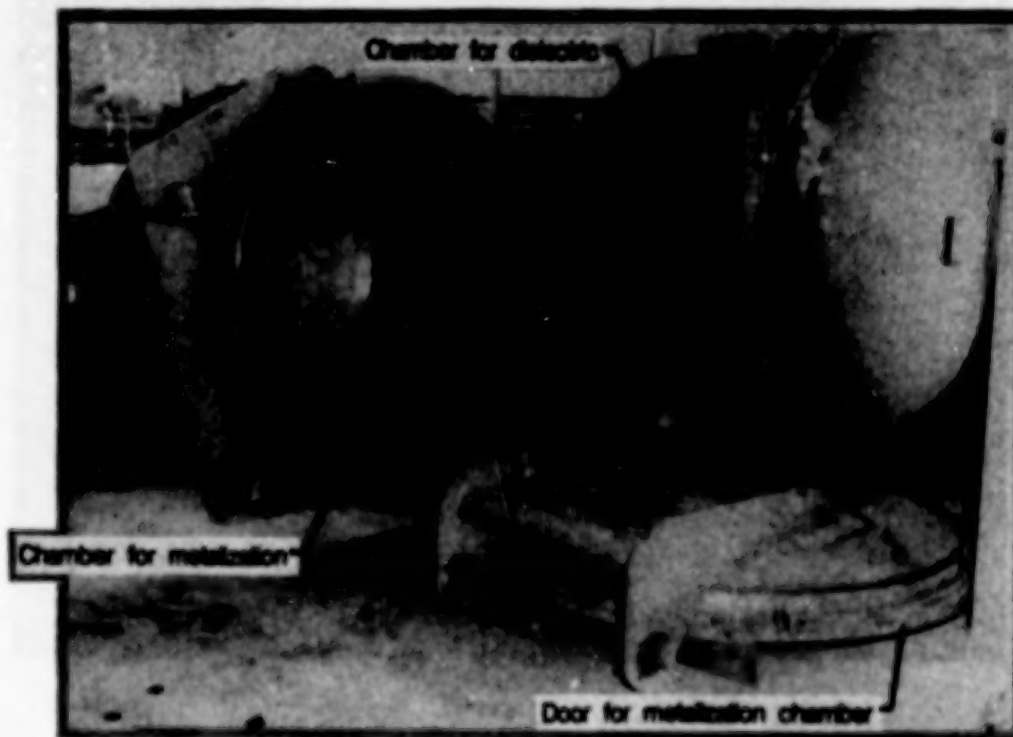


Figure 18

ORIGINAL PAGE
BLACK AND WHITE PHOTOGRAPH

ORIGINAL PAGE IS
OF POOR QUALITY

**PREDICTED AND HOT-FILM MEASURED
TOLLMIE-SCHLICHTING WAVE CHARACTERISTICS**

John P. Stack, Robert B. Yeaton, and J. R. Dagenhart
Langley Research Center
Hampton, Virginia

Time Traces Obtained From a Thin Film

The Tollmien-Schlichting (T-S) instability (ref. 28) is a time-dependent instability which can lead to transition of laminar boundary layers on airfoils. This paper presents a comparison of theoretical predictions and experimental observations of the T-S instability on the NLF(1)-0414F airfoil designed by Viken and Pfenninger (ref. 29). The theoretical predictions were obtained using the SALLY stability code (ref. 30). The experimental observation of the T-S instabilities was accomplished by enhancing the output obtained from the conventional hot film transition detection technique (refs. 10, 31, and 32).

The measurements were made in the Langley Low-Turbulence Pressure Tunnel (ref. 33) on a 3-foot chord model of the NASA designed NLF(1)-0414 at $M_\infty = 0.143$, $R_c = 3 \times 10^6$ and $\alpha = 3.0^\circ$. Pressure orifices on both surfaces were used to determine the pressure distribution, and hot-film gages were used to locate the beginning of transition.

Test results, from the same hot films that were used to detect transition, revealed that T-S waves could be detected by the hot film if the hot-film signal (fig. 1) was adequately amplified.

- Tests conducted in Langley's LTPT on 3.0 ft. chord NLF (1)-0414 airfoil at $M_\infty = 0.143$, $R_c = 3.0 \times 10^6$
- The hot film system also defined transition region
- Detection of T-S waves on laminar signal required high signal-to-noise ratio

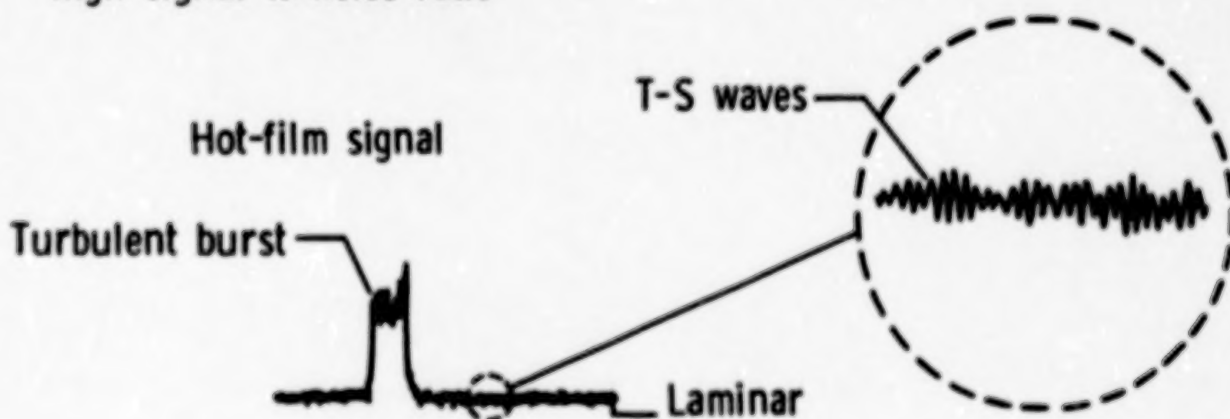


Figure 1

Wave Form and Spectra From a Thin Film

The spectral analysis from the wave form (fig. 2) clearly shows a dominant frequency at 1.4 KHz. The measurements were made at 70 percent of chord on the NLF(1)-0414 at $M_{\infty} = 0.143$ and $R_c = 3 \times 10^6$.

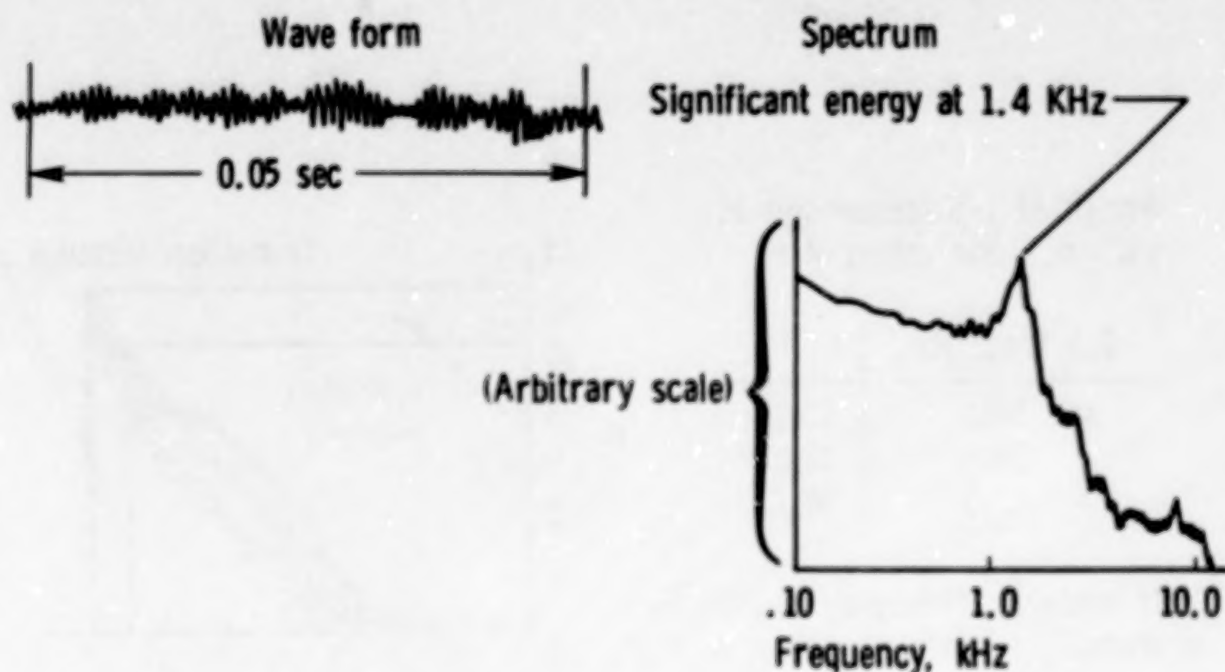


Figure 2

Predicted Tollmien-Schlichting Wave Characteristics

The dominant frequency, shown in figure 2, can be seen to fall within the theoretically predicted incompressible T-S amplification range for $M_\infty = 0.143$, and $R_c = 3 \times 10^6$ at 70 percent of chord on the for the NLF(1)-0414 airfoil (fig. 3). This comparison of the predicted and experimental measurement of the T-S instability on an NLF airfoil demonstrates that conventional hot films, generally used for the detection of boundary-layer transition, can be extended for use to measure the T-S most amplified frequency.

Amplified T-S frequencies at
 $x/c = 0.7$ and values of n

T-S freq., Hz	n
□ 1250	11.1
◇ 1500	12.2 *
△ 1750	10.7

* Most amplified frequency is 1500 Hz
at transition location, with $n_1 = 12.2$

Measured freq. is 1400 Hz

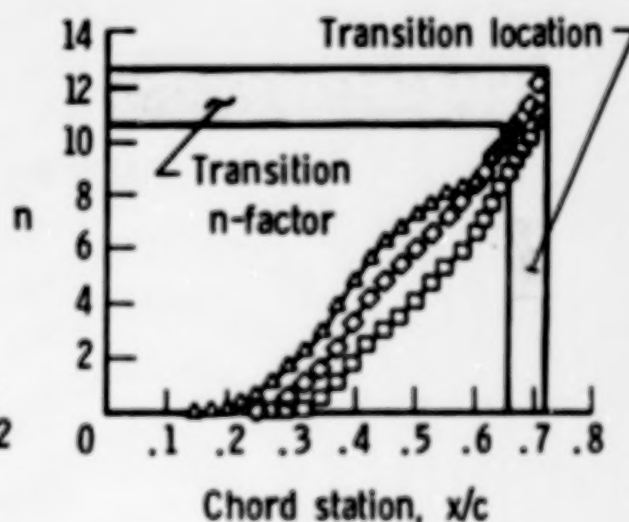


Figure 3

**REMOTE DETECTION OF BOUNDARY-LAYER TRANSITION
BY AN OPTICAL SYSTEM**

Robert M. Hall
Langley Research Center
Hampton, Virginia

Medhat Azzazy and Dariush Modarress
Spectron Development Laboratories, Inc.
Costa Mesa, California

**THE BOUNDARY-LAYER TRANSITION DETECTOR BASED ON
DIFFERENTIAL INTERFEROMETRY**

The boundary-layer transition detector, developed by Spectron Development Laboratories (see reference 11), uses a differential interferometer to nonintrusively detect transition in compressible boundary layers. The heart of the device is a highly sensitive differential interferometer capable of detecting optical path length differences of less than one-thousandth of the wavelength of the laser light. The high sensitivity of the interferometer is due, in part, to a compensator loop which is employed to adjust the phase relationship between the two beams of the interferometer to optimize the performance of the interferometer and to null out any low frequency (less than 1 kHz) signals that might result from, for example, model vibration. Twin photodetectors generate the output voltage signal as well as information for controlling the compensator loop. Electronic signal processing is also essential for real-time assessments of the boundary-layer activity. (Fig. 1.)

- Nonintrusive - two beam method
- Capable of detecting variations in optical path lengths (i.e., density fluctuations) on the order $\lambda/1000$
- Transition detector consists of:
 - Optical system
 - Compensator loop
 - Detection system
 - Electronic signal processing
- The RMS voltage output is proportional to the difference in density fluctuations between the two beams (i.e., initial rise indicates onset of transition)

Figure 1

SCHEMATIC OF OPTICAL DETECTION SYSTEM

The differential interferometer uses a 5-mW helium-neon laser for its light source. The beam is then passed through a polarizing plate, which aligns the beam at a 45 degree angle from vertical and results in one beam having components of polarization in both the vertical and horizontal directions. The Pockell's cell, the key element for the compensator loop, provides a means of adding pathlength to one of the components so that the relative phase between the two components of the polarized beam is controllable. The beam expander and lens provide a collimated beam to the beam splitter and Wollaston (1). Wollaston (1) splits the original beam into two beams of orthogonal polarization which leave the Wollaston prism at predetermined, but different angles. These two beams pass through the boundary layer on the model at different locations. Differences in density fluctuations in the boundary layer at the two model locations manifest themselves as optical path length differences between the two beams. Light reflecting back from the model surface returns through the lens and Wollaston (1) and is directed by the beam splitter to Wollaston (2) and the two photodetectors. The photodetectors generate the signal voltage out and provide information for adjusting the Pockell cell for optimum interferometer performance. (Fig. 2.)

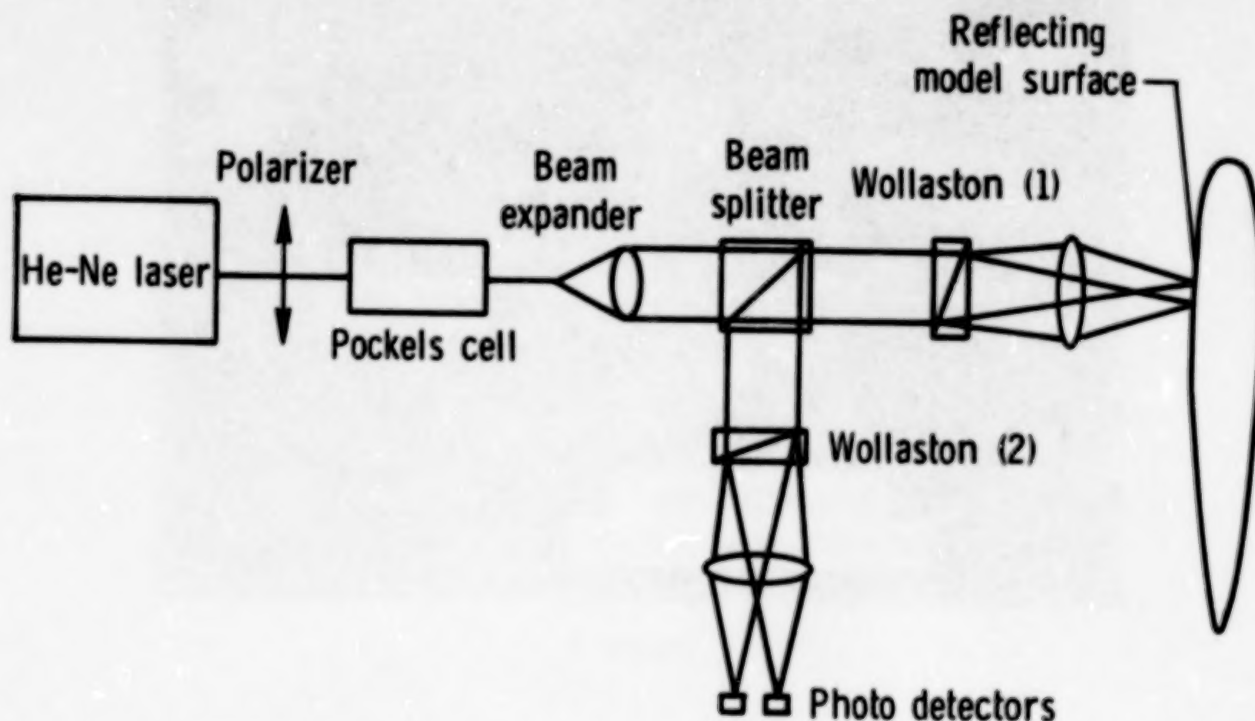


Figure 2

TRANSITION DETECTION SYSTEM AT THE BOEING MODEL TRANSONIC WIND TUNNEL

An important evaluation of the instrument occurred during June of 1986 when it was tested in the Boeing Model Transonic Wind Tunnel, which is a pilot tunnel with a 5- by 7-inch test section. The tunnel test section does not include a plenum and its sidewalls are of optical quality glass. As seen in figure 3, the instrument was set up on an optical bench next to the tunnel and the beam entered the tunnel normal to the test section side wall. An airfoil was mounted between the bottom and top walls. The beam struck the airfoil in a direction approximately normal to its surface. The electronic instruments that were used to store and assess the signal data in nearly real time are seen on the workbench behind the optical bench.

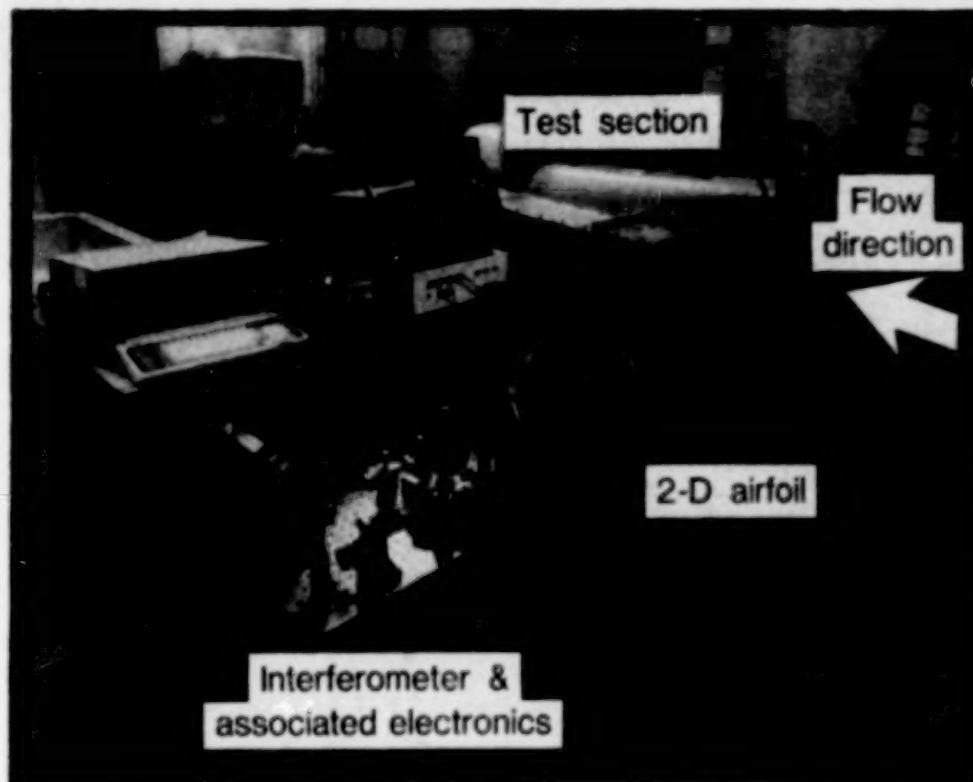


Figure 3

ORIGINAL PAGE
BLACK AND WHITE PHOTOGRAPH

~~ORIGINAL PAGE IS~~
~~OF POOR QUALITY~~

NATURAL AND TRIPPED BOUNDARY-LAYER TRANSITION PATTERN FROM FLOW VISUALIZATION

A 6-inch chord NACA 66-006 airfoil was used during the Boeing tests. Both laminar and turbulent flow are known to occur on this airfoil. Concurrently with the interferometry measurements, sublimating chemicals (napthalene) were used to independently determine where boundary-layer transition was occurring. The tunnel was operated at freestream Mach numbers of 0.7 and 0.8, which resulted in values of Reynolds number per foot approximately equal to 4 million. Figure 4 illustrates the type of pattern seen with the sublimating chemicals for a Mach number of 0.7 and with a roughness element attached to the leading edge of the airfoil.

Several interesting features of the flow are apparent. First, a distinct turbulent wedge emanates from the leading edge as a result of the roughness element, as marked by the absence of the sublimating chemical. (Absence of whitish chemical corresponds to a region of high heat transfer, or high surface shear stress, which is usually indicative of a turbulent boundary-layer state.) Second, at a location of about 5 inches from the leading edge (corresponding to the 1-inch location on the scale), it appears that natural transition is occurring independent of the turbulent wedges associated with either the tunnel side walls or the roughness element.

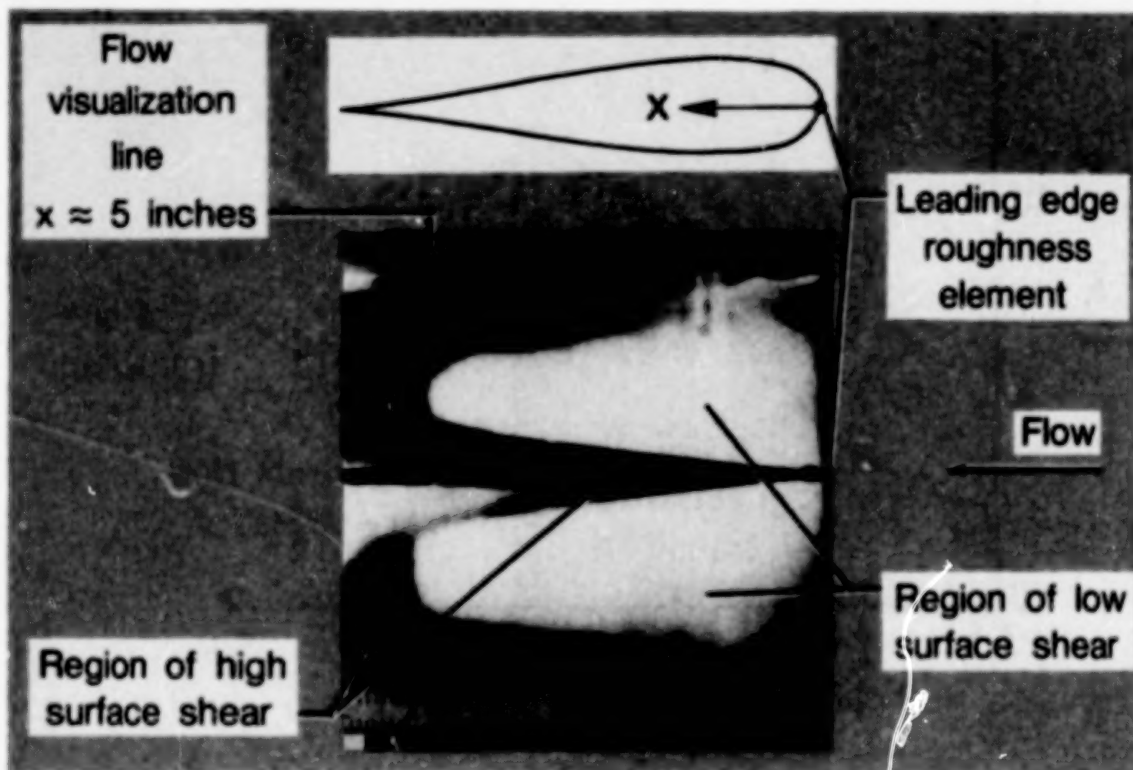


Figure 4

ORIGINAL PAGE
BLACK AND WHITE PHOTOGRAPH

COMPARISON OF INTERFEROMETER SIGNAL AND FLOW VISUALIZATION FOR NATURAL TRANSITION

As an example of the type of data generated by the interferometer, figure 5 shows a plot of the RMS level of the signal for natural transition. The freestream Mach number was 0.70 and the chord Reynolds number was approximately 2 million. No roughness elements were on the model.

The instrument data, shown by the circles, demonstrate an increase in signal fluctuations (indicative of density fluctuations in the boundary layer) from a region 3.5 inches from the leading edge rearward. This area near 3.5 inches appears to coincide with the beginning of boundary-layer transition. The unsteadiness in the signal increases until 5.0 inches from the leading edge, where the unsteadiness reaches a maximum and where, in fact, the line of demarcation between absence and presence of chemicals was photographically determined at an earlier time. After this peak in activity, the signal RMS once again falls off as the fully turbulent region develops. However, the RMS level in the fully turbulent region appears to be approaching a value of about 6 millivolts as opposed to the laminar value of about 2 millivolts.

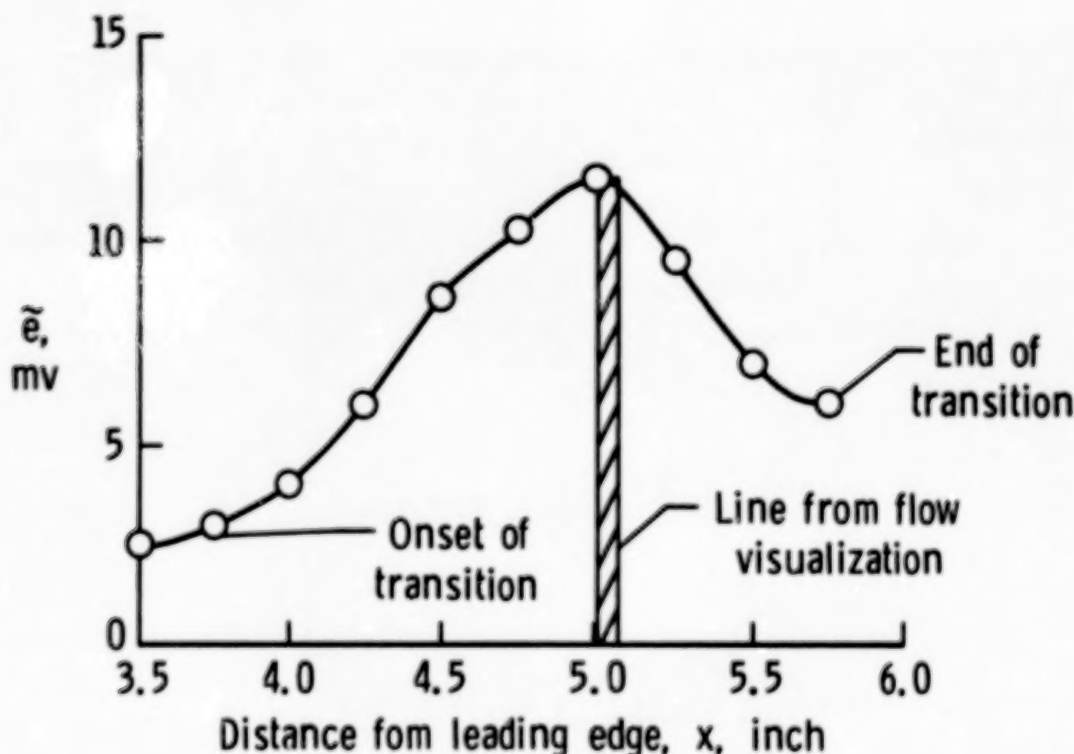


Figure 5

COMPARISON OF INTERFEROMETER SIGNAL AND FLOW VISUALIZATION FOR FORCED TRANSITION

A second example of transition detection is given for the case of transition triggered by the roughness element. The resulting turbulent wedge is traversed by the instrument in such a manner that the instrument moves from outside of the turbulent wedge to the centerline of the turbulent wedge. During the traverse, the chordwise distance is kept constant at 3.5 inches from the leading edge. The freestream Mach number was again equal to 0.70.

Once again, the RMS level of the signal is plotted on the vertical axis while the spanwise position of the beams is plotted along the horizontal axis. A spanwise distance of 0 inches is actually 1-inch from the centerline of the turbulent wedge while a spanwise distance of 1-inch corresponds to the centerline of the turbulent wedge. Again, the unsteadiness peak in the optical signal coincides with the boundary between the presence and absence of sublimating chemical. It is interesting that the interferometer would suggest that the actual turbulent wedge generated by the roughness element is not as well defined as the sublimating chemical test would suggest. (Fig. 6.)

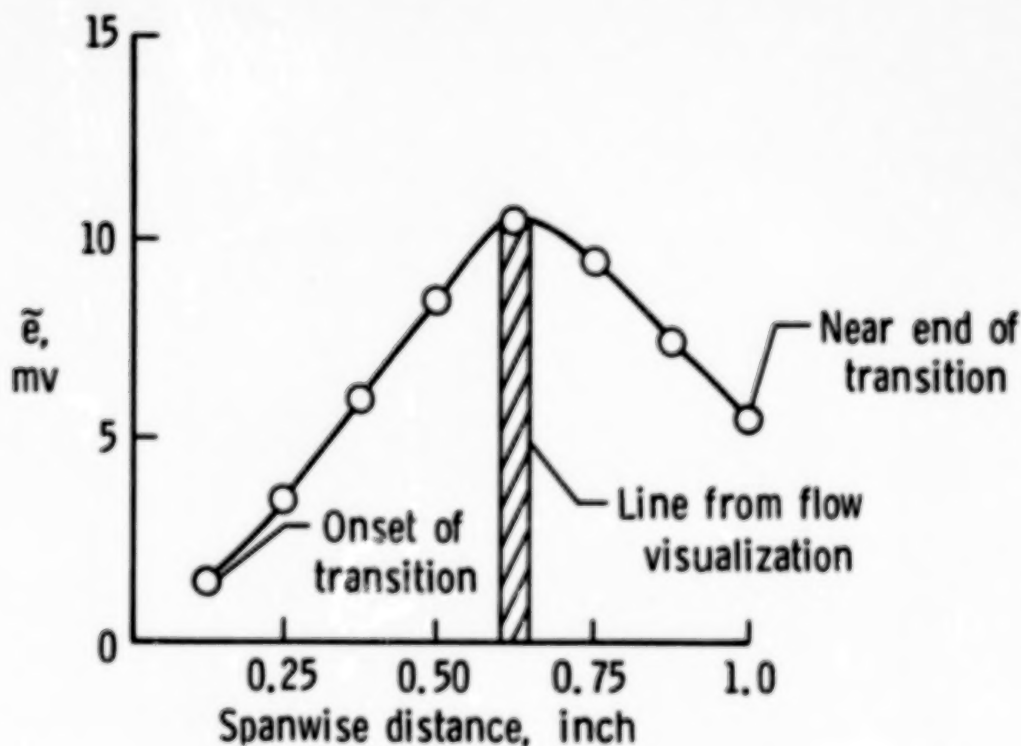


Figure 6

SUMMARY

This instrument development program has been funded because of the urgent need to measure boundary-layer transition in wind tunnels. In the course of this development program, a prototype instrument was designed, built, and tested. Recent transonic experiments in the Boeing Model Transonic Wind Tunnel show that the interferometer results correlate very well with sublimating chemical tests.

N90-12525

**THREE-COMPONENT LASER DOPPLER VELOCIMETER
MEASUREMENTS IN A JUNCTURE FLOW**

L. R. Kubendran and J. F. Meyers
Langley Research Center
Hampton, Virginia

INTRODUCTION

In a wing-fuselage juncture the oncoming turbulent boundary layer on the fuselage surface experiences steep adverse pressure gradients as it approaches the wing leading edge. These gradients cause the boundary layer to separate ahead of the leading edge, resulting in a vortex which rolls up and trails downstream in the juncture. The use of laser velocimetry facilitated making detailed measurements near the non-planar surfaces forming the juncture, and within near-separating flows close to the trailing edge of the wing (refs. 12, 13, and 14).

The experiment was carried out in the Low-Turbulence Pressure Tunnel (LIPT) at the NASA Langley Research Center. The LIPT is a single return, closed-circuit wind tunnel which can be operated at pressures from 0.1 to 10 atmospheres. It is capable of operating at Mach numbers from 0.05 to 0.50, and unit Reynolds numbers from 300,000 to 49,000,000/m. The turbulence level is very low because of the nine turbulence reduction screens and because of the 17.6:1 contraction ratio. The test section is 0.91 m (3 ft) wide, 2.29 m (7.5 ft) high, and 2.29 m (7.5 ft) long. Figure 1 gives the details of the experimental setup.

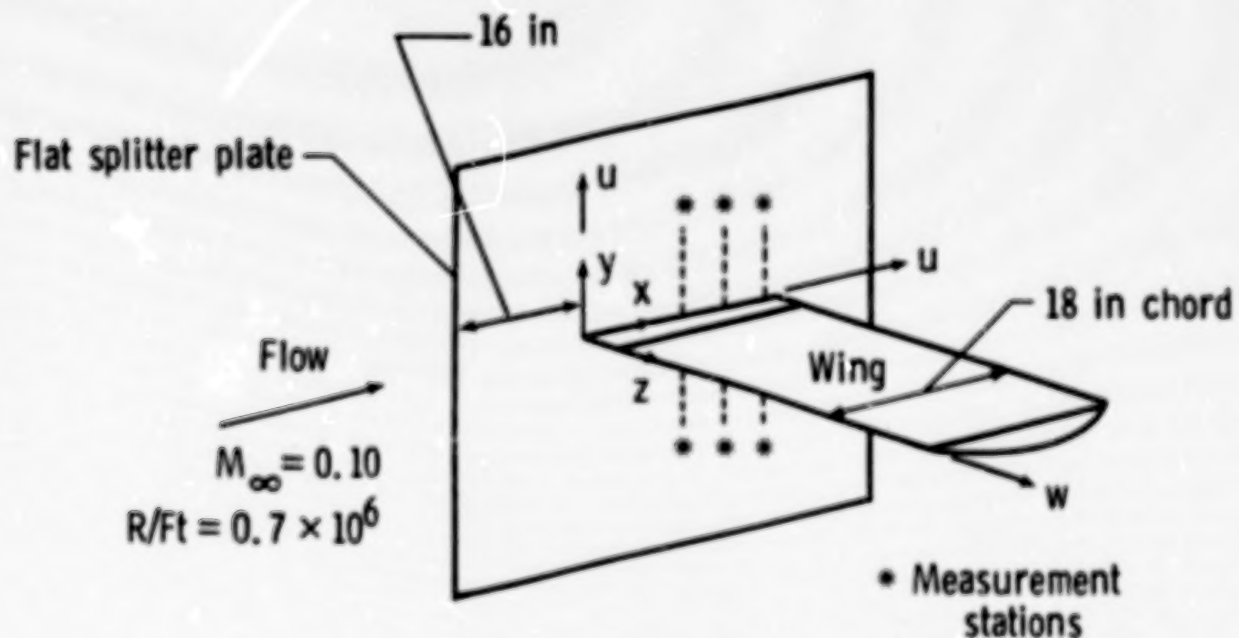


Figure 1

THREE-COMPONENT LDV SYSTEM USED IN LTPT

The single-axis, five beam optical configuration uses the standard two-color, two-component beam pattern with the two green beams arranged in the horizontal plane and the blue beams arranged in the vertical plane (ref. 12). The green beams are used to measure the U component and the blue beams to measure the V component. A third green beam is placed along the optical axis bisecting the angles between the original two green beams. The addition of this beam creates two additional fringe patterns, from which the W component is obtained. Bragg cells are used in the two outer green beams to separate the three signals obtained from the three green fringe patterns. (Fig. 2.)

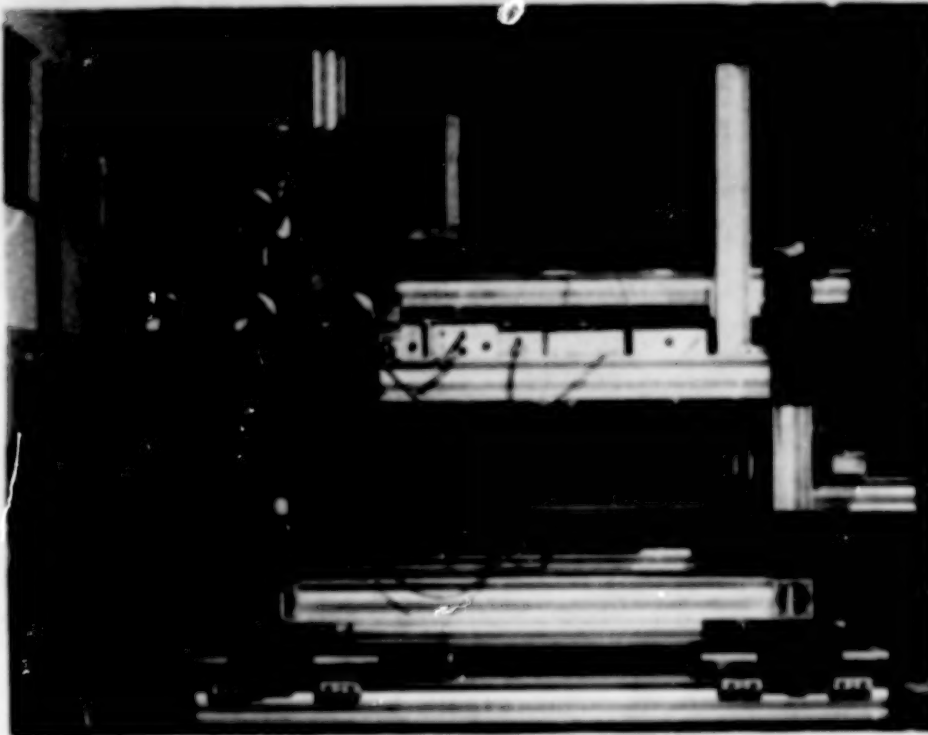


Figure 2

ORIGINAL PAGE
BLACK AND WHITE PHOTOGRAPH

OPTICAL ACCESS THROUGH SIDEWALL WINDOW

The optical access to the model was limited to a single window of diameter 0.75 m. This window was surrounded by a drum 0.978 m in diameter by 0.711 m in depth. This further complicated the design of the laser velocimeter (LV) system, resulting in a reduced cross-beam angle. Also, an off-axis backscatter collection mode had to be used in order to reduce the effect of background reflections from the splitter plate. (Fig. 3.)

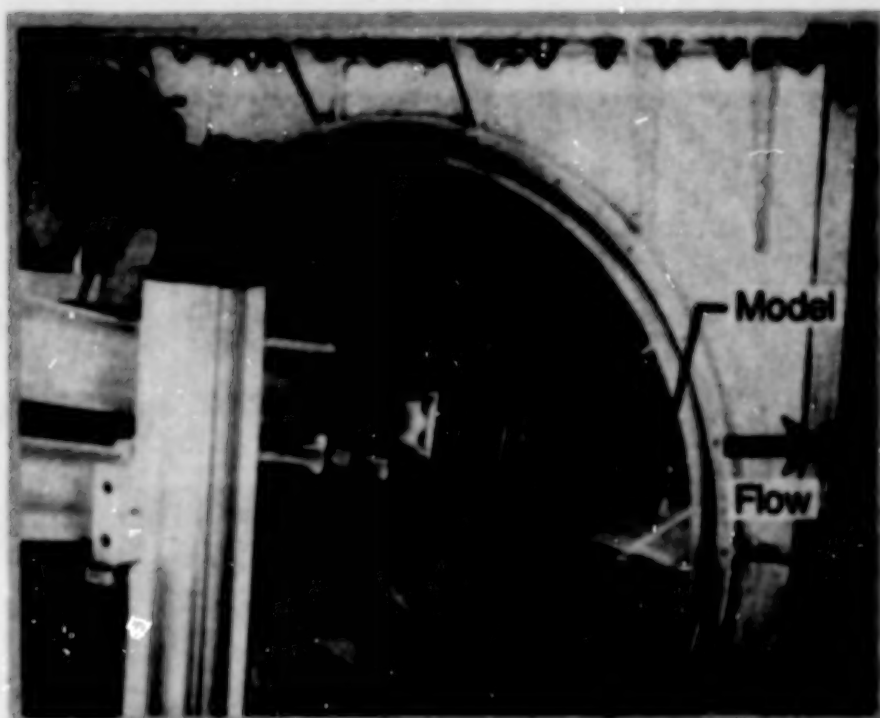


Figure 3

ORIGINAL PAGE
BLACK AND WHITE PHOTOGRAPH

ORIGINAL PAGE IS
OF POOR QUALITY

MODEL MOUNTED IN TEST SECTION

The LV system described here resulted in a sample volume of diameter 80 micrometers and a length of 120 micrometers. In order to make measurements very close to the juncture, the LV beam system was oriented at an angle of 11 degrees with respect to the horizontal wing. Flare from the juncture surfaces restricted the closest measurement distance to 3.5 mm from the vertical splitter plate, and to 1.0 mm from the horizontal wing. Tridecane, a kerosene derivative, was successfully used as the seeding material in this experiment (ref. 14). (Fig. 4.)



Figure 4

ORIGINAL PAGE
BLACK AND WHITE PHOTOGRAPH

C-2

COMPARISON OF LV DATA WITH HOT-WIRE RESULTS

In order to determine the accuracy of the LV data, measurements made at stations located farthest from the juncture have been compared here with the two-dimensional turbulent boundary layer results from Klebanoff's hot-wire measurements over a flat plate with zero pressure gradient (ref. 34). Even though these stations were chosen to minimize the influence of the juncture, some three-dimensional effects are expected to be present in the LV data. The mean velocity component U shown in figure 5 compares very well with the hot-wire results.

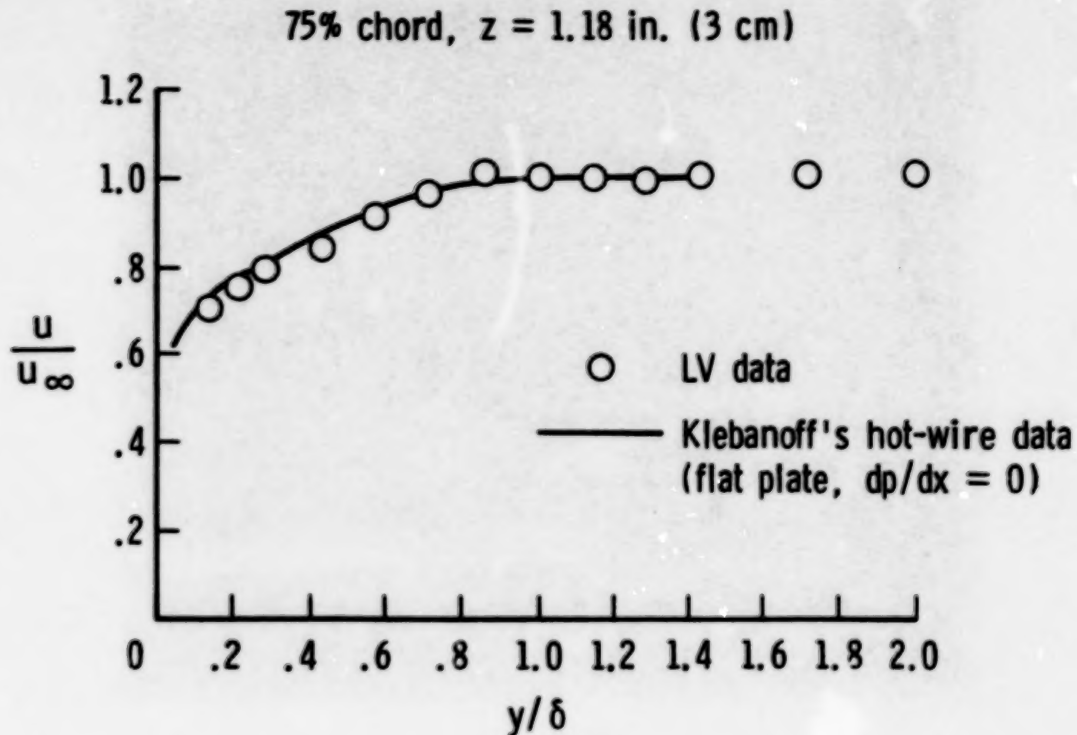


Figure 5

MEAN VERTICAL VELOCITY

In a flat plate boundary layer, the mean velocity component V is non-zero because of the displacement effect of the boundary-layer growth; it is directed away from the plate and has small magnitude. The values of mean velocity component V measured by the LV system satisfy this criterion. (Fig. 6.)

75% chord, $z = 1.18$ in. (3 cm)

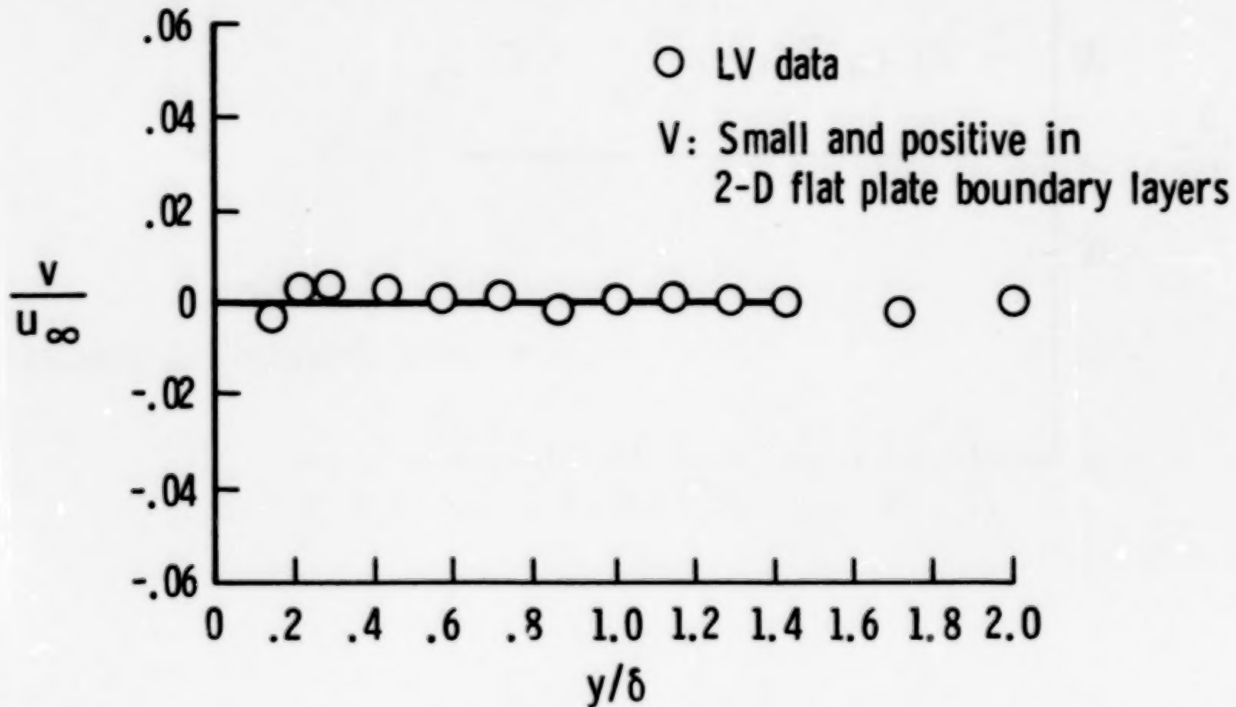


Figure 6

MEAN SPANWISE VELOCITY

The mean velocity component W is expected to be zero in a two-dimensional flow. But the flow in the juncture can still influence the measurements at the location where the data are being compared (fig. 7). This can partially explain the non-zero distribution of the W component.

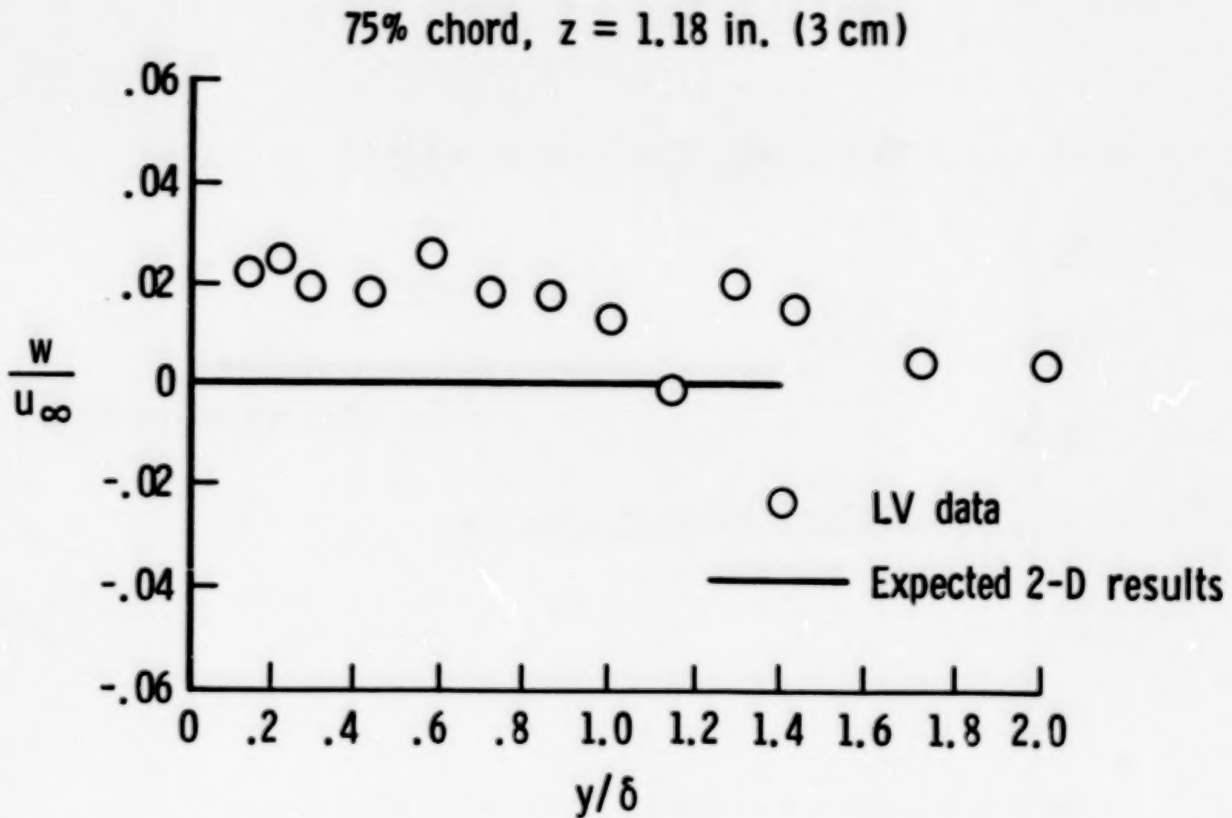


Figure 7

CHORDWISE VELOCITY FLUCTUATIONS

In the case of the turbulence intensity, \tilde{u}/u_∞ (where \tilde{u} is the RMS fluctuating component of velocity in the x direction), the LV data obtained inside the boundary layer compare well with Klebanoff's hot-wire results (ref. 34). The value outside of the boundary layer is higher than the freestream turbulence intensity of 0.04 percent, obtained from hot-wire measurements made in the same facility. The value is also higher than the LV resolution limit of 1 percent. This can be due to the following reason: hot-wire measurements normally filter out the very low frequency tunnel oscillations (< 2 Hz) whereas in the case of LV measurements, no such filtering is carried out. This will result in the higher-than-normal distribution of turbulence intensity u' as measured by the LV system. (Fig. 8.)

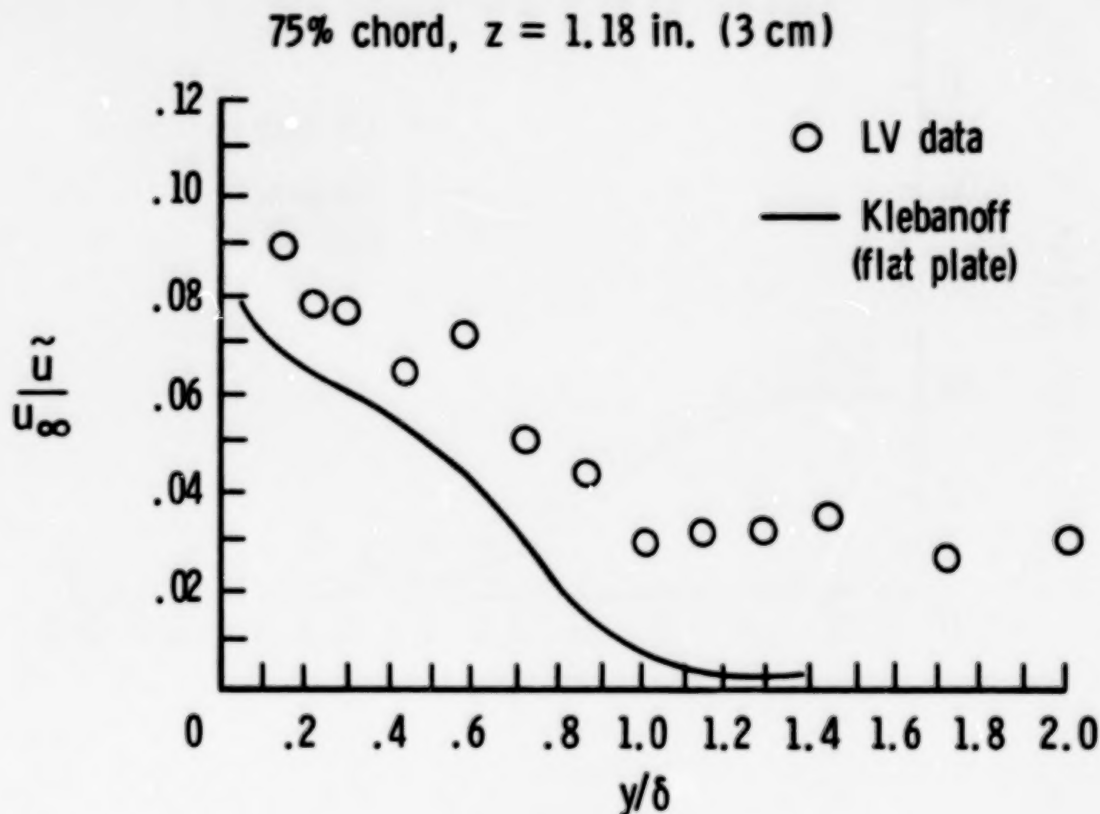


Figure 8

VERTICAL VELOCITY FLUCTUATIONS

Comparison of the turbulence intensity, \tilde{v}/u_∞ (where \tilde{v} is the RMS fluctuating component of velocity in the y direction), with Klebanoff's results (ref. 34) within the boundary layer is very good, but outside of the boundary layer the turbulence level is high. This is due to the fact that the lowest turbulence level that could be measured with the present LV system (or any other LV systems) is about 1 percent. (Fig. 9.)

75% chord, $z = 1.18$ in. (3 cm)

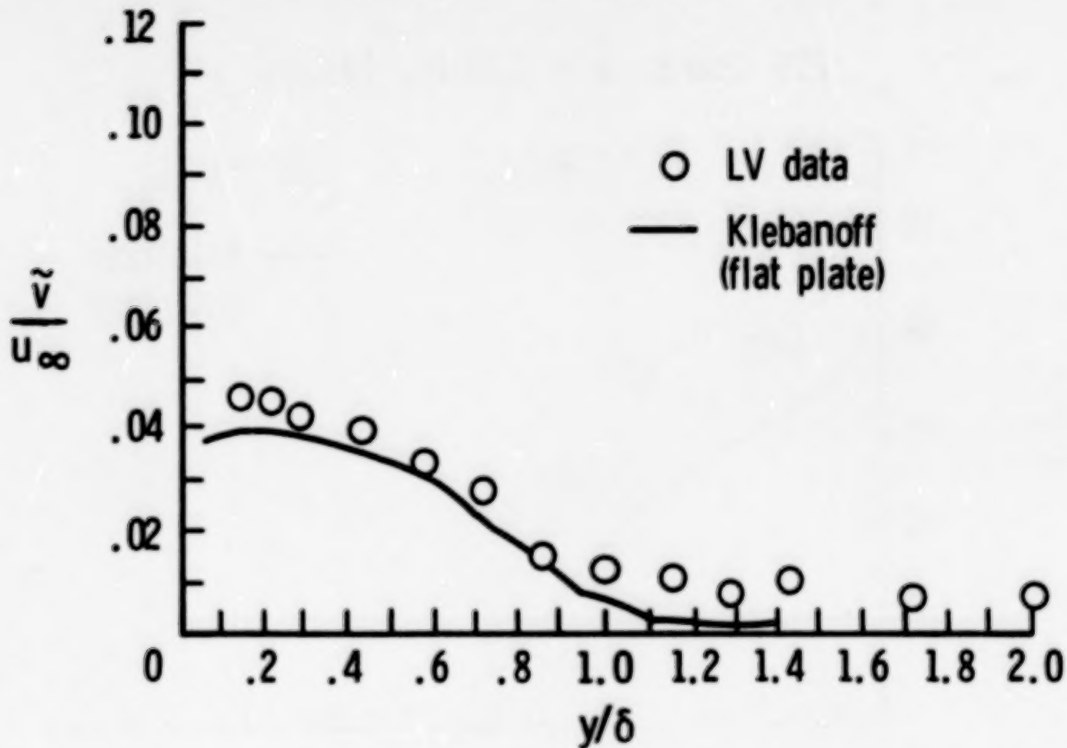


Figure 9

SPANWISE VELOCITY FLUCTUATIONS

The overall distribution of the turbulence intensity, \tilde{w}/u_∞ (where \tilde{w} is the RMS fluctuating component of velocity in the z direction), is much higher than Klebanoff's reference profile (Ref. 34). Part of it can be attributed to the three-dimensional effects of the juncture. Also, the narrow cross-beam angle between the laser beams that were used to obtain w -related components resulted in lower signal-to-noise ratio; this could have introduced some inaccuracies in this and other w -related components (fig. 10).

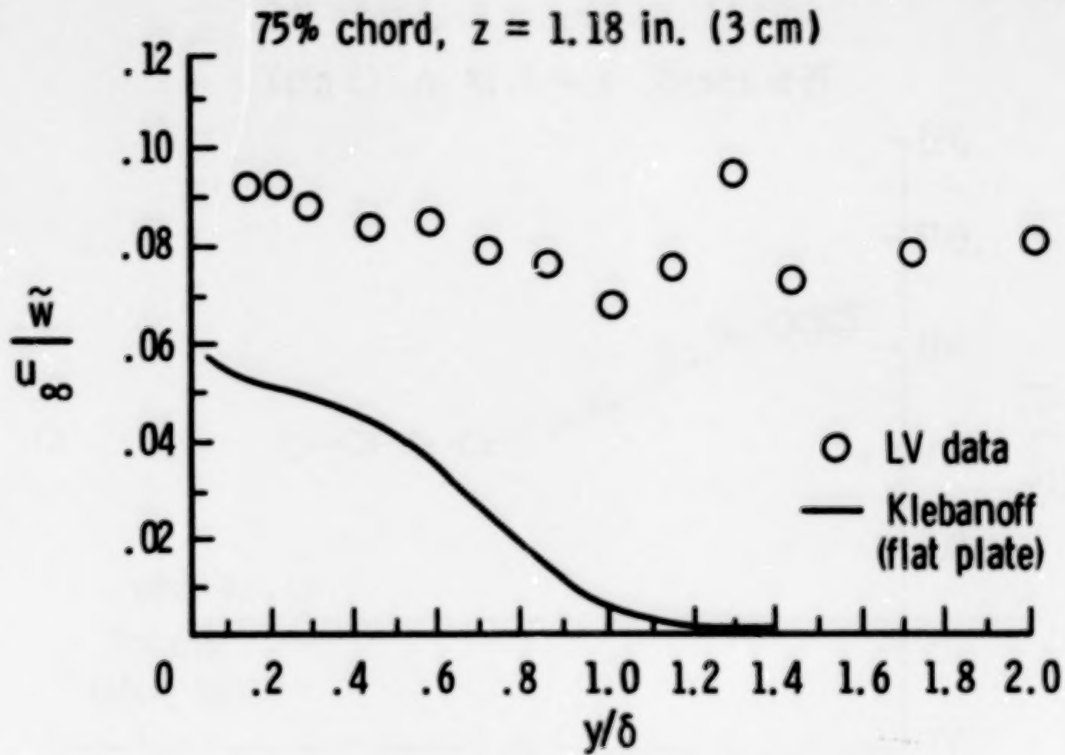


Figure 10

TURBULENT SHEAR STRESSES

There is excellent agreement between LV measurements of the Reynolds stress \overline{uv} and Klebanoff's hot-wire results (Ref. 34). The accuracy of w -related Reynolds stresses \overline{uw} and \overline{vw} was not as good because of the reasons detailed earlier.

In conclusion, a single-axis, five-beam, three-component laser velocimeter system has been used in a major experiment. Satisfactory results have been obtained with the LV system in the juncture flow. Limited optical access to the tunnel proved to be a problem for a three component LV system in determining the third component (w). (Fig. 11.)

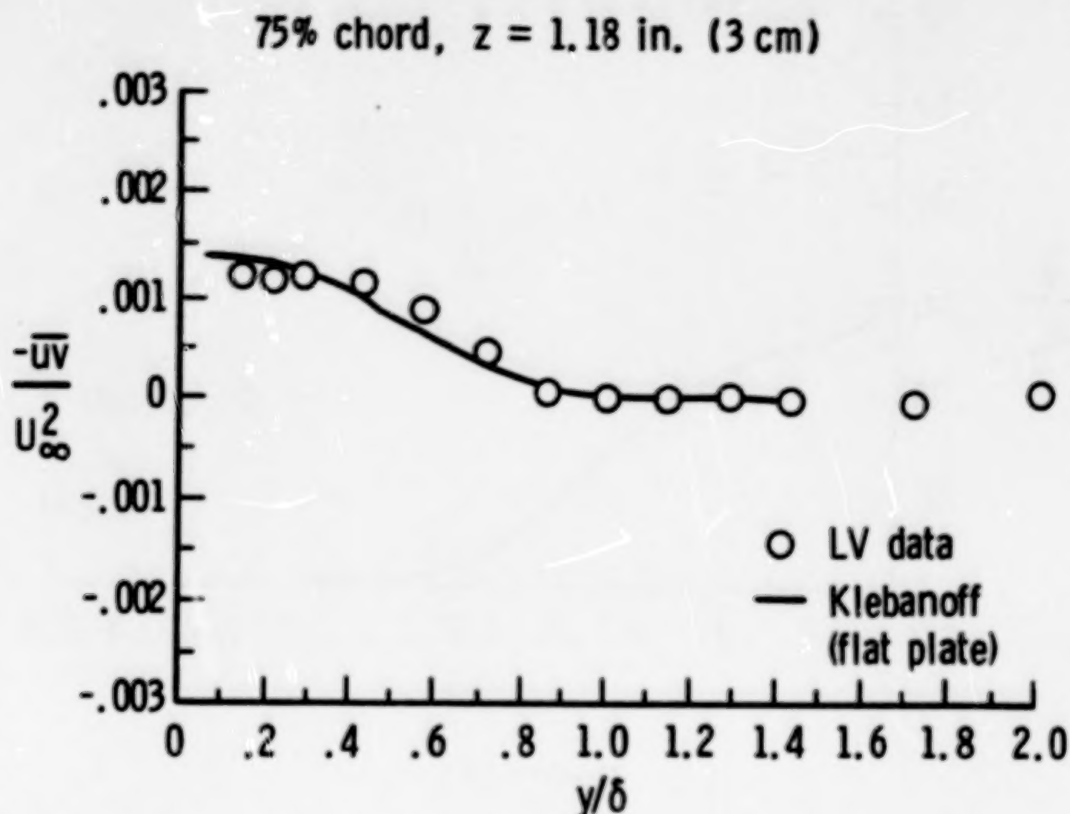


Figure 11

N90-12526

**BASIC AERODYNAMIC RESEARCH FACILITY
FOR COMPARATIVE STUDIES
OF FLOW DIAGNOSTIC TECHNIQUES**

Gregory S. Jones, Luther R. Gartrell, and P. Calvin Stainback
Langley Research Center
Hampton, Virginia

PURPOSE OF INVESTIGATION

The development of flow diagnostic techniques has gained renewed momentum in recent years due to the rising need to validate Computational Fluid Dynamics (CFD) results. While CFD has made great strides in the understanding of certain basic flow fields, there are still voids in the understanding of flow physics dealing with boundary-layer transition, turbulence, and separation.

For instance, the requirements of CFD for three component data of mean velocity, turbulence levels, and Reynolds stresses are limited to measurement techniques that can handle both mean and fluctuating flow quantities. While laser velocimetry (LV) systems have an advantage of being nonintrusive and very good at measuring mean velocity in unseparated and separated flow fields, they are weak in measuring low disturbance levels. In contrast, hot wire techniques are considered good in low turbulence flow fields, yet poor at measuring mean flow quantities. These strengths and weaknesses are expected to be compounded in the transonic flow regime where compressibility influences the outcome of each measurement. The flow regimes where the different instruments have general agreement is also expected to change with increased Mach number. These areas of mutual agreement will therefore be an area of interest in this test series. Thus, it is the basic purpose of this investigation to compare 3-D measurements obtained with a hot wire system to those obtained with an orthogonal LV system (fig. 1).

Current flow diagnostic research efforts are focusing on the higher order flow field data bases, such as those generated by laser velocimetry, hot wire anemometry, and multi-hole pressure probes. These instruments are being used in studies that range from simple 2-D flow fields, such as a flat plate boundary layer, to complex 3-D efforts, which include unsteady vortex flows generated by a delta wing.

Recent low-speed comparisons of results obtained with LV and hot wires (refs. 35 and 36) have revealed strengths and weaknesses of each instrument. To extend this comparative process to transonic speeds, the Basic Aerodynamic Research Facility was modified for a customized orthogonal 3-D LV system.

- Comparison of three-component measurements from hot-wire anemometry and orthogonal LV system
- Hot-wire anemometer suitable for low-level fluctuations
- Laser velocimeter suitable for higher levels of fluctuations and is nonintrusive
- Area of mutual agreement of two-methods to be determined

Figure 1

TEST FACILITY AND FLOW CONDITIONS

A test plan (fig. 2) has been derived that will focus on the differences in the two measurement techniques at both sub- and transonic speeds. The first phase is expected to show areas of mutual agreement at low speeds ($Mach < 0.4$). To eliminate mean velocity gradient and surface problems the initial test series will be performed behind a uniform turbulence grid. The classic turbulence decay format will represent turbulence magnitude and length scale variations. The second test series will be performed in a sub- and transonic 2-D shear flow field in the wake of a flat plate. Utilizing the velocity gradient, without a surface, will focus on the control volume size of both the LV and the hot wire. Moving upstream to the turbulent boundary layer of the flat plate will then introduce a surface effect, again concentrating on control volume size and laser flair. The final test series of this comparative study will address a 3-D vortical flow field at transonic speeds ($0.5 < Mach < 1.3$).

- Atmospheric — continuous tunnel
- Subsonic tests at Mach numbers from 0.1 to 0.4 for $\tilde{u}, \tilde{v}, \tilde{w}$ from both LV and hot wire measurements
- Transonic tests at Mach numbers from 0.4 to 1.2 for $\tilde{u}, \tilde{v}, \tilde{w}$ from LV system and $\tilde{u}, \tilde{p}, \tilde{T}_t$ from hot-wire system
- Top and side walls of test section made of glass

Figure 2

**TEST SECTION OF BASIC AERODYNAMIC RESEARCH FACILITY
FOR USE WITH ORTHOGONAL LV SYSTEM**

The test section of the Basic Aerodynamics Research Facility (fig. 3) was designed for optical access for an orthogonal 3 component LV system (ref. 15). This constraint required the slots to be moved to the corner of the test section. Comparison of the performance of the new LV test section to that of the uniform 6 slot configuration showed minimal deviation in the Mach number distribution through a Mach number range up to 1.3. The primary effect was a degradation of the re-entry flap performance and diffuser efficiency.

As part of the initial test plan, a seeding study will be initiated to determine particulate tracking ability. This will be performed over the entire Mach number range of the tunnel. The stagnation line on a sphere will be used as the test case. Spheres of different sizes will be used as computations of the stagnation flow may be influenced by model blockage.



Figure 3

ORIGINAL PAGE
BLACK AND WHITE PHOTOGRAPH

~~ORIGINAL PAGE IS
OF POOR QUALITY~~

OPTICS OF THREE-COMPONENT ORTHOGONAL LV SYSTEM

The 3-D orthogonal capability of the LV optics (fig. 4) makes the Basic Aerodynamics Research Facility a one-of-a-kind transonic facility. The flexibility of the paneled test section is enhanced by the flexibility of the LV optical system itself. Not only is the system capable of 3-D orthogonal measurements but also can be arranged in off-axis backscatter or forward scatter off-axis 3-D orientations. This allows the researcher to optimize the optical access to any variety of 2-D or 3-D models. It also gives the researcher the ability to compare different 3-D LV optical schemes directly.

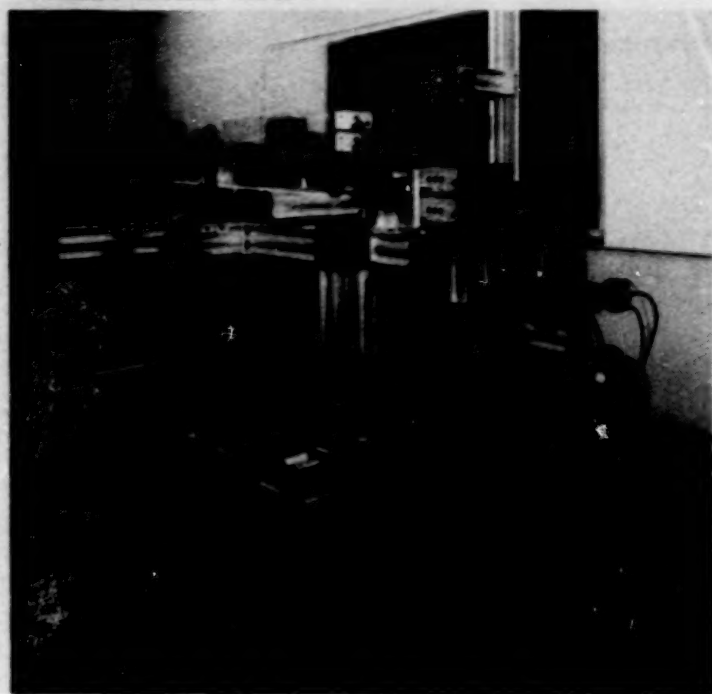


Figure 4

ORIGINAL PAGE
BLACK AND WHITE PHOTOGRAPH

LV TRAVERSING SYSTEM TO OFFER FLEXIBILITY IN STUDYING DIFFERENT 3-D OPTICAL CONFIGURATIONS

The LV traversing system is designed to offer flexibility in orienting the transmitting and/or receiving optics to either a forward scatter or backscatter system (fig. 5). This allows the researcher to optimize the optical access to any variety of 2-D or 3-D models. It also gives the researcher the ability to compare different 3-D and LV optical schemes directly.

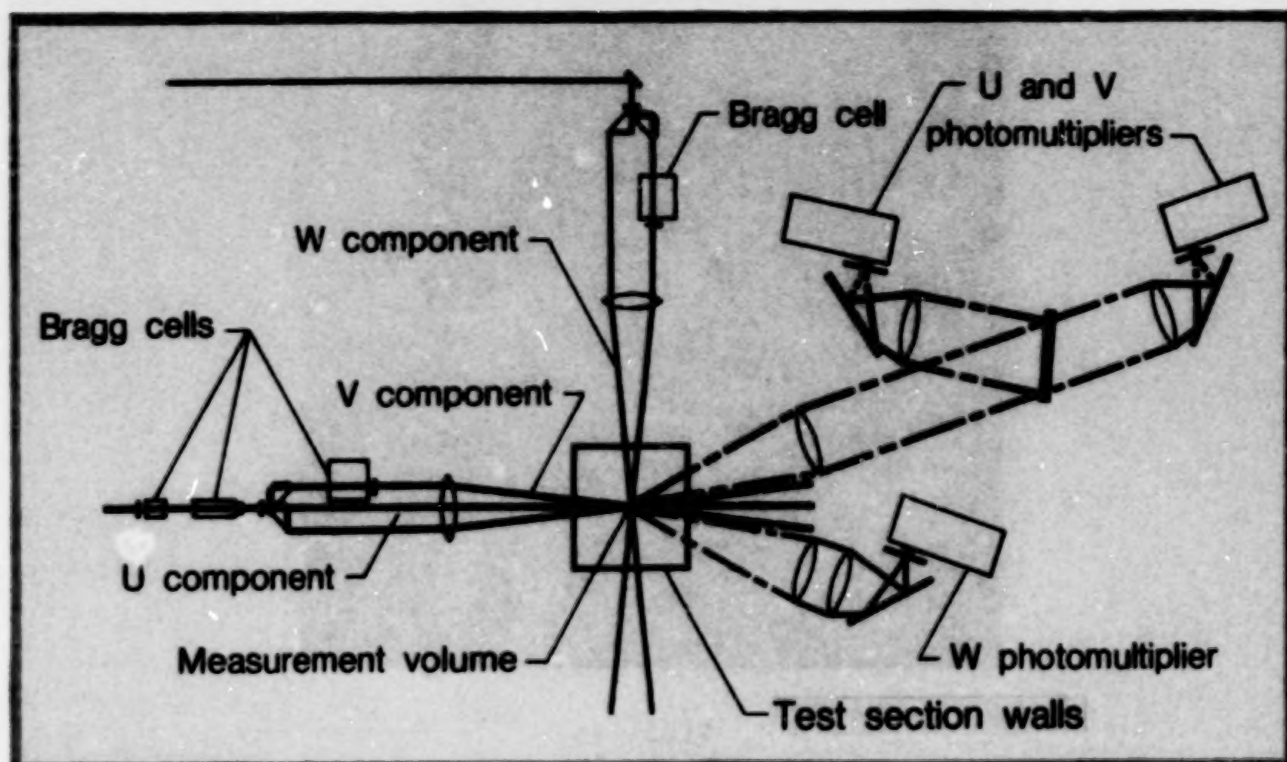


Figure 5

ORIGINAL PAGE
BLACK AND WHITE PHOTOGRAPH

**RECENT TESTS AT LANGLEY
WITH A
UNIVERSITY OF TENNESSEE SPACE INSTITUTE (UTSI)
SKIN FRICTION BALANCE**

**Pierce L. Lawing
Langley Research Center
Hampton, Virginia**

**A. D. Vakili and J. M. Wu
The University of Tennessee Space Institute
Tullahoma, Tennessee**

UTSI SKIN FRICTION BALANCE CONCEPT

Figure 1 serves to illustrate the principle of operation of the UTSI (University of Tennessee Space Institute) moving belt skin friction balances. The balance is mounted such that the belt part is flush with the surface to be investigated. The two drums that support the belt are in turn supported by flexures. When the belt experiences force due to the shear of a passing fluid, it rotates the drums against the restoring force of the flexures. The stiffness of the flexures is selected to allow a maximum of 3 degrees of rotation for the expected forces. Strain gages are attached to the flexures to produce a voltage proportional to, and linear with, the torque produced by the belt rotating the drums. Since the small gaps that are open to the flow do not change with this rotation, there is no need for a closed-loop nulling device to center the measuring element, as there is in the floating element type balances. Further details are available in reference 16.

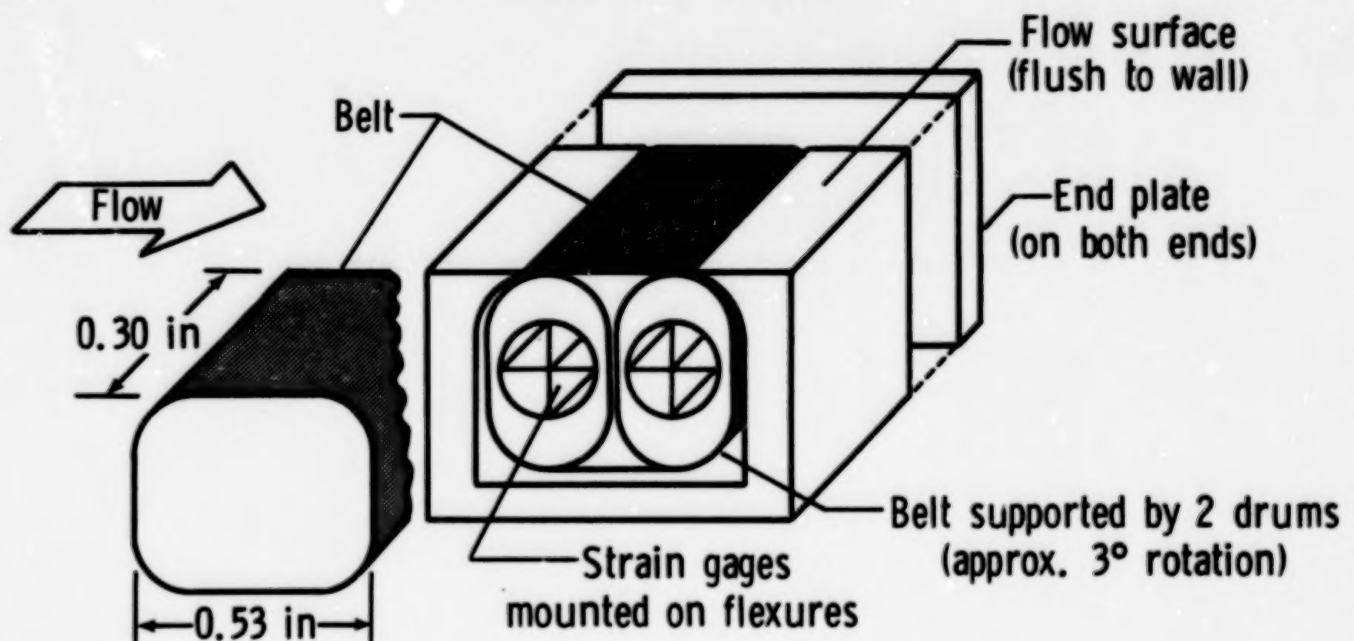


Figure 1

SUMMARY OF TEST EXPERIENCE ON TEST SECTION SIDEWALLS

Figure 2 summarizes the experience at LaRC with UTSI (University of Tennessee Space Institute) skin friction balances. The results shown were measured on the test section sidewalls of the 0.3-meter Transonic Cryogenic Tunnel, or 0.3-m TCT, and the Unitary Plan Wind Tunnel. The comparison is presented in the incompressible plane since the Mach number ranges from low subsonic to transonic in the 0.3-m TCT, and through the supersonic range in the Unitary tunnel. The Karman-Schoenherr flat plate skin friction formula is included for comparison. The shaded area represents data taken over the history of the Unitary tunnel with floating element skin friction balances (references 37, 38, and 39.)

The present results of testing on tunnel sidewalls should not be used to judge the accuracy of the skin friction balances. Rather, the data shown here should simply be taken as evidence of operational experience. Unless extraordinary precautions are taken, tunnel sidewall boundary layers are not classical flat-plate turbulent boundary layers. At a minimum, they are non-adiabatic and affected by wall roughness. Figure 3 shows that the 0.3-m TCT data level shown here can be represented by an equivalent wall roughness of only .02 mm. Since the ratio of boundary layer length to roughness height is the scaling parameter, and the boundary layer length increases with tunnel size, the large Unitary Plan Wind Tunnel would be only one-fourth as sensitive for the same absolute roughness height.

The appropriate conclusion to be drawn here is that the balance is capable of operation in environments as diverse as the cryogenic, transonic, high-shear rate of the 0.3-m TCT, and the high-temperature supersonic environment of the Unitary Plan Wind Tunnel.

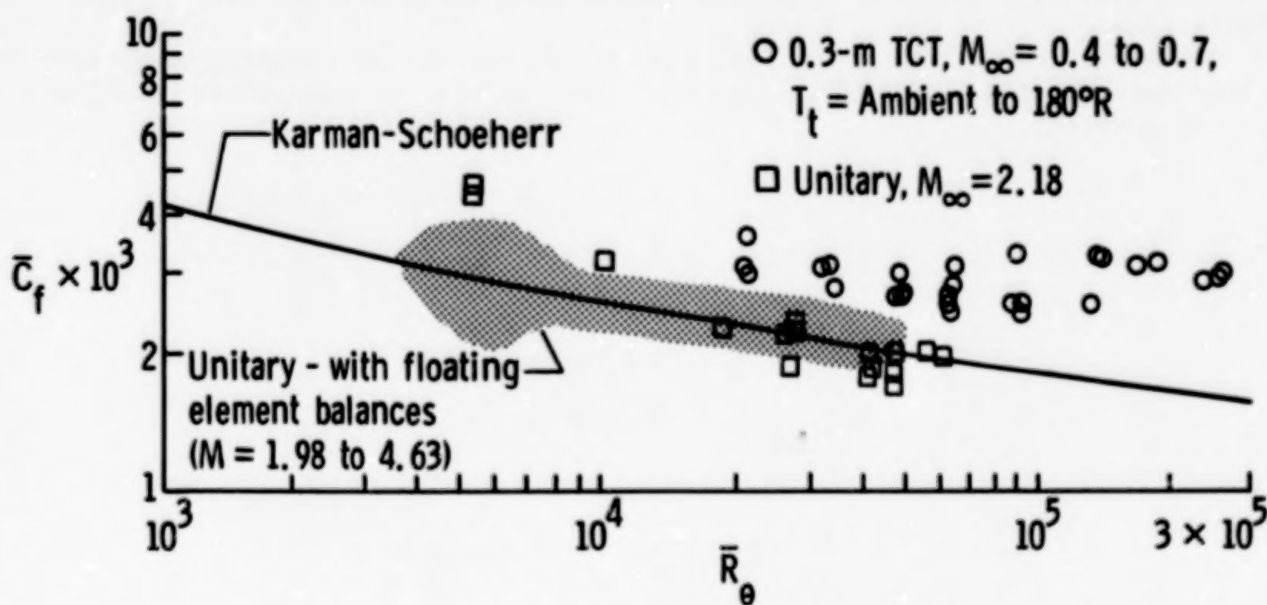


Figure 2

COMPARISON OF 0.3-M TCT DATA AND WALL ROUGHNESS EFFECTS

The data shown here (fig. 3) for the 0.3-m TCT are the same as shown on the previous plot, but have not been transformed to incompressible coordinates. Curves are shown for constant values of distributed roughness. The actual roughness was not measured. The approximate formula for rough flat plate flow used to generate the curves was

$$C_f = (2.87 + 1.58 \log(x/\epsilon))^{-2.5}$$

where ϵ is the roughness height and x is distance from the leading edge, reference 40. References 17 and 18 discuss the details of applying this formula to a test section wall boundary layer, by calculating an equivalent flat plate length. The curve labeled smooth in figure 3 was calculated from the relation,

$$C_f = 0.027 / (Re_x)^{1/7}$$

also from reference 40.

The intent of this figure is not to promote a rough wall prediction method or fully explain the data trends. It does serve to demonstrate the severe effects of small roughness heights in a turbulent boundary layer, and that an equivalent roughness height of only .02mm is sufficient to match the data. Further discussion may be found in references 17 and 18.

Current plans call for further testing of UTSI balances on a large flat plate in the NTF. Floating element balances as well as other types of skin friction measuring devices will also be tested for comparison. The surface finish will be carefully controlled and extensive boundary-layer profile surveys will be conducted. The result will be a boundary layer much better understood than the test section sidewall cases.

The basic feasibility of the UTSI balance to operate in cryogenic conditions has been demonstrated. Carefully controlled testing will be required to establish limits on accuracy.

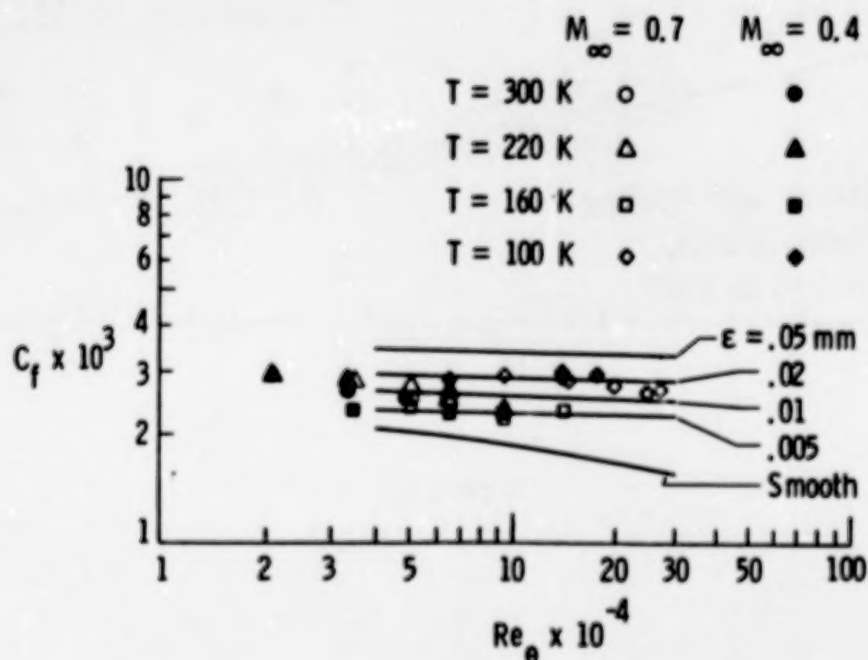


Figure 3

PROPOSED NEW RESEARCH

Work to be done under a new grant from LaRC to UTSI will include the use of fiber optics to read the movement of the belt rather than strain gages. This technique is expected to be less sensitive to temperature changes, thus simplifying balance calibration and use at cryogenic temperatures. Also electrical noise and error due to gage heat will be eliminated. Finally, eliminating the strain gage removes the primary barrier to miniaturization.

A concurrent effort is also under way to fabricate these balances using the relatively new wire-cut method (electron discharge machining using a wire for an electrode). The use of the wire-cut technique has the potential to lower the cost of the balances by reducing the part count and simplifying the assembly procedure. The combination of the wire-cut technique and the use of fiber optics may reduce the cost per balance sufficiently to allow them to be tailored to a specific test. It is conceivable that as many as 10 balances could be dedicated to a single airfoil configuration. A typical layout is shown in figure 4 on a 14 percent thick, 10-inch chord airfoil. Each balance would be contoured to match the airfoil surface. This would simplify measurement of the location of transition, separation and transonic shocks.

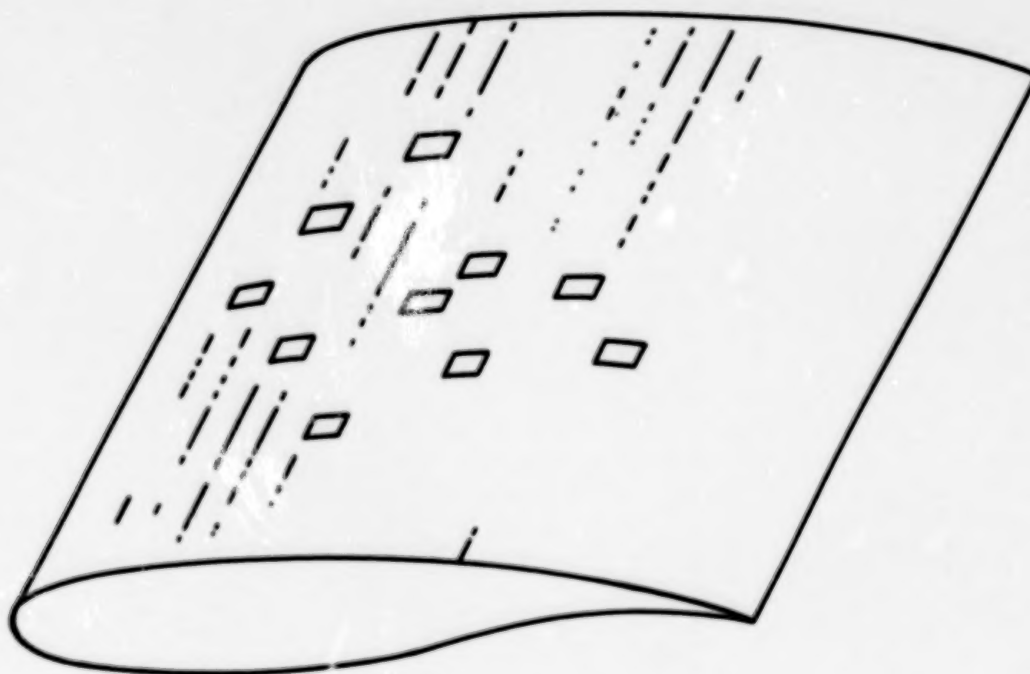


Figure 4

N90-12528

**RECENT FLOW VISUALIZATION STUDIES
IN THE 0.3-m TCT**

**Walter L. Snow, Alpheus W. Burner, and William K. Goad
Langley Research Center
Hampton, Virginia**

SCHEMATIC OF TYPICAL FLOW VISUALIZATION SETUP IN 0.3-M TCT

Light beams are altered by refractive index changes and indeed flow induced refractive index changes provides the impetus for conventional visualization techniques such as schlieren and shadowgraph. Unfortunately effects related to the flow can be masked by refractive index inhomogeneities external to the test section. For high-pressure cryogenic facilities this is especially true in the interface between the region of test and the more benign environment where equipment is housed. Since the refractive index is directly proportional to density, it depends upon pressure and temperature through the ideal gas law. Even mild temperature inhomogeneities can be detrimental when coupled with high pressures as occurs in the plenum. The simple shadowgraph scheme depicted in figure 1 was used to assess the flow quality of the Langley 0.3-Meter Transonic Cryogenic Tunnel. The light source was a pulsed (15 microsecond) 75-watt xenon arc lamp focused onto a 0.51 mm diameter pinhole. Light was collimated with an f/8 mirror with a 1.22-m focal length. Data were recorded on film with a 70mm format reflex camera.

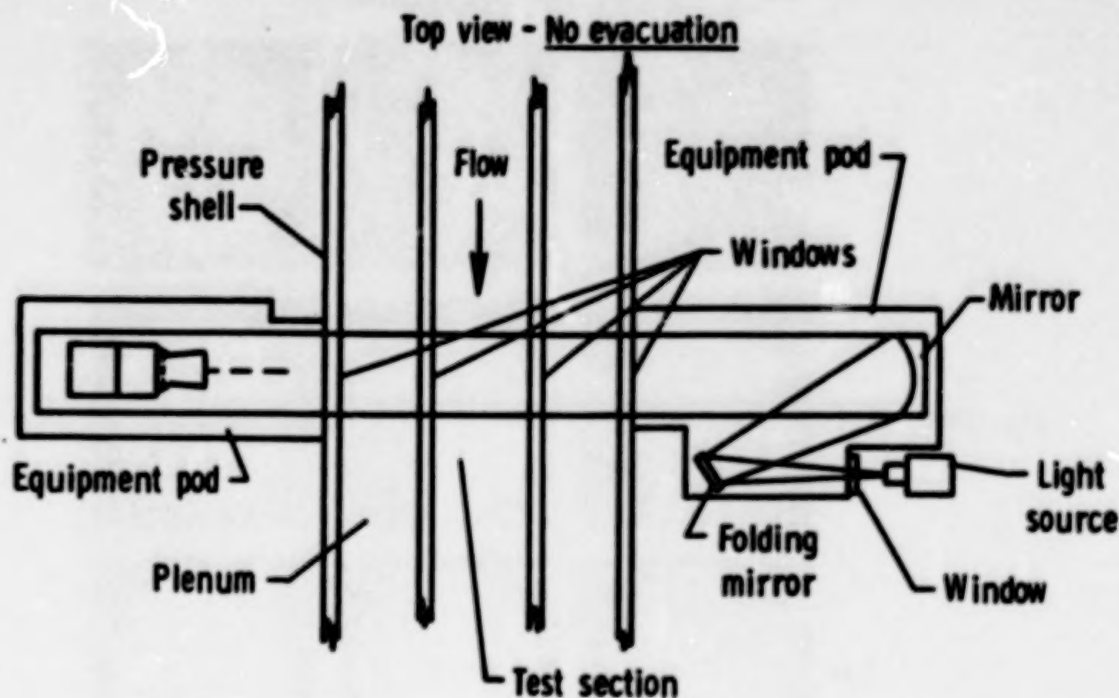


Figure 1

REPRESENTATIVE SHADOWGRAPH RESULTS PRIOR TO IMPROVEMENTS

The simple shadowgraph scheme depicted in figure 1 was used to characterize the flow quality of the Langley 0.3-Meter TCT with results shown in figure 2. This collage of photos was taken at Mach 0.65 conditions with stagnation pressure and temperature as indicated. The completely uniform light field which characterizes the pretest condition becomes increasingly mottled and jumbled as temperature decreases and pressure increases. This behavior is typical of earlier optical experiments conducted in this facility (see refs. 41, 42, and 43).

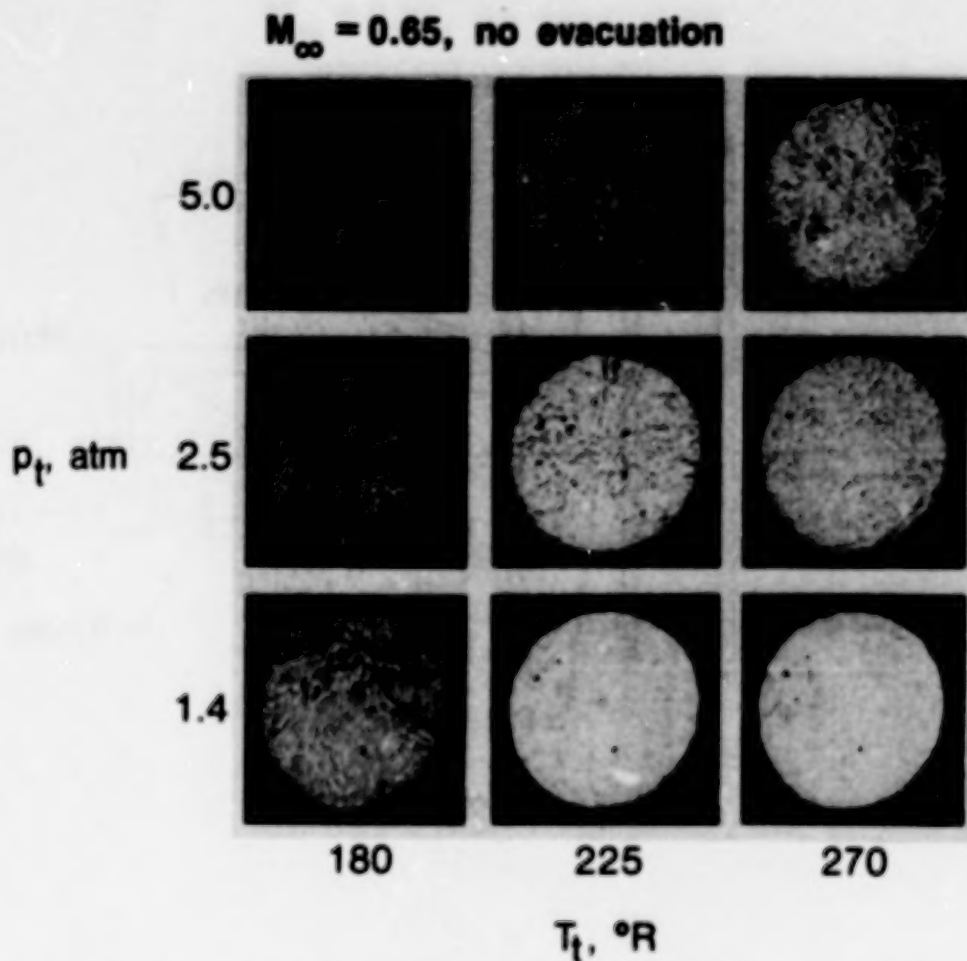


Figure 2

ORIGINAL PAGE
BLACK AND WHITE PHOTOGRAPH

MODIFIED SHADOWGRAPH SYSTEM TO EXCLUDE PLENUM EFFECTS

Several of the tests devised to determine the source of the image degradation are described in reference 19. The crucial test involved installation of tubes to penetrate the plenum. The tubes could be purged or evacuated to allow direct viewing of the test section. Figure 3 shows the same layout as figure 1 with the hatched area designating the region impacted by the isolation tubes. A bellows type of arrangement was required to accommodate the large differential expansion experienced in the structure of the facility. Details of the assembly are found in the reference.

Top view — With evacuation in equipment pods (cross hatched)

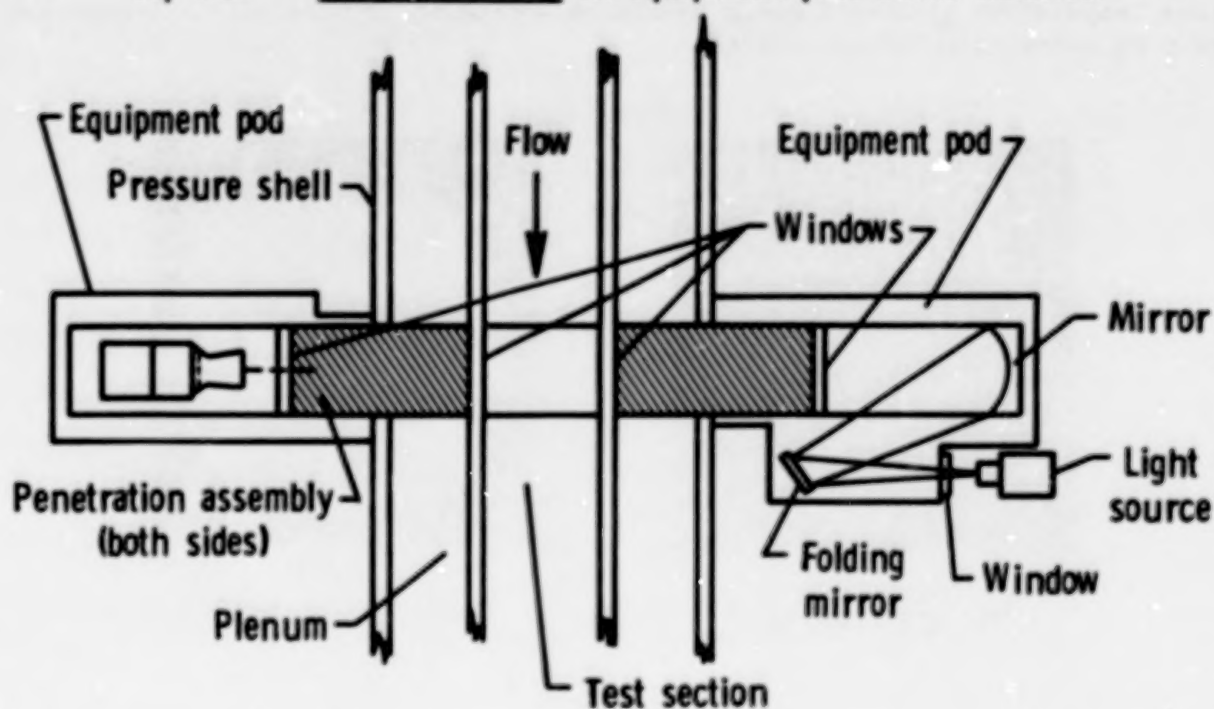


Figure 3

EFFECT OF PLENUM EVACUATION ON SHADOWGRAPH RESULTS

When the penetration tubes were evacuated the quality of the shadowgraphs improved dramatically. Results for the worst test condition of figure 2 ($T_t = 180$ R, $P_t = 5$ atm, Mach 0.65) are shown in figure 4. Residual "graininess" in the evacuated case is believed to be due to the flow field itself. Earlier difficulties were brought about by density inhomogeneities in the regions of strong temperature gradients especially in those areas under high pressure. Provisions for evacuated paths to and from the test section should be seriously considered in future flow visualization efforts for facilities of this type. In scaled up cryogenic facilities such as the National Transonic Facility equipment is completely housed within the plenum area (ref. 42). Much of the critical optical path would be in the controlled environment of the equipment enclosures. Nevertheless, regions near windows where extreme temperature gradients occur should be evacuated if possible to lessen the effects of convection induced mixing.

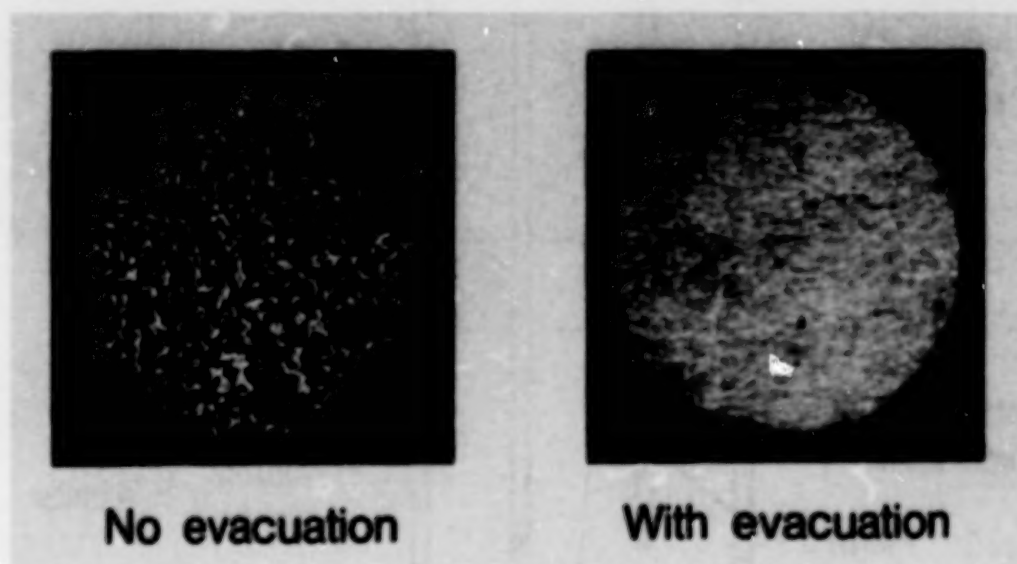


Figure 4

ORIGINAL PAGE
BLACK AND WHITE PHOTOGRAPH

REFERENCES

1. Stainback, P. C.; and Johnson, C. B.: "A Probe and Data Reduction Technique for Obtaining Hot Wire Data at Transonic Speeds" in the Flow Quality Measurements in Transonic Wind Tunnels and Planned Calibration of the National Transonic Facility Appendix. NASA CP-2183, pp. 113-121, High Reynolds Number Research - 1980, December 1980.
2. Stainback, P. C.; Johnson, C. B.; and Basnett, C. B.: Preliminary Measurements of Velocity, Density and Total Temperature Fluctuations in Compressible Subsonic Flow. AIAA-83-0384, presented at the AIAA 21st Aerospace Sciences Meeting, Reno, Nevada, January 10-14, 1983.
3. Stainback, P. C.; Johnson, C. B.; Holmes, B. J.; Obara, C. J.; Carraway, D. L.; et al.: Flow Diagnostics and Visualization in Wind Tunnels and Flight. NASA CP 2397, Volume I, presented at the Langley Symposium on Aerodynamics, April 1985.
4. Johnson, C. B.; Johnson, W. G., Jr.; and Stainback, P. C.: A Summary of Reynolds Number Effects On Some Recent Tests in the Langley 0.3-Meter Transonic Cryogenic Tunnel. SAE Technical paper 861765, presented at Aerospace Technology Conference and Exposition, Long Beach, California, October 13-16, 1986.
5. Lynch, F. T.; and Patel, D. R.: Some Important New Instrumentation Needs and Testing Requirements for Testing in a Cryogenic Wind Tunnel Such as the NTF. AIAA-82-0605, presented at the AIAA 12th Aerodynamic Testing Conference, Williamsburg, Virginia, March 22-24, 1982.
6. Fancher, M. F.: Aspects of Cryogenic Wind Tunnel Testing Technology at Douglas. AIAA-82-0606, presented at the AIAA 12th Aerodynamic Testing Conference, Williamsburg, Virginia, March 22-24, 1982.
7. Bobbitt, P. J.; Waggoner, E. G.; Harvey, W. D.; and Dagenhart, J. R.: A Faster "Transition" to Laminar Flow. SAE Technical Paper 851855, presented at the Aerospace Technology Conference and Exposition, Long Beach, California, October 14-17, 1985.
8. Johnson, C. B.; Carraway, D. L.; Stainback, P. C.; and Fancher, M. F.: A Transition Detection Study Using a Cryogenic Hot Film System in the Langley 0.3-Meter Transonic Cryogenic Tunnel. AIAA-87-0049, presented at the AIAA 25th Aerospace Sciences Meeting, Reno, Nevada, January 12-15, 1987.
9. Johnson, C. B.; Carraway, D. L.; Hopson, P., Jr.; and Tran, S. Q.: Status of a Specialized Boundary Layer Transition Detection System for Use in the U.S. National Transonic Facility. Presented at the 12th International Congress on Instrumentation in Aerospace Simulation Facilities, Williamsburg, Virginia, June 22-25, 1987.
10. Stack, J. P.; Mangalam, S. M.; and Berry, S. A.: A Nonintrusive Study of Laminar Separation Bubble Using Surface-Film Gages. AIAA-87-1271, presented at the AIAA 19th Fluid Dynamics, Plasma Dynamics, and Lasers Conference, Honolulu, Hawaii, June 8-10, 1987.
11. Azzazy, M.; Modarress, D.; and Trolinger, J. D.: Feasibility Study of Optical Boundary Layer Transition Detection Method. NASA CR-178109, June 1986.
12. Meyers, James F.; and Hepner, Timothy E.: Velocity Vector Analysis of a Juncture Flow Using a Three Component Laser Velocimeter. Presented at the Second International Symposium on Applications of Laser Anemometry to Fluid Mechanics, Lisbon, Portugal, July 2-4, 1984.
13. Scheiman, J.; and Kubendran, L. R.: Juncture Flow Measurements Using Laser Velocimetry. AIAA-85-1612, presented at the AIAA 18th Fluid Dynamics and Plasmadynamics and Lasers Conference, Cincinnati, Ohio, July 16-18, 1985.

14. Scheiman, J.; and Kubendran, L. R.: "LDV Seeding System for the Langley Low Turbulence Pressure Tunnel," in NASA CP-2393, presented at the Workshop on Wind Tunnel Seeding Systems for Laser Velocimeters, NASA Langley Research Center, Hampton, Virginia, March 1985.
15. Jones, G. S.; Gartrell, L. R.; Sewall, W. G.; and Stainback, P. C.: Designing Transonic Wind Tunnels for Flow Diagnostics and Laser Velocimeter Applications. AIAA-87-1434, presented at the AIAA 19th Fluid Dynamics, Plasma Dynamics, and Lasers Conference, Honolulu, Hawaii, June 8-10, 1987.
16. Vakili, A. D.; and Wu, J. M.: A New Instrument for Direct Measurement of Wall Shear Stress. Proceedings of the 28th International Instrumentation Symposium, Instrument Society of America Proceedings, vol. 19, part 1, pp. 147-152, May 1982.
17. Vakili, A. D.; and Wu, J. M.: Development of a New Instrument for Direct Skin Friction Measurements. NASA CR 176818, March 1986.
18. Vakili, A. D.; Wu, J. M.; and Lawing P. L.: Wall Shear Stress Measurements Using a New Transducer. AIAA-86-1092, presented at the AIAA/ASME 4th Joint Fluid Mechanics and Plasma Dynamics and Laser Conference, Atlanta, Georgia, May 12-14, 1986.
19. Snow, Walter L.; Burner, Alpheus W.; and Goad, William K.: Improvement in the Quality of Flow Visualization in the Langley 0.3-Meter Transonic Cryogenic Tunnel. NASA TM 87730, 1986.
20. Stainback, P. C.: A Review of Hot Wire Anemometry In Transonic Flows. ICIASF 85 Record, Stanford, California, pp. 67-78.
21. Stainback, P. C.: Some Influences of Approximate Values for Velocity, Density, and Total Temperature Sensitivities on Hot Wire Anemometer Results. AIAA-86-0506, presented at the AIAA 24th Aerospace Sciences Meeting, Reno, Nevada, January 6-9, 1986.
22. Rose, W. C.; and Otten, L. J., III: Airborne Measurement of Atmospheric Turbulence. Presented at the USAF/NASA Aero-Optics Symposium, NASA Ames Research Center, California, August 14-15, 1979.
23. Otten, L. J., III; Pavel, A. L.; Finley, W. E.; and Rose, W. C.: A Survey of Recent Atmospheric Turbulence Measurements from a Subsonic Aircraft. AIAA-81-0298, presented at the AIAA 19th Aerospace Sciences Meeting, St. Louis, Missouri, January 12-15, 1981.
24. Ehernberger, L. J.: The YF-12 Gust Velocity Measuring System. NASA Conference Publication 2054 - Volume 1, presented at YF-12 Experiments Symposium, Dryden Flight Research Center, Edwards, California, September 13-15, 1978.
25. Nagel, A. L.: Aerodynamic Research Applications at Boeing. In: Internal Council of the Aeronautical Sciences, Congress, 13th and AIAA Aircraft Systems and Technology Conference, Seattle, Washington, August 22-27, 1982, Proceedings, volume 2, pp. 1235-1242.
26. Fancher, M. F. A Transonic Cryogenic Wind Tunnel Test of a Supercritical Airfoil Model. Background and Progress. AIAA-80-0418, presented at the AIAA 11th Aerodynamic Testing Conference, Colorado Springs, Colorado, March 1980.
27. Fancher, M. F.: A Hot-Film System for Boundary-Layer Transition Detection in Cryogenic Wind Tunnels, presented to Euromech Colloquium 142 on Hot-Wire, Hot-Film Anemometry and Condition Measurement, July 1980.
28. Schlichting, Hermann: Boundary Layer Theory. McGraw-Hill, 1960.
29. Viken, J. K.: Aerodynamic Design Considerations and Theoretical Results for a High Reynolds Number Natural Laminar Flow Airfoil. M.S. Thesis, George Washington University, January 1983.
30. Srokowski, A. J.; and Orszag, S. A.: Mass Flow Requirements for LFC Wing Design. AIAA-77-1222, August 1977.

31. Owen, F. K.: Transition Experiments on a Flat Plate at Subsonic and Supersonic Speeds. AIAA-69-9 presented at the AIAA 7th Aerospace Sciences Meeting, New York, January 20-22, 1969.
32. McGhee, R. J.; Viken, J. K.; Pfenninger, W.; Beasley, W. D.; and Harvey, W. D.: Experimental Results for a Flapped Natural-Laminar-Flow Airfoil with High Lift/Drag Ratio. NASA TM-85788, May 1984.
33. Stainback, P. C.; McGhee, R. J.; Beasley, W. D.; and Morgan, H. L., Jr.: The Langley Research Center's Low Turbulence Pressure Tunnel. AIAA-86-0762, presented at the AIAA 14th Aerodynamic Testing Conference, West Palm Beach, Florida, March 5-7, 1986.
34. Klebanoff, P. S.: Characteristics of Turbulence in a Boundary Layer with Zero Pressure Gradient, NACA Report 1247, 1955.
35. Braden, J. A.; Whipkey, R. R.; Jones, G. S.; and Lilley, D. E.: Experimental Study of the Separating Confluent Boundary-Layer -- Volume II - Experimental Data. NASA Contractor Report 166018, March 1983.
36. Braden, J. A.; Whipkey, R. R.; Jones, G. S.; and Lilley, D. E.: Experimental Study of the Separating Confluent Boundary-Layer -- Volume I - Summary. NASA Contractor Report 3655, June 1983.
37. Allen, Jerry M.: Systematic Study of Error Sources In Supersonic Skin-friction Balance Measurements. NASA TN D-8291, October 1976.
38. Allen, Jerry M.: An Improved Sensing Element for Skin-friction Balance Measurements. AIAA-80-0049 presented at the AIAA 18th Aerospace Sciences Meeting, Pasadena, California, January 14-16, 1980.
39. Allen, Jerry M.: Evaluation of Compressible-flow Preston Tube Calibrations. NASA TN D-7190, May 1973.
40. White, Frank M.: Fluid Mechanics, McGraw-Hill Book Company, 1974.
41. Burner, A. W.; and Goad, W. K.: Flow Visualization in a Cryogenic Wind Tunnel Using Holography. NASA TM-84556, 1982.
42. Rhodes, D. B.; and Jones, S. B.: Flow Visualization in the Langley 0.3-Meter Transonic Cryogenic Tunnel and Preliminary Plans for the National Transonic Facility. Flow Visualization and Laser Velocimetry for Wind Tunnels, NASA CP-2243, 1982, pp. 117-132.
43. Snow, W. L.; Burner, A. W.; and Goad, W. K.: Image Degradation in Langley 0.3-Meter Transonic Cryogenic Tunnel. NASA TM-84550, 1982.

EXPERIMENTAL STUDIES ON GÖRTLER VORTICES

S. M. Mangalam
Analytical Services and Materials, Inc.
Hampton, Virginia

J. R. Dagenhart and J. F. Meyers
NASA Langley Research Center
Hampton, Virginia

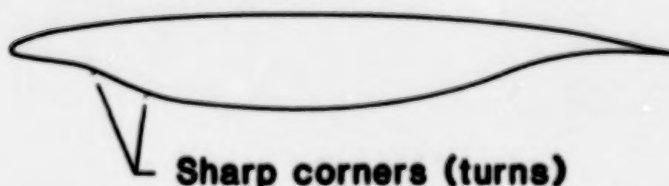
PRECEDING PAGE BLANK NOT FILMED

ABSTRACT

Görtler vortices arise in laminar boundary layers along concave walls due to an imbalance between pressure and centrifugal forces. In advanced laminar-flow control (LFC) supercritical airfoil designs (reference 1), boundary-layer suction is primarily used to control Tollmien-Schlichting instability and cross-flow vortices in the concave region near the leading edge of the airfoil lower surface. The concave region itself is comprised of a number of linear segments positioned to limit the total growth of Görtler vortices. Such an approach is based on physical reasonings but rigorous theoretical justification or experimental evidence to support such an approach does not exist. An experimental project was initiated at NASA Langley to verify this concept. In the first phase of the project an experiment was conducted on an airfoil whose concave region has a continuous curvature distribution. Some results of this experiment have been previously reported (references 2 and 3) and significant features are summarized in this paper. (Figures 1-3).

MOTIVATION

- LFC SC airfoil development
- 8-FT experiment
- Influence of curvature distribution



- Influence of suction
- Study of Görtler vortices in external flow

Figure 1

BACKGROUND

- Previous experiments used "bumps" on opposite walls to ensure attached flow in the concave region or were conducted in channels
- Results indicate invariance of wavelength with freestream parameters
- Information on effects of Suction, Pressure gradient, and Curvature distribution not available

Figure 2

PRESENT EXPERIMENT

- Airfoil model
 - Continuous, smooth curvature distribution
 - Concave region $0.175 < x/c < 0.275$
 - Perforated titanium panel $0.17 < x/c < 0.225$
 - Convex region $0.275 < x/c < 0.50$
- Flow visualization
- Laser velocimetry

Figure 3

AIRFOIL MODEL AND TEST SET-UP

The 1.83-m airfoil model was tested in the NASA Langley Low-Turbulence Pressure Tunnel (LTPT). The model consists of two parts - a structural element and a test insert (Figure 4). With this design several test region geometries can be examined. Attached laminar boundary-layer flow is maintained by means of suction through a perforated titanium panel located in the compression part of the concave region. The suction region is divided into three spanwise suction strips, each controlled independently by its own needle valve. The 10-percent chord flap is used to control the stagnation point location. The experiment was conducted at atmospheric pressure and the chord Reynolds number was varied from 1.0 million to 5.9 million yielding a Görtler number of up to 16.

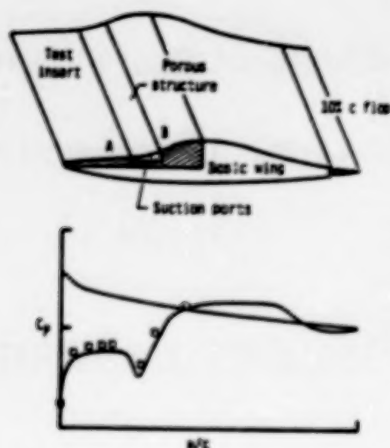
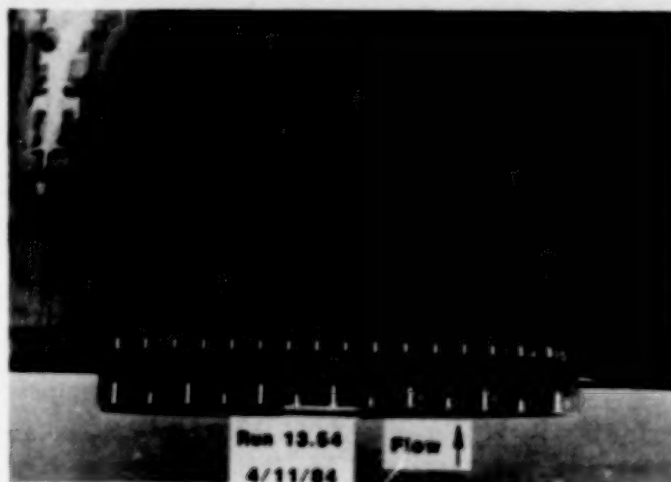


Figure 4

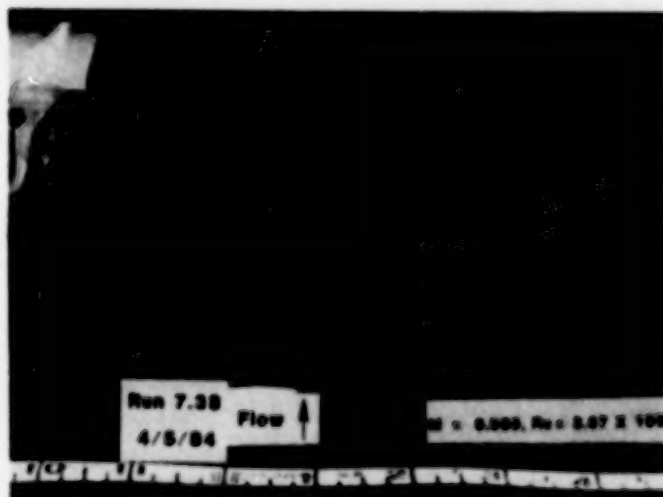
FLOW VISUALIZATION

ORIGINAL PAGE IS
OF POOR QUALITY

A thin layer of solid white biphenyl sublimating chemical was sprayed over the black model surface. The flow pattern is made visible due to the differential surface shear stress distribution under the layer of Görtler vortices which leave behind a trace of alternating white and black bands on the model surface. Elapsed times of about 30 minutes to 1 hour were required for the pattern to emerge clearly. A pair of white and black bands constitutes a wavelength. The wavelength was determined by taking the average of the number of pairs of bands over a 15 cm to 45 cm span. Beyond the concave region, the bands decrease considerably in contrast but are visible back to the jagged transition line. The decrease in contrast is attributed to damping in the convex region. (Figure 5).



$R_c = 2.24$ Million



$R_c = 3.67$ Million

Figure 5

SPANWISE VARIATION OF NORMALIZED STREAMWISE VELOCITY

A specialized, single-axis, three-component laser velocimeter was used to study the flow field in the test region (reference 2). The velocity field was measured by scanning the laser control volume spanwise in steps of 0.05 cm at a constant nominal height above the model surface. The control volume was then moved normal to the surface to the next measurement height and scanned back. This process normally took approximately five hours per chord location. The minimum and the maximum chord Reynolds numbers for laser velocimeter measurements were 1.0 and 3.67 millions, respectively. The spanwise distributions of mean streamwise velocity, normalized with respect to the local boundary-layer edge velocity, are given in Reference 2 for different chord locations and chord Reynolds numbers. Typical results at $x/c = 0.25$ are shown in Figures 6(a) and 6(b) for the lowest and the highest test chord Reynolds numbers. The perturbations are observed to vary across the boundary layer with an essentially constant periodicity along the span for a given chord Reynolds number. Appreciable difference in periodicity is clearly seen with a change in chord Reynolds number. Maximum spanwise fluctuations of as much as 45-percent in streamwise velocity can be observed in Figure 6(b).

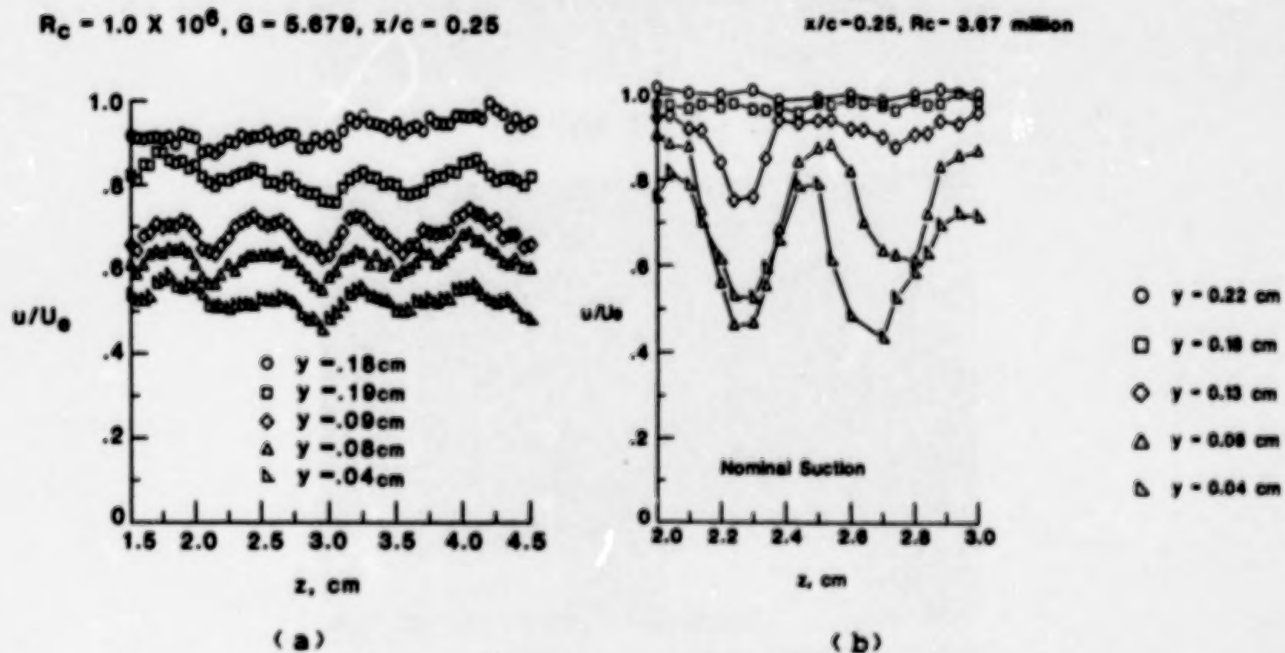
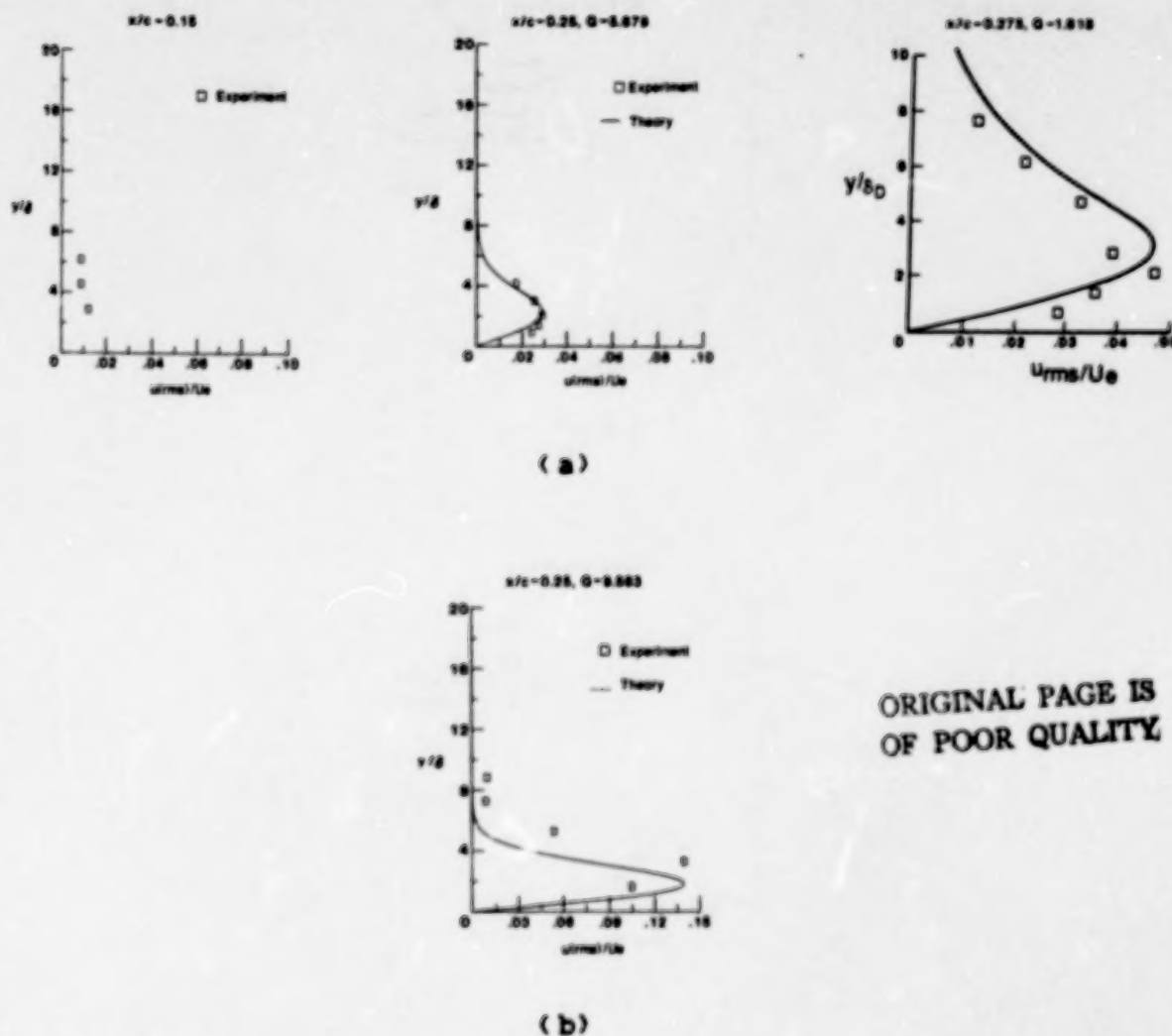


Figure 6

NORMALIZED STREAMWISE VELOCITY PERTURBATION

Normalized streamwise velocity perturbation functions at various chord locations are shown in Figure 7(a) for a chord Reynolds number of 1.0 million. The maximum amplitude of the streamwise perturbation grows to a maximum at the end of the concave region ($x/c = 0.275$) and then falls rapidly in the convex region. Linear theory was used to compute theoretical eigenfunctions corresponding to the measured wavelength. For the purposes of comparison, normalized streamwise velocity perturbation is shown in Figure 7(b) corresponding to chord Reynolds number of 3.67 million. The maximum amplitude reaches a value of nearly 15% of the boundary-layer edge velocity but it is instructive to note that the flow was still laminar.



ORIGINAL PAGE IS
OF POOR QUALITY

Figure 7

EFFECTS OF SUCTION

The influence of moderate amounts of additional suction is shown in Figures 8(a) and (b). Nominal suction corresponds to the minimum suction required to maintain an attached laminar boundary layer in the test region. The porous suction strip ends at $x/c = 0.225$ and at this location an increased suction level appears to have consistently reduced the streamwise velocity perturbation. However, at $x/c = 0.25$, where there is no local suction, the streamwise velocity perturbation is consistently larger than those obtained with nominal suction in the compression region. The available results are not sufficient to make major conclusions on the effects of suction. A more detailed study is necessary.

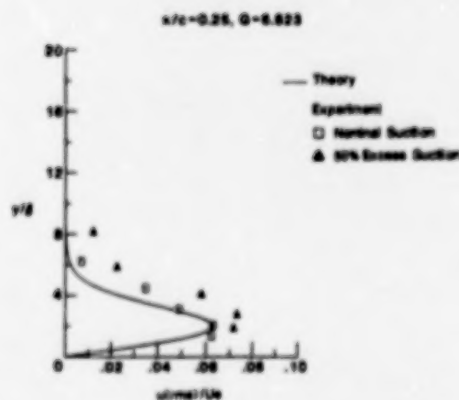
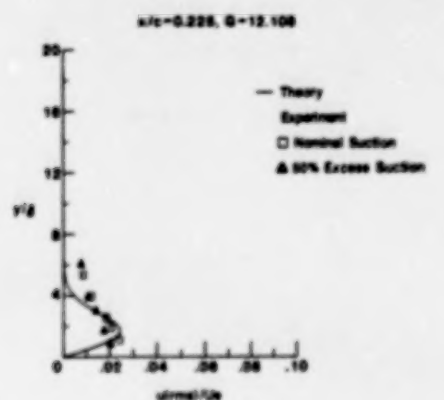


Figure 8

VARIATION IN WAVELENGTH AND MAXIMUM PERTURBATION AMPLITUDE

The variation in wavelength with Görtler number is shown in Figure 9(a). The Görtler number G_m is based on the conditions at the location of the minimum radius of curvature in the concave region. Theoretical results were computed using Floryan's code (reference 4). A good agreement is observed. Unlike all previous experiments, significant variation in wavelength was observed with changes in freestream parameters, as seen from this figure.

The variation in normalized maximum disturbance amplitude is shown in Figure 9(b). Local suction exists in the region $0.17 \leq x/c \leq 0.225$. In this region the growth appears to be gradual but is followed by a sharp increase to the maximum at the end of the concave region. The perturbation amplitudes decrease rapidly in the convex region. Increased levels of suction decrease the amplitude locally but appear to trigger a more rapid growth downstream.

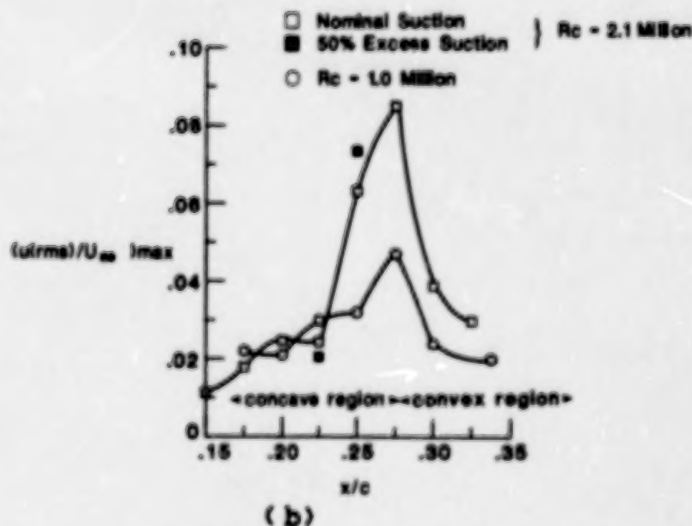
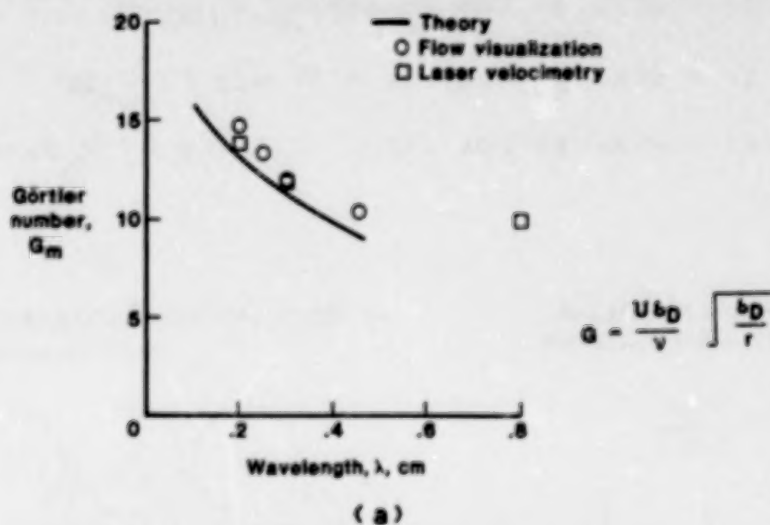


Figure 9

PHASE RELATIONS

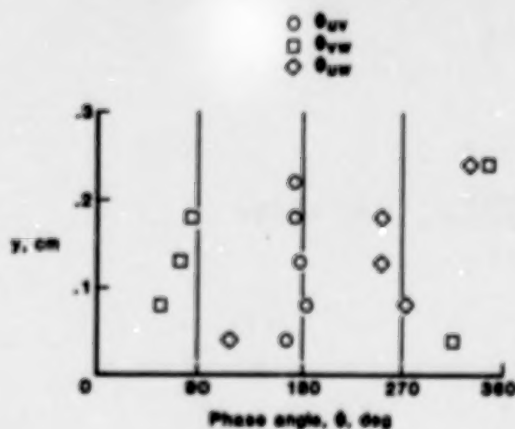
Current theoretical models for velocity perturbations due to the presence of Görtler vortices assume the streamwise and normal velocity components to be in phase and the spanwise component to be out of phase by 90° . However, cross-spectral analysis of experimental data consistently gave results at variance with these assumptions (Figure 10(a)). The streamwise (u) and the normal (v) velocity components were out of phase with each other by 180° whereas the spanwise component (w) was out of phase by 90° or 270° with the streamwise component (270° or 90° with the normal component) depending on the height above the surface. The w -component changes sign across the center of the vortex layer. Such a behavior is consistent with the correct physical model of Görtler vortices shown in Figure 10(b). Based on these results the following correct theoretical model is suggested for velocity perturbations:

$$u(x, y, z) = u(x, y) \cos \alpha z \exp \left(\int \beta_u dx \right)$$

$$v(x, y, z) = v(x, y) \cos (\alpha z + \pi) \exp \left(\int \beta_v dx \right)$$

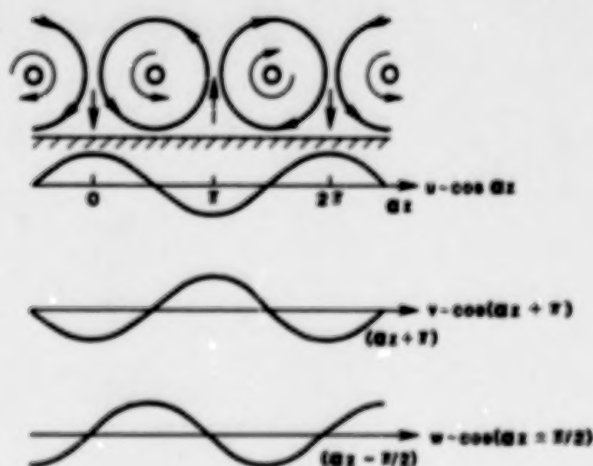
$$w(x, y, z) = w(x, y) \cos (\alpha z \pm \pi/2) \exp \left(\int \beta_w dx \right).$$

MEASURED PHASE RELATIONS
FOR VELOCITY PERTURBATIONS



(a)

PHASE RELATIONS FOR VELOCITY PERTURBATIONS
(Theoretical model)



(b)

Figure 10

SUMMARY OF RESULTS

- Flow visualization and Laser Velocimetry results corroborate dependence of vortex wavelength on freestream parameters
- Measured values agree well with theoretical wavelengths for maximum amplification
- Velocity perturbation profiles determined in the concave and convex regions
- Velocity perturbation profiles and vortex growth trends agree well with theory
- Vortex strength increases in the concave region followed by a rapid damping in the convex region
- Influence of moderate amounts of suction obtained
- Phase relationships between velocity components agree well with the correct physical model

FUTURE EFFORTS

- **More detailed boundary layer measurements to better define stability parameters**
- **Extend the scope of the experiment to study the influence of suction and curvature distribution more thoroughly**
- **Study vortex interaction between Tollmien-Schlichting waves and Görtler vortices**
- **Transition in the presence of Görtler vortices**

REFERENCES

1. Pfenninger, W.; Reed, H. L.; and Dagenhart, J. R.: Design Considerations of Advanced Supercritical Low-Drag Suction Airfoils. In: Viscous Flow Drag Reduction, Gary Hough (ed.), AIAA Progress in Astronautics and Aeronautics, Vol. 72.
2. Mangalam, S. M.; Dagenhart, J. R.; Hepner, T. E.; and Meyers, J. F.: The Gortler Instability on an Airfoil. AIAA Paper No. 85-0491, AIAA 23rd Aerospace Sciences Meeting, Reno, Nevada, January 1985.
3. Dagenhart, J. R.; and Mangalam, S. M.: Disturbance Functions of the Gortler Instability on an Airfoil. ICAS-86-1.8.11, 15th Congress of the International Council of the Aeronautical Sciences, London, England, September 1986.
4. Floryan, J. M.: Stability of Boundary-Layer Flows Over Concave Walls. Ph.D. Thesis, Virginia Polytechnic Institute and State University, Blacksburg, Virginia, January 1980.

**AN EXPERIMENTAL EVALUATION OF SLOTS VERSUS POROUS STRIPS
FOR LAMINAR-FLOW APPLICATIONS**

**Kenneth C. Cornelius
Lockheed-Georgia Company
Marietta, Georgia**

PRECEDING PAGE BLANK NOT FILM'D

INTRODUCTION

Laminar-flow control (LFC) has the potential for significant drag reduction in a wide range of aerodynamic vehicle applications. The primary objective of LFC is the achievement of extended areas of laminar flow by delaying boundary-layer transition where the primary drag reduction benefit is in the decrease in the skin friction. Two competing methods to apply wall suction are the use of discrete slots or a contiguous porous skin along the aerodynamic surface as discussed in (Refs. 1 and 2). The porous surface provides a nearly uniform continuous suction in contrast to a series of narrow slots which provide a discontinuous spatially localized suction distribution.

The estimation of suction quantities for LFC applications can be calculated by assuming continuously applied suction such that the growth factors for instability waves are below a prescribed level. Ref. 3 used boundary-layer theory and showed that if the same amount of suction is distributed at wide porous strips instead of continuous distribution, the integrated amplitudes of Tollmien-Schlichting waves are essentially unchanged. However it would be incorrect to extrapolate this result to the case of localized suction of a slot because the upstream influence of the slot or "sink effect" is not properly accounted for in boundary-layer calculations, which are parabolic in nature. Ref. 4 utilized a triple deck theory to account for the upstream effect and Ref. 5 provided experimental confirmation of these results for wide porous strips. However, the limitations of low wall suction velocities, an inherent assumption of the analytical development, raises a question of the accuracy of this procedure for the case of discrete suction through a series of multiple slots.

The first part of the present study concentrates on a comparative examination of the growth of instability waves in a Blasius boundary-layer flow by these two methods of wall suction. The second part of the paper includes design criteria for suction hardware to minimize velocity perturbations at the entrance of the slot. The slot blockage study demonstrates that a boundary-layer instability develops downstream which may lead to premature transition. The lower limit of this instability for a slot blockage width equivalent to the local boundary-layer displacement thickness represents the most restrictive criteria for the suction rate through a given slot.

EXPERIMENTAL CONFIGURATION

This study was conducted in the Lockheed-Georgia LTVT (Low Turbulence Wind Tunnel) which has a 0.6m X 0.9m rectangular test section by 6.5m length. The free stream turbulence level is of the order .02-.04% of the free stream velocity. The flat plate depicted in Figure 1 has an elliptical leading edge and is constructed of 1.27cm thick aluminum plate with dimensions 0.9m X 3.0m length. Chordwise and spanwise static pressure measurements were made with a total of 32 static surface ports. The pressure gradient was set close to zero over the test region by the adjustment of the tunnel walls with a C_p variation of $\pm 0.25\%$. A variable deflection trailing edge flap attached to the downstream end of the plate controlled the leading edge stagnation line.

Three suction locations were chosen on the flat plate at $x=1.22, 1.525$ and 1.83 m from the leading edge. The suction power was provided by a radial vane pump attached to a vacuum chamber, where the total mass flow was maintained at a constant value by a sonic nozzle at the entrance of the chamber. The flow rate from each panel was controlled by a ball socket valve and monitored by a calibrated pressure drop across a porous membrane installed in each pressure line. To accurately measure the mean flow and the dynamic fluctuations of the instability waves, the boundary-layer surveys were made with a computer driven three-axis probe survey mechanism of resolution .015mm which was mounted outside the test section of the tunnel. The hot wire anemometer used in this study was a Disa type 55D01.

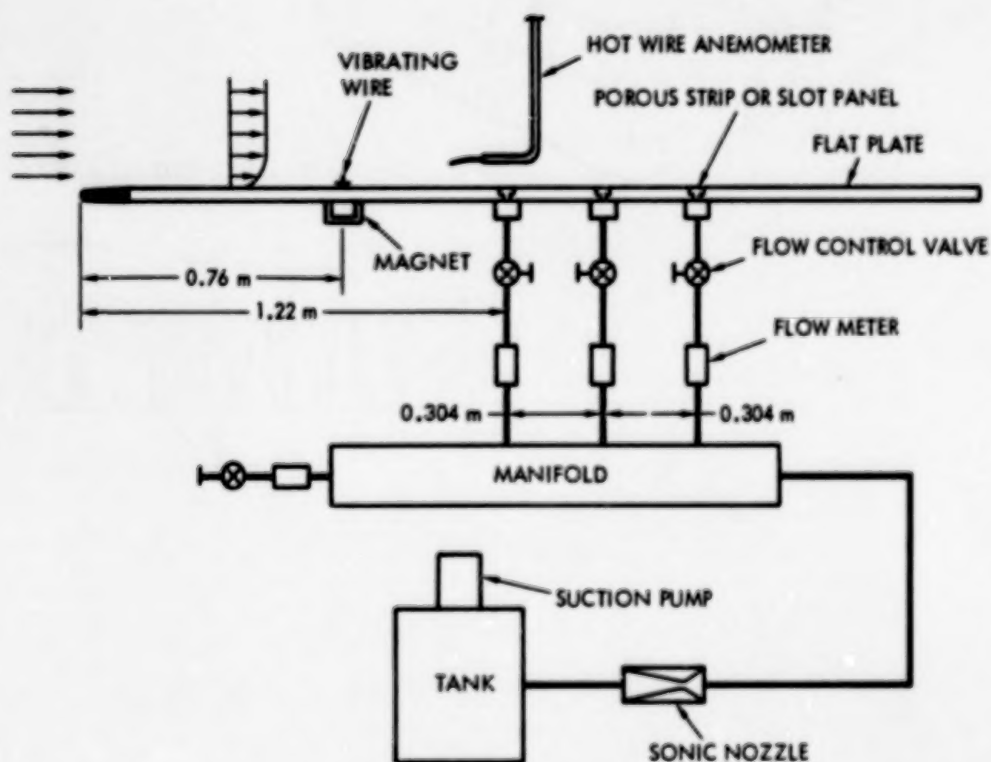


Figure 1

GEOMETRY OF SLOT AND POROUS STRIP PANEL

Figure 2 shows the details of the suction chamber design, where a 2-D slot panel or a wide porous-strip panel was alternately installed above each suction chamber. The porous panels were 2.3cm wide and 10mm thick and contained electron beamed holes of diameter 0.25mm spaced in a diamond pattern with a porosity value of 20% open. The slot panels were the same thickness material with a saw cut of 0.25mm width. A comparison of the slot vs. wide porous-strip data was made by replacing the slot panel with the porous panel without altering the external boundary conditions of the experiment. The slot dimension was 16% of the displacement thickness of the boundary layer as compared to the porous strip width of 15.0 displacement thicknesses. The 0.38cm diameter metering holes were displaced from the centerline of the suction chamber by 0.64cm with a pitch of $75v_s$. The suction chamber had a depth of $21v_s$ and a width of $105v_s$.

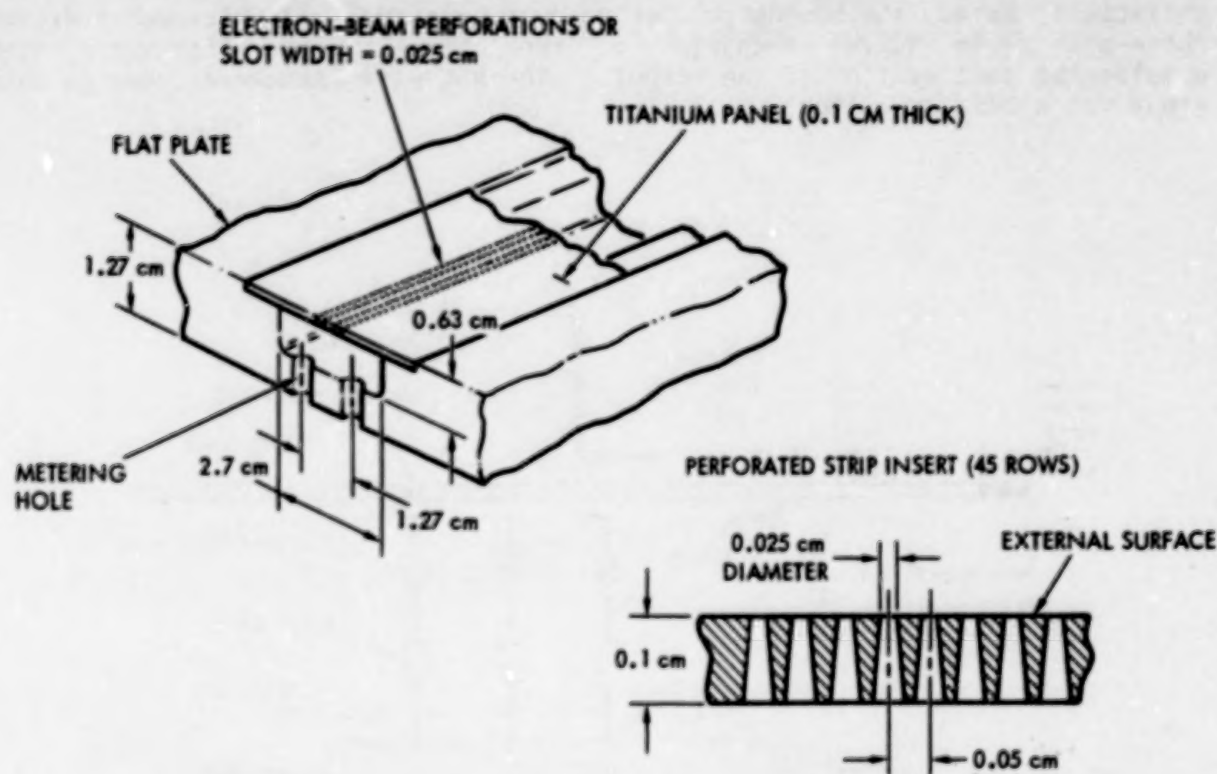


Figure 2

COMPARISON OF MEAN BOUNDARY-LAYER PARAMETERS

From dimensional analysis, with the initial condition specified as a Blasius profile, the change in the mean boundary-layer parameters due to discrete wall suction can be represented by the functional relationship:

$$\delta^*/\theta = g(y_k/\delta^*, v/\delta^*, R_{\delta^*})$$

The first term represents the streamline height of the suction mass flow far upstream of the influence of the wall suction normalized on the displacement thickness, the second term is the non-dimensional width of the wall suction, and the third term is the local Reynolds number. For low suction rates the following expression can be derived for the first term:

$$y_k/\delta^* = 1.88(m)^{1/2}; \quad \text{where } m = vv/U\delta^*.$$

For the data presented in this section $R_{\delta^*} = 2100$, which corresponds to a displacement thickness $\delta^* = 1.65\text{mm}$ and the unit Reynolds number per meter of $R = 1.336 \times 10^6$. The suction flow was maintained at the same value at each streamwise station during the acquisition of the mean and RMS velocity data. Figure 3a shows the boundary-layer shape factor comparison for slots and porous strips for a suction value of $m = .035$ at successive downstream locations. The corresponding displacement thickness variation normalized on the reference value is shown in Figure 3b.

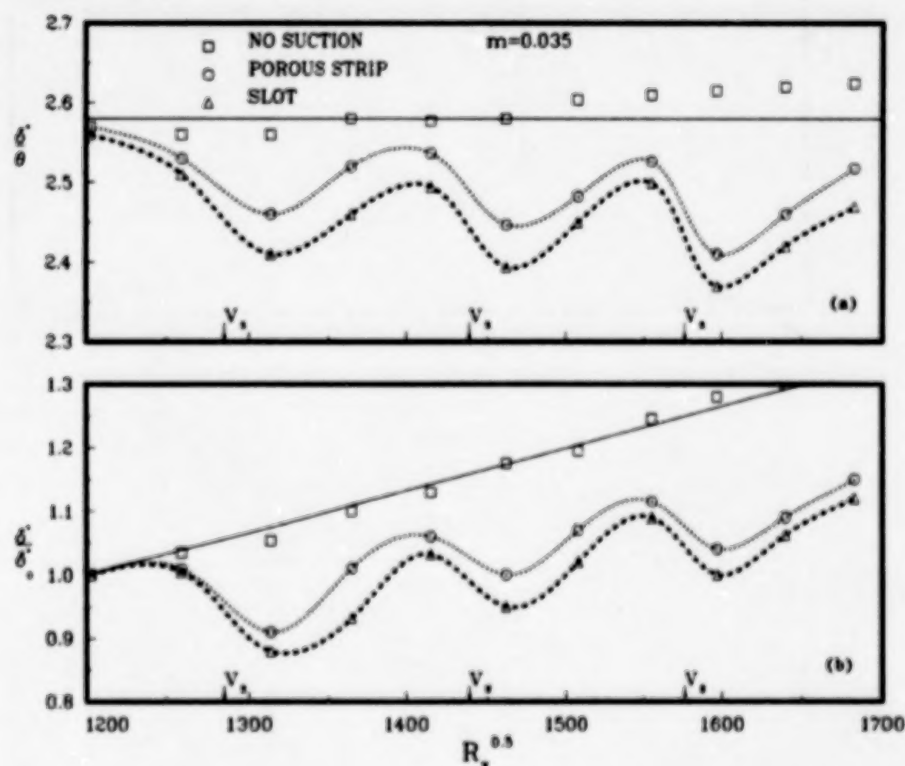


Figure 3

COMPARISON OF LOCALIZED C_p AND SHEAR

The variation of C_p in the near vicinity of the suction region at $x=1.22m$ was measured by a small static probe of diameter 0.28mm . The comparison of slot vs. wide porous strip is shown in Figure 4a for the suction parameter $m=0.035$. The main difference in the two suction methods is the higher peak value in C_p of the slot and larger adverse gradient across the slot-suction width. The corresponding skin friction data comparison shown in Figure 4b was obtained from the mean velocity gradient of the anemometer data at a normal distance of $0.15mm$ from the surface. The significant difference is the larger magnitude of the shear near the downstream edge of the slot.

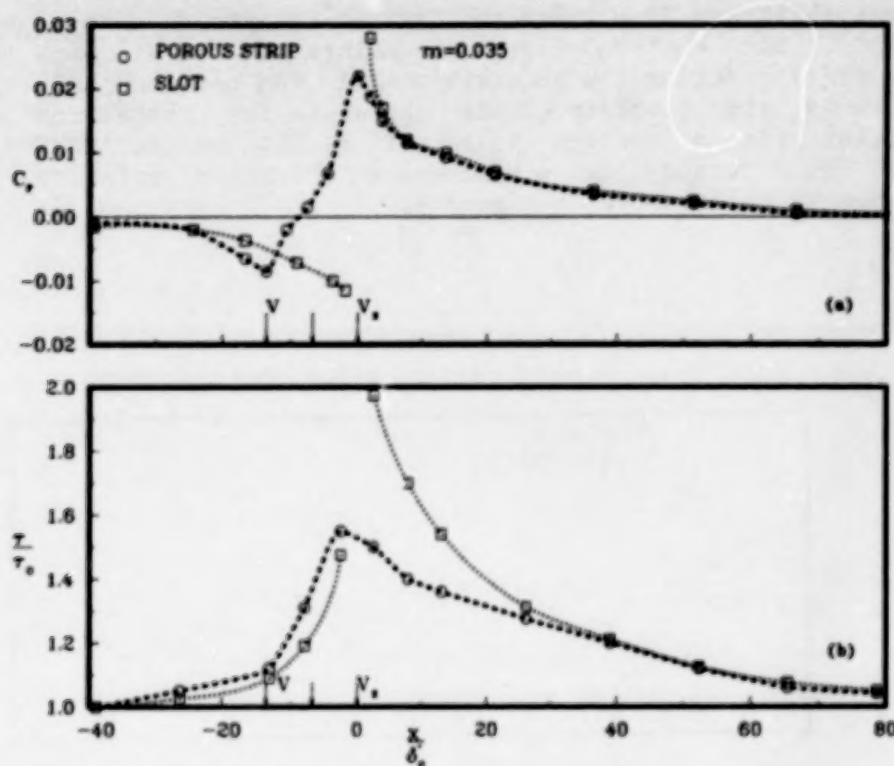


Figure 4

GENERATION OF TOLLMIEN-SCHLICHTING WAVE

The introduction of a controlled disturbance in the boundary layer was accomplished using the vibrating wire technique. An electromagnetically excited stainless-steel wire of diameter 0.025mm was positioned 0.76m from the leading edge and offset from the plate by 0.2mm spacers and allowed to freely vibrate over a length of 0.75m (see Figure 1 previously). A two dimensional array of permanent magnets located underneath the surface provided a constant magnetic field and a power amplifier with a sinusoidal wave generator provided the excitation current for the wire. A weight of 5 Newtons (1.1 lbs) attached to the wire provided the tension force, where the natural frequency of the taut wire was measured at $f=210$ Hz. This arrangement allowed a constant disturbance amplitude over a spanwise extent of length 0.5m. The measured disturbance wave in the boundary layer is compared to linear stability theory in Figure 5a for a dimensionless frequency of $F=64.4 \times 10^{-6}$. Figure 5b shows the corresponding mean velocity profiles.

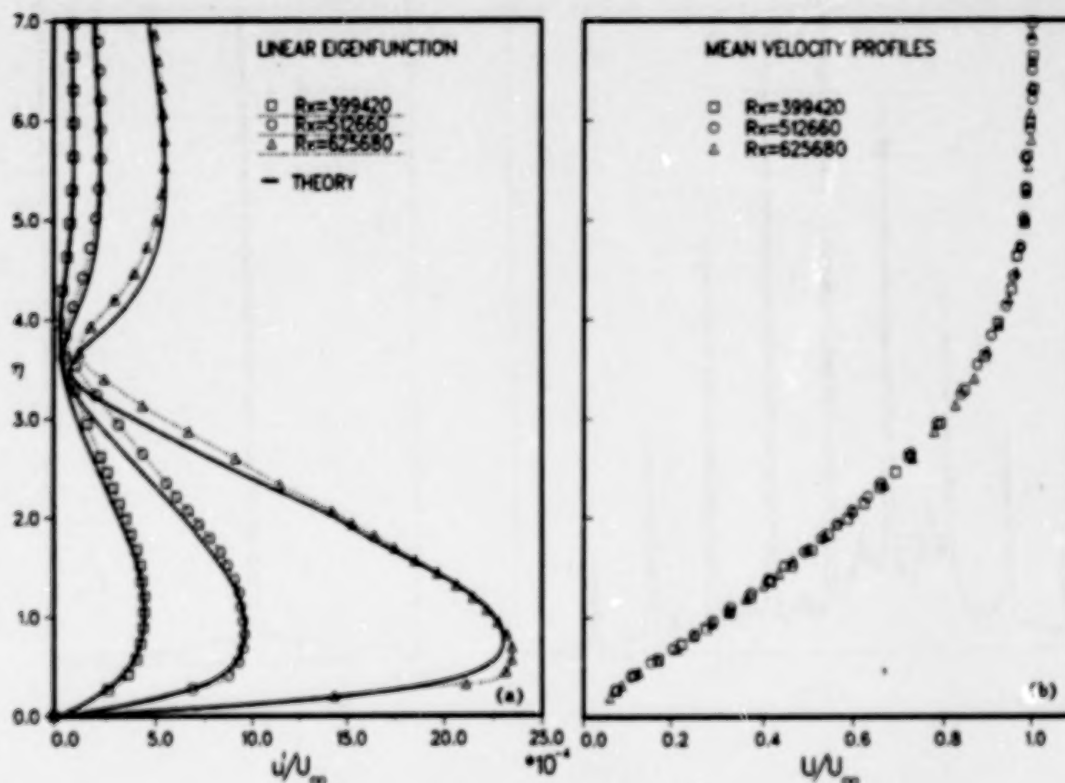


Figure 5

SPECTRAL PLOT OF DELTA FUNCTION VERSUS DISCRETE FREQUENCY

A cursory examination of the frequency which had the largest amplitude growth over the test region was ascertained by the generation of a delta function input to the wave generator at a frequency of 5 Hz. The anemometer was positioned downstream of the last slot at a position in the boundary layer of $y/\delta^* = 0.6$. The spectral plot of the anemometer fluctuations shown in Figure 6a demonstrates a wide band of instability waves were amplified. The suction test experiment was conducted at the relatively low non-dimensional frequency of $F = 28.3 \times 10^{-6}$, which corresponds to the maximum growth of the discrete frequency of the sine wave input at 127 Hz and is shown in Figure 6b. The maximum amplitude of the wave was maintained in the linear range over the test section region for the duration of the experiment.

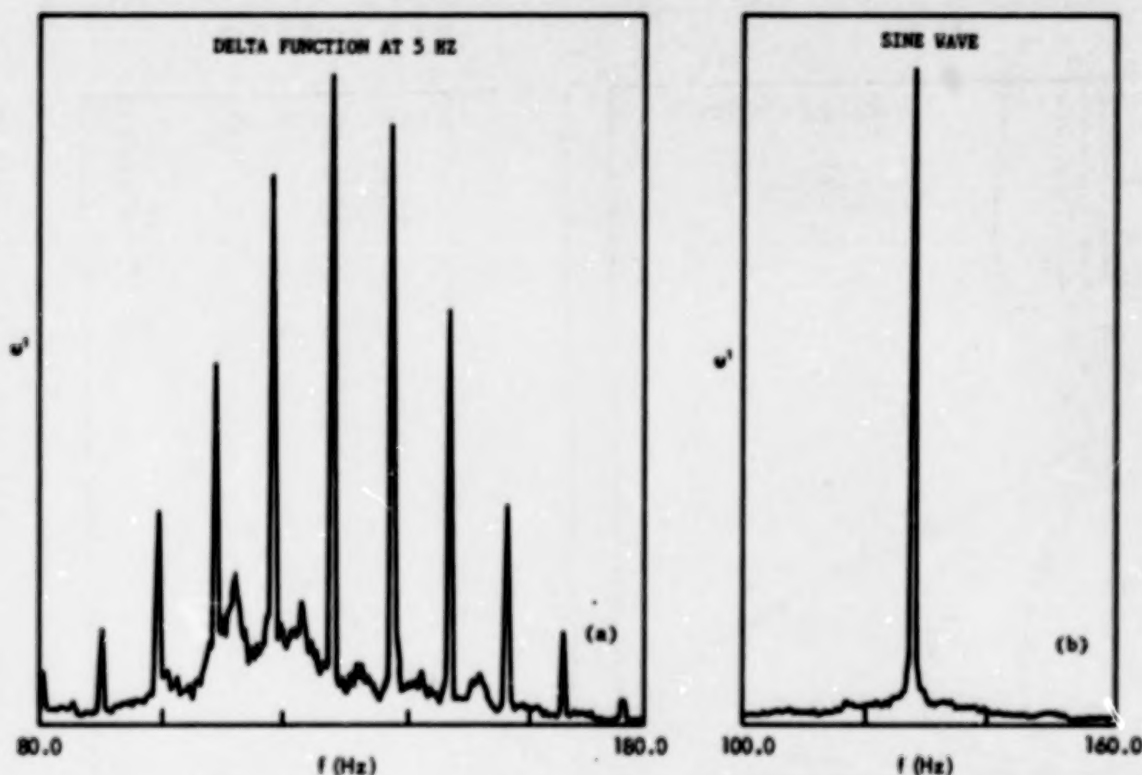


Figure 6

COMPARISON OF AMPLITUDE GROWTH OF INSTABILITY WAVE

The amplitude growth of the instability wave shown in Figure 7 represents a comparison of the porous strip versus slot for two suction quantities. The data in this figure represent the maximum fluctuation amplitude normalized on the maximum amplitude at $(R_x)^{1/2} = 1200$. To demonstrate the effect of suction width on the growth of the instability wave, tape of 0.05mm thickness was used to cover 80% of the width of the porous strip. This configuration had 8 rows of holes which were open on the porous strip panel. Figure 7 shows the amplitude growth for three cases, namely:

- a.) wide porous strip of width $v/\delta^* = 15.0$
- b.) narrow porous strip of width $v/\delta^* = 2.5$
- c.) and the slot of width $v/\delta^* = 0.16$

The effects on stability of the narrow porous strip as compared to the slot are nearly identical.

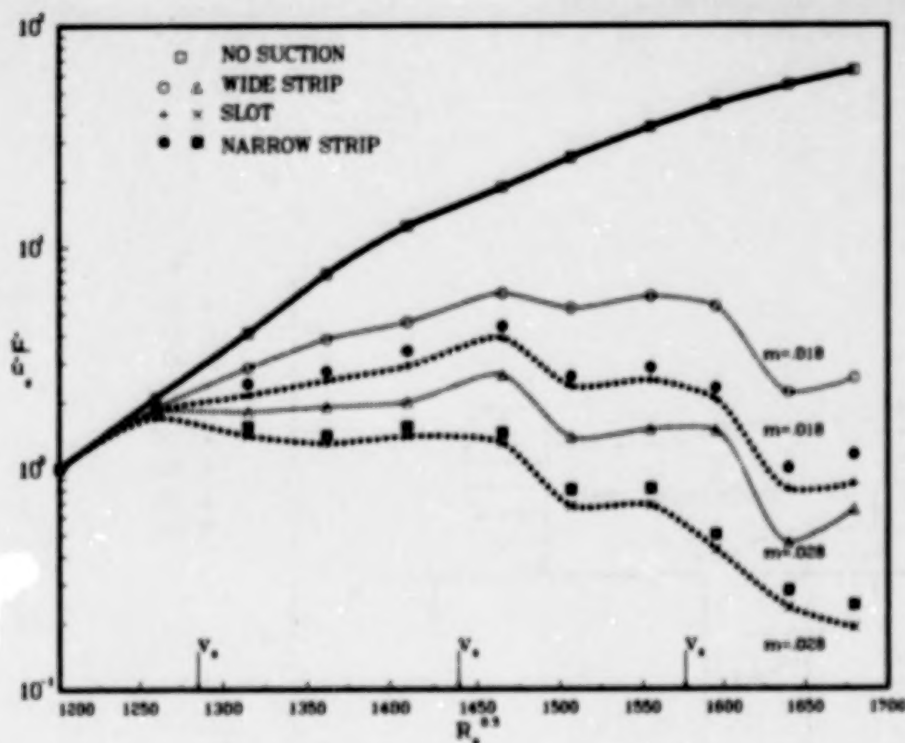


Figure 7

SUCTION HARDWARE DESIGN TO MINIMIZE PERTURBATIONS

Ref. 6 has demonstrated that premature transition of the boundary layer can occur if there is a breakdown of the internal flow in the suction chamber. Also, an analytical study (Ref. 7) and an experimental study (Ref. 8) have shown nonlinear interactions between three-dimensional and two-dimensional waves which excite exponential growth rates which may lead to premature transition. The amplitude of the three-dimensional waves in which the nonlinear interaction occurs has the low nominal value of $u'/U=0.01\%$. The frequencies where resonance occurs are those which have significant linear growth rates and the corresponding second harmonics and subharmonics. Therefore, from an LPC standpoint it is desirable to minimize the perturbations from the ducting system, since the generation of internal finite disturbances will propagate into the external boundary-layer flow. For this study a closed loop water tunnel was used for both flow visualization and the quantitative data reported in the subsequent sections. The measurements were obtained with a TSI^{*} anemometer using a hot film probe with linearizer, and a Nicolet FFT⁺ spectrum analyzer was used to obtain the frequency data from the velocity fluctuations. Figure 8a shows the parameters of the slot flow which were investigated, and Figure 8b shows the relationship of the width of the separated region on the parameters R_δ and α which are discussed in Ref. 9.

*Thermal Systems Incorporated (TSI).

+fast Fourier transform.

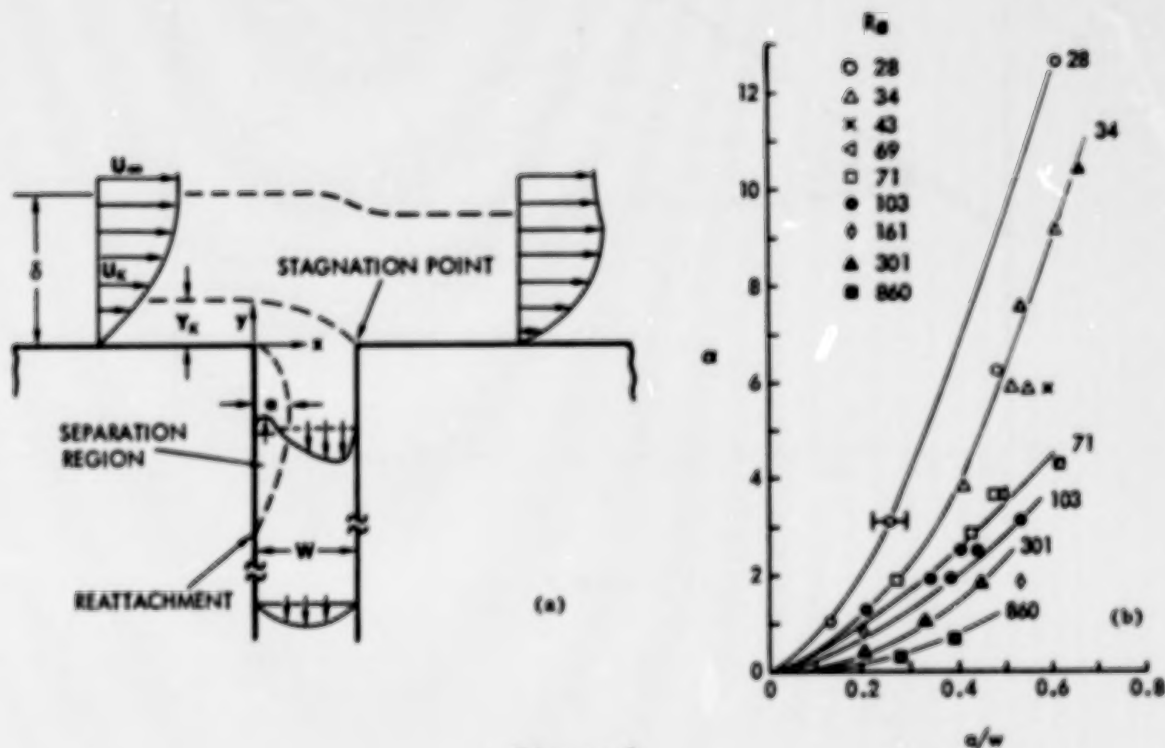


Figure 8

LAMINAR BUBBLE TRANSITION IN SLOT

Flow visualization using dye for a streamline marker demonstrated that the flow separates from the leading edge of the slot and reattaches within 4.0 slot widths depending on the slot Reynolds number and the boundary-layer shear parameter (α) as outlined in Ref. 9. For this experiment the suction chamber was designed with large dimensions to isolate perturbations from the shear layer flow in the slot. Velocity spectra were obtained with a boundary-layer probe located $0.25\delta^*$ downstream of the slot and $0.15\delta^*$ from the surface. The velocity spectra shown in Figure 9 demonstrate that transition and breakdown of the slot laminar bubble occur at a slot Reynolds number $R_s = 450$. The peak in the spectral data collapses to a dimensionless Strouhal frequency $fa/v_s = 0.038$, where the length scale a is the maximum bubble width in the slot.

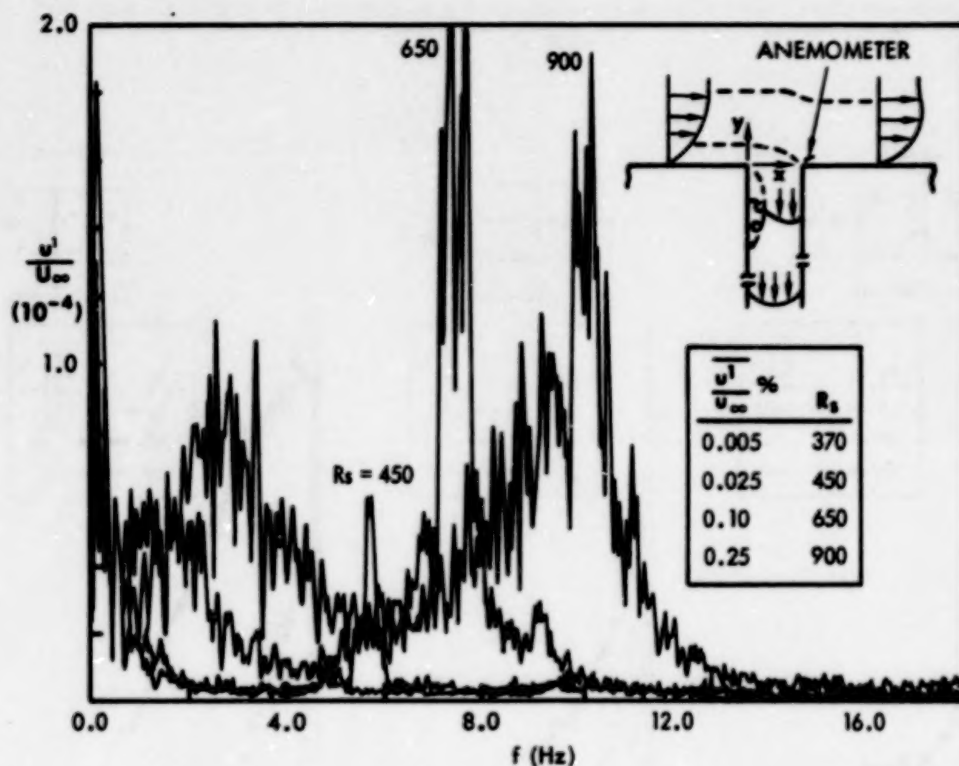


Figure 9

SUCTION CHAMBER OSCILLATIONS

Flow visualization using dye markers for the streamlines was used to observe the flow within the chamber below the slot. The two dimensional flow from the slot remains as a coherent jet and impinges on the floor of the duct. The jet then separates into two helical structures which are drawn into the metering holes. A study was undertaken to examine the effect of varying the geometry of the suction chamber on the RMS fluctuations at the mouth of the slot with no external boundary-layer flow above the slot. The hot film probe was positioned at the entrance of the slot. The metering holes had a pitch $p/v_s = 50$ with the hole $R_d < 1200$, to minimize perturbations of the flow through the holes. Figure 10 shows the spectral data for three geometries under investigation. The maximum amplitude occurs at a Strouhal frequency $Sf v/v_s = .0135$ where, at higher frequencies, the amplitudes have an exponential decay. The minimum RMS of the oscillations for a given flow rate occurs for a chamber depth = $17v_s$ and chamber width = $40v_s$.

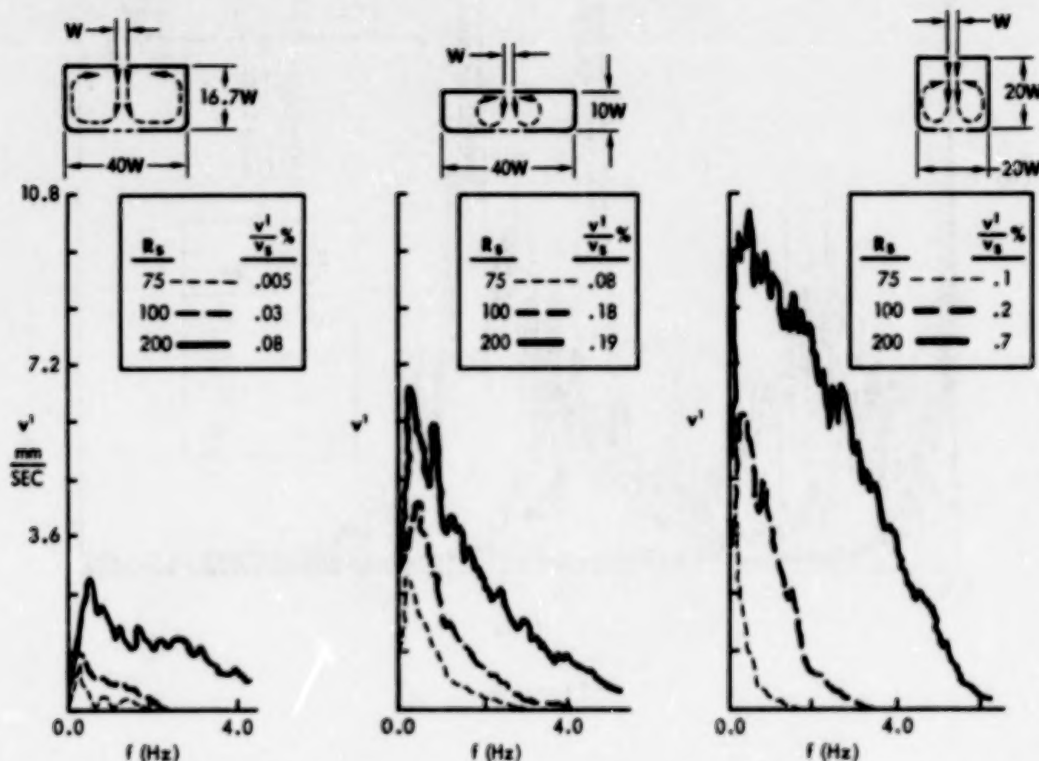


Figure 10

METERING HOLE INSTABILITY

Flow visualization showed that laminar separation of the streamlines occurs at the entrance of sharp-edged holes with reattachment within one diameter. An idealized experiment was studied where a round tube of diameter 2.8cm and length of two diameters was mounted flush in the center of a flat plate. The anemometer was positioned in the center of the exit hole and spectral data were taken at various suction rates. For this case the laminar separation bubble transitioned at $R_d \approx 2000$. The data in Figure 11 shows a well defined spectral peak at a Strouhal frequency $fd/u = 0.81$. At larger R_d a wider spectrum of fluctuations occurs as breakdown of the separation bubble encompasses a wider physical dimension of the core flow. Since these data were taken in an environment with no turbulence at the entrance flow it is recommended that for LPC applications $R_d \leq 1500$.

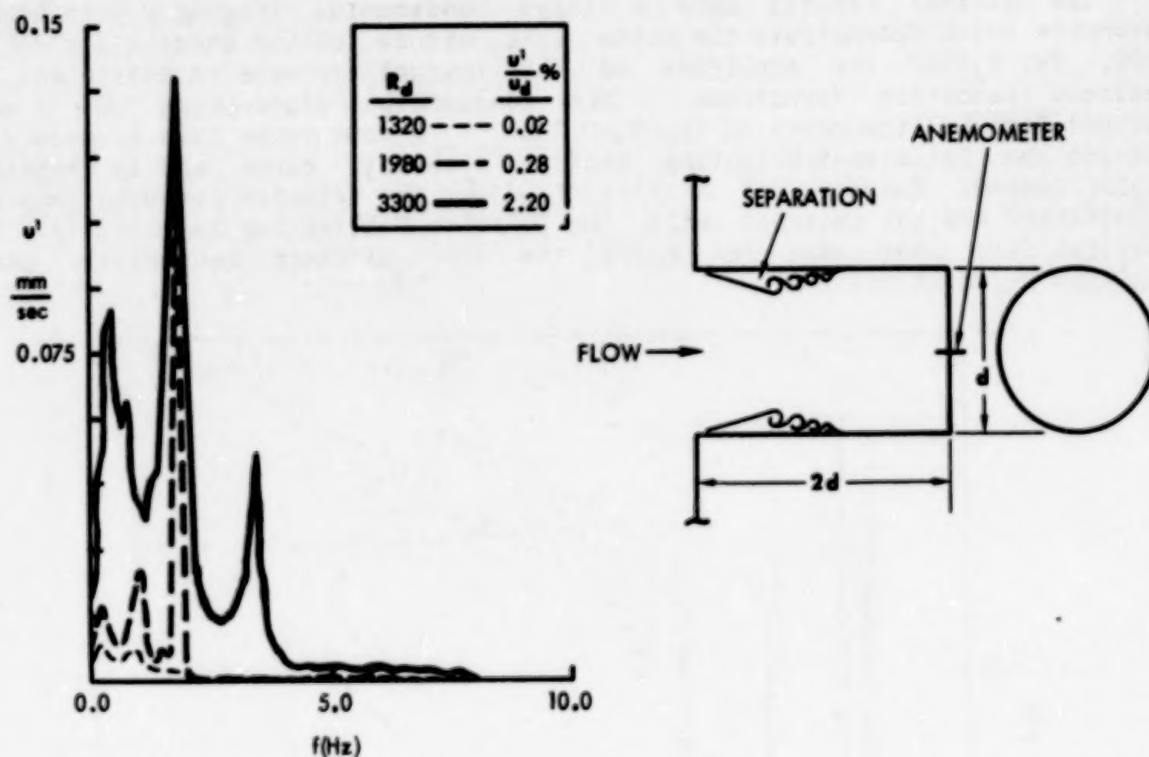


Figure 11

SLOT BLOCKAGE INSTABILITY

Ref. 10 has shown that a three-dimensional boundary-layer instability from a single row of suction holes will cause premature transition above a given suction rate. Blockage in the slot is analogous to the suction hole instability in that the mean boundary layer develops a strong spanwise gradient of vorticity adjacent to the obstruction in the slot. The three-dimensional instability growth rate will be dependent on the slot blockage width w_b and the value $R_k = U_k y_k / \nu$ which can be expressed in terms of the slot Reynolds number by the relationship $R_k = 2.0 R_s$. For the blockage study, a thin rectangular shim was placed flush across the slot width of dimensions $w_b / w_s = 1.3$ with an approaching boundary-layer displacement thickness of $\delta^* = 1.5 w_s$ and with a free stream $R_s^* = 1300$.

Flow visualization confirmed that the boundary-layer vorticity coalesced behind the blocked region and was convected downstream with a discrete frequency when the slot $R_s \geq 200$. To explore this instability further the hot film probe was positioned downstream of the blocked region at $x/\delta^* = 20$ at a vertical displacement of $y/\delta^* = 1.0$. The suction rate was varied and the velocity fluctuations were recorded and are shown in Figure 12.

The spectral results show a large fundamental frequency with higher harmonics which demonstrate the pulse like nature of the instability for $R_s \geq 200$. For $R_s \geq 300$ the amplitude of the instability wave is sufficient for imminent transition downstream. The fundamental disturbance has a well defined Strouhal frequency of $fy_k/U_\infty = 0.036$. In most cases this frequency is outside the Tollmien-Schlichting neutral stability curve and is therefore highly damped. However, at a slot $R_s = 110$ the velocity perturbations are significant and may interact with the Tollmien-Schlichting instability. The spectral data show that for $R_s \leq 75$ the slot blockage instability has a negligible growth rate.

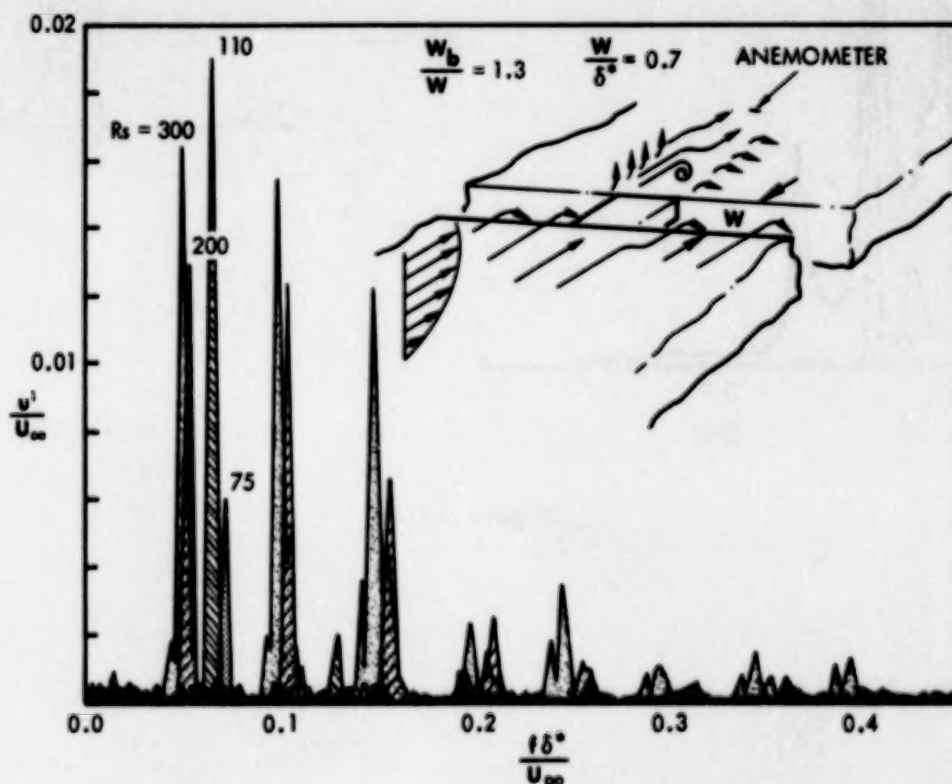


Figure 12

CONCLUSIONS

Detailed mean velocity and disturbance amplitude measurements were conducted in a Blasius boundary-layer flow with wall suction applied at three downstream locations. The main emphasis of this study was a direct comparison of the growth rate of the instability wave with discrete spanwise slots versus wide porous strips. The results demonstrate that the local effects of suction through slots or very narrow porous strips have a greater beneficial effect on the stability of the boundary-layer flow relative to the suction influence of a wide porous strip.

Codes which use continuous suction for the growth rates of the instability waves to determine the suction quantities for a multiple series of slots will be quite conservative in the estimation of the suction quantity. To accurately determine the mean boundary-layer changes from a narrow suction strip the "sink" effect of the local suction must be accounted for in the neighborhood of the slot. This has been demonstrated in the Navier-Stokes analysis of Ref. 11.

The second part of the paper concerned an experimental study to provide guidelines for suction-chamber design and flow rates to minimize internal oscillations which propagate into the boundary-layer flow. Based on this study, the following observations are summarized:

1. The flow inside the slot has a characteristic inflectional profile due to the presence of a separation bubble, which reattaches within four slot widths. The experimental data show that the resulting shear-layer transitions at $R_s \geq 450$.
2. Oscillations from the suction chamber below the slot exit are caused from the two-dimensional jet interactions at the boundaries of the suction chamber. The velocity perturbations at the slot entrance can be minimized by a suction chamber of depth $= 17v_s$ and width $= 40v_s$.
3. The flow into the metering hole has a separated region which reattaches within one diameter. The perturbations of the entrance velocity becomes significant for $R_d \geq 2000$. For LFC applications it is recommended that $R_d \leq 1500$.
4. Localized slot blockage from any external debris in the environment causes a mean spanwise gradient of vorticity in the boundary layer downstream of the blocked region. The local three-dimensional boundary-layer instability which results for $w_b/\delta^* = 1.0$ has large amplitude growths for $R_s \geq 110$ with imminent transition at $R_s \geq 300$. The blockage instability has negligible growth rates for $R_s \leq 75$. Therefore, the suction Reynolds number $R_s \leq 75$ represents the upper limit to desensitize the three-dimensional instability for intermittent blockage of the slot during flight.

ACKNOWLEDGMENT

The work reported in this paper was supported by the Lockheed-Georgia IRAD Program. The author extends his gratitude to Dr. A. S. W. Thomas who provided guidance through various phases of this research.

LIST OF SYMBOLS

a	laminar separation bubble length scale inside slot
C_p	defined as $(P_0 - P_\infty)/1/2\rho U_\infty^2$
d	diameter of metering hole
f	frequency
F	dimensionless stability parameter $2\pi f v/U_\infty^2$
m	suction parameter v/U_∞
p	pitch of metering holes
P_∞	free stream static pressure
P_0	surface static pressure
R	unit Reynolds number U_∞/ν
R_k	defined as $U_k y_k/\nu$
R_x	Reynolds number $U_\infty x/\nu$
R_s	slot Reynolds number $v_s v_s/\nu$
R_d	hole Reynolds number $v d/\nu$
R_{δ^*}	displacement thickness Reynolds number $U_\infty \delta^*/\nu$
S	Strouhal frequency
U	mean velocity in boundary layer
U_∞	free stream velocity
u'	velocity fluctuation
\bar{u}	RMS of velocity fluctuation
U_k	streamline velocity upstream of suction influence
v	average suction velocity at surface
v'	velocity fluctuation
w	width dimension of wall suction
x	streamwise coordinate
y	normal coordinate to surface
y_k	streamline coordinate upstream of suction influence
α	dimensionless velocity gradient parameter $\delta U/\delta y (v_s/v_s)$
δ^*	displacement thickness
η	$y(U_\infty/\nu x)^{1/2}$
θ	momentum thickness
ν	kinematic viscosity
ρ	density
τ	shear stress

SUBSCRIPTS

b	blockage
d	metering hole
k	suction streamline parameter in the boundary layer
o	reference value
s	slot
∞	free stream

REFERENCES

1. Harvey, W. D. and Pride, J. D. : The NASA Langley Laminar Flow Control Experiment. AIAA-82-0567, 12th AIAA Aerodynamic Testing Conference, 1982.
2. Wagner, W. D., Maddalon, D. V. and Fischer, M. C. : Technology Developments for Laminar Boundary Layer Control on Subsonic Transport Aircraft. 54th Fluid Dynamics Panel Symposium on Improvement of Aerodynamic Performance Through Boundary Layer Control and High Lift Systems, Brussels, Belgium, 1984.
3. Nayfeh, A. H. and Elhady, N. M. : An Evaluation of Suction Through Strips for Laminar Flow Control. AIAA-79-1494.
4. Reed, H. L. and Nayfeh, A. H. : Stability of Flow Over Plates With Porous Suction Strips. AIAA-81-1280, 1981.
5. Reynolds, G. A. and Saric, W. S. : Experiments on the Stability of the Flat Plate Boundary Layer With Suction. AIAA-82-1026, AIAA/ASME Joint Fluids Conference, 1982.
6. Pfenninger, W., Bacon, J., and Goldsmith, J. : Flow Disturbances Induced by Low Drag Boundary Layer Suction Through Slots. Physics of Fluids, 1967.
7. Nayfeh, A. H. and Bozatti, A. N. : Nonlinear Wave Interaction in Boundary Layers. AIAA-79-1496, 1979.
8. Saric, W. S. and Thomas, A. S. W. : Experiments on the Subharmonic Route to Transition, Turbulence and Chaotic Phenomena in Fluids, ed: T. Tatsumi, North-Holland, 1984.
9. Thomas, A. S. W. and Cornelius, K. C. : An Experimental Investigation of the Flow of a Laminar Boundary Layer into a Suction Slot. AIAA Journal Vol.20, 1982.
10. Gregory, N., : Research on Suction Surfaces for Laminar Flow Control. Boundary Layer and Flow Control, Pergamon Press, 1961, pp. 925-959.
11. Khan, M. M. S., Cornelius K. C., and Tassa, Y. : Effect of Suction on Boundary Layer Flow Over a 2-D Slot. AIAA-82-0222, AIAA 20th Aerospace Science Conference, 1982.

W88-12521

**RESULTS OF LFC EXPERIMENT ON
SLOTTED SWEEPED SUPERCRITICAL AIRFOIL
IN LANGLEY'S 8-FOOT TRANSONIC PRESSURE TUNNEL**

**C. W. Brooks, Jr. and C. D. Harris
NASA Langley Research Center
Hampton, Virginia**

PRECEDING PAGE BLANK NOT FILMED

LAMINAR-FLOW CONTROL (LFC) EXPERIMENT OBJECTIVE

A large chord swept supercritical laminar-flow control (LFC) airfoil has been designed, constructed, and tested in the NASA Langley 8-Foot Transonic Pressure Tunnel (8-Ft. TPT). The LFC airfoil experiment was established to provide basic information concerning the design and compatibility of high-performance supercritical airfoils with suction boundary-layer control achieved through discrete fine slots or porous surface concepts. It was aimed at validating prediction techniques and establishing a technology base for future transport designs and drag reduction. Good agreement was obtained between measured and theoretically designed shockless pressure distributions. Suction laminarization was maintained over an extensive supersonic zone up to high Reynolds numbers before transition gradually moved forward. Full-chord laminar flow was maintained on the upper and lower surfaces of the slotted suction wing at the design Mach number of 0.82 up to a chord Reynolds number of 12×10^6 . When accounting for both the suction and wake drag, the total drag could be reduced by at least one-half of that for an equivalent turbulent airfoil. Specific objectives for the LFC experiment are given in figure 1.

Conduct basic aerodynamic and fluid dynamics research program on a high-performance, swept supercritical, LFC airfoil to determine:

- Ability to laminarize over extensive supercritical region
- Ability of stability theories to predict transition and suction laminarization requirements
- Relative merit of slotted and perforated suction surfaces for LFC and HLFC
- Effects of surface conditions and boundary layer influences on laminarization

Figure 1

REPRODUCED FROM NASA REPORT 80-2020

LFC EXPERIMENT DESIGN CONSIDERATIONS

The Langley LFC airfoil experiment was established to provide basic information concerning the design and compatibility of high-performance, swept supercritical airfoils with boundary-layer control. Several methods of laminarization were considered and more than one will be employed during the experiment. The integration of laminar-flow control with swept supercritical wing technology required advanced materials and fabrication processes to construct a suitable airfoil. The tests required modifications to the wind tunnel to provide low levels of free-stream turbulence and acoustic disturbances to ensure that the background disturbance environment would not severely affect the maintenance of laminar flow. In addition, the necessity for a very large chord airfoil posed a problem that required extensive analysis and modification to the 8-Ft. TPT test section to provide a near disturbance-free representation of the flight environment. The test section walls were contoured with a foam liner to conform to the theoretical streamline shape (including wing and wall boundary-layer effects) of the flow about the wing at the design condition. The tunnel stagnation chamber was fitted with suitable honeycomb and screens to reduce turbulence at transonic speeds, and the test section downstream of the model was fitted with an adjustable sonic throat to block diffuser noise (figure 2).

- Design advanced high-performance, large chord, swept supercritical LFC airfoil
- Design and modify 8-FT TPT test section for simulation of free air about infinite-span yawed wing at transonic speeds
 - Contoured walls
- Design and modify 8-FT TPT for flow quality improvement at transonic speeds
 - Honeycomb, screens, sonic choke

Figure 2

TEST SETUP FOR LFC EXPERIMENT IN THE 8-FT. TPT

A schematic of the overall LFC experiment in the Langley 8-Ft. TPT is shown in figure 3 along with tunnel modifications. The major component was a large chord, 23° swept supercritical LFC airfoil of aspect ratio near one, which spanned the full tunnel height. Laminar-flow control by boundary-layer removal was achieved by suction through closely spaced fine slots extending spanwise on the airfoil surface. After passing through the slots, the air passed through metering holes located in plenums beneath each slot and was collected by spanwise ducts with nozzles located at the ends. From the duct/nozzles, the air passed through airflow system evacuation lines, through airflow control boxes which controlled the amount of suction to each individual duct nozzle, and through sonic nozzles to a $10,000 \text{ ft}^3/\text{min}$ compressor which supplied the suction. All four walls of the tunnel were contoured in order to produce a transonic wind tunnel flow which simulated unbounded free-air flow about an infinite yawed wing at model design conditions. The contoured liner was shaped to conform to computed streamlines around the wing and corrected for growth of the wall boundary layer. The success of the LFC experiment depended to a large extent on the environmental disturbance levels in the test section. Isolation of the test section from downstream disturbances was achieved by an adjustable two-wall choke (sonic throat). Reduction of upstream disturbances such as pressure and vorticity fluctuations was achieved by the installation of a honeycomb and five screens in the settling chamber.

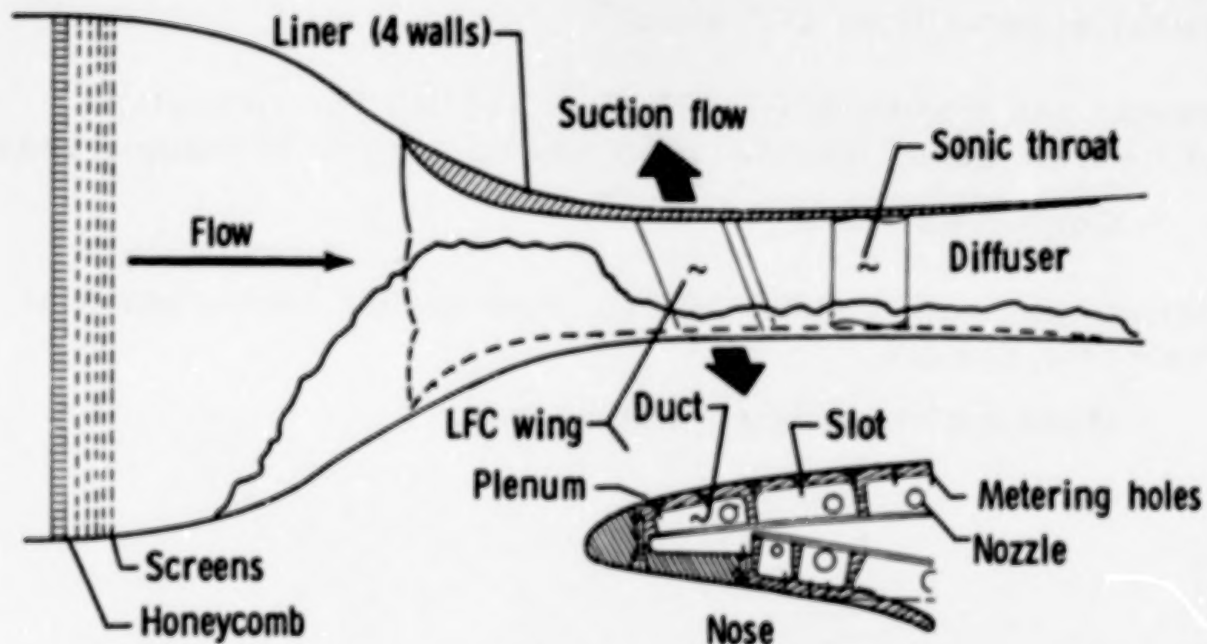


Figure 3

MODEL INSTALLED IN TUNNEL - DOWNSTREAM VIEW

Figure 4 is a downstream view of the upper surface of the model taken immediately upstream of the model. This figure illustrates the smooth streamline contour of the liner and how it blended with the model. The dark areas at the top and bottom liner model juncture regions are suction panels in the "collar" around the ends of the model to control the growth of the boundary layer in these regions. The dark area on the left vertical wall and downstream of the model is one of the flexible two-wall chokes (sonic throat). The choke plate on the opposite wall is hidden behind the model. The dark area immediately in back of the model is the tunnel test section access door followed by the downstream high-speed diffuser.

~~ORIGINAL PAGE IS~~
~~OF POOR QUALITY~~

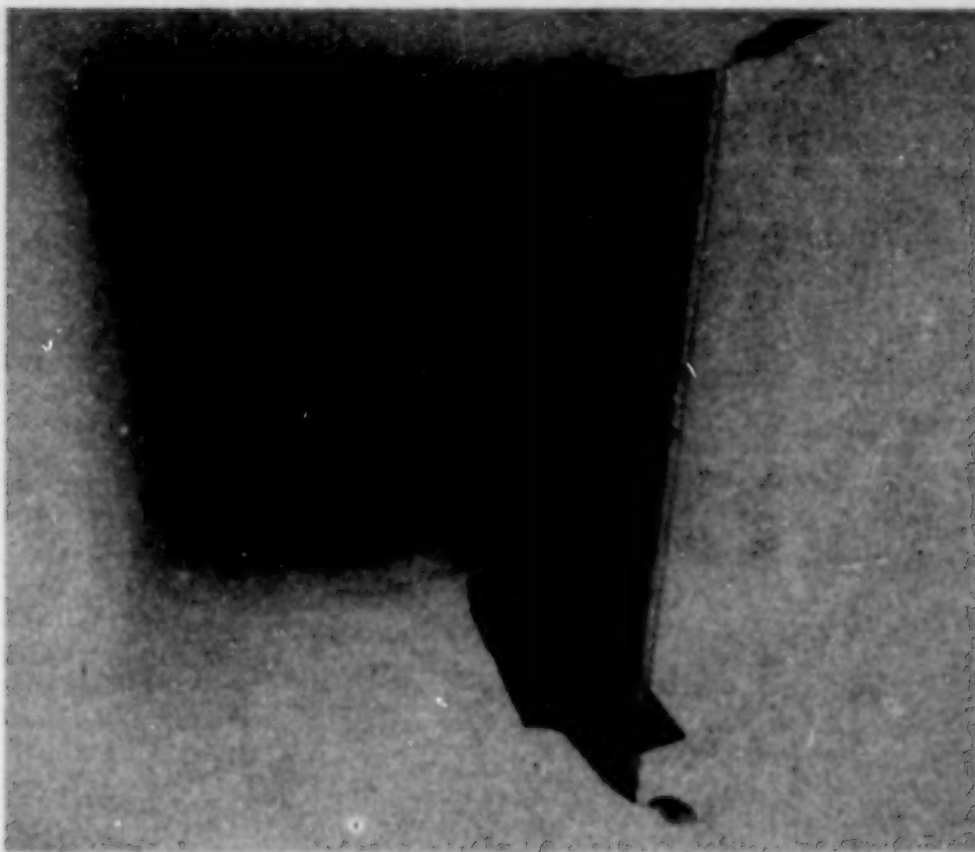


Figure 4

ORIGINAL PAGE
BLACK AND WHITE PHOTOGRAPH

MODEL INSTALLED IN TUNNEL - UPSTREAM VIEW

Figure 5 is an upstream view of the finished liner and wing trailing edge as seen from the test section diffuser entrance where the liner faired into the original tunnel lines. The LFC model extended from floor to ceiling and blended with the liner. The offset of the wing mean plane from the tunnel centerline may be seen as well as the development of the liner floor and ceiling step which resulted from the differential spanwise flow displacement in the tunnel channels "above" and "below" the wing surfaces. The dark vertical area on the left of the photograph and downstream of model trailing edge is the edge of the test section access door. The dark rectangular area ahead of the model is the tunnel contraction region.

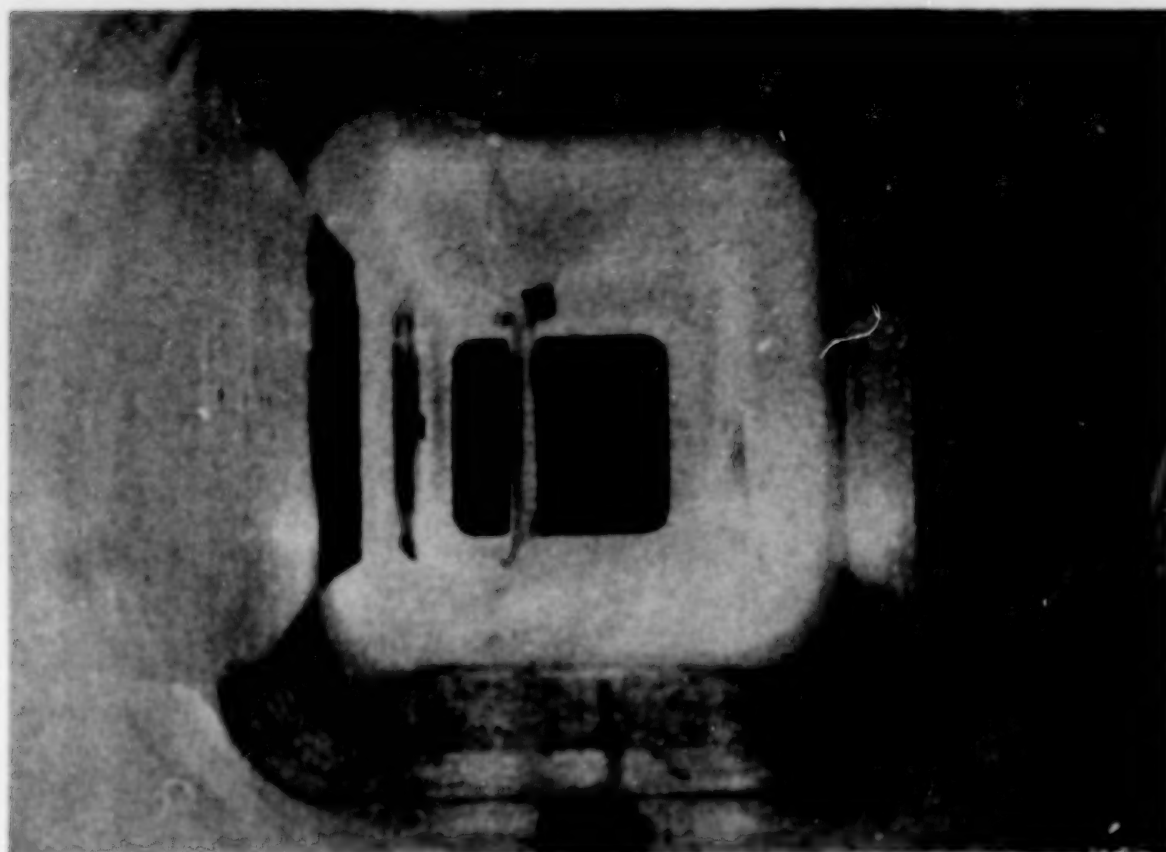


Figure 5

~~ORIGINAL PAGE IS~~
~~OF POOR QUALITY~~

ORIGINAL PAGE
BLACK AND WHITE PHOTOGRAPH

MEASURED AND DESIGN PRESSURE DISTRIBUTIONS

Measured and design chordwise pressure distributions on the upper and lower surfaces of the LFC model are shown in figure 6 for two chord Reynolds numbers at the design Mach number of 0.82. In general, these representative results indicate measured pressure distributions very close to design. Shockfree flow is shown for a 10 million Reynolds number and nearly shockfree flow for 20 million. The slightly overall higher velocities on the upper surface and the chordwise deviation from the design pressure distribution were attributed to classical problems associated with wind tunnel testing, wall interference, and model deformation under design air loads. The velocity field between the upper surface and tunnel wall (supersonic bubble zone) was slightly higher than predicted due to the liner contour and inability to completely account for boundary-layer displacement effects in the design analysis. The irregularity in the upper surface pressure distributions appears to be associated with local surface contour deviations, caused by deformation of the model under load, and perhaps amplified by the proximity of the contoured wall. As chord Reynolds number increased above 10 million, transition moved forward rapidly on the lower surface and the flow could no longer sustain the adverse pressure gradient leading into the trailing-edge cusp, and separation occurred at about 80-percent chord. This separated flow changed the local effective area distribution of the test section resulting in a slightly higher free-stream Mach number and increased upper surface shock strength at a chord Reynolds number of 20 million.

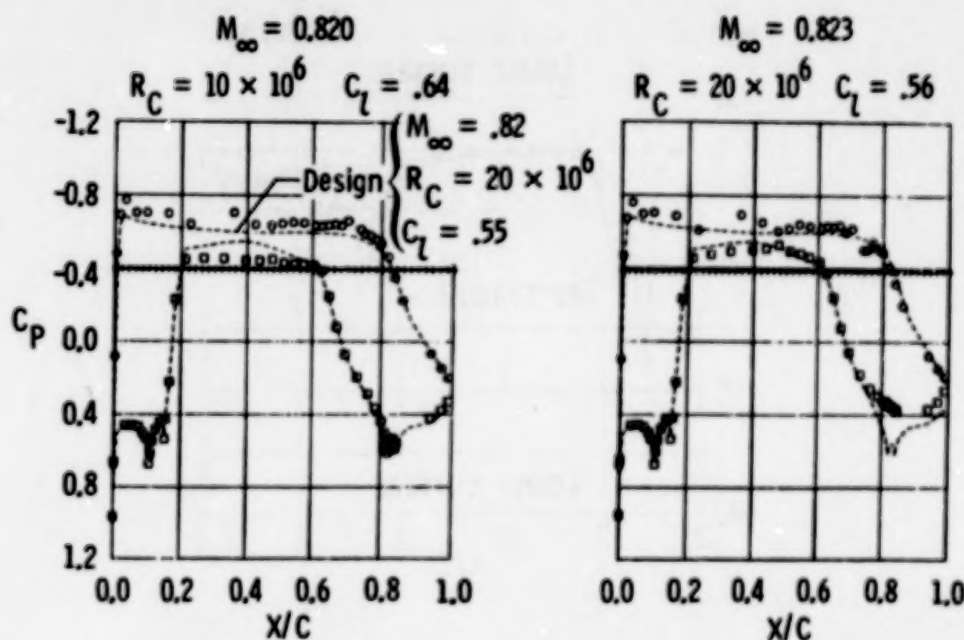


Figure 6

MEASURED AND THEORETICAL SUCTION DISTRIBUTIONS

The measured chordwise suction coefficient (C_Q) distribution required to maintain full-chord laminar flow over both surfaces at 0.82 Mach number and 10-million chord Reynolds number is shown in figure 7 compared to the theoretical suction distribution. The required suction level was higher than the theory over most of the upper and lower surfaces. Only about one-third of the total suction requirement is attributable to the upper surface and the remaining two-thirds to the lower surface. The higher suction requirements were due to the upper surface overvelocities and the surface pressure irregularities, as well as to higher suction required to overcome the cross-flow instabilities associated with the steep pressure gradients on the upper and lower surfaces and the minimization of centrifugal Taylor-Görtler-type boundary-layer instabilities and interactions in the concave regions of the lower surface. The overall higher suction levels are also influenced by tunnel disturbance levels which are inherently higher than free-air turbulence levels expected in flight.

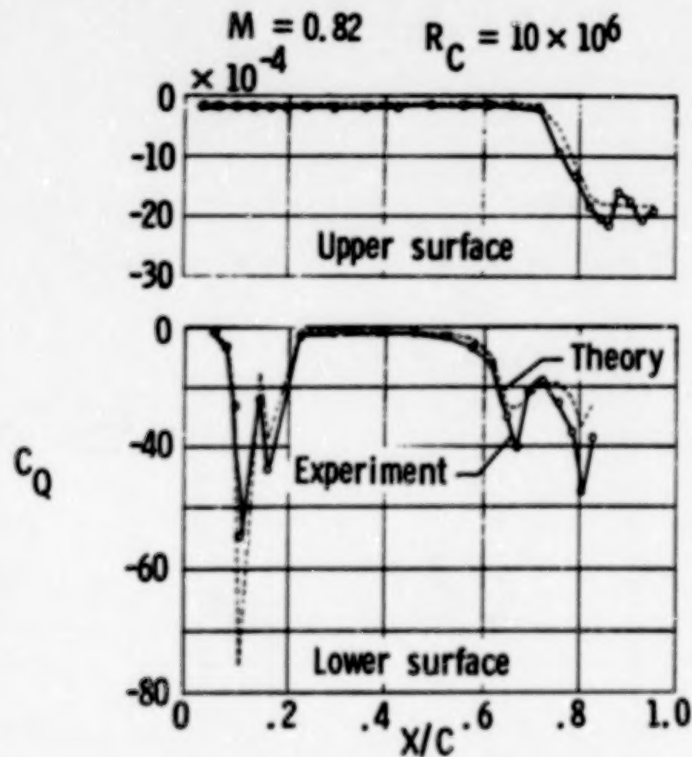


Figure 7

EFFECT OF REYNOLD'S NUMBER ON UPPER-SURFACE TRANSITION PATTERN

A planform view of the laminar region of the LFC wing upper surface is shown in figure 8 with flush-mounted surface thin-film sensors for transition detection indicated. The thin-film sensor oscillograph output trace for fully laminar flow is essentially flat, while that for fully turbulent flow resembles "white noise" and is easily distinguishable. Intermediate cases are assigned a measure based on the percentage of time in a local sample that is taken up with turbulent bursts. On these diagrams, lines have been drawn to indicate the estimated boundaries of the laminar, transitional, and turbulent regions. For a Reynolds number of 10 million (at design Mach number), the flow is laminar to the trailing edge over most of the span. As the Reynolds number increases to 20 million, the transition zone sweeps forward. The bottom end of the wing has more upstream transition at all Reynolds numbers, and this is thought to be an endplate effect.

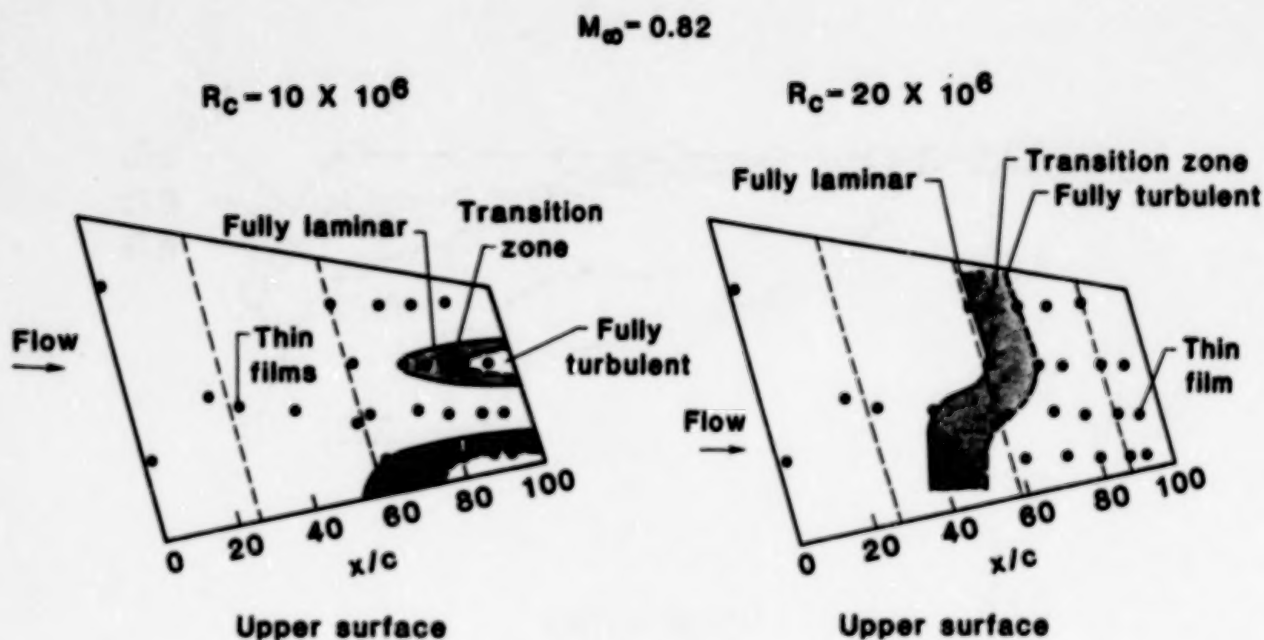


Figure 8

TRANSITION VARIATION WITH REYNOLDS NUMBER

The data presented in figure 9 show the chordwise extent of laminar flow achieved on the upper surface for several Mach numbers up to the design Mach number of 0.82, as determined by a grid of flush-mounted surface thin film gages (fig. 8). At $R_C = 10$ million, full-chord laminar flow could be maintained over the upper and lower surfaces for all Mach numbers. As Reynolds number was increased for constant Mach number, transition moved gradually forward on the upper surface. The Reynolds number at which this forward movement began was dependent on Mach number and occurred at progressively lower Reynolds numbers as Mach number increased. For the design Mach number of 0.82, the forward movement began between 11 and 12 million and reached about 65-percent chord at $R_C = 20$ million. Transition on the lower surface moved more rapidly than on the upper surface and occurred near the leading edge for $M = 0.82$ and $R_C = 20$ million. It was concluded that suction laminarization over a large supersonic zone is feasible to high-chord Reynolds numbers even under non-ideal surface conditions on a swept LFC airfoil at high lift.

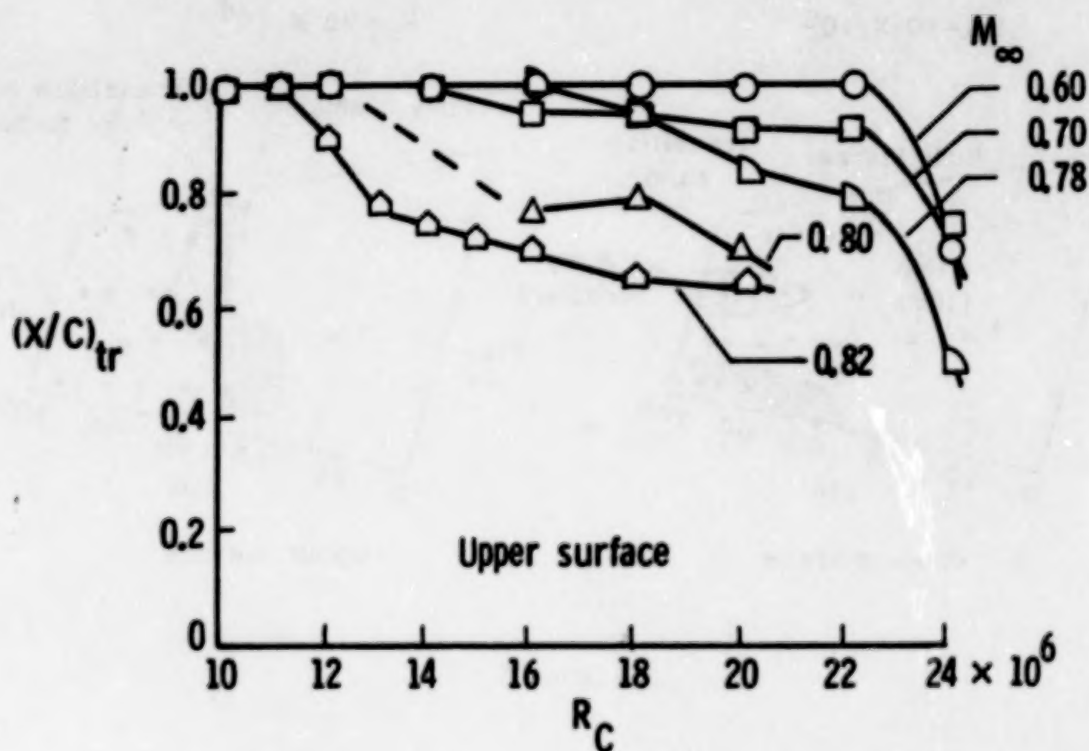


Figure 9

UPPER- AND LOWER-SURFACE TRANSITION VARIATION WITH R_C

At a chord Reynolds number of 10 million, the airfoil is fully laminar on both upper and lower surfaces (fig. 10). For chord Reynolds numbers above 11 million, transition moves forward on both the upper and lower surfaces. Between 11 and 13 million, the upper surface transition moves just upstream of 80 percent, and then more gradually to about 65 percent at 20 million. On the lower surface, the transition line moves from the trailing edge at a Reynolds number of 10 million to about 75 percent at 13 million. At a Reynolds number of 15 million, the lower-surface transition has moved to 30-percent chord (just beyond the end of the favorable pressure gradient) and the flow in the aft cusp is separated.

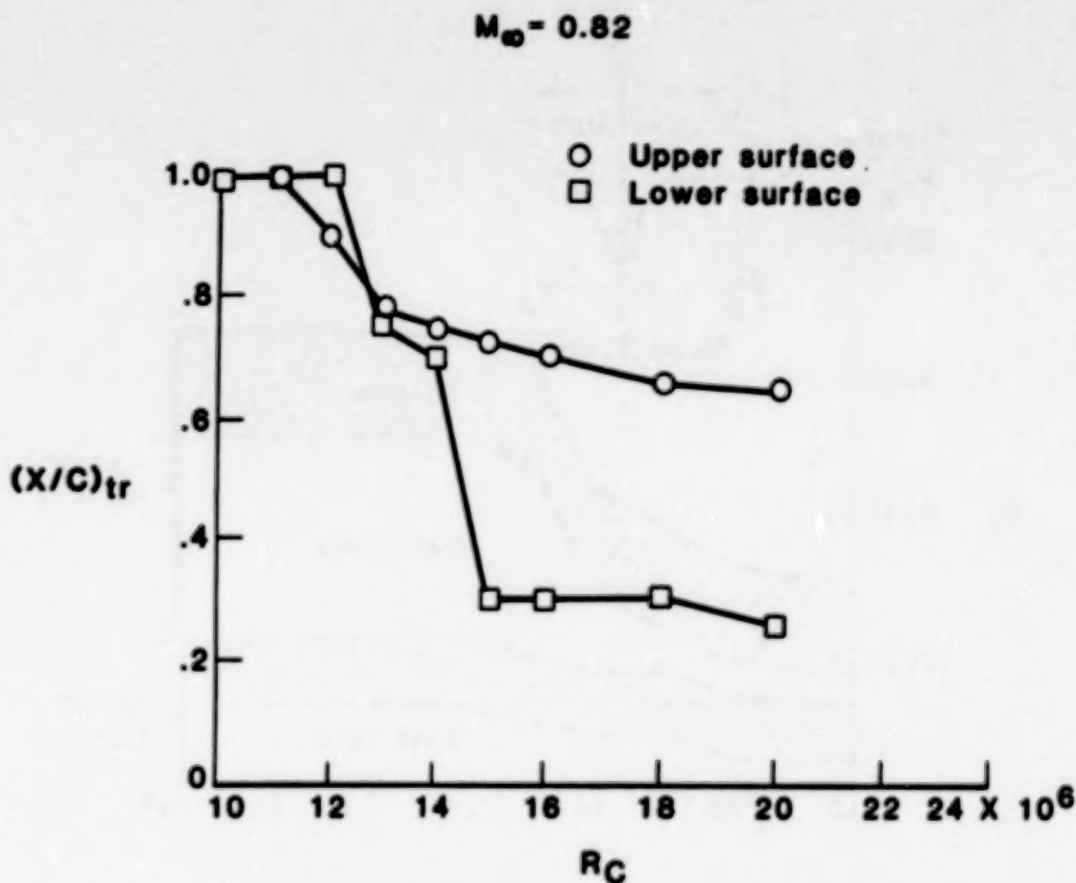


Figure 10

EFFECT OF REYNOLDS NUMBER ON DRAG AT DESIGN MACH NUMBER

The contributions to total section drag coefficient are shown in figure 11 for the Mach number of 0.82 over the chord Reynolds number range of 10 to 20 million. The assignment of suction drag contributions to the upper or lower surface is accountable since the suction drag is computed duct-by-duct. The wake drag is separated into upper and lower surface components on the basis of the assumption that the wake can be divided between the upper- and lower-surface at the point on the wake rake where the stagnation pressure loss is the greatest. The data indicate that the larger contribution to the total drag is from the lower surface. The sharp rise in wake drag on the lower surface between 14 and 15 million Reynolds number is associated with rapid forward movement of transition (fig. 10) and separation of the boundary layer in the pressure recovery region of the lower aft cusp.

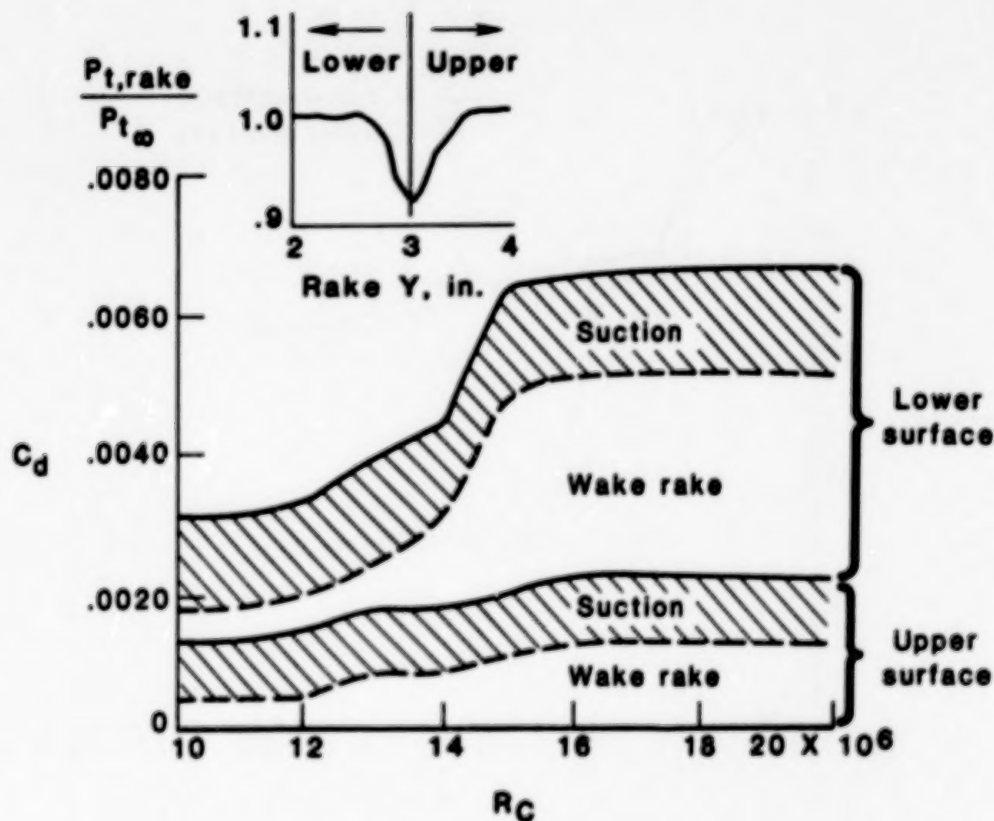


Figure 11

MEASURED TOTAL DRAG ON AIRFOILS WITH/WITHOUT SUCTION CONTROL

A comparison of the measured drag of the present LFC supercritical airfoil (identified as SCLFC(1)-0513F) with an equivalent turbulent supercritical airfoil is shown in figure 12. The total drag of the swept supercritical LFC airfoil with suction slots (solid symbols) includes the suction drag penalty required to maintain full-chord laminar flow and thus represents drag levels obtained with the maximum extent of laminar flow at the design lift conditions. The open symbols indicate drag levels obtained with an unswept supercritical airfoil with fully turbulent (tripped) attached flow in the same Langley 8-Ft. TPT. In general, the results indicate that about 60-percent drag reduction may be achieved with boundary-layer control over the speed range when compared with a turbulent drag level of about 80 counts.

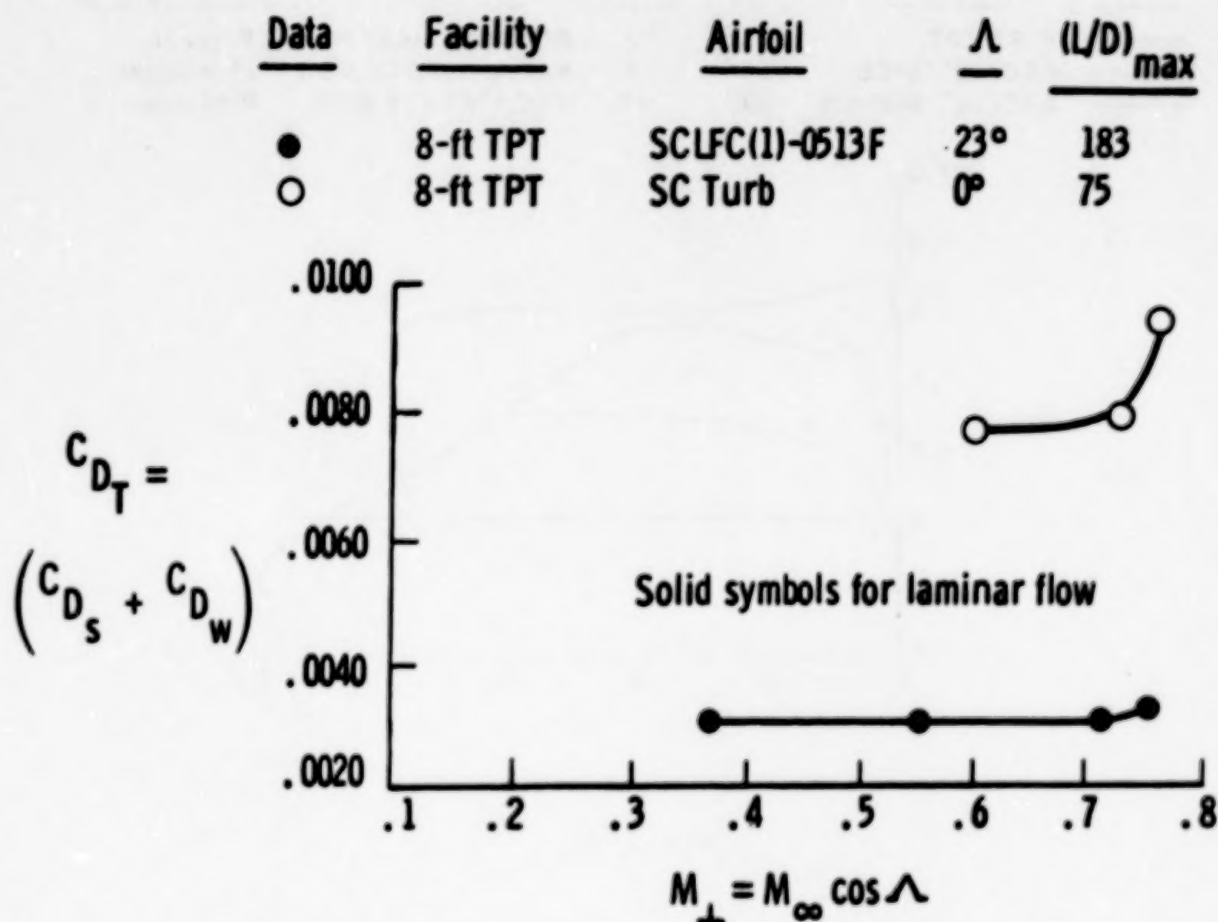


Figure 12

PRESSURE DISTRIBUTIONS ON SWEEP LAMINAR SUCTION MODELS

Figure 13 shows the upper-surface pressure distributions at the design lift condition ($C_L = .3$) on two earlier low-speed LFC airfoils of different sweep as compared to the supercritical LFC design pressure distribution. These low-speed LFC designs, based on standard NACA airfoil profiles, have favorable pressure gradients over the first 50 percent or more of the chord, and much less severe adverse pressure gradients aft than the supercritical design.

Upper surface, $R_C = 10 \times 10^6$

DATA	FACILITY	Λ	C, FT	AIRFOIL	REFERENCE
—	8-FT TPT	23°	7	SCLFC(1)-0513F	Present
----	ARC/12', MICH.	30°	7	NACA 66-012 MOD	Pfenninger
- - -	ARC/12', NORAIR	33°	10	NACA 64016 MOD	Pfenninger

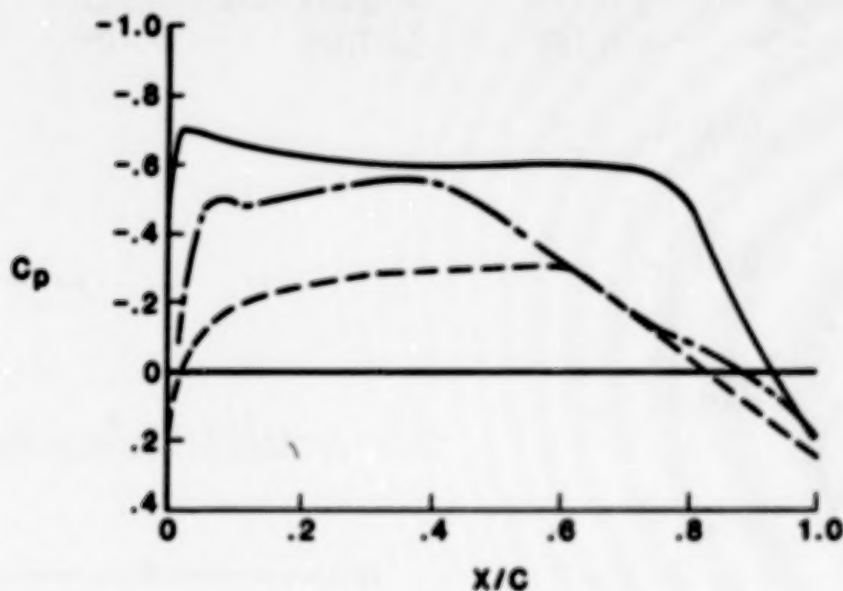


Figure 13

MEASURED MINIMUM PROFILE DRAG ON SWEEP LAMINAR SUCTION MODELS

Figure 14 shows only the upper-surface measured minimum profile drag coefficients corresponding to the upper-surface pressure distributions of figure 13. The breakdown shows that, as might be expected, the supercritical design has a somewhat larger suction drag penalty than the NORAIR model, which has the greatest extent of favorable pressure gradient (fig. 13), and only a slightly larger suction drag penalty than the University of Michigan 5- by 7-Foot Tunnel model while the wake drag contribution is about the same in all cases.

Upper surface, $R_c = 10 \times 10^6$

DATA	FACILITY	Λ	C, FT	AIRFOIL	REFERENCE
□ ○	8-FT TPT	23°	7	SCLFC(1)-0513F	Present
■ ●	ARC/12', MICH.	30°	7	NACA 66-012 MOD	Pfenninger
■ ●	ARC/12', NORAIR	33°	10	NACA 64016 MOD	Pfenninger

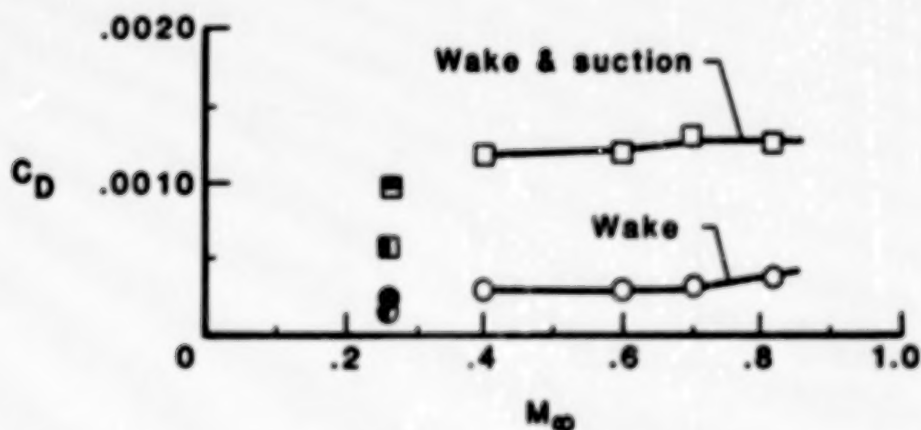


Figure 14

VARIATION OF TRANSITION FOR SIMULATED HLFC

A natural follow-on to full chord active laminar-flow control will be a hybrid configuration which will combine suction over forward regions of the upper surface with natural laminar-flow concepts over rearward regions. An attempt was made to simulate such hybrid laminar-flow conditions by turning off suction over rear portions of the LFC model while maintaining suction for $0 < x/c < .25$ on the lower surface. The simulation involved first establishing laminar flow to the most rearward thin film location (about 95 percent chord), then progressively turning off upper surface suction starting at the most rearward suction slots and measuring the extent of laminar flow downstream of the turn-off point. The variation of transition location on the upper surface with chordwise extent of suction is shown in figure 15 for $M = 0.82$ and two chord Reynolds numbers. The data indicate that extensive laminar flow could be maintained beyond the point where suction stopped. Clearly, this simulated HLFC approach must be considered somewhat "non-idealistic" and the results conservative since no effort was made to seal or smooth the unsucked regions of the airfoil. Furthermore, the pressure distribution (fig. 6) is not like that which would be designed for a hybrid configuration.

Accomplishments of the swept LFC airfoil experiment in the 8-foot TPT are listed in figure 16, and current and future tests are outlined in figure 17.

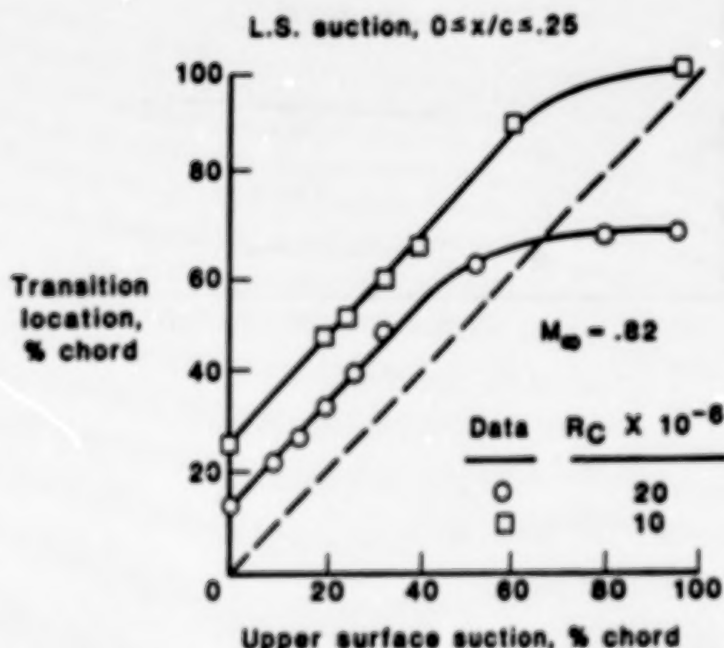


Figure 15

SWEPT LFC AIRFOIL EXPERIMENT IN 8-FT TPT

Accomplishments

- Achieved shockless pressure distribution
- Achieved full chord laminar flow on upper and lower surfaces for $0.4 \leq M_\infty \leq 0.82$
- Maintained full chord laminar flow at subcritical speeds and over large supercritical zone at transonic speeds for $R_C \leq 22 \times 10^6$
- Achieved about 80% drag reduction for upper surface only and 60% for both surfaces for $0.4 \leq M_\infty \leq 0.82$
- Demonstrated feasibility of combined suction laminarization and supercritical airfoil technology

Figure 16

SWEPT LFC AIRFOIL EXPERIMENT IN 8-FT TPT

Current and Future Tests

- Complete evaluation of porous-suction upper surface model for comparison with geometrically identical slotted model
- Evaluate hybrid LFC design with reshaped non-suction aft upper surface

Figure 17

**BOUNDARY-LAYER STABILITY ANALYSIS OF
LaRC 8-FOOT LFC EXPERIMENTAL DATA**

**Scott Berry
Analytical Services and Materials, Inc.
Hampton, VA**

**J. R. Dagenhart, C. W. Brooks, and C. D. Harris
NASA Langley Research Center
Hampton, VA**

PRECEDING PAGE BLANK NOT FILMED



ABSTRACT

An analytical study of linear-amplifying instabilities of a laminar boundary layer as found in the experimental data of the LaRC/8-Ft. laminar-flow control (LFC) experiment was completed and the results are presented. The LFC airfoil used for this experiment was a swept, supercritical design which removed suction air through spanwise slots. The amplification of small disturbances by linear processes on a swept surface such as this can be due to either Tollmien-Schlichting (TS) and/or crossflow (CF) mechanisms. This study consists of the examination of these two instabilities by both the commonly used incompressible (SALLY and MARIA) analysis and the more involved compressible (COSAL) analysis. A wide range of experimental test conditions with variations in Mach number, Reynolds number, and suction distributions were available for this study. Experimentally determined transition locations were found from thin-film techniques and were used to correlate the "n-factors" at transition for the range of test cases.

BACKGROUND/MOTIVATION

The design of laminar-flow airfoils is dependent upon the use of transition prediction techniques which accurately model the characteristics of the boundary layer. A technique which is widely used today is the e^n method that was developed separately by Smith¹ and Van Ingen². This semi-empirical technique examines the tendency of a small disturbance wave within the laminar boundary layer to amplify over a given surface to the point where breakdown to turbulence occurs. The logarithmic amplification ratio, or n -factor as defined in figure 1, is a measure of the spatial growth in amplitude of a disturbance wave from the initial point of instability. Stability theory assumes that the most amplified disturbance (for a critical combination of frequency, wave-angle, and wavelength) is the driving mechanism behind transition. Based on calibrations of a linear incompressible theory with low-disturbance wind tunnel data, stability analyses have shown fairly consistently that transition corresponds to n -factors on the order of ten. However, since stability theory does not account for the influence of the free-stream disturbances, it seems fair to assume that n -factor calibrations are only valid between data sets with similar disturbance environments³.

This research was conducted for several reasons: to examine the amplification of small disturbances by linear processes on a modern swept airfoil; to verify the use of a linear stability theory as a design tool through transonic speeds; and to compare and contrast the incompressible and compressible methods.

- Accurate transition prediction techniques are essential for laminar-flow airfoil design

- e^n method developed separately by Smith and Van Ingen

- Semi-empirical technique
- Relates stability theory (O-S Eq.) to transition
- Uses amplification ratio as indicator of transition

- Solutions to O-S equation give local amplification rates

$$n = \ln(A/A_0) = \int_{x_0}^x (\text{local amplification rate}) dx$$

- Items to note:

- Solutions depend on proper selection of f , ψ , and λ
- Theory does not account for initial disturbance levels (A_0)

- Objectives of analysis

- Validate codes used in design (SALLY & MARIA)
- Examine effect of compressibility (COSAL)

Figure 1

BASIC CORRELATION METHOD

Figure 2 depicts the basic approach employed for this research. Measured pressure and suction distributions were used to calculate streamwise and crossflow velocity profiles along the chord. A stability analysis of these profiles revealed the amount of TS and CF disturbance amplification from the initial point of instability. Comparisons of the measured transition locations with these calculations determined the correlated n -factors at transition.

Solutions to the governing stability equation, which is the celebrated Orr-Sommerfeld (OS) equation, provide the necessary information for analyzing the growth of disturbances within the boundary layer. Two of three disturbance variables, frequency (f), wavelength (λ), or wave-angle (ψ), must be specified with the third given by the solution to the OS equation. Analysis of TS disturbances was accomplished using a fixed frequency and wave-angle method. For incompressible flow it was assumed that the TS disturbances which amplify most are those moving in the direction of the free-stream ($\psi = 0$). Thus, the incompressible TS (SALLY)⁵ analysis consisted of analysis of a range of frequencies with a wave-angle of zero. Since the two-dimensional disturbance assumption could not be used for compressible calculations, the compressible TS (COSAL)⁶ analysis consisted of analysis of, first, a range of frequencies with a wave-angle of zero, then a range of wave angles for the most critical frequency. Suffice to say that the COSAL analysis can be quite time consuming. The CF analysis was accomplished with the MARIA⁷ code which gives approximate solutions using a fixed wavelength and frequency method.

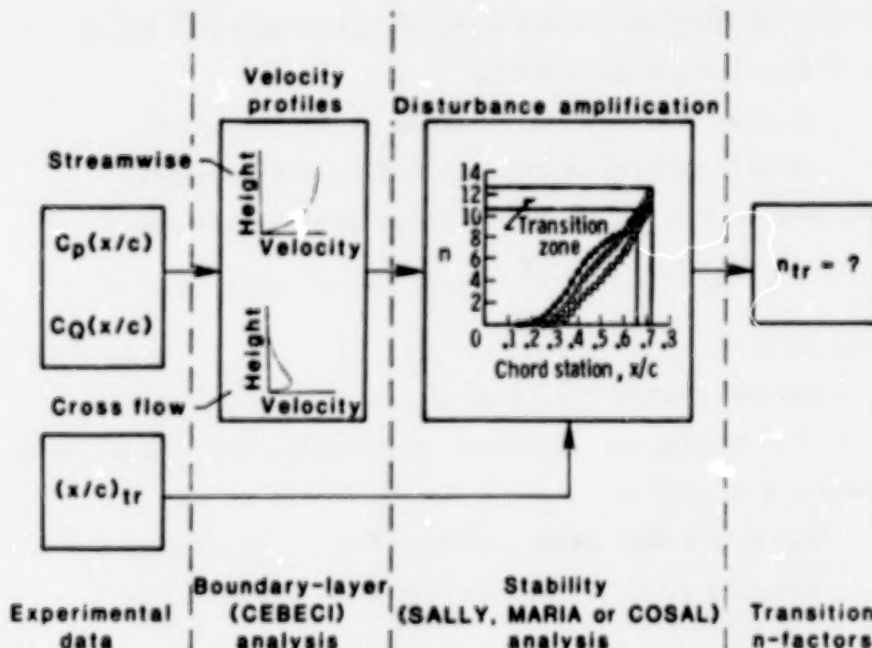


Figure 2

EXPERIMENTAL DATA

The 8-Foot LFC experiment had all the basic information necessary for a stability theory correlation - a pressure and suction distribution as well as transition measurements. Because the upper surface was designed as the primary test surface, only upper surface data were analyzed. A wide range of experimental test conditions with variations in free-stream Mach number (M_∞), chord Reynolds number (R_c), and surface suction (C_q) were available for this study. As shown in figure 3, the available data encompassed both the subsonic and transonic regimes.

For the subsonic cases, the pressure distributions all had a strong leading-edge peak as is shown in figure 3 by a representative case at $M_\infty = .7$. The suction distributions available for these cases were all of the type designed for the airfoil with suction over the full chord. Only the overall suction levels were changed between cases without any attempt to optimize the distributions. At moderate to high overall suction levels, full-chord laminar flow was achieved for the entire subsonic range of M_∞ and R_c .

The transonic cases available were all at the design Mach number ($M_\infty = .82$). As is shown in figure 3, the pressure distributions for these cases closely followed the design distribution except for the slight waviness and slightly higher velocities towards the nose. The waviness in the pressure distributions was thought to be due in part to the model deflecting under loads. A sonic bubble encompassed most of the upper surface and culminated in a weak shock at the higher Reynolds numbers ($R_c \geq 12$ million). Full-chord laminar flow was achieved until the shock appeared and then transition occurred ahead of the shock. Because of this, analysis was done on the "hybrid"-type suction distributions in which suction was systematically shut off at the trailing edge, moving towards the leading edge.

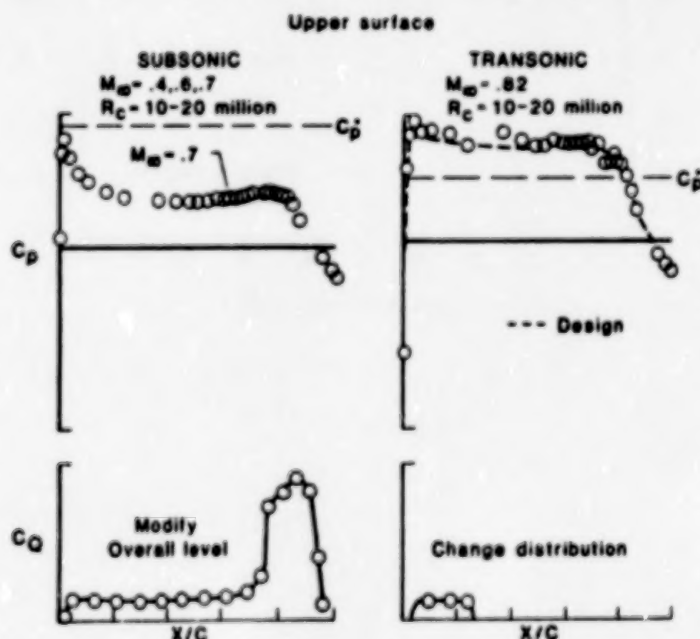


Figure 3

SAMPLE SUBSONIC CALCULATIONS

Figure 4 shows the results of an incompressible TS analysis of a sample subsonic case ($M_\infty = .6$ and $R_c = 10$ million). For the pressure and suction distributions shown in the figure, n -factors were calculated for a range of frequencies with a wave-angle of zero. The combination of the strong adverse pressure gradient near the leading edge and the full-chord suction distribution confined the TS amplification to within the first 15% chord followed by a stable region to the trailing edge. For this case, with its relatively low overall suction level, transition was measured to be around 10-15% chord. As is shown in figure 4, the TS growths reached a logarithmic amplification ratio of $n = 10$ in this region, for the critical frequency of $f = 10$ kHz.

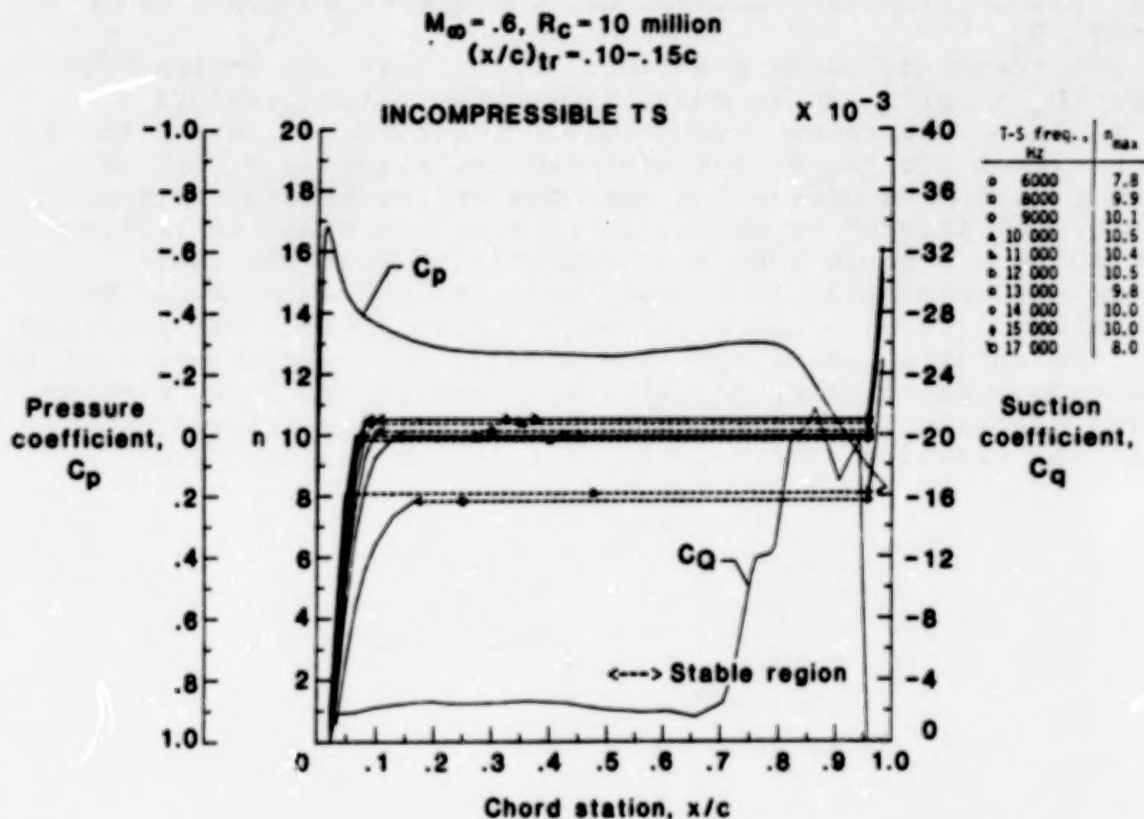


Figure 4

SAMPLE SUBSONIC CALCULATIONS

Figure 5 shows the results of an incompressible CF analysis of the sample subsonic case. The analysis indicates that CF instability is not strong enough to cause transition in this case. In fact, over the entire subsonic range of M_∞ and R_c cases available, CF logarithmic amplification ratios did not exceed $n = 2.5$ in the nose region where the cross-flow instability is considered to be most critical.

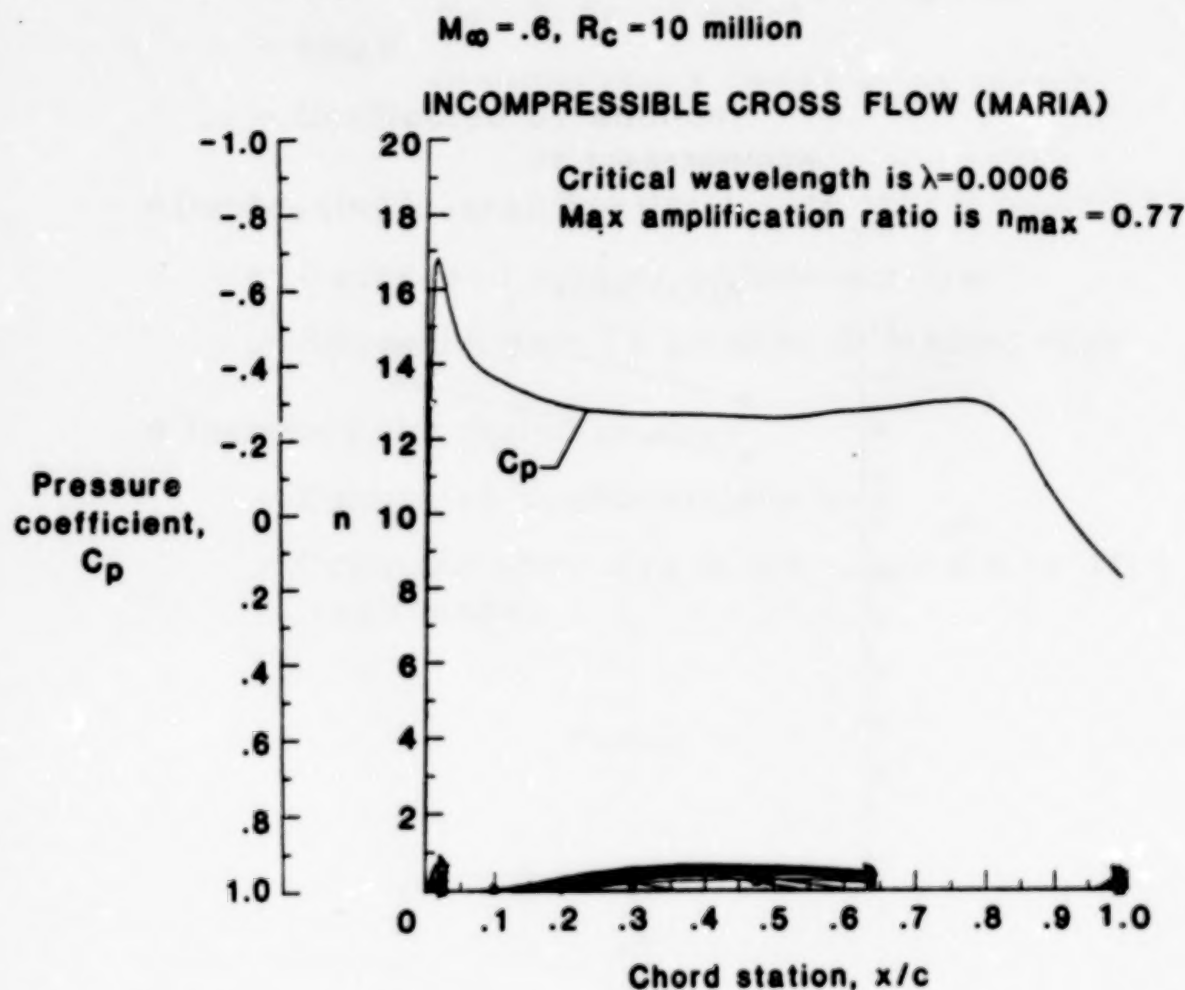


Figure 5

RESULTS OF SUBSONIC ANALYSIS

The results of the subsonic incompressible analysis are summarized in figure 6 which shows the calculated transition n-factors versus the subsonic range of Mach numbers for the Reynolds numbers of 10 and 20 million. Since CF amplification was shown to be insignificant, transition was due entirely to TS amplification. The figure shows the TS logarithmic amplification ratios that correlated with transition. The TS transition n-factors varied from $n = 8.5$ to 10.5 over the range of M_∞ and R_C analyzed. This variation in n-factor is attributed to the fact that the wind tunnel disturbance environment is changing with M_∞ and R_C .

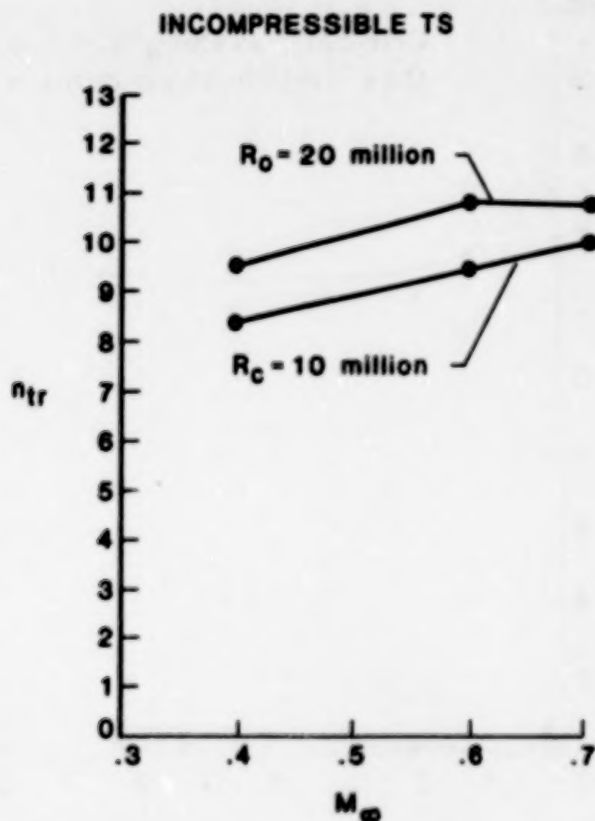


Figure 6

CONCLUSIONS OF SUBSONIC ANALYSIS

The main conclusions that were drawn from the incompressible subsonic analysis⁹ are listed in figure 7. The transition process was found to be dominated by TS amplification. For these subsonic cases, transition occurred when TS logarithmic amplification ratios in the range of $n = 8.5$ to 10.5 was reached near the leading edge.

- CF disturbance amplification at leading edge
 - Small
 - Unaffected by suction
- Decreasing overall suction levels
 - Decreased amount of laminar flow
 - Allowed higher TS growths at leading edge
- Therefore, transition process
 - Dominated by TS disturbances
 - Occurred when n_{TS} in the range 8.5 to 10.5 was reached

Figure 7

SAMPLE TRANSONIC CALCULATIONS

Figure 8 shows the results of an incompressible TS analysis of a sample transonic case ($M_\infty = .82$ and $R_c = 20$ million). For the pressure and suction distribution shown in the figure, n-factors were calculated for a range of frequencies with a wave-angle of zero. The combination of the wavy pressure distribution and suction being turned off after 8% chord allowed strong TS amplification to begin. For this "hybrid" case, transition was measured to occur between 20 and 28% chord. As is shown in the figure, TS disturbances grew to a logarithmic amplification ratio of $n = 10$ to 13 in this region, for a critical frequency of $f = 9$ kHz.

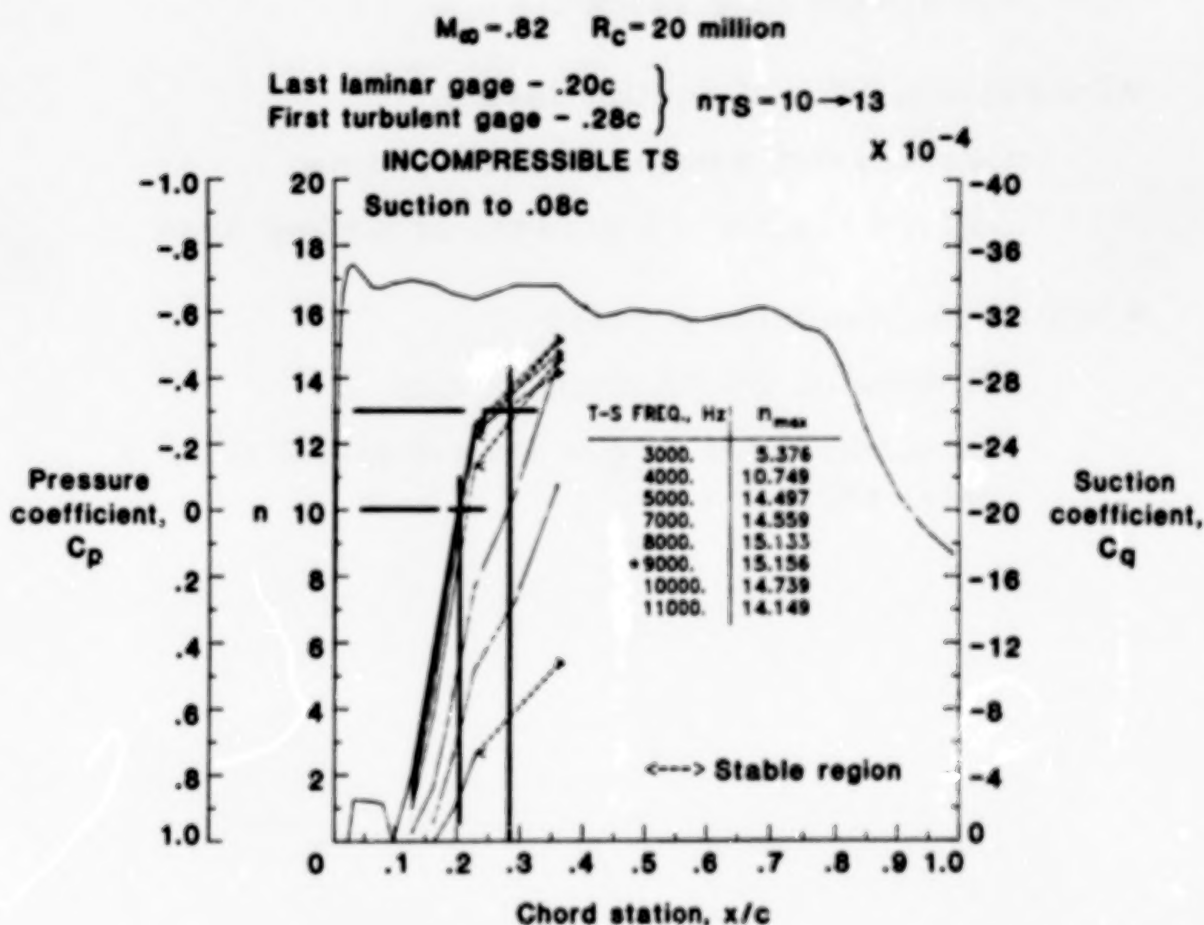


Figure 8

SAMPLE TRANSONIC CALCULATIONS

Figure 9 shows the results of an incompressible CF analysis of the sample transonic case. As is shown in the figure, CF disturbances grew quickly to a peak logarithmic amplification ratio of $n = 4.5$ at about 5% cord and then rapidly damped out. There was no calculated CF amplification in the region of measured transition. For this reason, it was concluded that CF disturbances did not contribute to transition. The case shown here illustrates the "worst" case calculations in terms of CF disturbances over the entire range of M_∞ and R_c .

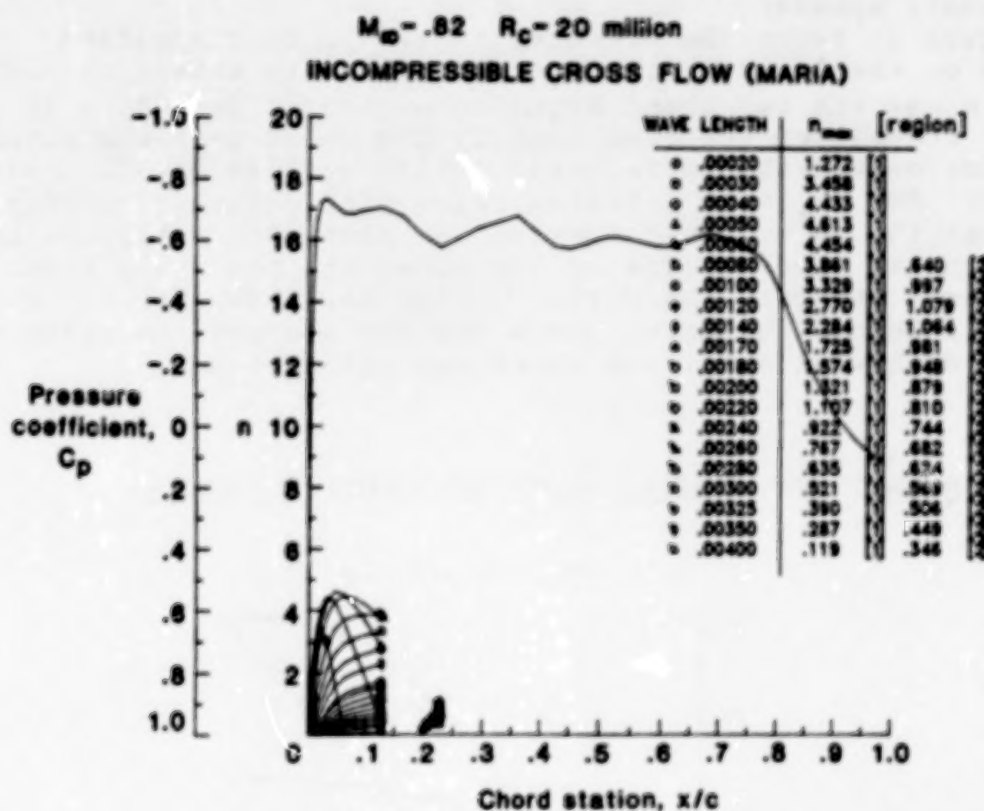


Figure 9

VARIATION OF TRANSITION FOR SIMULATED HLFC

During the experiment, an attempt was made to simulate possible "hybrid" laminar-flow control (HLFC) conditions by turning off the suction level at various chord locations. The HLFC cases consisted of measuring the extent of laminar flow as the upper surface suction was systematically shut off, at the same time maintaining lower surface suction on only the first 25% chord. This simulated HLFC approach is considered somewhat "non-idealistic" since no effort was made to seal or smooth the unsucked regions of the airfoil. Furthermore, it is clear that the current pressure distribution (measured or theory) is not like that which would be designed for HLFC. However, these cases provide data for which transition occurs far forward of shock location thereby being ideal for a stability theory correlation at transonic speeds.

Figure 10 shows the measured variation of transition location on the LFC airfoil upper surface with extent of suction for $M_\infty = .82$ and two chord Reynolds numbers. For $R_c = 10$ million, transition occurred roughly 20% chord past the point where suction was shut off, until full-chord laminar flow was achieved. For $R_c = 20$ million, transition occurred roughly 10% chord past the point where suction was shut off, until the shock present on the rearward end of the model tripped transition. The data clearly indicate the extent of laminar flow that could be maintained beyond the point where suction stopped for transonic airfoils with weak-shock and shockless conditions.

SWEPT LFC AIRFOIL SLOTTED UPPER SURFACE

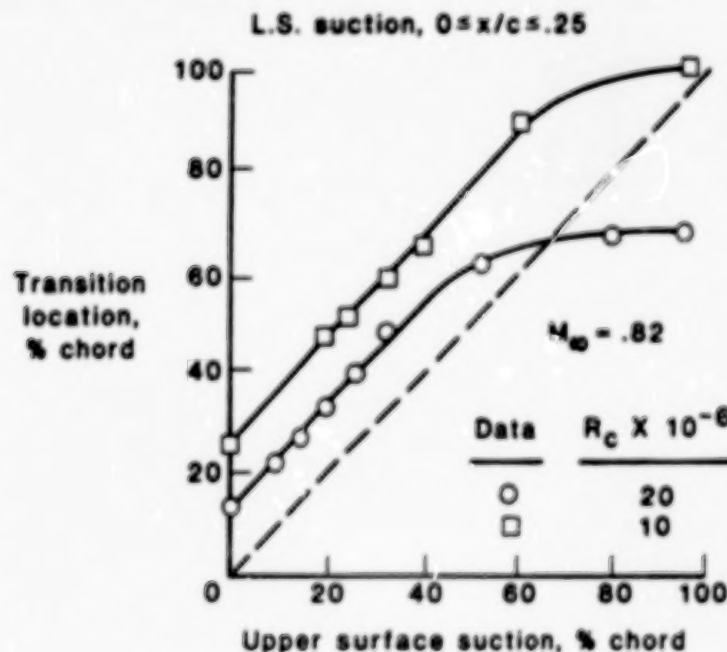


Figure 10

TRANSONIC RESULTS

Figure 11 indicates the results of the incompressible stability analysis of the HLFC data that has shockless flow on the upper surface ($R_C = 10$ million). The figure shows the range of TS amplification at transition versus the extent of suction applied to the airfoil. For each case in which the suction was turned off at a different chord location, symbols were plotted for the calculated incompressible TS logarithmic amplification ratio that corresponded with the measured transition zone. The open symbols indicate the n -factor calculation that corresponded to the chord location of the last fully laminar thin-film gage, while the closed symbols indicate the calculation that corresponded to the first fully turbulent gage. The transition zone shown on the figure helps illustrate the correlated n -factors for the extent of suction used. For this model at test conditions $M_\infty = .82$ and $R_C = 10$ million, the TS transition n -factors for cases with suction past 30% chord are slightly lower than those found with little or no suction. The cases with the extent of suction less than 30% chord have incompressible TS amplification ratios at transition of $n = 10$. The cases with suction past 30% chord have correlated n -factors closer to $n = 7$. Perhaps this indicates that the transition process on swept LFC/HLFC airfoils becomes increasingly non-linear as the extent of desired laminarization increases.

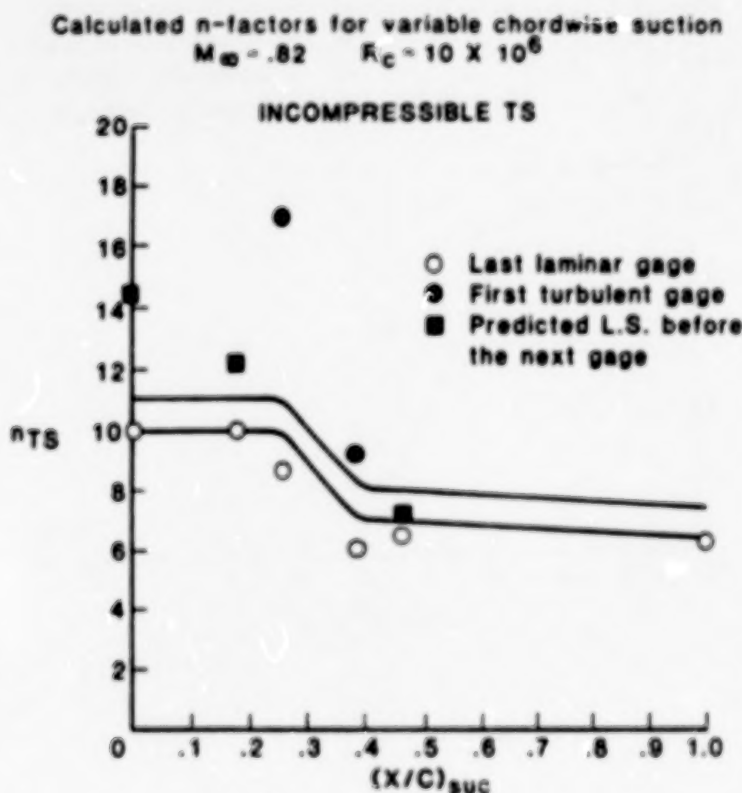


Figure 11

TRANSONIC RESULTS

Figure 12 indicates the results of the incompressible stability analysis of the HLFC data that has a weak shock formed on the rear of the upper surface ($R_C = 20$ million). As is shown in figure 11 the range of TS amplification at transition is plotted against the extent of suction applied to the airfoil. For the cases ranging from no suction to suction over the first 30% chord, the same trend of correlated n-factors of $n = 10$ was found. Suction beyond 30% chord, however, shows that transition is increasingly being dominated by non-linear processes as the extent of suction approaches the shock location. These results demonstrate that for a wind tunnel environment, transition can be very sensitive to the formation of a shock.

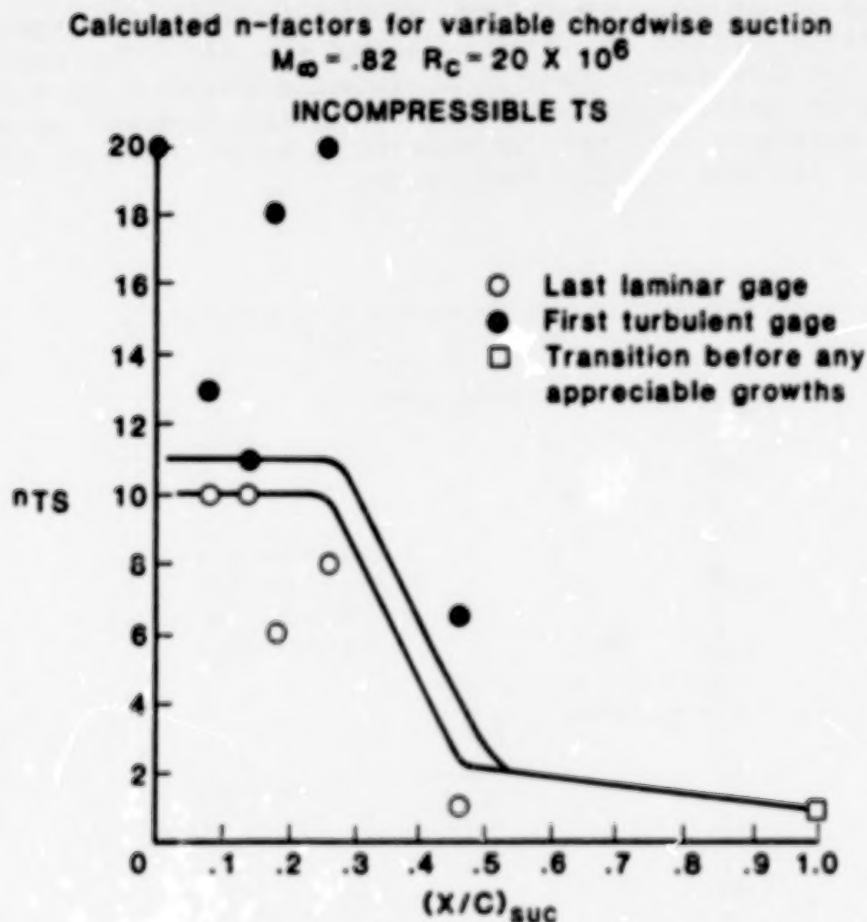


Figure 12

CONCLUSIONS OF TRANSONIC ANALYSIS

The conclusions that were drawn from the incompressible analysis of the transonic data are listed in figure 13. For cases in which full-chord suction distributions were used, transition was sensitive to the rearward attachment point of the sonic bubble. If shockless flow was attained ($R_C < 12$ million) then transition could be maintained very close to the trailing edge. However, if a weak shock appeared ($R_C \geq 12$ million) then transition occurred ahead of the shock for a wide range of overall suction levels which could not be explained with a linear stability theory. Turning off suction ahead of shock, which simulated an HLFC concept, allowed transition to occur as a consequence of disturbance wave amplification and good theory correlations were found for the available range of R_C . The CF disturbances were generally small and unaffected by suction, while TS disturbances grew rapidly to transition once suction was turned off. The incompressible n-factor correlations at transition for this transonic data were $n = 10$ when suction was applied up to 30% chord and $n = 7$ when suction was applied further than 30% chord.

● Full-chord suction cases

- Transition occurs ahead of shock location for $R_C \geq 12$ million which could not be explained by linear stability theory
- Transition occurs at trailing edge for shockless flow ($R_C < 12$ million)

● "Hybrid" suction cases

- Turning off suction ahead of shock allowed natural transition and good theory correlations for range of R_C
- CF disturbances small and unaffected by suction
- TS disturbances grew rapidly to transition after suction turned off

● Incompressible correlations at transition

- 10 near leading edge
- 7 in the mid-chord region

Figure 13

SAMPLE TRANSONIC CALCULATIONS

Figure 14 shows the results of a compressible TS analysis of the sample transonic case ($M_\infty = .82$ and $R_c = 20$ million). For the pressure and suction distribution shown, compressible n -factors were calculated first for a range of frequencies with a wave angle of zero, then for a range of wave angles for the most critical frequency. Since transition was measured between 20 and 28% chord, the compressible TS n -factor at transitions corresponds to $n = 5 - 7.5$ for the most critical disturbance ($f = 7$ kHz and $\psi = -50^\circ$).

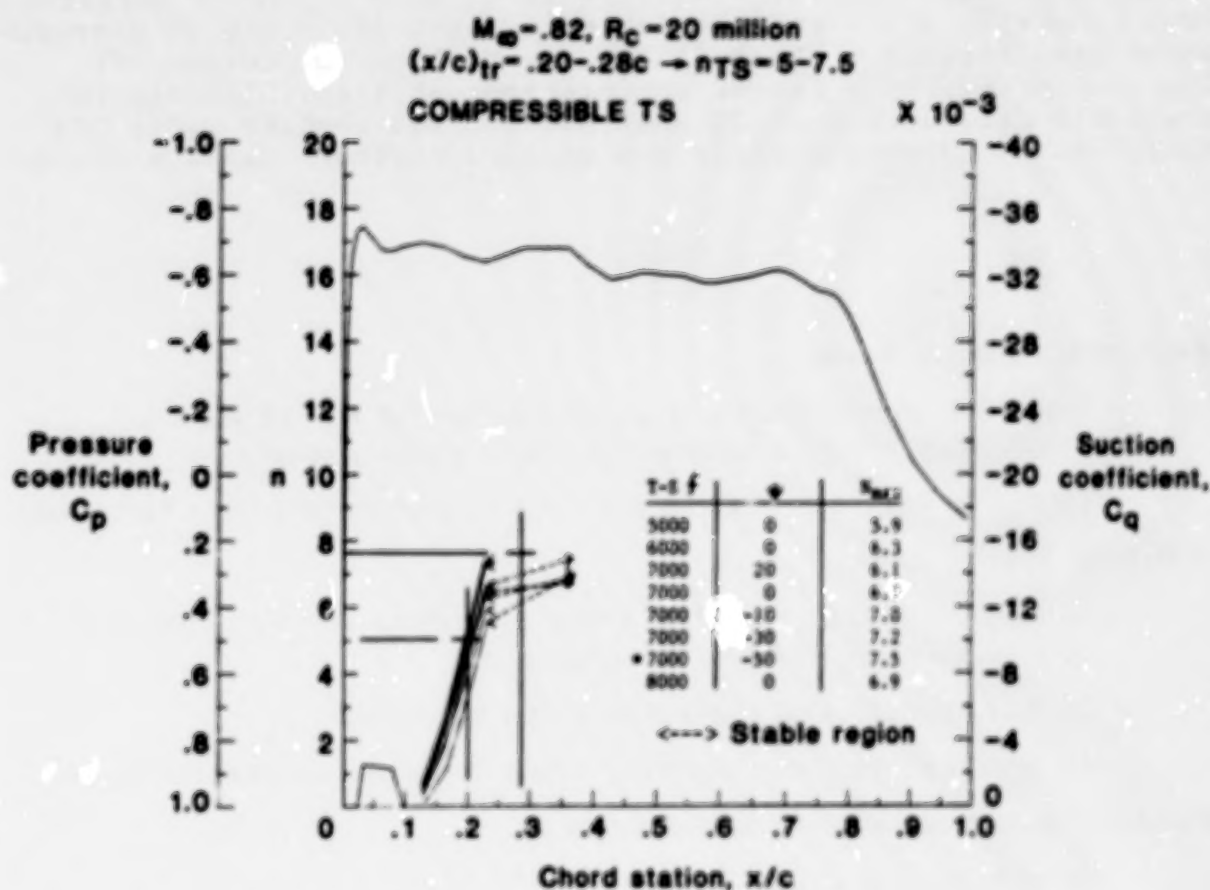


Figure 14

COMPARISONS OF SALLY AND COSAL RESULTS AT TRANSITION

Comparisons of incompressible and compressible stability analysis methods were conducted for a range of M_∞ and the results are tabulated in figure 15. As shown in the figure, compressibility effects reduced the calculated n-factors at transition. The difference accounts for nearly 25% reduction of the calculated amplification for the $M_\infty = 0.4$ to over 50% reduction at $M_\infty = .82$. Both have fairly consistent correlations with the incompressible n-factors of 9 to 10 and the compressible n-factors of 5 to 6. However, as noted earlier, the COSAL analysis involves solutions based on a second unknown (ψ) which increases the time and expense of each compressible case.

M_∞	R_c	n_{TS} -SALLY	n_{TS} -COSAL
.82	20	10.0	4.8
.70	14	10.5	6.3
.40	12	9.0	6.8

- Both have fairly consistent correlation
- COSAL introduces another unknown - ψ
- COSAL is more expensive and time consuming

Figure 15

C-3

SUMMARY

A wide range of low-disturbance wind tunnel data with variations in M_∞ , R_c and suction were analyzed based on a linear boundary-layer stability theory. The data, which were from a large chord, swept, supercritical LFC experiment, encompassed both the subsonic and transonic flow regimes. The analysis showed that as far as laminarization through the control of disturbance amplification, the model performed as designed. The CF amplification was successfully controlled through design by using a proper combination of Reynolds number, pressure gradients and sweep angle. The TS amplification could be successfully controlled by suction as long as strong non-linearities (e.g. shocks) were not present on the airfoil. As is shown in figure 16, the TS logarithmic amplification ratios that were calculated at transition were $n = 9$ to 11 for incompressible theory and $n = 4$ to 6 for compressible theory. Based on these results, it seems fair to conclude that linear stability theory can be used as a guide in the design of laminar-flow airfoils through transonic speeds. However, a word of caution is needed, increasing conservatism in the choice of a design n -factor is required with increasing lengths of LFC, especially at transonic speeds.

- For the range of subsonic and transonic cases
TS disturbances dominated the transition process
- Transition corresponded to
 - Incompressible values of $9 \leq n_{TS} \leq 11$
 - Compressible values of $5 \leq n_{TS} \leq 6$
- Linear stability theory can be used as a guide in
the design of laminar flow airfoils at transonic speeds
- Increasing conservatism in choice of n -factor is required
with increasing length of LFC

Figure 16

REFERENCES

1. Smith, A. M. O.: Transition, Pressure Gradient and Stability Theory. IX International Congress for Applied Mechanics, Brussels, 1956.
2. Van Ingen, J. L.: A Suggested Semi-Empirical Method for the Calculation of the Boundary Layer Transition Region. University of Technology, Department of Aeronautical Engineering, Report UTH-74, Delft, 1956.
3. Spangler, J. G.; and Wells, C. S., Jr.: Effect of Freestream Disturbances on Boundary-Layer Transition. AIAA Journal, Vol. 6, 1968, pp. 543-545.
4. Kaups, K.; and Cebeci, T.: Compressible Laminar Boundary Layers with Suctions on Swept and Tapered Wings. J. Aircraft, Vol. 14, No. 7, July 1977, pp. 661-667.
5. Srokowski, A. J.; and Orzag, S. A.: Mass Flow Requirements for LFC Wing Design. AIAA Paper 77-1222, August 1977.
6. Malik, Mujeeb R.: COSAL - A Black-Box Compressible Stability Analysis Code for Transition Prediction in Three-Dimensional Boundary Layers. NASA CR-165925, May 1982.
7. Dagenhart, J. R.: Amplified Crossflow Disturbances in the Laminar Boundary Layer on Swept Wings with Suction. NASA TP-1902, November 1981.
8. Harvey, W. D.; and Pride, J. D.: The NASA Langley Laminar Flow Control Experiment. AIAA Paper 82-0567, March 1982.
9. Berry, S. A.: "Incompressible Boundary Layer Stability Analysis of LFC Experimental Data for Sub-Critical Mach Numbers," NASA CR-3999, July 1986.

**SENSITIVITY OF LPC TECHNIQUES
IN THE NON-LINEAR REGIME**

**D. M. Bushnell
NASA Langley Research Center
Hampton, Virginia**

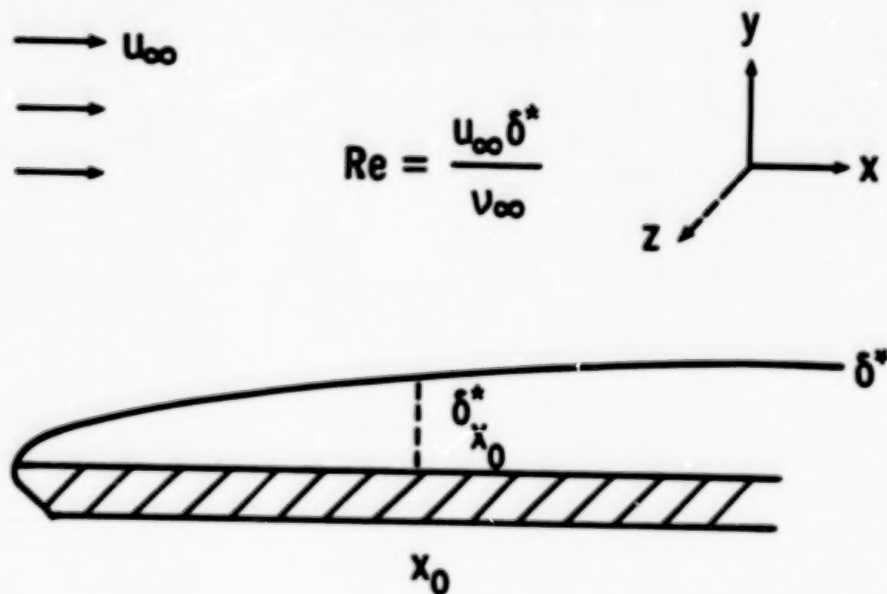
**M. Y. Hussaini
ICASE, NASA Langley Research Center
Hampton, Virginia**

**T. A. Zang
NASA Langley Research Center
Hampton, Virginia**

GROWING BOUNDARY LAYER

The boundary layer on a flat plate is illustrated in Figure 1. The streamwise, normal, and spanwise directions are denoted by x , y , and z , respectively. The displacement thickness δ^* increases in the streamwise direction. At any distance x_0 from the leading edge, one can define a Reynolds number Re based on the velocity u_∞ and kinematic viscosity ν_∞ in the free stream and the local displacement thickness.

The transition process of the growing boundary layer is influenced by significant non-linear, three-dimensional and non-parallel effects. Unfortunately, existing computer resources are only adequate for treating two out of these three effects.



Non-linear

Three-dimensional

Non-parallel

Figure 1

PARALLEL BOUNDARY LAYER

A common compromise is to study the parallel boundary layer (see Figure 2) instead of the true, growing one. Here the focus is on the vicinity of some point x_0 (see Figure 1) and the approximation is that the displacement thickness remains constant (in x) at the value $\delta_{x_0}^*$. As a consequence, only the non-linear and the three-dimensional effects are taken into account. The neglect of the non-parallel effects should be serious only if there is appreciable growth on the scale (λ_{TS}) of the Tollmien-Schlichting (TS) waves. Since the mean flow in the parallel boundary layer is uniform in x , a Fourier approximation in x is highly accurate; moreover, only one spatial wavelength needs to be resolved for the temporal transition problem. Thus, highly resolved computations can be performed, well into the strongly non-linear regime.

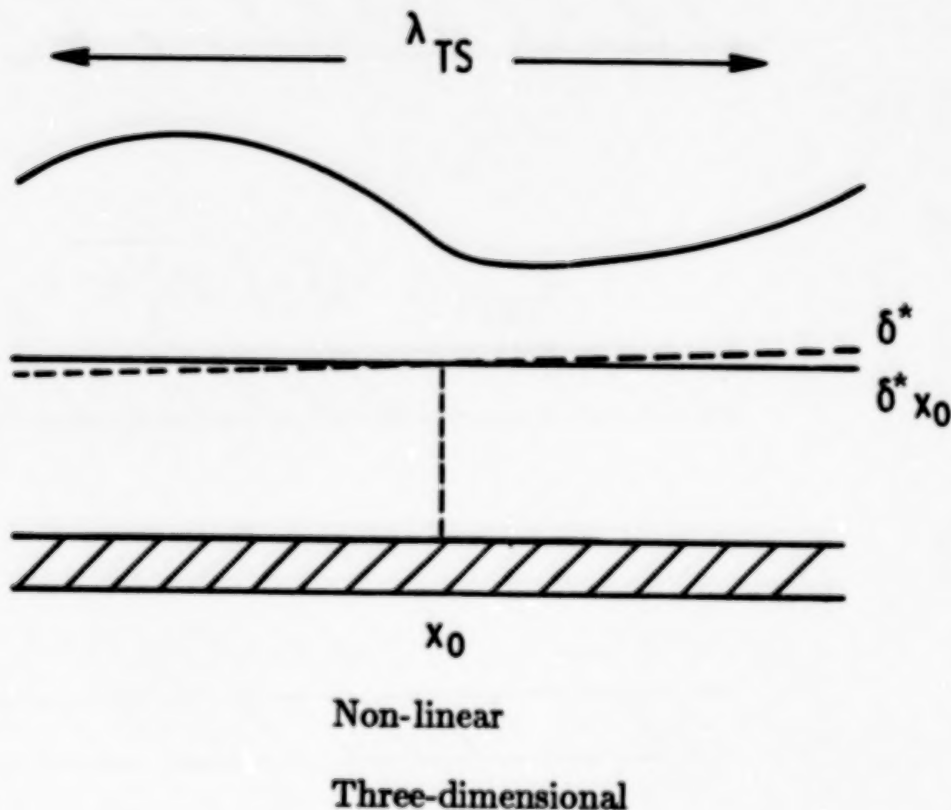


Figure 2

BOUNDARY-LAYER CONTROLS

Figure 3 depicts three types of laminar-flow control (LFC) techniques. The dimensionless parameters describing self-similar solution of the Falkner-Skan boundary-layer equations are defined in the figure. These are β for pressure gradient, F_w for suction, and τ for heating. In the last case, the free stream and wall temperatures, denoted by T_∞ and T_w , respectively, (and given in degrees Kelvin), differ and the kinematic viscosity depends upon the temperature T .

Pressure gradient

$$u_\infty \propto x^{\frac{\beta}{2-\beta}}$$



Suction

$$v_{\text{wall}} = -1/2 \sqrt{\frac{u_\infty v_\infty}{x}} F_w$$



Heating

$$\tau = T_w / T_\infty$$

$$\nu = \nu(T)$$



Figure 3

CONTROLLED, PARALLEL BOUNDARY LAYER

The essential features of the controlled, parallel water boundary layer are summarized in Figure 4. The mean flow is taken to be the solution of the appropriate self-similar boundary-layer equations. The temperature dependence of the viscosity and conductivity are taken from Ref. 1. (However, the specific heat and density are presumed to be independent of temperature; their values in the free stream are used throughout the flow field.) The parallel flow assumption permits the use of a periodic approximation in x and z . Shown below is the form of a single Fourier component. This alone is appropriate for the linearized stability problem, but for the full non-linear simulations reported in this paper a finite Fourier series is employed in both x and z .

- Parallel flow assumption

$$U(X, Y, Z, T) = \hat{U}(Y) e^{i(\alpha X + \beta Z - \omega T)}$$

- Mean flow described by Falkner-Skan equation with pressure gradient, suction and/or heating controls
- Viscosity and conductivity based on empirical formulas for water
- Reynolds numbers based on displacement thickness and free stream conditions

Figure 4

LINEAR THEORY RESULTS FOR HEATED BOUNDARY LAYERS

The linear stability of heated water boundary layers has been examined by Wazzan, Okamura, and Smith [2] and by Lowell and Reshotko [1]. Wazzan et al. included the effects of temperature only insofar as they modified the mean flow; their stability analysis admitted only velocity and pressure fluctuations. The linear results of Lowell and Reshotko, on the other hand, included the effects of temperature fluctuations. Figure 5, taken from Ref. 1, compares the neutral stability curves that ensue under heating control for $T_w = 60^\circ\text{F}$ when the temperature is allowed to fluctuate (solid lines) and when it is held fixed at its mean value (dashed lines). Note that the boundary layer is actually more stable than is suggested by linear theory calculations which neglect temperature fluctuations. Note also that although the flow initially becomes more stable as the wall is heated, its stability eventually degrades with additional wall heating. Lowell and Reshotko have performed further calculations in which the effects of the temperature upon the density are included. They found that this effect moves the neutral stability curves to the left, e.g., for the $T_w = 90^\circ\text{F}$ case, the solid curve moves one-third of the distance to the dashed curve when density fluctuations are admitted.

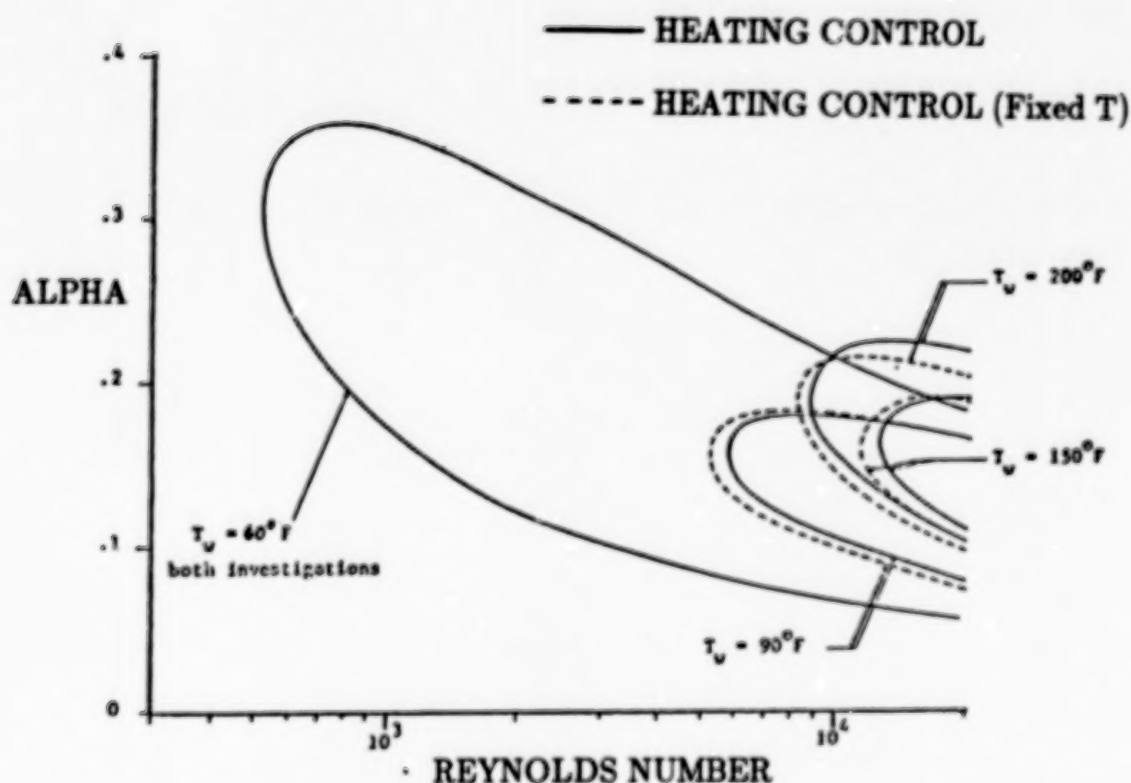


Figure 5

INCOMPRESSIBLE HEATED BOUNDARY LAYER

This paper examines LFC techniques in the non-linear regime via direct numerical solution of the time-dependent, incompressible Navier-Stokes equations, with temperature dependent viscosity and conductivity. These equations (Figure 6) are augmented with an equation for the time evolution of the temperature. In order to conform to the parallel flow assumption, forcing terms need to be added to the momentum and temperature equations. These are denoted by F_u and F_θ respectively. See Zang and Hussaini [3, 4] for more details.

$$\begin{aligned}\nabla \cdot \mathbf{u} &= 0 \\ \frac{\partial \mathbf{u}}{\partial t} + \boldsymbol{\omega} \times \mathbf{u} &= -\nabla P + \frac{1}{Re} \nabla \cdot (\mu \nabla \mathbf{u}) + F_u \\ \frac{\partial \theta}{\partial t} + \mathbf{u} \cdot \nabla \theta &= \frac{1}{RePr} \nabla \cdot (\kappa \nabla \theta) + F_\theta \\ \boldsymbol{\omega} &= \nabla \times \mathbf{u} \\ P &= p + (1/2)|\mathbf{u}|^2 \\ \theta &= (T - T_\infty)/(T_w - T_\infty)\end{aligned}$$

Figure 6

NUMERICAL METHODS

In this work, numerical methods are needed for three problems. The mean flow is calculated from the Falkner-Skan boundary-layer equations via a fourth-order finite-difference scheme [5]. The linear eigenmodes (and linear stability properties) are computed by a Chebyshev Tau method [6]. The time dependent Navier-Stokes equations are solved by a Fourier-Chebyshev collocation method [7]. The mean flow and the linear eigenfunctions are used for the initial conditions of the direct simulation (Figure 7).

- Non-linear mean flow

- 4th-order compact finite difference scheme

- Linear modes

- Chebyshev Tau method

- Navier-Stokes solution

- Fourier-Chebyshev collocation in space
 - 3rd-order Adams-Bashforth on explicit terms
 - Crank-Nicholson on implicit terms
(vertical diffusion, pressure and continuity)

Figure 7

SPLITTING METHOD

The Navier-Stokes algorithm used a splitting method which is outlined in Figure 8. The first (velocity) step accounts for the advection and diffusion terms. (Although not indicated below, the temperature equation is also integrated in this step.) The second (pressure) step enforces the incompressibility constraint. The boundary conditions in the velocity step are chosen to minimize the slip velocity which is present after the pressure step. More details are given by Zang and Hussaini [7]. The book by Canuto, Hussaini, Quarteroni, and Zang [8] contains an exhaustive discussion of spectral methods for simulations of incompressible flow.

The results reported in this paper were obtained on the NAS Cray 2. The collocation grids ranged from 16×48 to 64×64 (in x and y) for the 2-D cases and from $16 \times 48 \times 8$ to $64 \times 64 \times 16$ (in x , y , and z) for the 3-D problems. Typical simulations took several thousand time-steps and covered from two to five periods of the primary 2-D TS wave.

Velocity step	$(t_n \rightarrow t^*)$
	$\underline{u}_t^* = \underline{u}^* \times \underline{\omega}^* + \nabla \cdot (\mu \nabla \underline{u}^*)$
	$\underline{u}^*(\underline{x}, t_n) = \underline{u}(\underline{x}, t_n)$
	$\underline{u}^* _{\text{bdy}} = \underline{g}^*$
Pressure step	$(t^* \rightarrow t_{n+1})$
	$\underline{u}_t^{**} = -\nabla P^{**}$
	$\nabla \cdot \underline{u}^{**} = 0$
	$\underline{u}^{**}(\underline{x}, t_{n+1}) = \underline{u}(\underline{x}, t^*)$
	$\underline{u}^{**} \cdot \hat{n} = \underline{g} \cdot \hat{n}$
Final result	$\underline{u}(\underline{x}, t_{n+1}) = \underline{u}^{**}(\underline{x}, t_{n+1})$

Figure 8

MEAN FLOW AT $Re = 8950$

The specific cases chosen for this investigation of non-linear stability are illustrated in Figure 9. The Reynolds number was 8950 and was chosen in part because some linear theory results were reported for this Reynolds number in Ref. 1. The free-stream temperature was 293 K. The amounts of pressure gradient, suction, and heating were chosen so that the flow was neutrally stable. (The linear theory results for the heated case did not include the temperature fluctuations.) The mean flow of both the controlled and uncontrolled cases are given in the figure. In the heated case, the viscosity varies by 50% and the conductivity by 7%. The specific heat and density (whose variations are not accounted for in the non-linear simulation) vary by 0.1% and 1%, respectively.

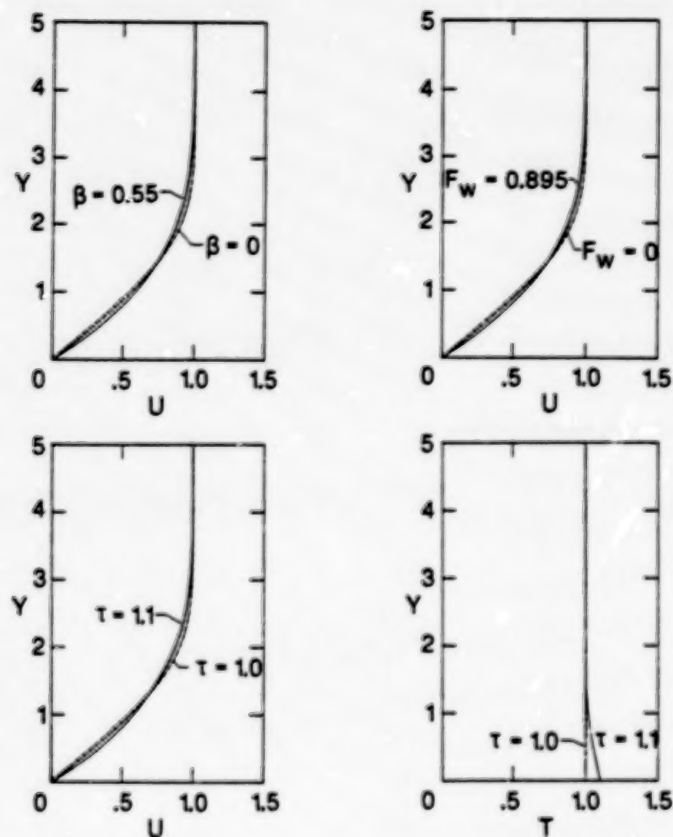


Figure 9

MEAN FLOW CHARACTERISTICS FOR $Re = 8950$

The use of the LFC techniques has a dramatic effect upon the actual displacement thickness of the boundary layer. This is quantified in Figure 10. The Reynolds number based on the displacement thickness of the corresponding uncontrolled boundary is also listed there. Note that in terms of the growing boundary layer, the controlled cases correspond to different positions x_0 , with the pressure gradient case having the greatest distance from the leading edge and the uncontrolled case having the least distance.

CONTROL	$\delta^* / \sqrt{\frac{\nu x_0}{U_\infty}}$	Re_{δ^*} BLASIUS
NONE	1.7244	8,950
$\beta = 0.55$	0.9448	16,330
$\tau = 1.10$	1.3986	11,040

Figure 10

BOUNDARY-LAYER MODES FOR $Re = 8950$

The accuracy of the fully non-linear, time-dependent Navier-Stokes code is documented in Figure 11. For each of the linear modes specified in the first four columns, a highly accurate temporal eigenvalue ω and eigenfunction were generated using the Chebyshev Tau code. This eigenfunction was then input at very low amplitude into the non-linear code as the initial condition. The code was run for two TS periods and the growth rate of the eigenfunction was measured. This is listed in the last column. Listed next to it is the growth rate (imaginary part of ω) produced by the linear stability code. This growth rate is effectively zero—the real part of ω is roughly 0.04. Keeping in mind the size of the real part of ω , it is clear from Figure 11 that the non-linear code is accurate to four or five digits.

Control	Mode	α	β	Linear growth rate	Computed growth rate
Pressure	TS 2-D	0.168	0.000	0.000095	0.000096
	TS 3-D	0.168	0.168	-0.001012	-0.001028
Suction	TS 2-D	0.162	0.000	0.000093	0.000093
	TS 3-D	0.162	0.162	-0.000968	-0.000993
Heating	TS 2-D	0.150	0.000	0.000093	0.000097
	TS 3-D	0.150	0.150	-0.000798	-0.000793

Figure 11

INITIAL CONDITIONS

The initial conditions for the direct numerical simulations are depicted in Figure 12. The initial velocity field consists of the appropriate mean flow plus a 2-D TS wave and (possibly) a symmetric pair of oblique 3-D waves (only one of which is shown). The arrow denotes the streamwise direction and the indices k_x and k_z label the streamwise and spanwise Fourier components relative to the wavenumbers α and β of the 3-D TS waves given in Figure 11. The initial amplitude of the waves is measured by their maximum streamwise velocity relative to the free-stream mean flow velocity.

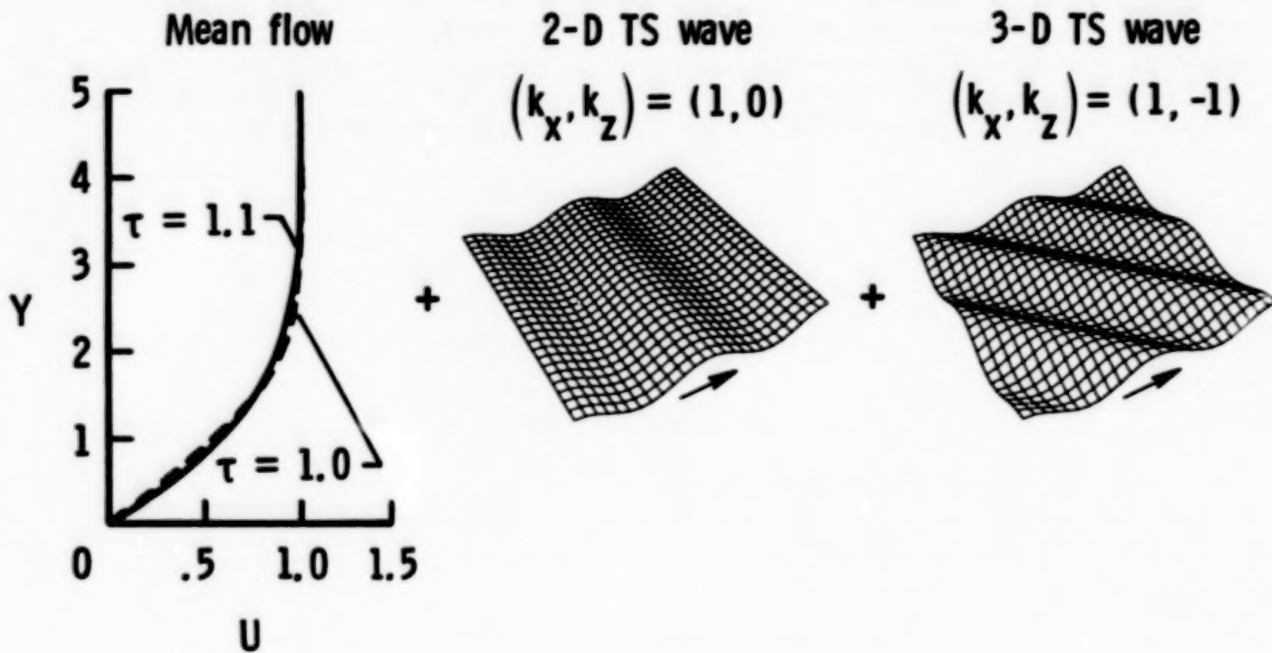


Figure 12

GROWTH OF FINITE AMPLITUDE 2-D WAVES

The first set of results pertains to finite amplitude effects upon 2-D TS waves. Results of simulations for which the initial amplitude of the 3-D wave was zero and the initial amplitude of the 2-D was 1/2, 1, 2, and 4% are summarized in Figure 13. Suction control yields behavior similar to that for pressure gradient control [4] and is therefore not given. Two types of heating control simulations were performed: in one case the temperature was held fixed at its initial mean value (corresponding to the linear theory study of Wazzan et al. [2]), and in the other the temperature fluctuations were properly accounted for (as in the work of Lowell and Reshotko [1]). The initial conditions for both types of heating simulations, however, were identical.

The strength of the perturbation at any instant is measured here by the kinetic energy E of the $(k_x, k_z) = (1, 0)$ Fourier component of the velocity field. This is plotted on a semi-log scale in Figure 13, with the time measured in units of the period of the 2-D TS wave; the energy at $t = 0$ is denoted by E_0 . Thus, one indication of the impact of non-linear effects is the departure of the curves from a straight (and nearly horizontal) line. Another is the failure of the curves to lie on top of each other.

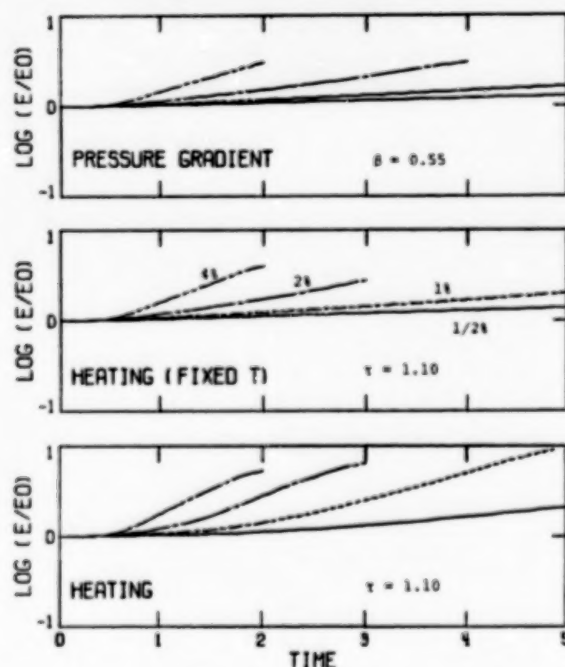


Figure 13

NON-LINEAR EFFECTS ON 2-D WAVES

In all cases, the initial growth of the 2-D TS wave is faster than exponential. Note that in the non-linear regime the heated boundary layer appears to be less stable, i.e., subjected to faster growth of the 2-D wave, when temperature fluctuations are included. This is precisely the opposite of how temperature fluctuations affect the linear stability results. It is also apparent that non-linear effects lead to a more rapid destabilization of a water boundary layer controlled by heat than one controlled by pressure gradient.

The tables below (Figure 14) summarize the departure from linear growth for 2-D waves with initial amplitudes of 1/2% and 2%. The numbers give the ratios (after 1, 2, and 3 TS periods) of the actual amplitude of the 2-D wave to that given by linear theory. These numbers, of course, just reinforce the data presented in Figure 13.

NON-LINEAR/LINEAR AMPLITUDE RATIO FOR 1/2% 2-D WAVES

TIME	PRESSURE GRADIENT	HEATING (FIXED T)	HEATING
1	1.004	1.005	1.001
2	1.013	1.017	1.016
3	1.022	1.030	1.080

NON-LINEAR/LINEAR AMPLITUDE RATIO FOR 2% 2-D WAVES

TIME	PRESSURE GRADIENT	HEATING (FIXED T)	HEATING
1	1.050	1.065	1.184
2	1.189	1.257	1.605
3	1.378	1.567	2.387

Figure 14

FUNDAMENTAL VERSUS SUBHARMONIC SECONDARY INSTABILITIES

The transition to turbulence is a strongly three-dimensional process. The next part of this investigation focuses on finite amplitude effects upon the secondary instability of the primary 2-D wave to small, 3-D perturbations. The secondary instabilities may be categorized as fundamental or subharmonic. These are identified in flow visualization of the early three-dimensional stage of transition as ordered or staggered arrays of lambda vortices [9], and have been explained by weakly nonlinear theory [10]. Figure 15 sketches the periodic array of vortices associated with these secondary instabilities. The distance L_x is the length of the primary 2-D TS wave and it is given by $2\pi/\alpha$.

The 3-D waves that lead to the fundamental instability are TS waves, i.e., solutions to the Orr-Sommerfeld equation, whereas the subharmonic instability arises from the interaction of the 2-D wave with a solution of the vertical vorticity (or Squire) equation with streamwise wavenumber $\alpha/2$. These so-called Squire modes are all linearly stable.

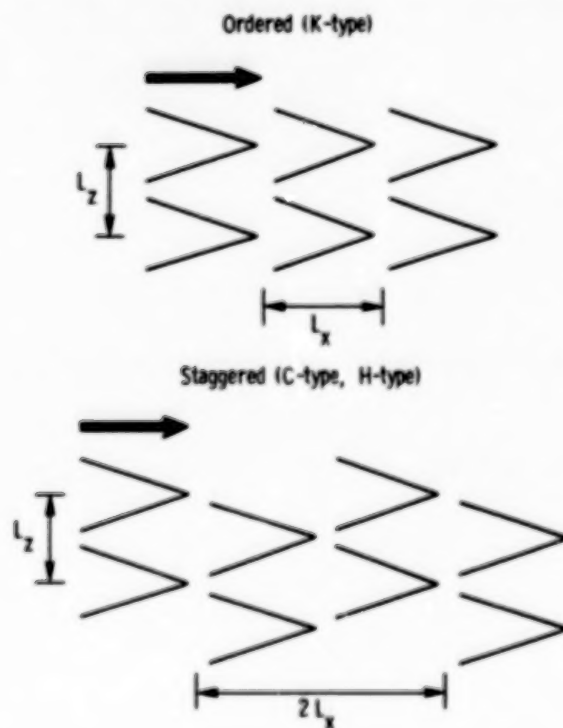


Figure 15

SECONDARY INSTABILITY FOR PRESSURE GRADIENT CONTROL

Figures 16, 17, and 18 summarize the results of numerical simulations of the secondary instability of controlled boundary layers. In all cases, the initial 3-D amplitude was 0.01% and the initial 2-D amplitude varied between 1/2% and 4%. In these plots, the kinetic energy is shown for the 2-D Fourier component $(k_x, k_y) = (1,0)$ and for the appropriate 3-D component—(1,1) for the fundamental instability and (1/2,1) for the subharmonic. The 3-D curves are labeled by the amplitude of the 2-D wave for the simulation.

SECONDARY INSTABILITY at $Re = 8950$

Fundamental

Subharmonic

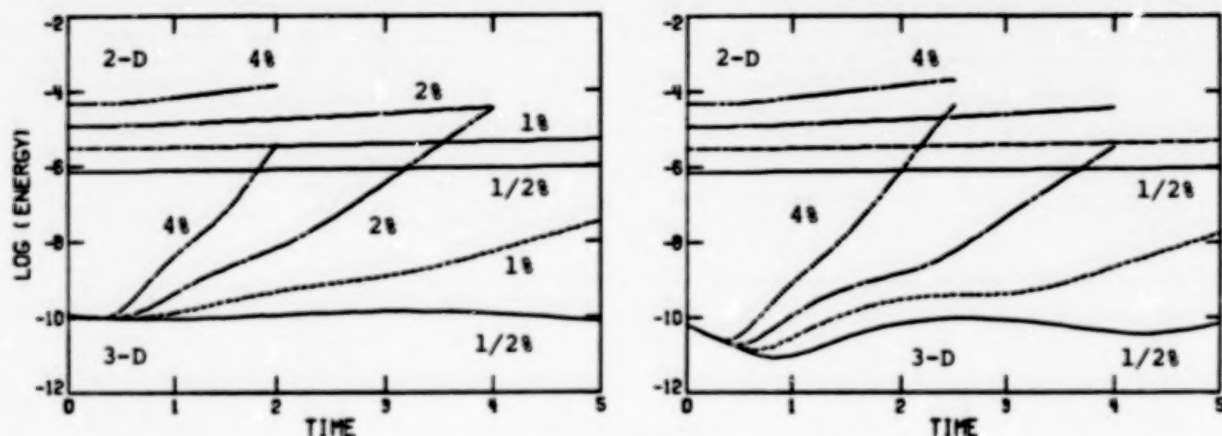


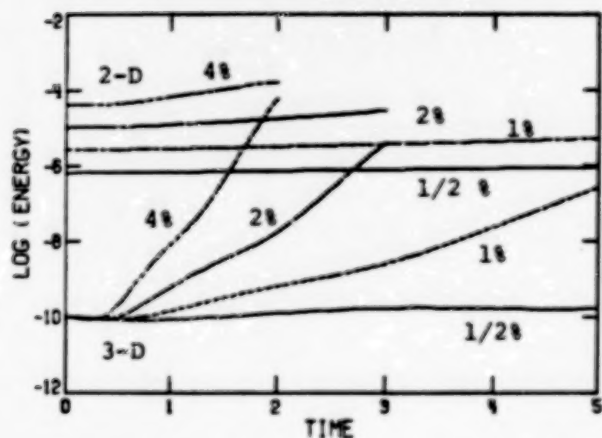
Figure 16

SECONDARY INSTABILITY FOR HEATING CONTROL (FIXED T)

The secondary instabilities have the same general character here that they do in uncontrolled boundary layers: they are triggered by 2-D amplitudes on the order of 1% or more; their growth rate increases with the 2-D amplitude; they grow much faster than the primary wave; and the fundamental and subharmonic instabilities have comparable growth rates (Figure 17).

SECONDARY INSTABILITY at $Re = 8950$

Fundamental



Subharmonic

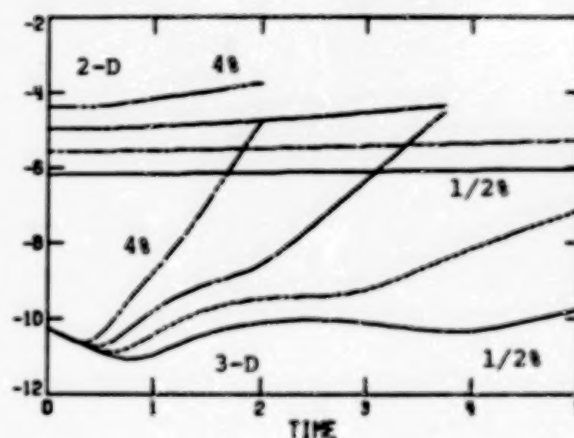


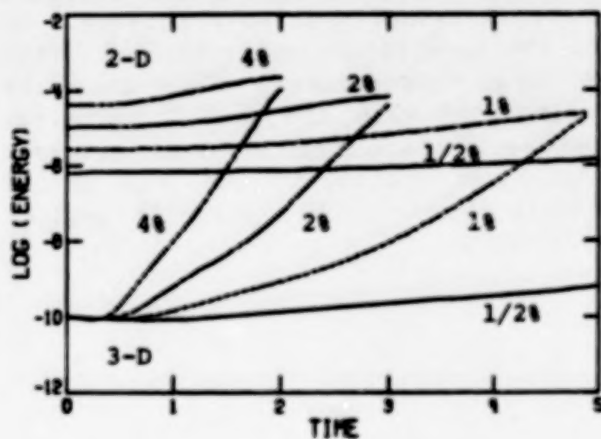
Figure 17

SECONDARY INSTABILITY FOR HEATING CONTROL

Among these three cases, the secondary instability is strongest for the heated boundary-layer simulation which includes temperature fluctuations. But the more rapid growth of the 3-D waves in this case is clearly tied to the more rapid growth of the 2-D wave. Hence, the principal effect of the temperature fluctuations is upon the 2-D waves (Figure 18).

SECONDARY INSTABILITY at $Re = 8950$

Fundamental



Subharmonic

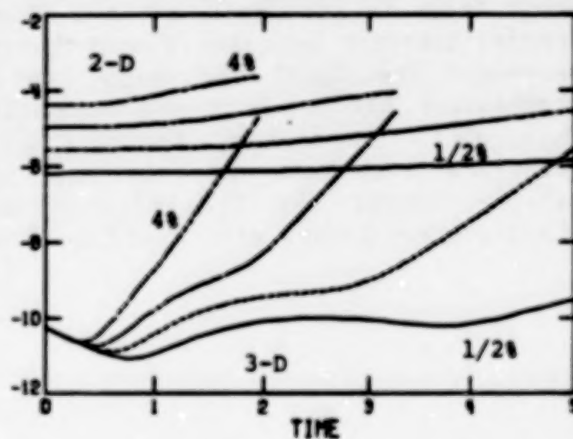


Figure 18

FLOW FIELD STRUCTURE

Figures 19 to 23, taken from the work of Zang and Hussaini [4], illustrate the flow field which develops for a fundamental (K-type) secondary instability in a heated boundary layer. The calculations were performed at a Reynolds number of 1100 and for wall heating of 2.75%. The initial amplitude was 2.7% for the 2-D wave and 0.8% for the 3-D wave. This simulation was run for nearly five periods of the 2-D TS wave; a grid of 96 x 162 x 216 (in x, y, and z) was employed in the later stages. Figures 20 - 23 display the key features at a very advanced stage of the transition process. The flat plate is indicated by the solid surface and the mean flow is from the lower right to the upper left.

The vortex lines indicate the presence of a hairpin vortex. The spanwise vorticity displays the strong detached shear layer which forms on top of the vortex. The normal velocity contours indicate the regions in which low speed fluid from the wall region is injected upward towards the free stream. The plane in the middle of the spanwise direction is known as the peak plane. It is located at the center of the hairpin vortex. In this plane, the detached shear layer is strongest and the upward normal velocity is most intense. Of special interest here are the contours of the temperature perturbation. They represent the local departure from the mean temperature. Note that the temperature fluctuations are strongly correlated with the normal velocity. There is a temperature increase in the peak plane and an even stronger temperature decrease near the wall on the outer regions of the legs of the hairpin vortex. The line drawings in figure 19 are from a slightly earlier stage and are marked with specific contour levels.

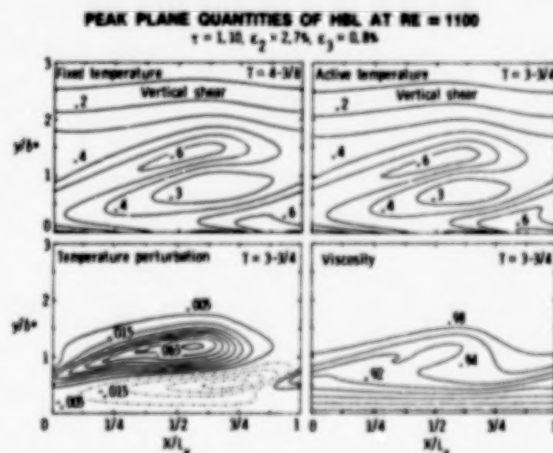


Figure 19

CONCLUSIONS

The principal conclusions from this work are summarized below. For all of the LFC techniques examined here, finite-amplitude effects are destabilizing, i.e., finite-amplitude 2-D TS waves grow faster than predicted by linear theory. We also find, in direct contrast to the results from linear theory for low-amplitude waves, that temperature fluctuations exert a further de-stabilizing influence on finite amplitude 2-D TS waves. The controlled boundary layers are, of course, subject to intense 3-D secondary instabilities. The instantaneous growth rates of both the fundamental and subharmonic instabilities are strongly tied to the amplitude of the primary 2-D wave. The principal finite-amplitude effects upon the 3-D secondary instabilities occur through the faster growth of the 2-D wave.

VORTEX LINES AT $T = 4 \frac{7}{8}$

Heated boundary layer K-type transition

$Re = 1100$ $T_w/T_\infty = 1.0275$ $\epsilon_2 = 2.7\%$ $\epsilon_3 = 0.8\%$

Figure 20

SPANWISE VORTICITY AT $T = 4 \frac{7}{8}$

Heated boundary layer K-type transition

$Re = 1100$ $T_w/T_\infty = 1.0275$ $\epsilon_2 = 2.7\%$ $\epsilon_3 = 0.8\%$

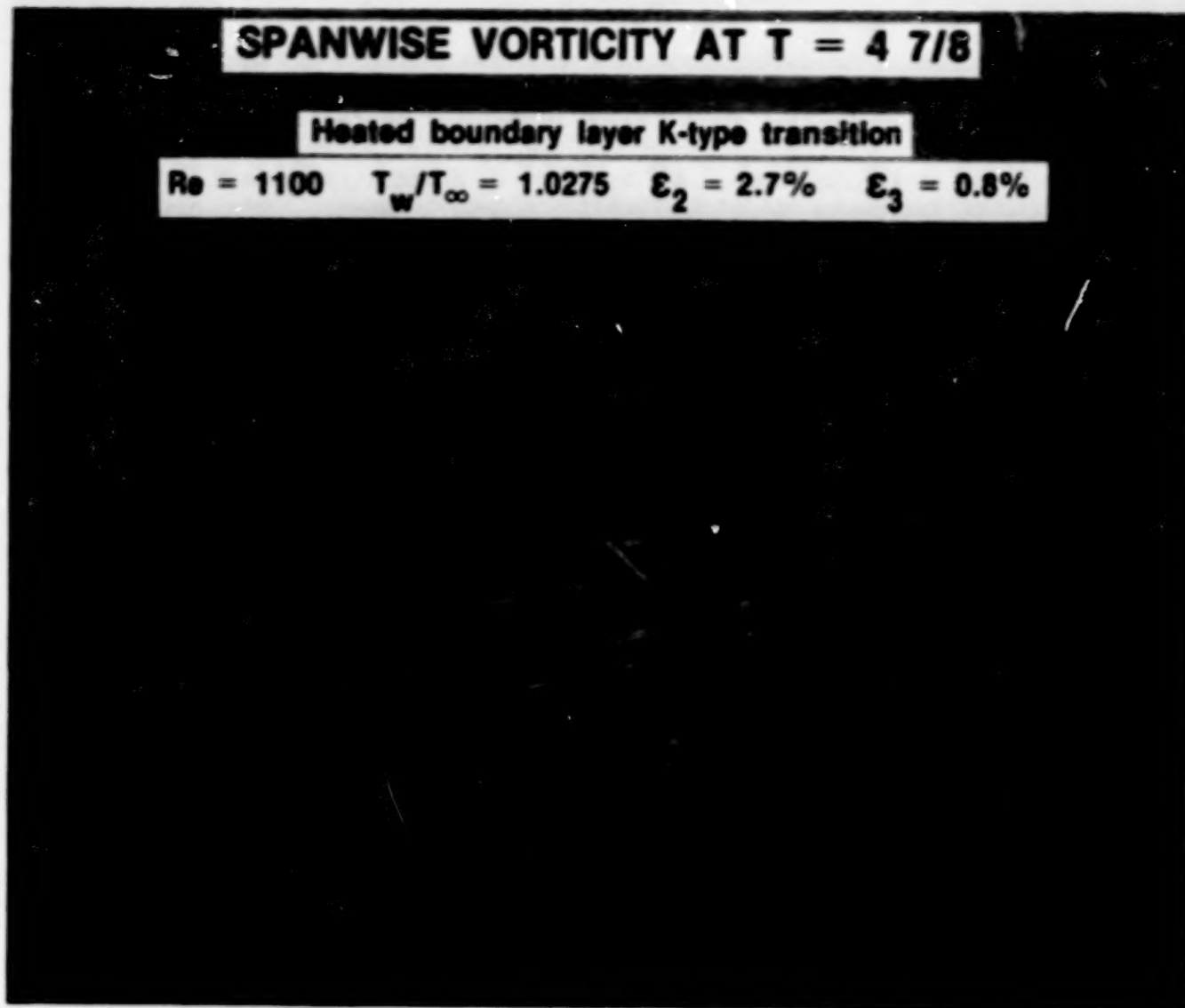


Figure 21

~~ORIGINAL PAGE IS
OF POOR QUALITY~~

ORIGINAL PAGE
BLACK AND WHITE PHOTOGRAPH

NORMAL VELOCITY AT $T = 4 \frac{7}{8}$

Heated boundary layer K-type transition

$Re = 1100$ $T_w/T_\infty = 1.0275$ $\epsilon_2 = 2.7\%$ $\epsilon_3 = 0.8\%$

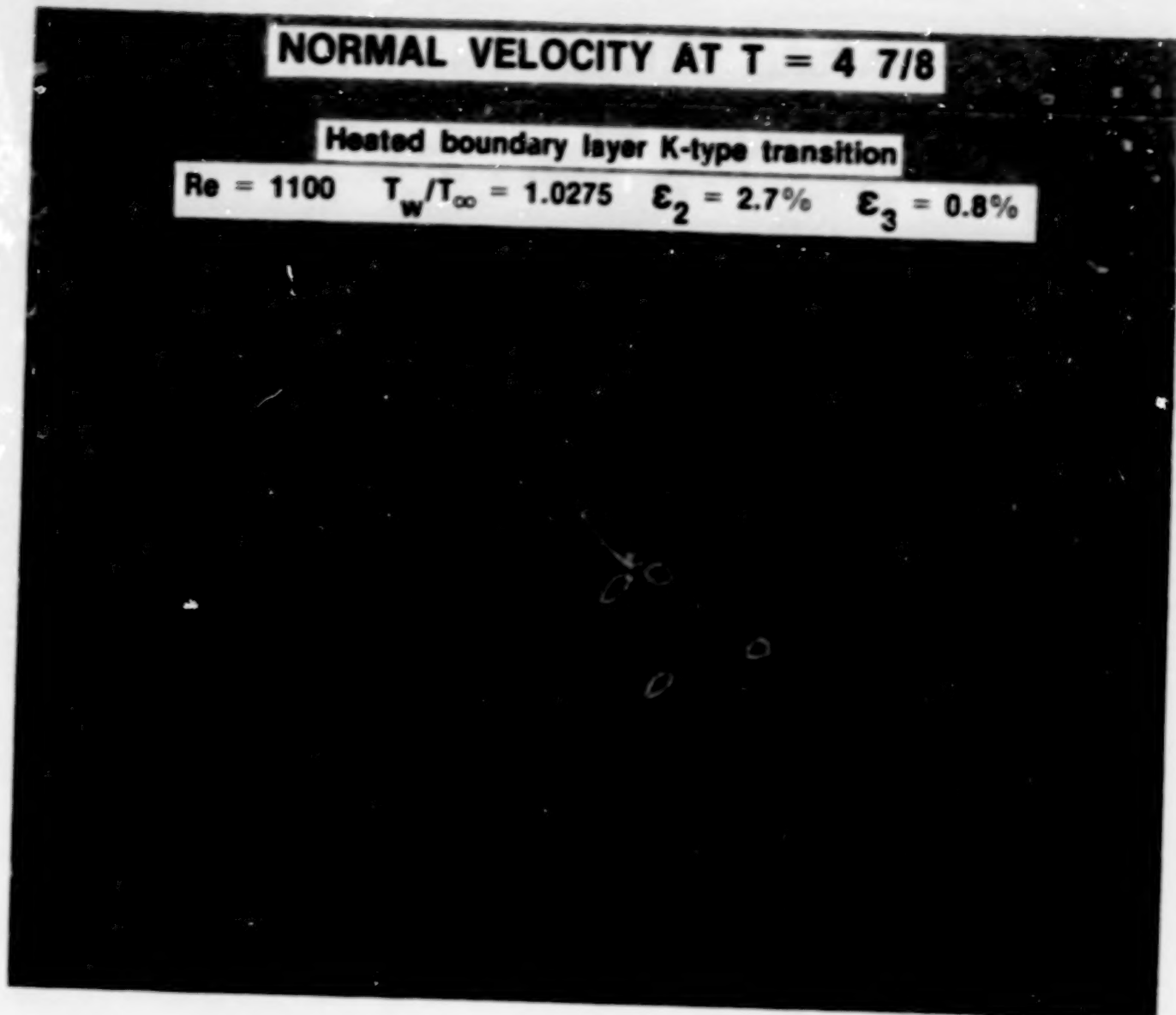


Figure 22

~~ORIGINAL PAGE IS
OF POOR QUALITY~~

ORIGINAL PAGE
BLACK AND WHITE PHOTOGRAPH

TEMPERATURE PERTURBATION AT $T = 4 \frac{7}{8}$

Heated boundary layer K-type transition

$Re = 1100$ $T_w/T_\infty = 1.0275$ $\epsilon_2 = 2.7\%$ $\epsilon_3 = 0.8\%$

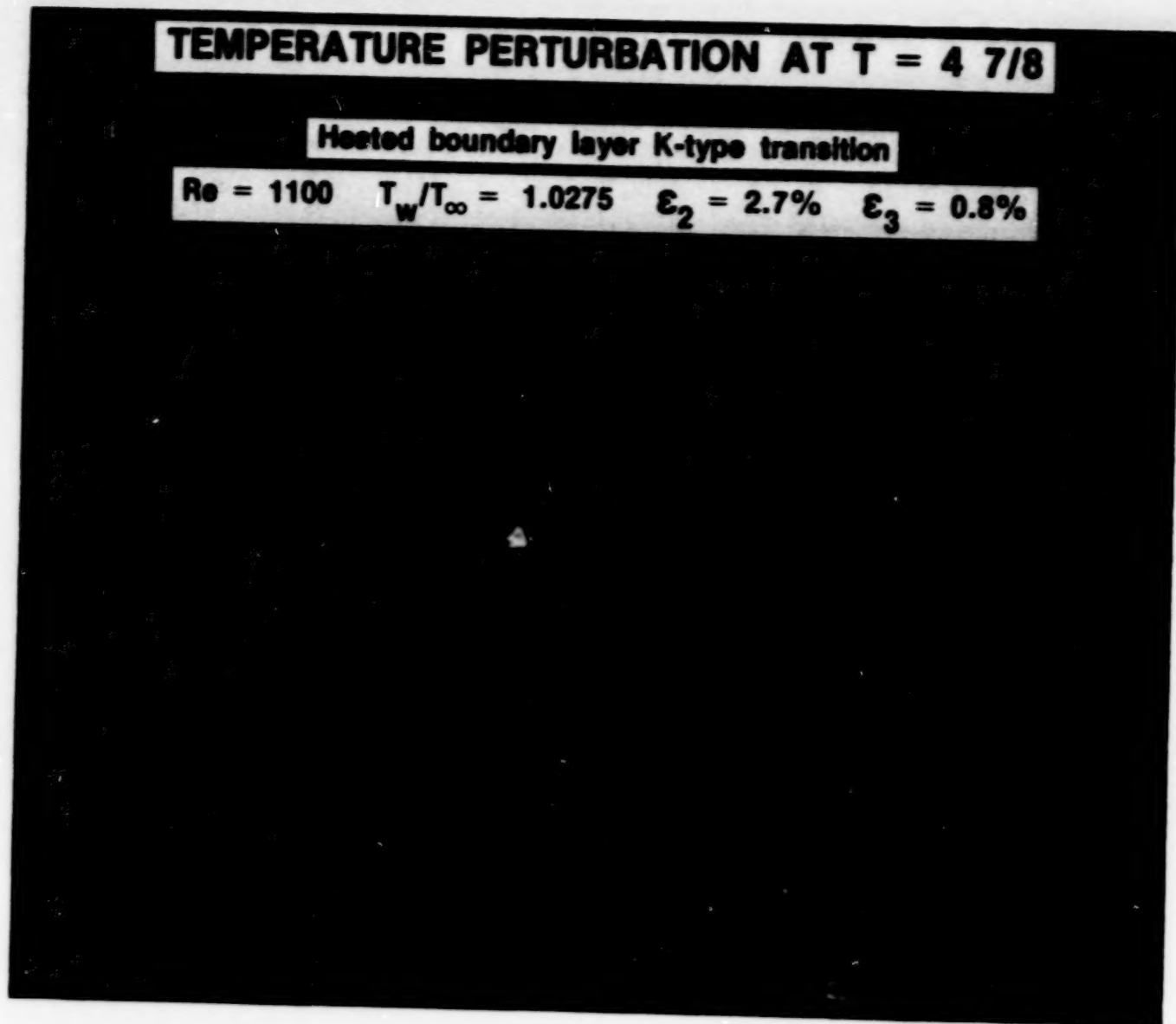


Figure 23

ORIGINAL PAGE
BLACK AND WHITE PHOTOGRAPH

~~ORIGINAL PAGE IS
OF POOR QUALITY~~

CONCLUSIONS

- Finite amplitude effects lead to enhanced growth of 2-D waves
- Temperature effects are further destabilizing for finite amplitude 2-D waves
- More rapid growth of the primary wave leads to more rapid development of 3-D secondary instabilities
- The fundamental and subharmonic instabilities have comparable growth rates

Figure 24

REFERENCES

1. Lowell, R. L.; and Reshotko, E.: Numerical Study of the Stability of a Heated Water Boundary Layer. Case Western Reserve University, FT AS/TR-73-93, 1974.
2. Wazzan, A. R.; Okamura, T.; and Smith, A. M. O.: The Stability of Water Flow Over Heated and Cooled Flat Plates. J. of Heat Transfer, Vol. 90, Feb. 1968, pp. 109-114.
3. Zang, T. A.; and Hussaini, M. Y.: Numerical Experiments on Subcritical Transition Mechanisms. AIAA Paper 85-0296, 1985.
4. Zang, T. A.; and Hussaini, M. Y.: Numerical Experiments on the Stability of Controlled Shear Flows. AIAA Paper No. 85-1698, 1985.
5. Malik, M. R.; Chuang, S.; and Hussaini, M. Y.: Accurate Numerical Solution of Compressible Stability Equations. ZAMP, Vol. 33, No. 2, March 1982, pp. 189-201.
6. Orszag, S. A.: Accurate Solution of the Orr-Sommerfeld Equation. J. Fl. Mech., Vol. 50, No. 4, December 1971, pp. 689-703.
7. Zang, T. A.; and Hussaini, M. Y.: On Spectral Multigrid Methods for the Time-Dependent Navier-Stokes Equations. Appl. Math. Comp., Vol. 19, pp. 359-372, 1986.
8. Canuto, C.; Hussaini, M. Y.; Quarteroni, A.; and Zang, T. A.: Spectral Methods in Fluid Dynamics. Springer-Verlag, Berlin, 1987.
9. Saric, W. S.; Kozlov, V. V.; and Levchenko, V. Y.: Forced and Unforced Subharmonic Resonance in Boundary-Layer Transition. AIAA Paper NO. 84-0007, 1984.
10. Herbert, T.: Analysis of the Subharmonic Route to Transition in Boundary Layers. AIAA Paper No. 84-0009, 1984.

N90-12534

**NUMERICAL SOLUTIONS OF THE COMPRESSIBLE 3-D BOUNDARY-LAYER
EQUATIONS FOR AEROSPACE CONFIGURATIONS WITH
EMPHASIS ON LPC**

**Julius E. Harris
NASA Langley Research Center
Hampton, Virginia**

**Venkit Iyer
Vigyan Research Associates, Incorporated
Hampton, Virginia**

**Samir Radwan
High Technology Corporation
Hampton, Virginia**

**THREE-DIMENSIONAL BOUNDARY-LAYER PROGRAM
LAMINAR FLOW CONTROL RESEARCH
NASA LANGLEY RESEARCH CENTER**

The application of stability theory in Laminar Flow Control (LFC) research requires that density and velocity profiles be specified throughout the viscous flow field of interest. These profile values must be as numerically accurate as possible and free of any numerically induced oscillations. To date, a high percentage of the boundary-layer solutions for use in three-dimensional (3-D) stability analysis programs have been obtained using quasi-3-D procedures due to the general unavailability of 3-D boundary-layer programs.

Several mature 3-D boundary-layer programs based on finite-difference techniques (note: integral approaches are not considered in the present paper) currently exist, for example, references 1 through 4. Unfortunately, these programs are not available for general use by the LFC research community due to company proprietary controls. In addition to proprietary controls, most of the programs are not structured or adequately documented for ease of use; that is, their use would generally require direct interaction with and/or assistance from the group or individual that developed the program.

Guidelines for the present research project are presented in figure 1 and are as follows: (1) develop an efficient and accurate procedure for solving the 3-D boundary-layer equations for aerospace configurations; (2) develop an interface program to couple selected 3-D inviscid programs that span the subsonic to hypersonic Mach number range; and (3) document and release software to the LFC research community.

● Reasons for development

- No general program exists that is readily available to all groups involved in laminar flow control research
- No general program exists that is coupled directly with the most often used inviscid programs over the subsonic to hypersonic Mach number range
- Most existing programs are at best second-order accurate and often degenerate to first-order accuracy

● Guidelines for development

- User friendly
- High-order accuracy; $O(\Delta Z^4)$, $O(\Delta X, \Delta Y)^2$
- Flexible interface
- Document and release to LFC Research community

(Finite difference numerics)

FIGURE 1

ORDER OF PRESENTATION

As a result of time constraints for the present symposium, it was necessary to condense the material that would have been included in three presentations into a simple co-authored paper. Consequently, no attempt will be made to either (1) give a review of current boundary-layer literature or (2) compare numerical results from the present solution procedure with previously published numerical and/or experimental results. The material to be presented is outlined in figure 2 and is divided into two basic categories. The interaction between these categories will not be discussed due to time limitations.

Within the inviscid area the focus of the presentation will be on the processing of the inviscid flow field data required as input to the boundary-layer program. The surface Euler equations will be defined together with the numerical procedure for solving the nonlinear system. Several test cases will be presented where results obtained from standard interpolation procedures will be compared with results from the surface Euler equations.

Within the viscous area the focus of the presentation will be on the numerical procedure and the establishment of its accuracy and numerical efficiency. The boundary-layer equations will not be presented in equation form; however, their mathematical character and the required boundary and initial conditions will be discussed. The reader interested in the full equations can find them in several publications (see refs. 1 through 6, for example).

- Inviscid
 - Interface program
 - Inviscid data treatment
 - Surface Euler equations
 - Boundary conditions
 - Numerical procedure
 - Test cases
- Viscous
 - Governing equations
 - Boundary conditions
 - Initial conditions
 - Transformation
 - Solution technique
 - Numerical scheme
 - Matrix structure
 - Test cases

FIGURE 2

INTERFACE PROGRAM

The interface program provides the required linkage between the most appropriate inviscid code for the configuration and flight Mach number regime and the three-dimensional boundary-layer program. The functions of the interface program are presented in figure 3. The interface program must be capable of (1) generating a sufficiently refined boundary-layer grid; (2) calculating the metric coefficients and related geometric parameters for this grid; (3) interpolating the pressure field from the relatively coarse grid used for the inviscid flow field solution to the relatively fine boundary-layer grid with automatic smoothing capability as required; (4) solving the surface Euler equations on the wall boundary to obtain the inviscid velocity components and their gradients in the ξ, η coordinate system; and (5) generating all required input files for the boundary-layer program. In addition to these primary functions, the interface program prepares diagnostic plot files and will act as the interactive link for viscous-inviscid interaction calculations.

Success (measure of acceptance and use of software by LFC research groups) of the boundary-layer program will depend, to a large extent, on the structure of the interface software.

- General function
 - Provide the required linkage between selected inviscid programs that span the subsonic to hypersonic Mach number range and the boundary-layer program under development
- Specific functions
 - Generation of boundary-layer grid and related metric coefficients
 - Interpolation of inviscid pressure distribution from the relatively coarse inviscid grid to the sufficiently fine boundary-layer grid
 - Solution of the surface Euler equations to obtain the inviscid velocity distribution over the boundary-layer grid
 - Generation of input and output files for the boundary-layer program
 - Interface for viscous-inviscid interaction

FIGURE 3

TREATMENT OF INVISCID DATA

The sensitivity of stability theory to oscillations in the viscous flow field requires that the inviscid data and body geometry (metric coefficients, etc.) be carefully treated in order to avoid the introduction of nonphysical oscillations. Alternate approaches to inviscid flow-field data treatment are presented in figure 4. A conventional approach has been to use spline interpolation to transfer data from the relatively coarse inviscid grid to the sufficiently fine boundary-layer grid. These interpolated results are then numerically smoothed. The interpolation approach is the most straightforward; however, large errors can occur in the interpolation and arbitrary smoothing of vector quantities. This approach yields results that are not consistent; that is, they do not satisfy the governing inviscid equations within an acceptable error bound.

The present approach is to interpolate the pressure field from the coarse inviscid grid to the fine boundary-layer grid. This pressure distribution $P_w(\xi, \eta)$, together with known initial and boundary values, is used in the numerical solution of the surface Euler equations. The advantage of the approach is that exact values of u and v can be enforced on certain boundaries, the velocity components (u, v) and their gradients in the ξ, η plane are smooth, and the numerical results are consistent.

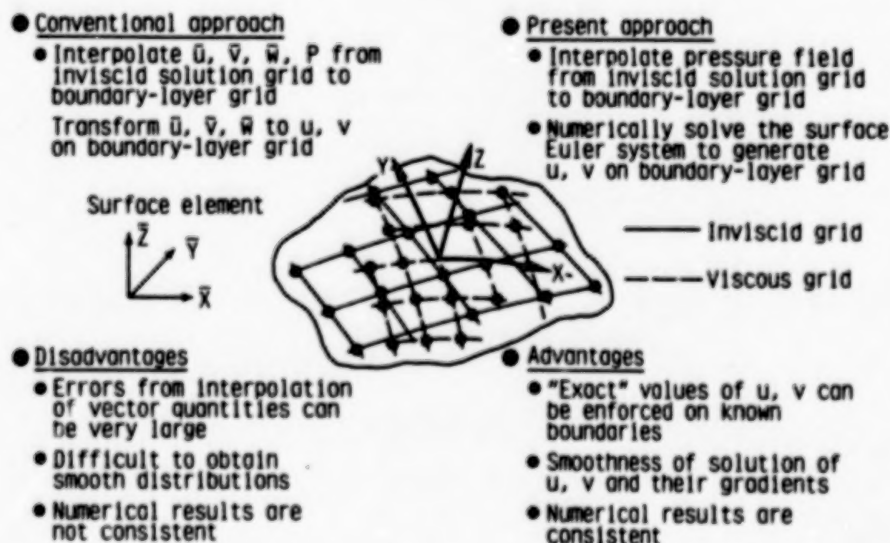


FIGURE 4

SURFACE EULER EQUATIONS

The surface Euler equations are obtained from the three-dimensional boundary-layer equations in the limit as $\zeta \rightarrow \infty$. The system obtained from the ξ and η momentum equations are presented in figure 5. The system consists of two nonlinear hyperbolic equations for the ξ and η momentum equations and an algebraic relationship for the energy equation (perfect gas). The b_{ij} values are known functions of the grid system. The pressure is known from the interpolation procedure. The unknowns are ρ , u , and v , where ρ , u , and v are the density, ξ -velocity component, and η -velocity components, respectively. The equations are a first order, nonlinear hyperbolic system where the local streamlines are characteristic. The system can be solved with an explicit march in ξ while remaining fully implicit in η provided the initial conditions and boundary conditions can be specified as indicated in figure 5.

A method for calculating the inviscid velocity vectors from a specified pressure field was first reported by Cebeci and Meier (ref. 6) for incompressible flow around an ellipsoid at angle of attack. Vollmers (ref. 7) and Gleyzes and Cousteix (ref. 8) improved the approach by integrating the Euler equations. Anderson (ref. 3) described a method using experimental pressure distributions on rotating turbine blades using the Euler equations. The current procedure extends these concepts to complex geometry associated with wings and fuselages using a second-order numerical scheme.

• Equation system obtained from boundary-layer equations in limit as $\zeta \rightarrow \infty$

• Equations

ξ -momentum

$$\rho \left(b_{11} u \frac{\partial u}{\partial \xi} + b_{12} v \frac{\partial u}{\partial \eta} + (b_{12} u^2 + b_{14} uv + b_{15} v^2) \right) = (b_{16} \frac{\partial p}{\partial \xi} + b_{17} \frac{\partial p}{\partial \eta})$$

η -momentum

$$\rho \left(b_{21} u \frac{\partial v}{\partial \xi} + b_{22} v \frac{\partial v}{\partial \eta} + (b_{23} u^2 + b_{24} uv + b_{25} v^2) \right) = (b_{26} \frac{\partial p}{\partial \xi} + b_{27} \frac{\partial p}{\partial \eta})$$

• Character of system

- First order, nonlinear hyperbolic system
- Local streamlines are characteristics
- Explicit march in ξ ; implicit in η

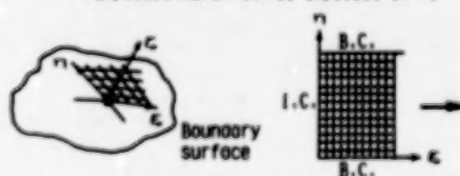


FIGURE 5

BOUNDARY CONDITIONS FOR FUSELAGE "TYPE" GEOMETRY

As previously noted in figure 5, initial and boundary conditions must be specified for physical flows corresponding to aerospace configurations. These conditions are presented in figure 6(a) for a fuselage type body. The fuselage type body with a plane of symmetry relative to the flow field has well defined initial and boundary conditions. The initial conditions at the stagnation point in the physical plane are $u = v = 0$. These conditions from the required initial values along the $\xi = \xi_0$ line in transformed space. Along both the leeward and windward lines of the symmetry plane in physical space one can specify the conditions $v = 0$ and $\partial u / \partial \eta = 0$. These form the boundary conditions in the transformed plane for the lines $\eta = \eta_0$ and $\eta = \eta_{\max}$.

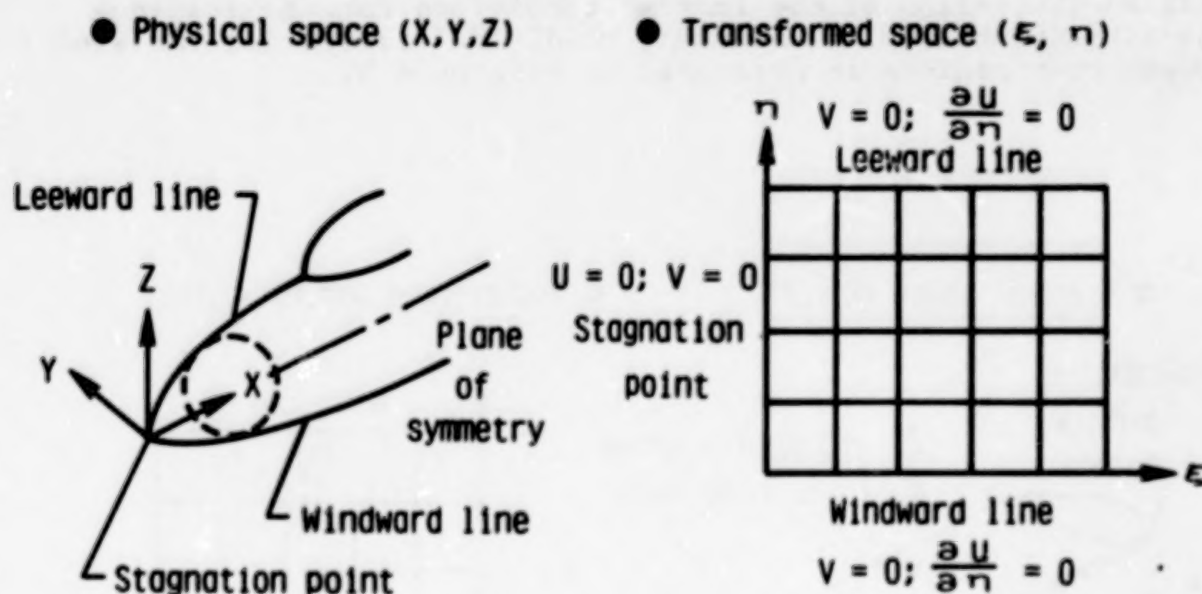


FIGURE 6(A)

BOUNDARY CONDITIONS FOR WING GEOMETRY

Boundary and initial conditions for wing type geometry are somewhat more complex than those for fuselages. A schematic of a typical wing element is presented in figure 6(b) where α and Λ denote the angle of attack and leading-edge sweep, respectively. At angle of attack, the leading-edge attachment line will be displaced from the geometrical leading edge as shown in the sketch. The location of the attachment line is not known a priori and must be obtained by an iterative solution procedure that positions the line such that $u = 0$ to within a specified error bound. This becomes the $\xi = \xi_0$ line in the transformed plane. The remaining initial condition along the $\xi = \xi_0$ line is obtained from the inviscid flow field results (see ref. 9). The boundary conditions along either the root chord or symmetry plane chord and a chord near, but not located at the wing tip, must be specified. The extrapolation conditions shown in the ξ, η plane in figure 6(b) for the wing tip and root chord regions have been used for the results contained in the present material. A more detailed discussion of the initial conditions for the leading-edge attachment line and boundary condition studies for the wing tip and root regions is presented in reference 9.

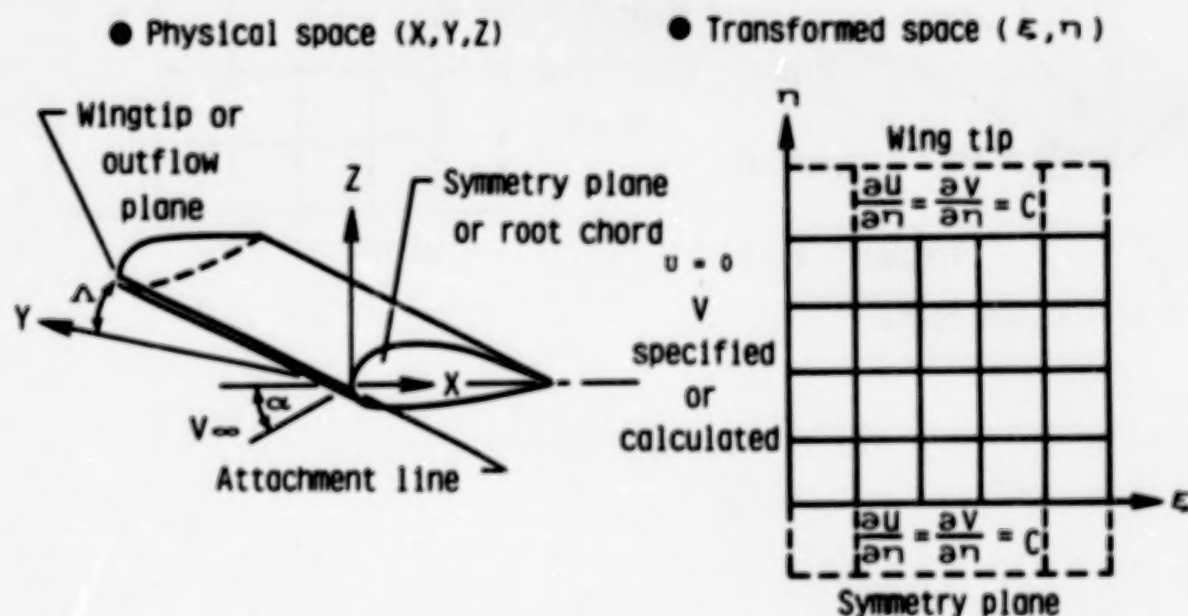


FIGURE 6(B)

NUMERICAL PROCEDURE

As previously mentioned, the surface Euler equations are hyperbolic. In order to satisfy the stability requirement, the difference stencil must be rotated in relation to the cross flow velocity as shown in figure 7(a).

● Difference stencil

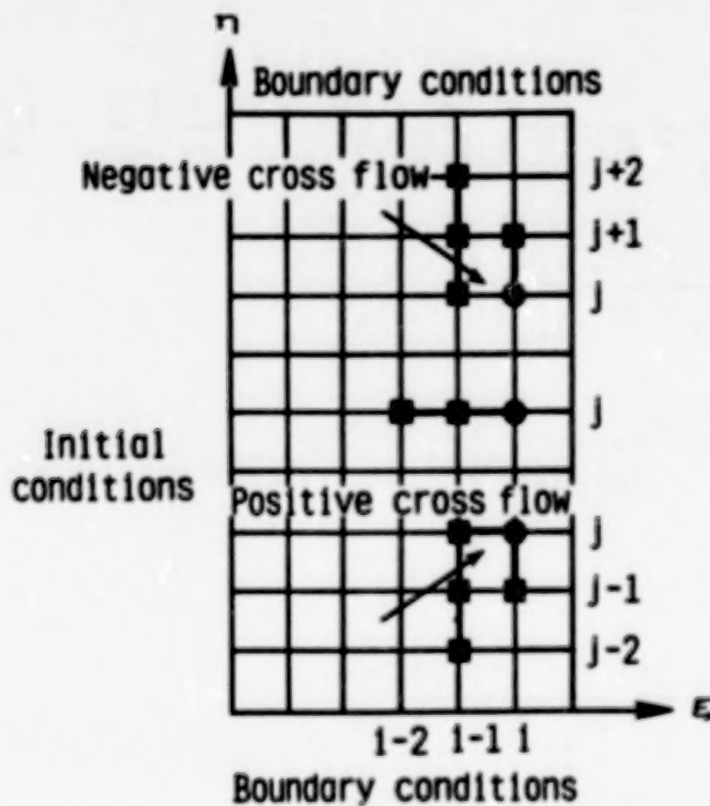


FIGURE 7(A)

DIFFERENCE APPROXIMATIONS

The point upwind differences are used to approximate derivatives with respect to ξ (see fig. 7(b)). For derivatives with respect to η a 5-point stencil is used and rotated to satisfy stability where $e = 1$ for $v < 0$; $e = -1$ for $v > 0$.

Nonlinear terms are treated in an iterative sense by lagging the nonlinear quantity by one iterative step. The final set of discretized equations are "locally block diagonal."

$$\frac{\partial f}{\partial \xi_{1,j}} = \frac{1}{(\xi_{1,j} - \xi_{1-1,j})} \left\{ f_{1,j}(1+g) - \frac{f_{1-1,j}}{(1-g)} + f_{1-2,j} \frac{g^2}{(1-g)} \right\}$$

$$g = \frac{(\xi_{1,j} - \xi_{1-1,j})}{(\xi_{1,j} - \xi_{1-2,j})}$$

$$\frac{\partial f}{\partial \eta_{1,j}} = \frac{1}{(\eta_{1,j} - \eta_{1,j+\epsilon})} \left\{ f_{1,j} - f_{1,j+\epsilon} + \frac{f_{1-1,j} - f_{1-1,j+\epsilon}}{1+\lambda} + \frac{f_{1-1,j+2\epsilon}}{\lambda(1+\lambda)} \right\}$$

$$\lambda = \frac{\eta_{1-1,j+\epsilon} - \eta_{1-1,j+2\epsilon}}{\eta_{1,j} - \eta_{1,j+\epsilon}}$$

$$\epsilon = +1 \quad v < 0$$

$$\epsilon = -1 \quad v > 0$$

FIGURE 7(B)

PRESSURE COEFFICIENT CONTOURS

ORIGINAL PAGE IS
OF POOR QUALITY

A test case of interest to the Langley Research Center's LFC program involves experimental and analytical studies of the stability characteristics of a fuselage forebody shown in figure 8. Figure 8(a) presents contours of the pressure coefficient distribution interpolated from a relatively coarse inviscid solution onto a fine boundary-layer grid. The initial inviscid distribution was obtained using the method of reference 10.

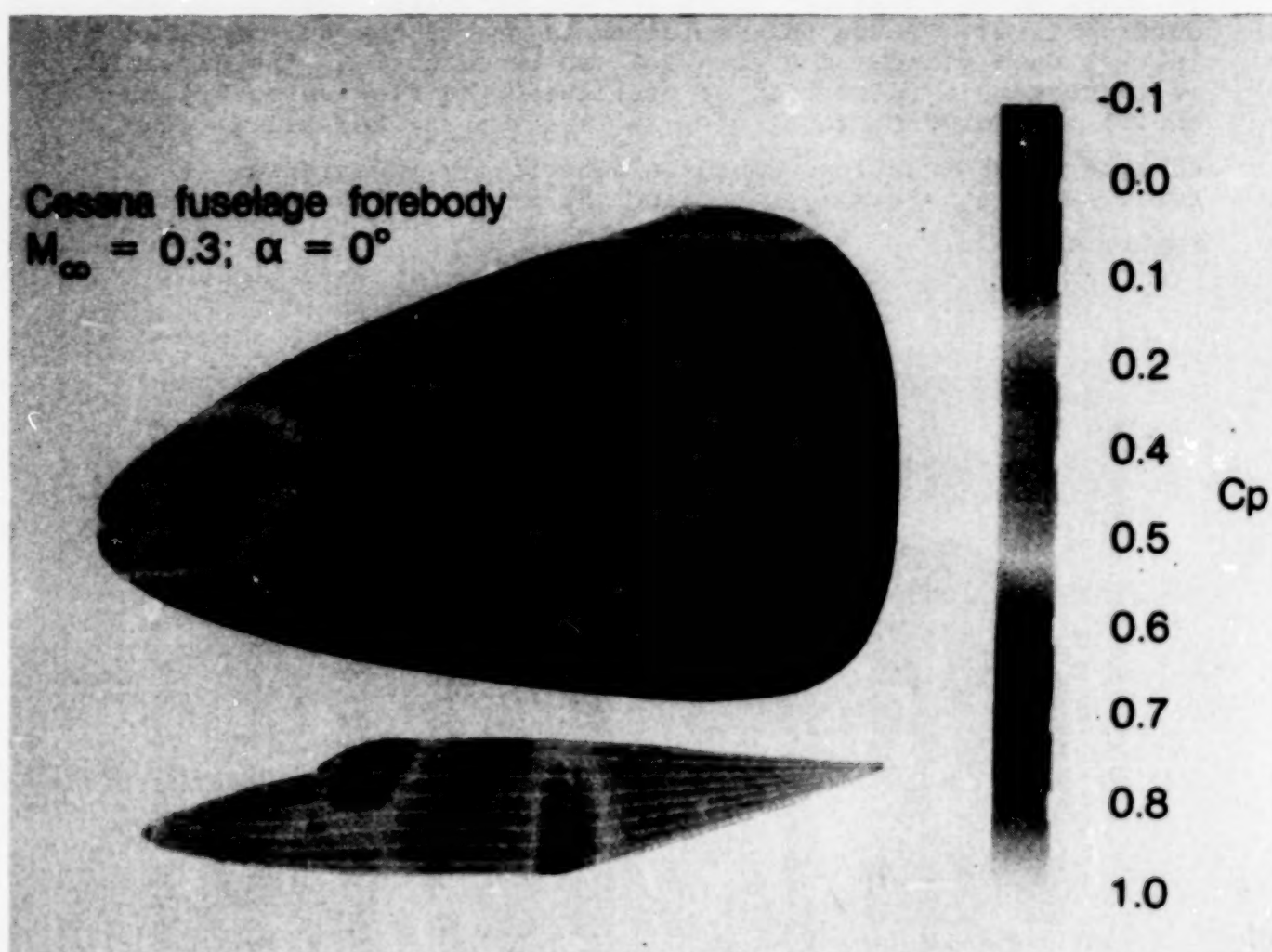


FIGURE 8(A)

ORIGINAL PAGE
BLACK AND WHITE PHOTOGRAPH

INVISCID FLOW-FIELD CONTOURS

The pressure contours in figure 8(a) indicate a smooth and "well behaved" flow field; however, close examination of the cross flow velocity contours in figure 8(b) indicates a physical problem not easily solved by traditional boundary-layer procedures. The solid line on figure 8(b) indicates the locus of a $v = 0$ contour line. In the region above this line $v > 0$ (positive cross flow) while below the line $v < 0$ (negative cross flow). Consequently, both the leeward and windward lines of the plane of symmetry are inflow lines. This presents a severe problem for traditional boundary-layer approaches where one normally obtains a numerical solution of the reduced set of boundary-layer equations along the windward line (generally an outflow line). Using this solution as one of the two required initial data planes, the solution can be marched in the direction of increasing η (direction of positive cross flow velocity) to obtain the solution for $\xi = \xi_1$, $\eta_0 < \eta < \eta_{\max}$, and all ζ . The surface Euler equations could be numerically integrated for $\xi = \xi_1$, $\eta_0 < \eta < \eta_{\max}$ because the entire η -line was treated implicitly.

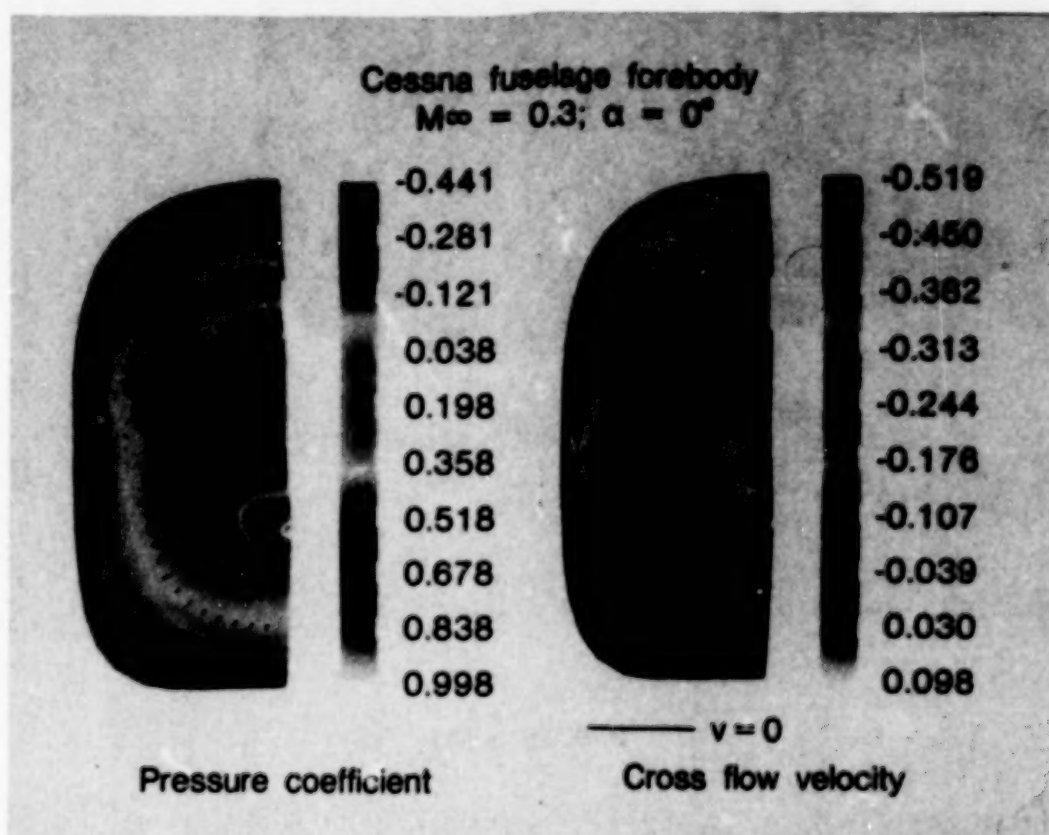


FIGURE 8(B)

SURFACE EULER VERSUS STANDARD INTERPOLATION

Comparisons of interpolated u and v values with those obtained from solving the surface Euler equations are presented in figure 9. The interpolated values were carefully smoothed to get the results presented in figure 9(a) as opposed to no smoothing for the velocity field obtained from the surface Euler equations. In addition, the interpolated values are not consistent.

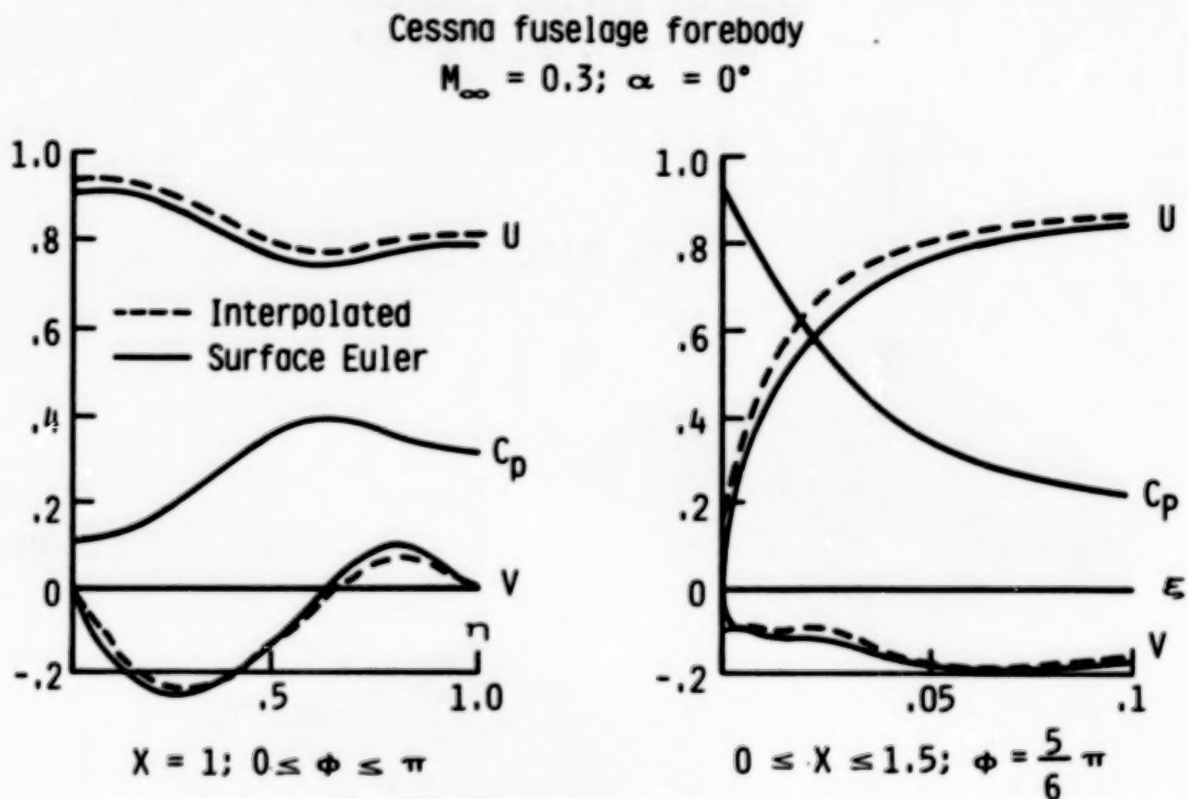


FIGURE 9(A)

CROSS FLOW VELOCITY CONTOURS

The carpet plots of cross flow velocity presented in figure 9(b) are indicative of oscillations resulting from interpolation of the velocity components. Stability theory is critically sensitive to oscillations of cross flow velocity; consequently, the surface Euler approach should be used to obtain smooth and consistent input data for the boundary-layer solution.

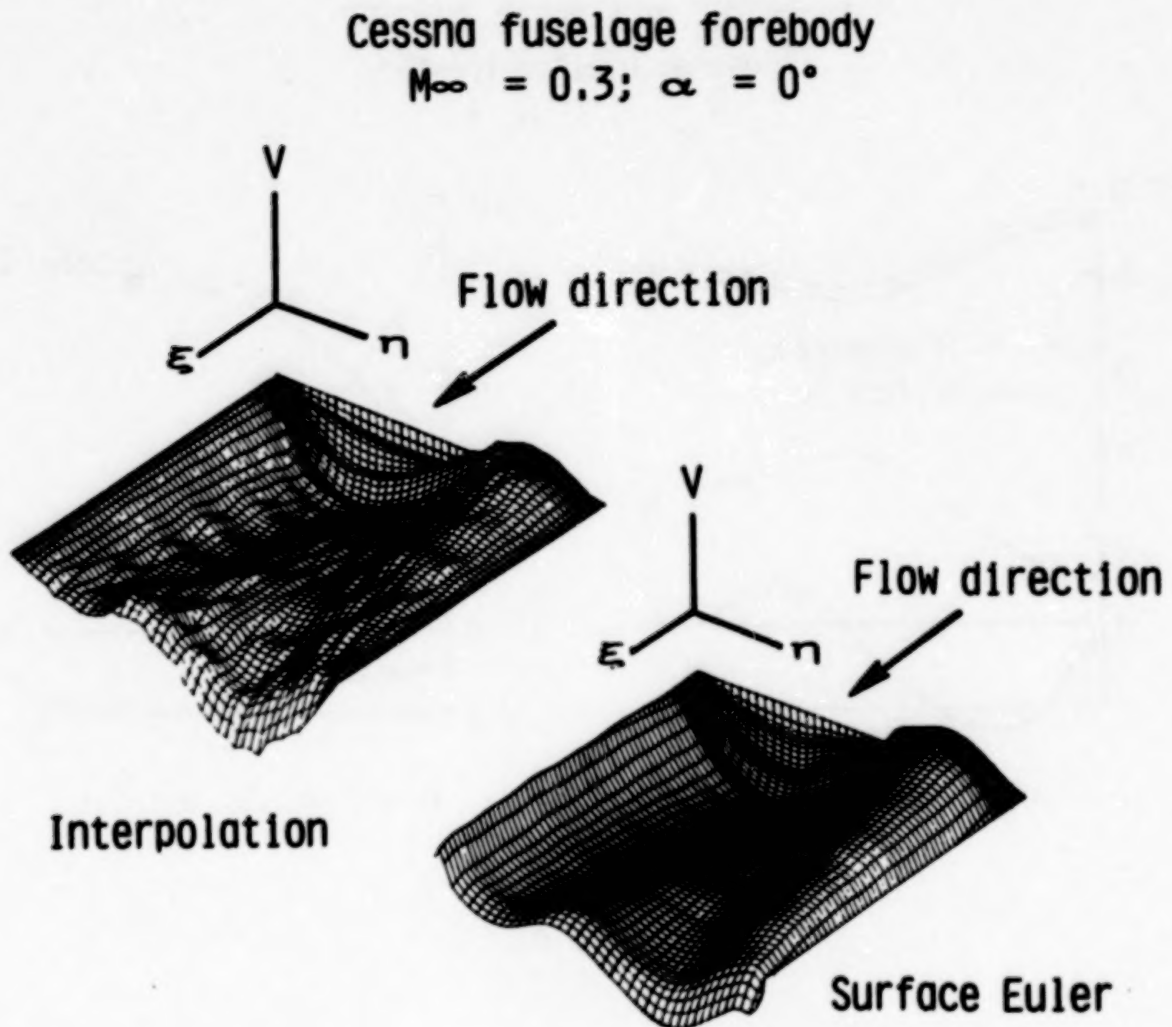


FIGURE 9(B)

COMPARISON OF SURFACE EULER WITH INTERPOLATION

Numerical results are presented in figure 10 for a wing having an NACA-0012 airfoil section. The inviscid flow field was obtained using the method of reference 10. Comparisons of the interpolated and smoothed streamwise velocity are compared with surface Euler results in figure 10(a). The agreement in magnitude appears to be satisfactory with the exception of a region just downstream of the leading-edge attachment line. The agreement appears to be independent of span location.

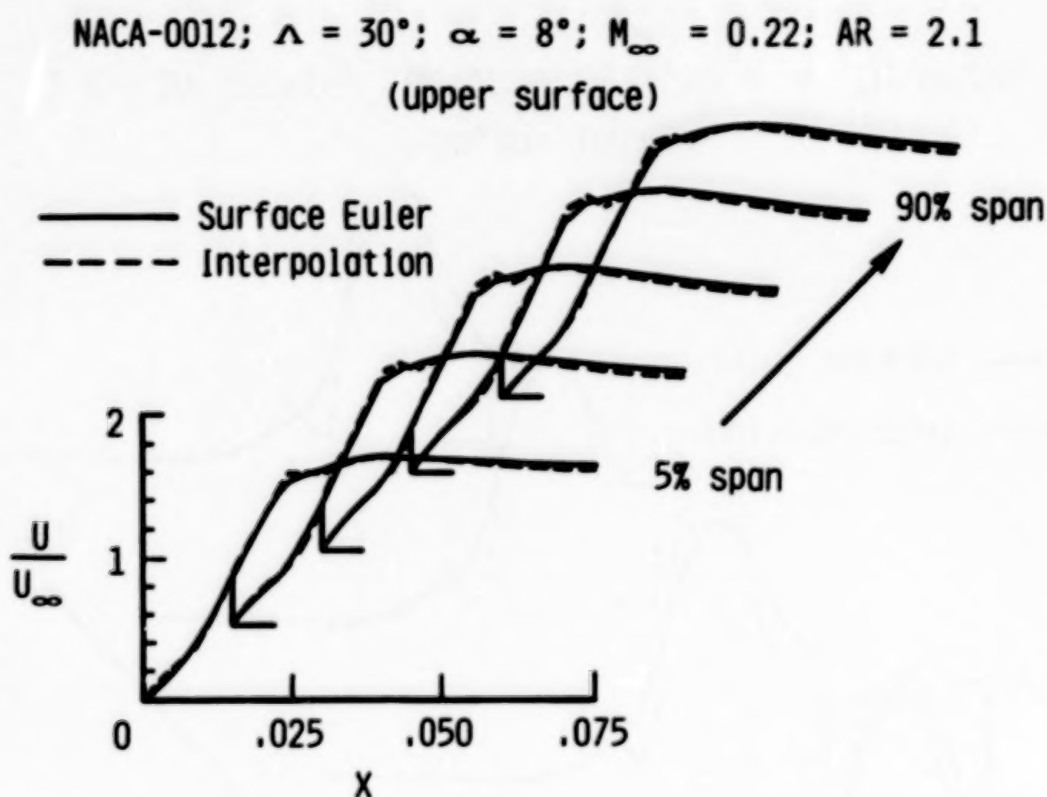


FIGURE 10(A)

COMPARISON OF SURFACE EULER WITH INTERPOLATION

The stability equations will be integrated forward in space beginning at the leading-edge attachment line. A closer examination of the results presented in figure 10(a) is presented as a derivative with respect to x in figure 10(b). The oscillation in $\partial \tilde{U} / \partial \xi$ presented in figure 10(b) for the interpolated values is not acceptable. It can be seen that the surface Euler equations yield smooth values of $\partial \tilde{U} / \partial \xi$ without requiring smoothing. These values are consistent with the governing equations.

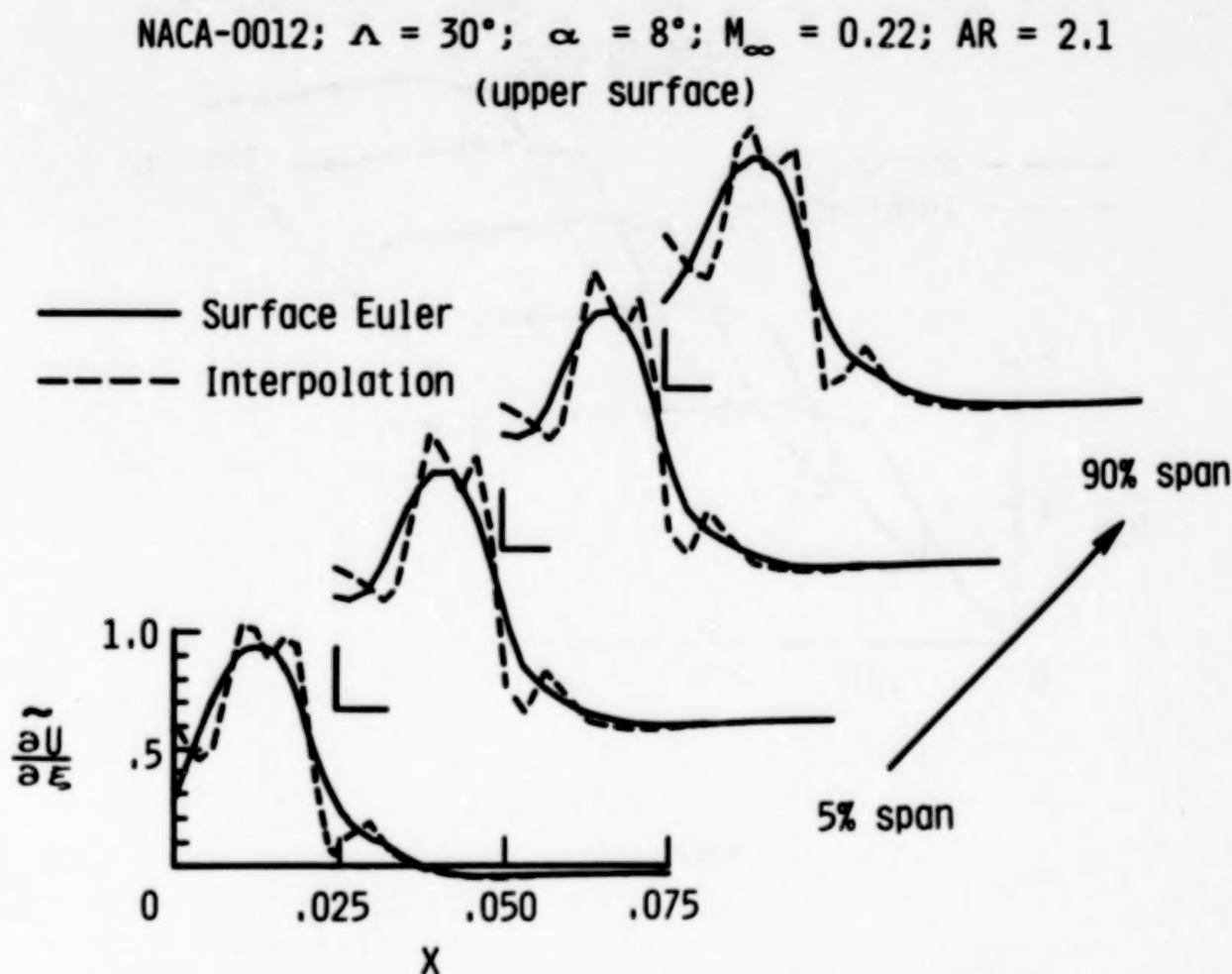


FIGURE 10(B)

THREE-DIMENSIONAL BOUNDARY-LAYER SYSTEM

Researchers involved in the numerical aspects of LFC are familiar with the three-dimensional boundary-layer equations; consequently, the equations are not presented. Readers interested in the equations are referred to references 1 through 5. Certain characteristics of the system are presented in figure 11 and warrant further discussion.

The system consists of four nonlinear partial-differential equations (PDEs) of mixed type. The system is hyperbolic in planes parallel to the boundary surface (ξ, η planes) and parabolic in the direction normal to these planes.

For perfect gas flow, the system is closed with algebraic equations for state and viscosity. The unknowns are u, v, w, T and ρ representing the velocity components in the ξ, η, ζ directions, static temperature and density, respectively. Pressure is constant normal to the wall boundary.

The present work focuses on laminar flow; however, the software has been structured to model the turbulent terms using eddy viscosity and eddy conductivity closure. Careful studies will be made in this area at some future date. This would allow a uniform approach for boundary-layer calculations to be developed for laminar, transitional, and turbulent flows.

● Equations

- | | | |
|----------------------|---|---------------|
| ● Continuity | } | Nonlinear PDE |
| ● Momentum (2; X, Y) | | |
| ● Energy | | |
| ● State; viscosity | } | Algebraic |

● Turbulence

- | | | |
|------------------------------------|---|---------------------|
| ● Eddy viscosity/eddy conductivity | } | Not LFC requirement |
|------------------------------------|---|---------------------|

FIGURE 11(A)

THREE-DIMENSIONAL BOUNDARY-LAYER SYSTEM

Boundary conditions have been treated as generally as possible. Wall mass transfer can be specified together with either wall temperature or heat transfer distributions. Edge values are obtained from the interface software solutions of the surface Euler equations. Initial values can currently be generated for fuselage and wing geometries. The reader interested in the special equation sets for the initial value planes is referred to reference 5.

- Boundary conditions

- Wall boundary

- $U; V$ (no slip)
 - $W_w = W_w(X, Y)$
 - $T_w = T_w(X, Y)$
or $q_w = q_w(X, Y)$

- Edge values

- Surface Euler system

- Initial values

- Fuselage "type" geometry

- 3-D stagnation point
 - Symmetry plane

- Wing "type" geometry

- Leading edge attachment line
 - Symmetry plane
 - Root chord approximation

FIGURE 11(B)

NUMERICAL SCHEME

The difference stencil together with a sketch depicting the Raetz influence principle (ref. 5), and the difference approximations are presented in figure 12(a). Two separate stencils are used for convective derivatives in the ξ, η -plane. The particular stencil utilized at each ζ point depends upon the sign of the cross flow velocity. For negative cross flow the Krause et al. (ref. 11) zig-zag scheme is used to satisfy the zone of influence principle.

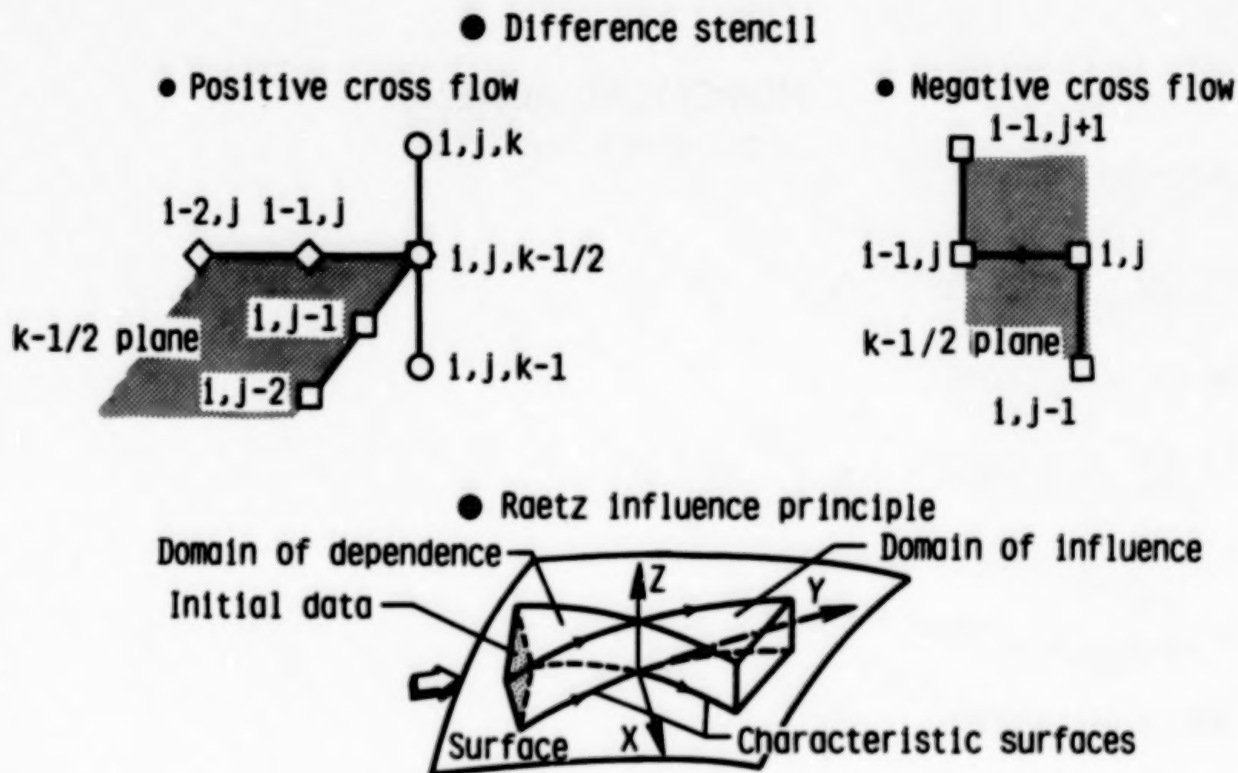


FIGURE 12 (A)

DIFFERENCE APPROXIMATIONS

The difference approximations are presented in figure 12(b). The approximations are second-order accurate in planes parallel to the wall and fourth-order accurate in the direction normal to the wall boundary. In the planes parallel to the wall, a weighted three-point upwind scheme is used to approximate the convective partial-derivatives (see ref. 12).

In the direction normal to the wall boundary, a 2-point compact scheme with fourth-order accuracy is used (see refs. 13 and 14).

NUMERICAL SCHEME

Difference relations

● ξ - derivatives

$$\frac{\partial \phi}{\partial \xi}_{1,j}^{k-\frac{1}{2}} = (a_1 \phi_1 + a_2 \phi_{1-1} + a_3 \phi_{1-2})_j^{k-\frac{1}{2}}$$

● η - derivatives

$$\frac{\partial \phi}{\partial \eta}_{1,j}^{k-\frac{1}{2}} = (b_1 \phi_j + b_2 \phi_{j-1} + b_3 \phi_{j-2}) \quad v > 0$$

$$\frac{\partial \phi}{\partial \eta}_{1,j}^{k-\frac{1}{2}} = (c_1 \phi_{j-1} + c_2 \phi_j)_1^{k-\frac{1}{2}} + (c_3 \phi_j + c_4 \phi_{j+1})_1^{k-\frac{1}{2}} \quad v < 0$$

● ζ = derivatives

$$(\bar{q}^k - \bar{q}^{k-1})_{1,j} - \Delta \zeta (g_1 \bar{q}^k + g_2 \bar{q}^{k-1})_{1,j} - \Delta J^2 (g_3 \bar{q}^k + g_4 \bar{q}^{k-1})_{1,j} = O(\Delta \zeta)^4$$

where

$\bar{q}_{1,j}^k$ = Solution vector

FIGURE 12 (B)

SOLUTION TECHNIQUE

Substitution of the difference relations into the transformed governing equations yields a set of seven nonlinear, coupled difference equations in seven unknowns (see fig. 13). Newton's method is used to linearize the system. The linearized system is solved using an efficient block-tridiagonal matrix inversion based on LU factorization.

The two momentum equations yield a 4x4 block tridiagonal system in F , F' , G , G' , where $F = u/u_e$, $G = v/v_e$, $F' = \partial F / \partial \zeta$ and $G' = \partial G / \partial \zeta$. The energy equation yields a 2x2 block for H and H' . The normal component of velocity, w is updated from the finite-difference form of the continuity equation. The system is solved in an iterative loop until convergence is obtained within a fixed error bound.

- Difference equations are coupled and nonlinear
- Newton's method used for linearization

$$\bar{Q}^P = \bar{Q}^{P-1} + \delta \bar{Q}^{P-1}$$

- The linearized system of equations in δQ forms a block tri-diagonal system of the form

$$\{A\} \delta \bar{Q}^{k-1} + \{B\} \delta \bar{Q}^k + \{C\} \delta \bar{Q}^{k+1} = \bar{R}^k$$

Where

$\{A\}$, ..., $\{C\}$ are block matrices of system

\bar{Q} is solution vector

4 x 4 block tri-diagonal for momentum eqs

2 x 2 block tri-diagonal for energy eq

w updated from difference form of continuity eq

FIGURE 13

ACCURACY OF METHOD

The results of a study of the accuracy of the numerical scheme together with the effect of the number of grid points normal to the wall boundary for a fixed ζ_{\max} are presented in figure 14. The truncation error study for Blasius flow clearly indicates a slope of 4 to 1 as compared with 2 to 1 for the second-order scheme of reference 12.

The numerical advantage of the fourth-order method is shown for 3-D stagnation point flow where streamwise velocity profiles (u/u_e) are presented for a fixed ζ_{\max} for 40, 16, and 8 points normal to the wall boundary (note that only a sample of the computed points is presented for clarity). Comparisons of the results for NPZ = 8 with NPZ = 40 indicate that the correct profile values can be predicted with as few as 8 points. This comparison represents a speed/storage advantage of 5 to 1.

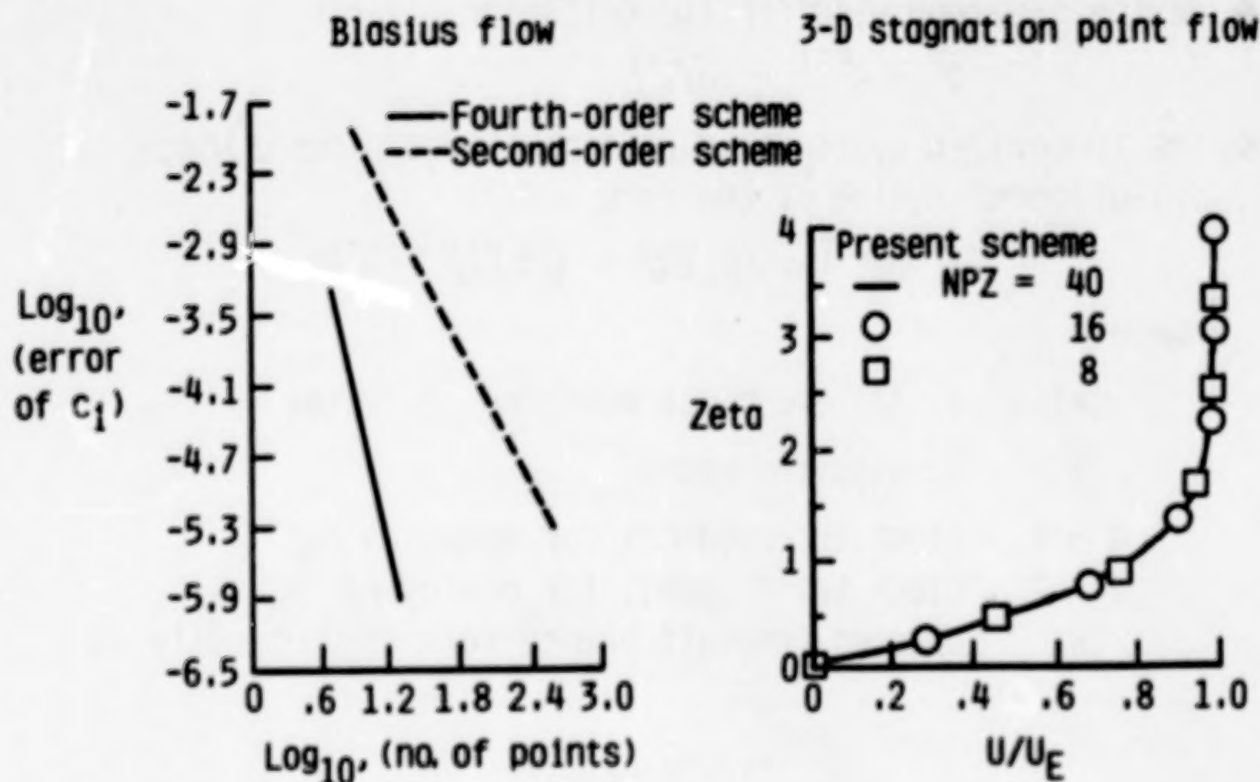


FIGURE 14

CYLINDER ON FLAT PLATE

Numerical results for incompressible flow past a cylinder mounted normal to a flat plate are presented in figure 15. Total and cross flow velocity profiles are presented for 50, 25, and 12 points normal to the wall as well as compared with the second-order theory of reference 12. The present fourth-order method produces excellent results for as few as 12 grid points normal to the wall boundary for this test problem.

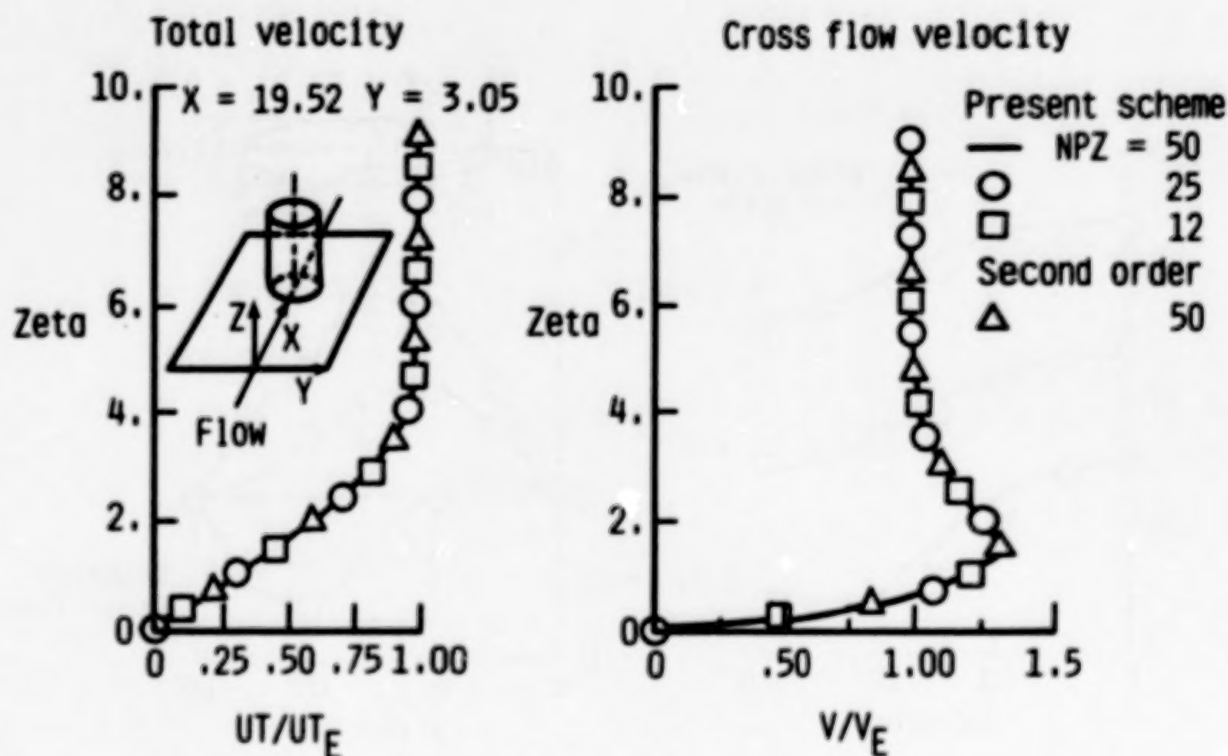


FIGURE 15

PROLATE SPHEROID AT ANGLE OF ATTACK

Numerical results for F'_w and G'_w for incompressible flow past a prolate spheroid at 8° angle of attack is presented in figure 16. The results are presented for three x locations where η varies from 0° on the most windward line of symmetry to 180° on the leeward line. Of particular importance is the reverse region of cross flow: $G'_w < 0$; $x = 1.52$; $60^\circ < \eta < 180^\circ$ (note that $G'_w = (\partial G / \partial \zeta)_w$; $G = v/v_e$).

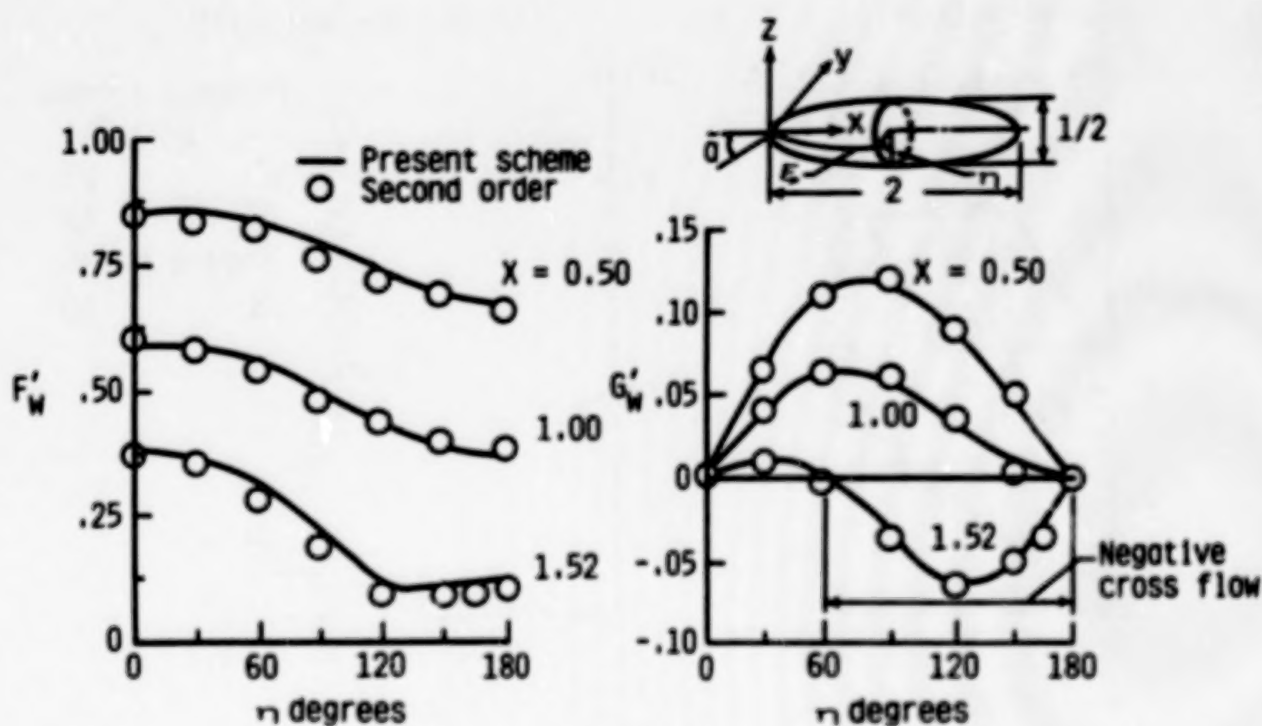


FIGURE 16

SWEPT WING FLOW

The final swept wing flow test case presented is for a wing having an NACA-0012 airfoil section. A schematic of the geometry and test conditions is presented in figure 17(a) together with calculated values of the chordwise (ξ) and spanwise (η) skin friction coefficients.

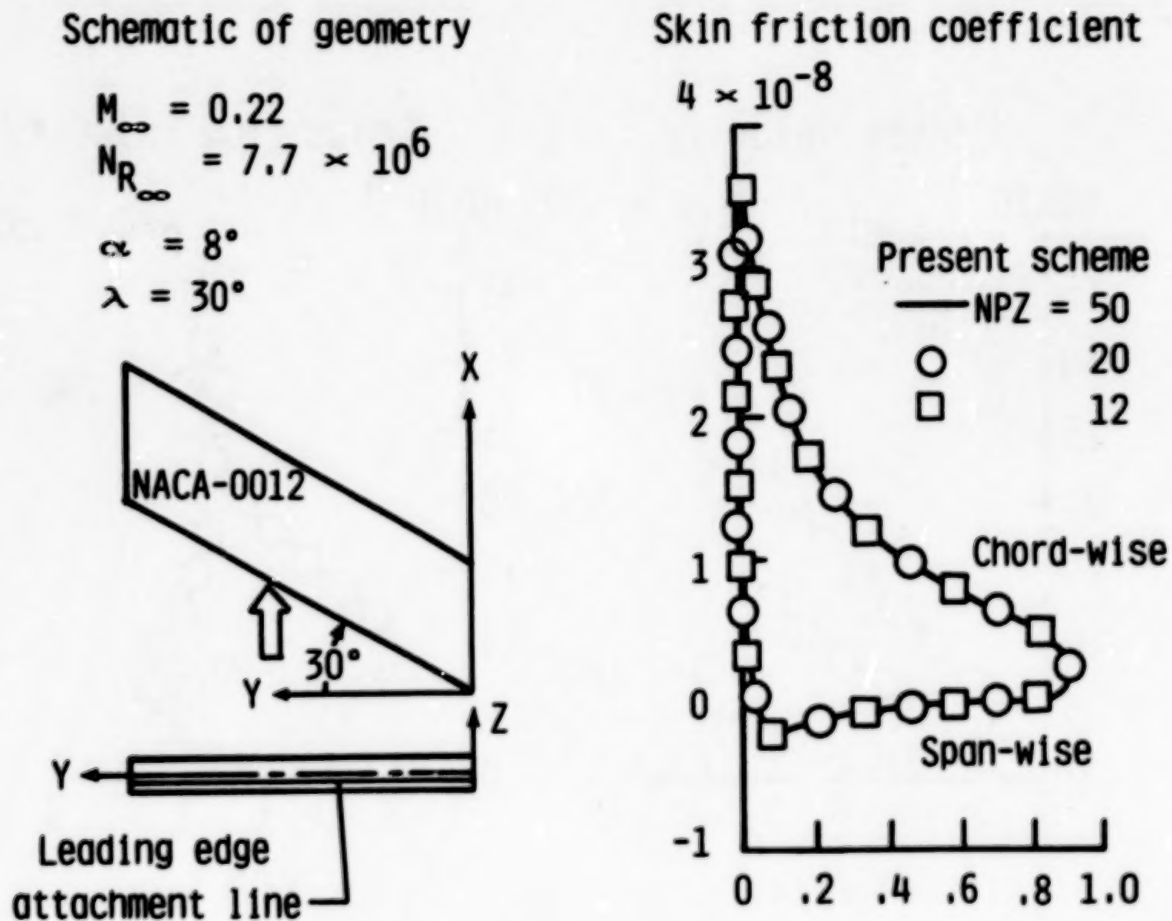


FIGURE 17 (A)

SWEPT WING FLOW: VELOCITY PROFILES

Calculated total and cross flow velocity profiles are presented in figure 17(b). The numerical results were obtained for grid point distributions normal to the wall boundary of 12, 20, and 50 points. The profile calculations are presented at chord stations of 0, 50, and 90 percent. The present fourth-order method obtained accurate results with as few as 12 points normal to the wall boundary.

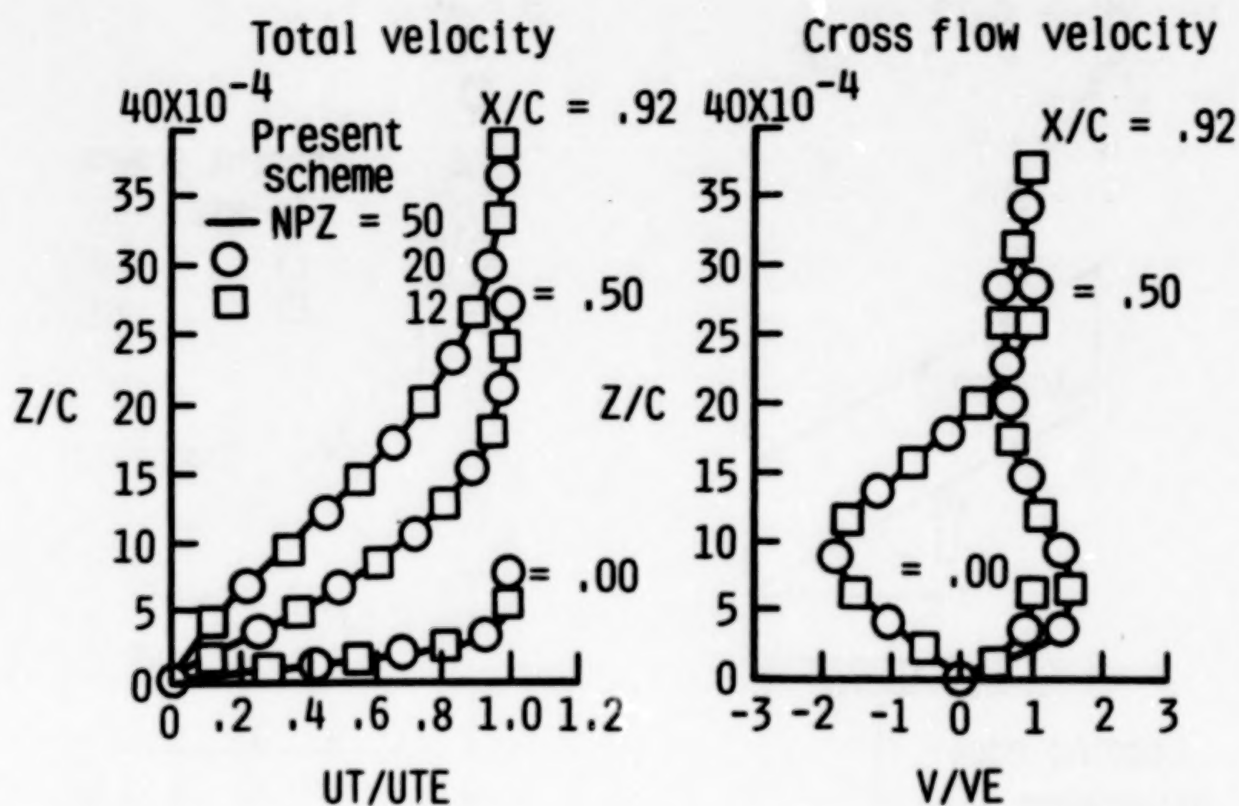


FIGURE 17(B)

CONCLUDING REMARKS

In concluding, the current software package (interface software; boundary-layer software) is operational and has been tested for several 3-D flows (see figure 18).

The interface program has been found to be a dependable approach for developing a user friendly procedure for generating the boundary-layer grid and transforming an inviscid solution from a relatively coarse grid to a sufficiently fine boundary-layer grid. The surface Euler equations used for this procedure yield smooth inviscid velocity components and gradients along the boundary-layer coordinate lines. These data are consistent with the governing equations in satisfying the boundary-layer equations in the limit as the distance normal to the wall boundary becomes very large. The interface program will eventually function as the iterative link between the selected inviscid software and the boundary-layer software for inviscid/viscous interactions studies.

The boundary-layer program has been shown to be fourth-order accurate in the direction normal to the wall boundary and second-order accurate in planes parallel to the boundary. The fourth-order accuracy allows accurate calculations with as few as one-fifth the number of grid points required for conventional second-order schemes.

- Basic programs have been developed and verified for several test cases
 - Surface Euler equation approach yields smooth and consistent inviscid edge data
 - Boundary-layer procedure has been verified as computationally efficient with fourth order accuracy

FIGURE 18

REFERENCES

1. McLean, J. D.; and Randall, J. L.: Computer Program to Calculate Three-Dimensional Boundary Layer Flows Over Wings with Wall Mass Transfer. NASA CR-3123, 1979.
2. Cebeci, T. Kaups, K.; Ramsey, J.: A General Method for Calculating Three-Dimensional Compressible Laminar and Turbulent Boundary Layers on Arbitrary Wings. NASA CR-2777, 1977.
3. Anderson, O. L.: Assessment of a 3-D Boundary Layer Analysis to Predict Heat Transfer and Flow Field in a Turbine Passage. NASA CR-174894, 1985.
4. Tassa, A.; Atta, E. H.; and Lemmerman, L. A.: A New Three-Dimensional Boundary Layer Calculation Method. AIAA-82-0224.
5. Hirschel, E. H.; and Kordulla, W.: Shear Flow in Surface-Oriented Coordinate. Notes on Numerical Fluid Mechanics, vol. 4, Friedr. Vieweg & Son, Braunschweig/Wiesbaden, 1981.
6. Cebeci, T.; and Meier, H. U.: A Note on the Specification of Freestream Velocity in the Calculation of the Boundary Layer Flow Around Bodies of Revolution at Incidence. Z. Flugwiss, Weltraumforsch 6 (1982), Heft 6, p. 416-418.
7. Vollmers, H.: Integration of Streamlines from Measured Static Pressure Fields on a Surface. AIAA 82-4236.
8. Gleyzes, C.; and Cousteix, J.: Calculation of Streamlines from Wall Pressures on a Fusiform Body. Rech. Aerosp., 1984-3, pp. 69-77.
9. Iyer, V.; and Harris, J. E.: Solution of the Surface Euler Equations for Accurate Three-Dimensional Boundary-Layer Analysis of Aerodynamic Configurations. AIAA 87-1154-CP.
10. Hess, J. L.: Calculation of Potential Flow About Arbitrary 3-D Lifting Bodies. McDonnell Douglas, MDC J5679-01, 1972.
11. Krause, E.; Hirschel, E.; and Boltman, : Numerical Stability of Three-Dimensional Boundary-Layer Solutions. Z Angew Math. and Mech., vol. 48, no. 8, pp. 205-208, 1968.
12. Radwan, S. F.; and Lekoudis, S. G.: Calculations of the Incompressible Turbulent Boundary Layer on an Ellipsoid in the Inverse Mode. AIAA Paper No. 85-1654.
13. Wornom, S. F.: Critical Study of Higher Order Numerical Methods for Solving the Boundary Layer Equations. NASA TP-1302, 1978.

14. Linger, W.; and Willoughby, R. A.: Efficient Integration Methods for Stiff Systems of Ordinary Differential Equations. SIAM J., Numer. Analysis, vol. 7, no. 1, March 1970.

**THEORETICAL METHODS AND DESIGN STUDIES FOR NLF AND HLFC
SWEPT WINGS AT SUBSONIC AND SUPERSONIC SPEEDS**

**Suresh H. Goradia
Vigyan Research Associates
Hampton, Virginia**

**Harry L. Morgan, Jr.
NASA Langley Research Center
Hampton, Virginia**

INTRODUCTION

Laminarization of the boundary layer on the surface of aircraft wings can be accomplished by the use of concepts such as Natural Laminar Flow (NLF), Laminar-Flow Control (LFC) which uses suction over the entire surface of the wing, and Hybrid Laminar-Flow Control (HLFC) which uses suction only over 15 to 20 percent of the wing upper surface near the leading edge. The experimental data obtained at NASA Langley for the LFC wing have demonstrated that substantial reductions in wing profile drag can be obtained at transonic Mach numbers by the use of suction over the entire surface of the airfoil.¹ This drag reduction is primarily the result of the presence of laminar boundary-layer flow over a large portion of the airfoil surface.

Extension regions of laminar flow can also be maintained on wing surfaces with the NLF concept, which involves the appropriate choice of pressure distribution to limit the amplification of the disturbances that trigger the transition of the laminar boundary layer to a turbulent boundary layer. Flight tests at the Dryden Flight Research Center on a variable sweep TACT F-111 fighter aircraft with an NLF wing glove have shown that laminar flow can be maintained over a large portion of the wing surface at transonic speeds.² However, NLF is restricted to flight applications at low Reynolds number conditions and to wings with relatively low sweep angles.

HLFC which combines the features of both LFC and NLF applies suction forward of the front wing-box spar to prevent the transition of the laminar boundary layer due to cross-flow and attachment-line instabilities that occur on swept wings. Laminar boundary-layer flow is maintained aft of the front spar by the selection of a pressure distribution which suppresses the growth of the disturbances due to Tollmien-Schlichting waves or due to cross flow. Although the extent of laminar flow is less for HLFC than for LFC, the conventional wing box structure can be retained and the mechanical complexities are not as great.

The design of the HLFC wing sections to minimize the wake drag requires the optimization of the drag due to laminar skin-friction and the turbulent boundary-layer separation. The trailing-edge recovery pressure is fixed due to the Kutta condition for subsonic and transonic flow and the aft pressure gradient, free-stream Reynolds number, and forward suction levels determine whether or not the turbulent flow will remain attached close to the trailing edge. Examination of existing experimental data on the LFC wing has shown that if turbulent separation occurs upstream of the 95-percent chord position on either the upper or lower wing surfaces, a pressure distribution necessary to maintain laminar flow cannot be realized. Therefore, the design of HLFC wings sections necessitates the use of reliable theoretical methods which accurately predict the locations of laminar boundary-layer transition and turbulent boundary-layer separation.

Several finite-difference boundary layer, stability, and full Navier-Stokes equation solvers are available and have produced very encouraging results. However, these methods are not well suited for the routine optimization studies that were performed during the design of the HLFC wing section. Several new integral boundary-layer methods, which are applicable to swept wings with varying amounts of surface suction, have been developed for the prediction of laminar, transition, and separating turbulent boundary layers. These methods have been developed for use at either subsonic or supersonic speeds, have small computer execution times, and are simple to use. The purpose of this presentation is to briefly outline the theoretical equations and assumptions which form the basis of these boundary-layer

methods and to present the results of several correlation cases with existing experimental data. The results of the application of these methods to the design of the HLFC wing scheduled to be tested in the Langley 8-Foot Transonic Pressure Tunnel will also be presented.

THEORETICAL METHODS USED DURING DESIGN OF HLFC WING

The theoretical methods used during the design and analysis of the HLFC wing are listed in figure 1 and are classified as 1) potential/viscous design and analysis, 2) boundary-layer analysis, 3) wake and suction drag computations, and 4) a modified strip method for finite wings.

Design of the upper surface of the HLFC wing in the local supersonic region at the design transonic free-stream Mach number was performed using the Perturbation Method of Characteristics technique.³ Modifications to the HLFC airfoil section were analyzed at transonic conditions using the Korn/Garabedian airfoil code⁴ and at subsonic conditions using the Multi-Component (MCARF) airfoil code.⁵

Analysis of design modifications on the viscous characteristics of the HLFC wing were performed using several recently developed integral boundary-layer methods. These methods consist of 1) an integral compressible laminar boundary-layer method for swept wings in the presence of suction at subsonic and supersonic speeds,⁶ 2) criteria for prediction of laminar boundary-layer separation and reattachment,⁶ 3) criteria for prediction of the location transition due to either the amplification of Tollmien-Schlichting waves, cross flow, or leading-edge contamination, and 4) new integral separating turbulent boundary layer.⁷

Theoretical methods were also developed to determine the effect of design modifications on the drag characteristics of the HLFC wing. These methods account for both the changes in the wake drag and suction drag as a result of applying suction on the upper surface leading-edge region of the HLFC airfoil.

A modified strip method was developed during this design study to account for the finite and swept wing properties of the HLFC wing. This strip method also accounts for taper and both spanwise and chordwise pressure gradients.

● Potential/viscous design and analysis

- Perturbation method of characteristics for inverse design at transonic speeds
- BGK (Bauer-Garabedian-Korn) for transonic analysis
- MCARF for subsonic analysis

● Boundary-layer analysis

- Integral compressible laminar boundary layer with sweep and suction at subsonic thru supersonic speeds
- Short bubble and reattachment criteria
- T.S. and C.F. transition criteria
- Separating turbulent boundary layer method (AIAA 86-1832-CP)

● $C_{D, wake}$ and $C_{D, suction}$

● Modified strip method

Figure 1

GOVERNING EQUATIONS

The usual governing equations for compressible hydrodynamic laminar boundary-layer flow which consist of the continuity, streamwise-momentum, normal-momentum, and cross-flow-momentum equations are presented in figure 2. These equations contain the terms consisting of variable physical properties, such as, density, ρ , and dynamic viscosity, μ . The values of these physical properties vary across the boundary layer as well as along the flow direction, and these variations are non-negligible for boundary-layer flow at transonic speeds. At supersonic speeds, these variations in the physical properties of fluid within the boundary layer are quite appreciable. This means that there is a strong coupling between solutions of hydrodynamic and thermal boundary-layer equations at high transonic and supersonic speeds.

In order to simplify the governing equations for solution by integral techniques while maintaining realistic, computational results for the hydrodynamic and thermal boundary layers, Stewartson's transformations are used. These transformations reformulate the boundary-layer equations of motions into a transformed plane which is independent of the varying physical properties of fluid. The relations between the velocities in the transformed and physical planes are also shown in figure 2.

GOVERNING EQUATIONS AND TRANSFORMATIONS

GOVERNING EQUATIONS

$$\frac{\partial}{\partial s} (\rho u) + \frac{\partial}{\partial \xi} (\rho v) + \frac{\partial}{\partial z} (\rho w) = 0 \text{ (Continuity)}$$

$$\rho u \frac{\partial u}{\partial s} + \rho v \frac{\partial u}{\partial \xi} + \rho w \frac{\partial u}{\partial z} = - \frac{dP}{ds} + \frac{\partial}{\partial \xi} \left(\mu \frac{\partial u}{\partial \xi} \right) \text{ (Streamwise Momentum)}$$

$$\frac{\partial P}{\partial \xi} = 0 \text{ (Normal Momentum)}$$

$$\rho u \frac{\partial w}{\partial s} + \rho v \frac{\partial w}{\partial \xi} + \rho w \frac{\partial w}{\partial z} = - \frac{\partial P}{\partial z} + \frac{\partial}{\partial \xi} \left(\mu \frac{\partial w}{\partial \xi} \right) \text{ (Crossflow Momentum)}$$

Stewartson's Transformation

$$X = \int_0^s \frac{\rho_0 P_0}{\rho P} ds; \quad Y = \frac{\rho_0}{\rho} \int_0^\xi \frac{\rho}{P_0} d\xi$$

Relation Between Velocities in Physical and Transformed Planes

$$U = \frac{\rho_0}{\rho} u; \quad V = \frac{\rho_0}{\rho} v \text{ for } P_r = 1; \quad W = w$$

Figure 2

TRANSFORMED BOUNDARY-LAYER EQUATIONS AND BOUNDARY CONDITIONS

The transformed boundary-layer equations using Stewartson's transformations are presented in figure 3. These transformed boundary-layer equations are applicable to infinite swept wings. The relation between the pressure gradient in the transformed and physical planes and the transformed boundary conditions needed to derive the integral equations is also shown. The several groups of physical dimensionless parameters used in the development of the integral compressible boundary-layer method are also presented. The subscript "w" indicates that the parameter is defined at the wall.

TRANSFORMED BOUNDARY LAYER EQUATIONS

$$\frac{\partial U}{\partial X} + \frac{\partial V}{\partial Y} = 0$$

$$U \frac{\partial U}{\partial X} + V \frac{\partial U}{\partial Y} = U_e \frac{dU_e}{dX} + v_o \frac{\partial^2 U}{\partial Y^2}$$

$$U \frac{\partial W}{\partial X} + V \frac{\partial W}{\partial Y} = v_o \frac{\partial^2 W}{\partial Y^2}$$

$$\frac{dU_e}{dX} = \frac{1}{\lambda} a_o \frac{dM_e}{ds} \left(1 + \frac{\gamma - 1}{2} M_e^2\right)^{1/2}$$

where $\lambda = \left(\frac{T_w}{T_o}\right)^{1/2} \left(\frac{T_o + 198.6}{T_w + 198.6}\right)$ and $\frac{\mu}{\mu_o} = \lambda \frac{T}{T_o}$

Boundary Conditions in Transformed Plane

$$\text{at } Y = 0: U = W = 0, V = V_s = -\frac{a_o}{a_e} v_o$$

$$\text{at } Y = \delta_s: U = U_e = a_o M_e, \frac{\partial U}{\partial Y} = \frac{\partial^2 U}{\partial Y^2} = 0$$

$$\text{at } Y = \delta_z: W = W_e = w_e, \frac{\partial W}{\partial Y} = \frac{\partial^2 W}{\partial Y^2} = 0$$

Define

$$L = \frac{a_o}{U_e} \left(\frac{\partial U}{\partial Y}\right)_w; S = \frac{V_s a_o}{v_o}; K = \frac{a_o^2}{v_o} \frac{dU_e}{dX}$$

$$M = \frac{a_o^2}{U_e} \left(\frac{\partial^2 U}{\partial Y^2}\right)_w; N = \frac{a_o^3}{U_e} \left(\frac{\partial^3 U}{\partial Y^3}\right)_w$$

Figure 3

COMPATIBILITY CONDITIONS AND STREAMWISE MOMENTUM-INTEGRAL EQUATION WITH SUCTION

The compatibility conditions used to derive the integral boundary-layer equations are presented in figure 4. The streamwise momentum-integral equation with suction included was derived by integrating the transformed boundary-layer equations from the wall to the edge of the boundary layer and by making use of Leibnitz's rule. Furthermore, by making use of the dimensionless parameters defined on figure 3, a set of simultaneous equations is derived for the solution for the boundary-layer momentum thickness and form factor in the transformed plane in the presence of suction. The form of function $F(S, K_s)$ is derived by the curve fit of the exact solution results for the Falkner-Skan type flow in the presence of suction.

Compatibility Conditions

$$\begin{aligned} \text{at } Y = 0: & -V_s \left(\frac{\partial U}{\partial Y} \right)_w = U_e \frac{dU_e}{dX} + v_o \left(\frac{\partial^2 U}{\partial Y^2} \right)_w \\ \text{at } Y = 0: & -V_s \left(\frac{\partial^2 U}{\partial Y^2} \right)_w = v_o \left(\frac{\partial^3 U}{\partial Y^3} \right)_w \\ \text{at } Y = 0: & -V_s \left(\frac{\partial W}{\partial Y} \right)_w = v_o \left(\frac{\partial^2 W}{\partial Y^2} \right)_w \end{aligned}$$

Streamwise Momentum Integral Equation in Transformed Plane

$$\frac{d\theta_s}{dX} + \frac{\theta_s}{U_e} \frac{dU_e}{dX} (H_s + 2) = \frac{v_o}{U_e^2} \left(\frac{\partial U}{\partial Y} \right)_w - \frac{V_s}{U_e}$$

Integral Equation Up To Transonic Mach Number

$$\begin{aligned} U_e \frac{d}{dX} \left[\frac{K}{(\partial U_e / \partial X)} \right] &= 2 [L - K_s (H_s + 2) - S] \\ &= F(S, K_s) \end{aligned}$$

where

$$\begin{aligned} F(S, K_s) &= 0.44 + 5.56903K_s + 3.19594K_s^2 - 6.35857K_s^3 - 1.28S + 0.76S^2 \\ \text{and } K_s &= -M - 1.0S \end{aligned}$$

Figure 4

BOUNDARY-LAYER PARAMETERS AND CROSS FLOW MOMENTUM-INTEGRAL EQUATION

The application of reverse Stewartson's transformations yields the relationships between the parameters in the physical and transformed planes as presented in figure 5. The transformed cross-flow momentum-integral equation is derived in a manner similar to that for the streamwise momentum-integral equation. The numerical solution of this equation gives the computational results in the transformed plane in the form of the ratio of the boundary-layer thickness in the cross-flow direction to that in the streamwise direction as a function of the dimensionless parameter, S , which is the ratio of the distance along the normal section in the streamwise direction to the chord of normal section. The cross-flow boundary-layer thickness, δ_x , can be calculated by multiplying the ratio δ_x/δ_s , which is obtained by solving the cross-flow momentum-integral equation, by the streamwise boundary-layer thickness δ_s . The dimensionless shape of the velocity profile w/W_0 can immediately be calculated from the knowledge of δ_x , momentum thickness, and displacement thickness.

Relation Between Physical and Transformed Boundary Layer Parameters

$$\delta_x = \delta_s \cdot F_1(X_s, S)$$

where

$$F_1(X_s, S) = .032 + 73.1X_s + 10.587X_s^2 - 129.6X_s^3 + 4669.6X_s^4 + 43865X_s^5$$

$$\delta_{x_{phy}} = \delta_s \left(1 + \frac{\gamma-1}{2} M_\infty^2\right)^{1/2}; \quad \delta_{s_{phy}} = \delta_s \left(1 + \frac{\gamma-1}{2} M_\infty^2\right) + \frac{\gamma-1}{2} M_\infty^2$$

$$\delta_{x_{phy}} = \delta_{s_{phy}} \left[\frac{\delta_x}{\delta_s} + \frac{\gamma-1}{2} M_\infty^2 (M_\infty + 1) \right]$$

Cross-flow Momentum Integral Equation in Transformed Plane

$$\frac{d}{dX} \left[U_\infty \frac{\delta_x}{\delta_s} \right] \left(\frac{U_\infty}{U_0} \left(1 - \frac{W}{U_\infty}\right) dY \right) = v_0 \left(\frac{W}{U_0} \right)_w - v_s \frac{W}{U_0}$$

where δ_x is greater of δ_1 or δ_2

$$\frac{U}{U_\infty} = 2\eta_s - 2\eta_s^3 + \eta_s^5; \quad \text{where } \eta_s = \frac{Y}{\delta_s}$$

$$\frac{U}{U_\infty} = A_1 \eta_s + A_2 \eta_s^2 + A_3 \eta_s^3 + A_4 \eta_s^4; \quad \text{where } \eta_s = \frac{Y}{\delta_s}$$

$$A_1 = 2 + \frac{\delta_s^2}{U_\infty} \frac{dU}{dX}; \quad A_2 = -0.5 \frac{\delta_s^2}{U_\infty} \frac{dU}{dX}; \quad A_3 = -2 - A_2; \quad A_4 = 3 - A_1$$

Figure 5

THERMAL BOUNDARY-LAYER EQUATIONS

Equations for thermal boundary layers in transformed and physical planes are presented in figure 6. As a first approximation, assuming that the external pressure gradient is negligible (which is approximately the case for the supersonic wing at low lift cruise conditions) and that the Prandtl number is close to unity, an analytical expression for the temperature profile can be derived. This expression is then modified as shown to account for real pressure gradients and the exact value of Prandtl number. The real pressure gradient is accounted for through the polynomial expression for the velocity ratio u/U_e where the A_i 's are functions of the local pressure gradient. Once the temperature profiles are computed, the variations of dynamic viscosity, kinematic viscosity, and density across the boundary layer can be calculated and their average values determined. These averaged values are then utilized to compute dimensionless parameters which are used to determine the transition location of the laminar boundary layer.

Thermal Boundary Layer Equation in Physical Coordinate System

$$\rho g C_p (u \frac{\partial T}{\partial s} + v \frac{\partial T}{\partial \xi}) = u \frac{dP}{ds} - \frac{\partial}{\partial \xi} (K \frac{\partial T}{\partial \xi}) + \nu (\frac{\partial^2 u}{\partial \xi^2})^2$$

$$\frac{dP}{ds} = -\rho_e U_e \frac{dU_e}{ds} = \rho_e g C_p \frac{dT_e}{ds}; \rho(s, \xi) T(s, \xi) = \rho_e(s) T_e(s)$$

Equation in Transformal Coordinate System

$$U_e \frac{dU_e}{dx} (g C_p \frac{dT}{dU} + U) + v_o C_p \frac{P_r - 1}{P_r} (\frac{dT}{dU}) \frac{\partial^2 U}{\partial Y^2} = \alpha (\frac{d^2 T}{dY^2} C_p + P_r) (\frac{\partial U}{\partial Y})^2$$

Assume as a first approximation (i) zero pressure gradient and then (ii) $P_r = 1$

$$\text{at } Y = 0, U = 0, T = T_w; \text{ at } Y = \infty, U = U_e = U_\infty, T = T_e = T_\infty$$

$$\frac{T - T_w}{T_e - T_w} = \frac{T_w - T_{aw}}{T_e - T_{aw}} (\frac{U}{U_e}) - \sqrt{P_r} \frac{U_e^2}{2g C_p T_o} (\frac{U}{U_e})^2$$

where,

$$\frac{U}{U_e} = A_1 \eta_s + A_2 \eta_s^2 + A_3 \eta_s^3 + A_4 \eta_s^4$$

$$T_{aw} = T_e (1 + \sqrt{P_r} \frac{\gamma - 1}{2} M_e^2)$$

$$\eta_s = \frac{1}{\delta_{phy}} \int_0^{\eta} v d\xi; v = v_o (1 + \frac{\gamma - 1}{2} M_e^2)^{1.5} (\frac{T}{T_e})^2$$

Figure 6

CRITERIA FOR DETERMINING LOCATION OF BOUNDARY-LAYER NEUTRAL INSTABILITY

The relationship between the dimensionless pressure-gradient parameter and an "equivalent" Reynolds number based on momentum thickness for neutral instability is presented in figure 7. The curve presented is used for determining the location of neutral instability for either the streamwise or cross-flow laminar boundary layer. The effects of pressure gradients, Mach number less than 1.3, and suction were accounted for during the derivation of this curve from the solution of Orr-Sommerfeld equations in conjunction with Stewartson's transformations.

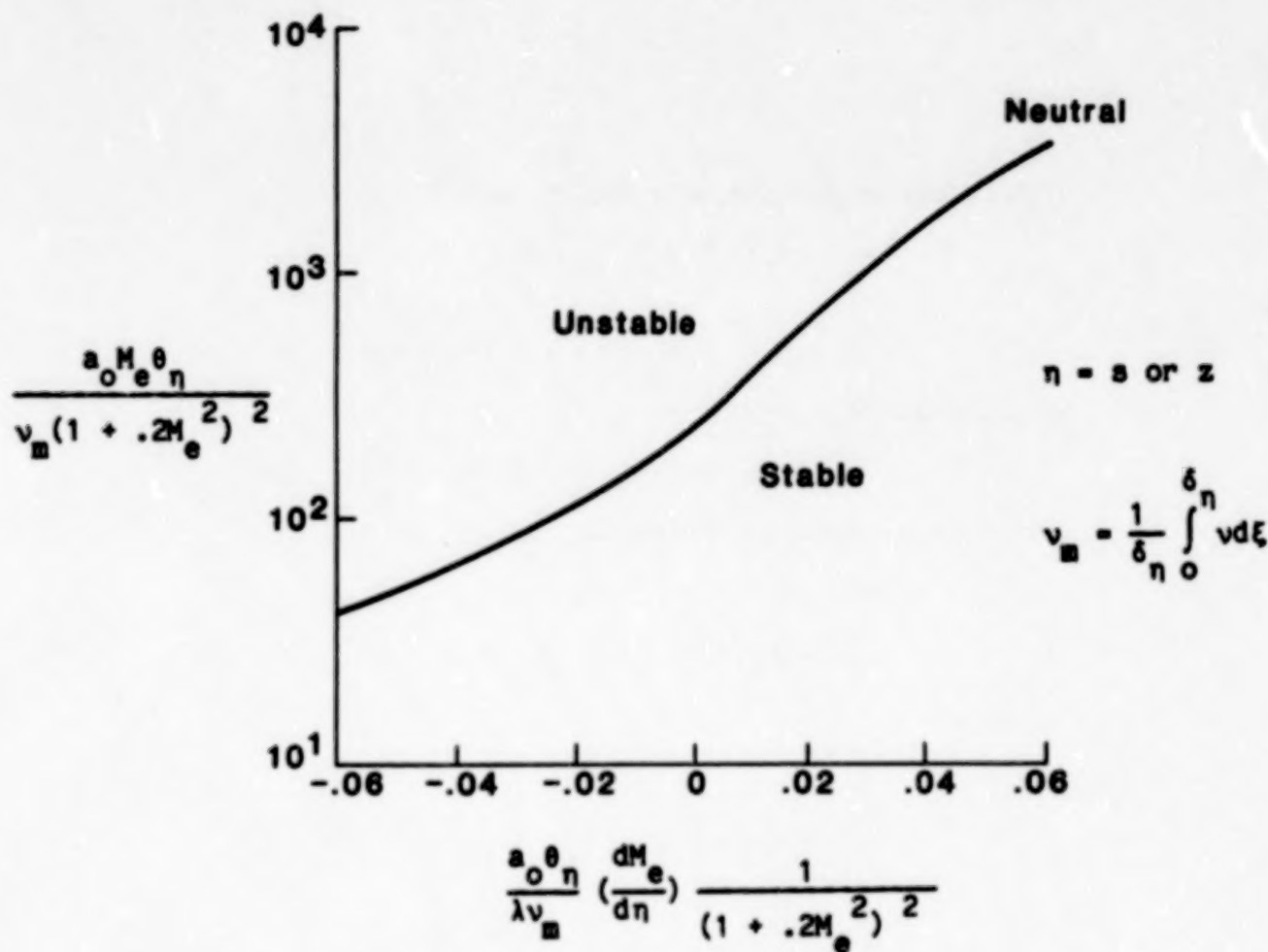


Figure 7

EFFECT OF FREE-STREAM TURBULENCE ON DIFFERENCE BETWEEN TRANSITION- AND NEUTRAL-INSTABILITY REYNOLDS NUMBER FOR FLOW ON A FLAT PLATE

The effect of free-stream turbulence on the transition location on a flat-plate laminar boundary-layer subjected to zero pressure gradient is shown in figure 8. The transition data were obtained by several investigators in the range of free-stream Mach numbers from low subsonic to a supersonic value of 3. The temperature profile data used to construct this curve were obtained either from experimental data or calculated from the previously stated theoretical expression for the temperature profile presented in figure 6. The curve shows the difference in "equivalent" Reynolds number at the transition location and at the point of neutral stability. The equations for the averaged value of kinematic viscosity ν and "equivalent" integral thickness δ^* which were used to derive this curve from the experimental data are also presented.

$$R_\eta = \frac{U_e \delta_\eta^*}{\nu_m} \quad \text{and} \quad \delta_\eta^* = \int_0^\infty \left(1 - \frac{U}{U_e}\right) \frac{T_e}{T} d\eta$$

where $n=s$ or z

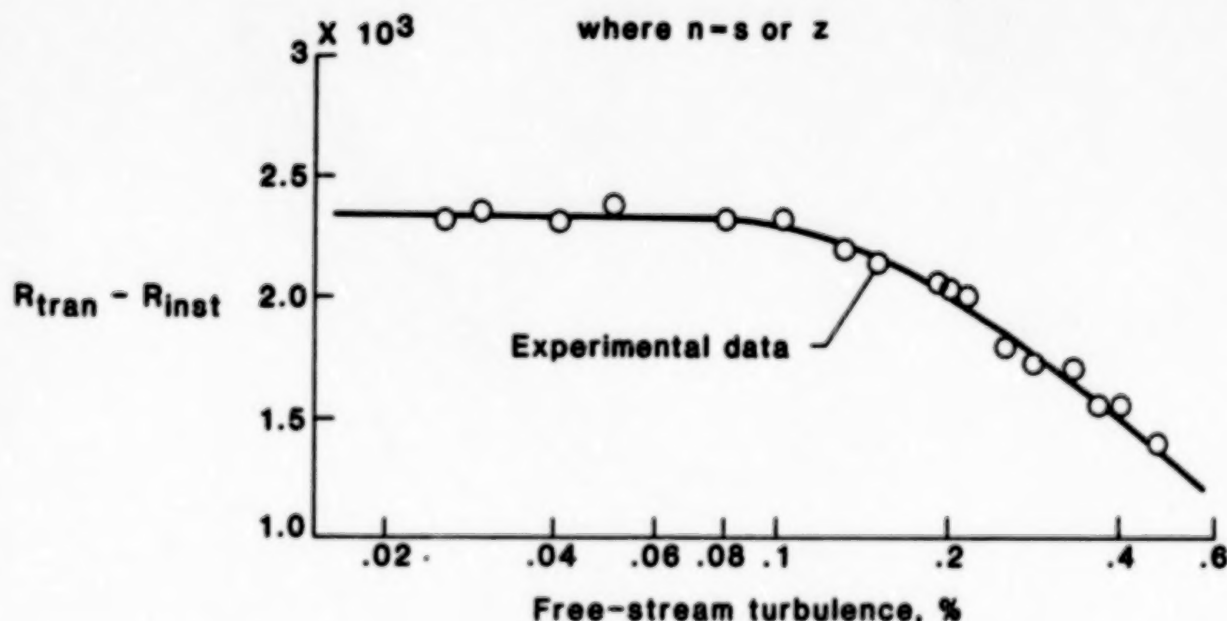


Figure 8

BOUNDARY-LAYER TRANSITION CRITERIA

The criteria used in the compressible laminar boundary-layer method to determine the transition location due either to the amplification of Tollmien-Schlichting waves or to cross flow is presented in figure 9. The dimensionless expression on the abscissa contains several implicit and explicit physical parameters that are significant during the transition of laminar boundary layer. In deriving the curves shown in this figure for several values of free-stream turbulence intensities, use has been made of information presented in figure 8. It was assumed that the effect of free-stream turbulence on the transition of laminar boundary layer without a pressure gradient behaves in a manner similar to a laminar boundary layer with a pressure gradient.

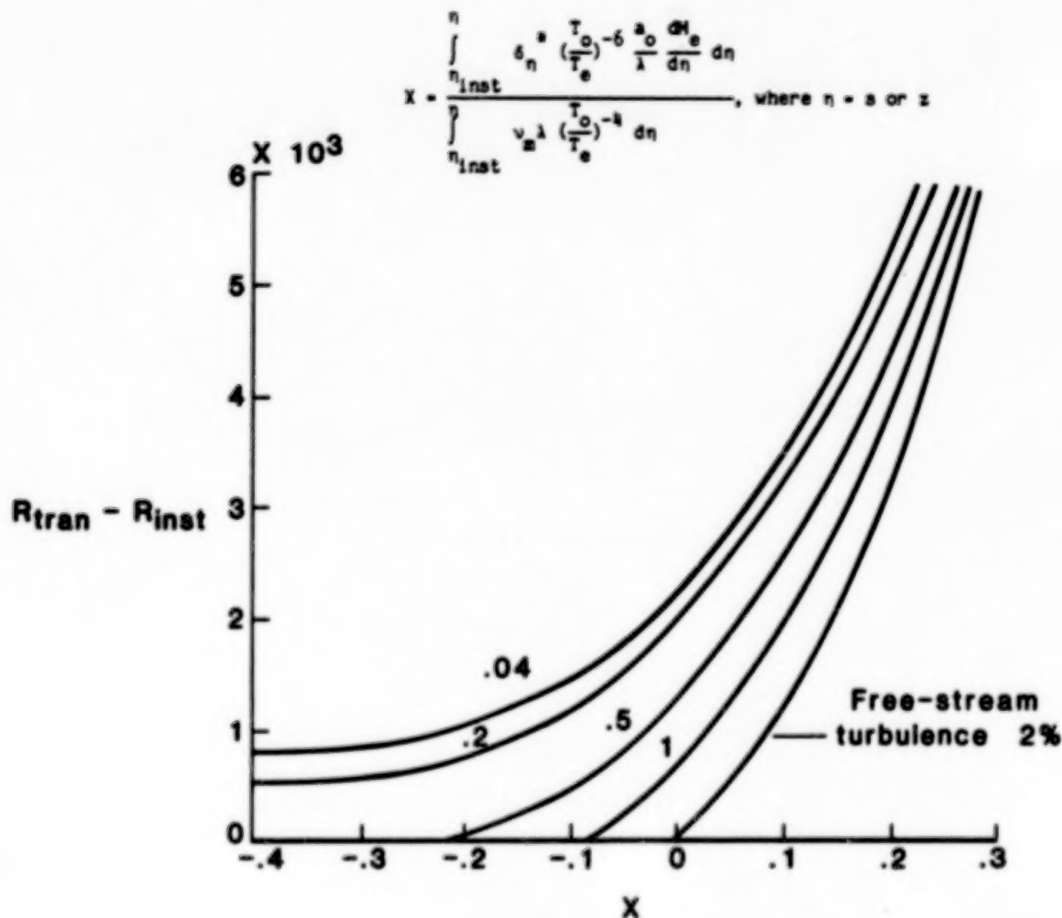
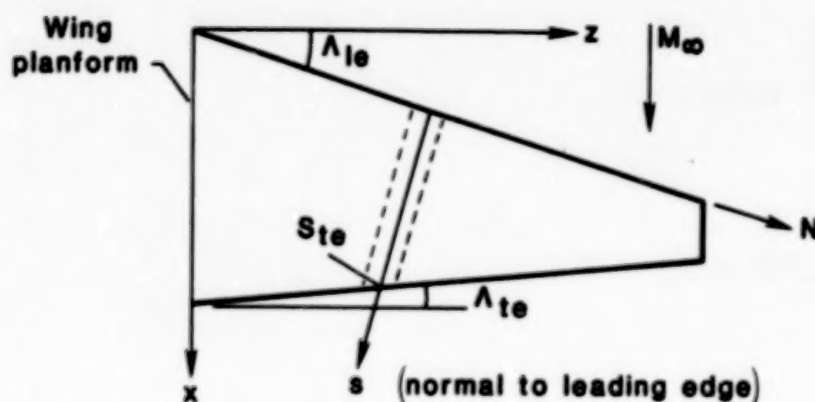


Figure 9

EQUATIONS FROM APPLICATION OF SWEEP THEORY

A schematic illustrating the application of "Strip Theory" for the prediction of laminar boundary-layer transition on a finite swept, tapered, and twisted wing is presented in figure 10. The wing is divided into a large number of finite strips oriented normal to the leading edge (more accurately normal to the local aerodynamic center-of-pressure line). The pressure distribution C_p on the edge as well as on the centerline of each strip can be determined either by the available two- or three-dimensional theoretical flow codes. The local Mach number distributions in the direction parallel and normal to the strip are also presented in this figure. These local Mach number distributions, $M_{1,s}$ and $M_{1,n}$, are input into the compressible laminar boundary-layer method to determine whether or not transition will occur due to either Tollmien-Schlichting waves or cross-flow instabilities.



- $\Lambda_{1(\text{local})} = \Lambda_{le} + (\Lambda_{te} - \Lambda_{le}) (s/s_{te})$
- $(y/c)_1 = (y/c)_\infty / \cos(\Lambda_1)$
- $M_S = M_\infty \cos(\Lambda_1), M_N = M_\infty \sin(\Lambda_1)$
- $C_p = C_{p,s}$ (on normal section)
- $M_{1,s} = [5 (1 - (1 + .2M_S^2)/(1 + .7C_{p,s}^2)^{2/7})]^{1/2}$
- $M_{1,n} = [5 (1 - (1 + .2M_N^2)/(1 + .7C_{p,N}^2)^{2/7})]^{1/2}$

Figure 10

CORRELATIVE STUDIES

The present integral boundary-layer method for predicting transition was used extensively during the design of the Hybrid Laminar-Flow Control (HLFC) wing to be tested in the Langley 8-Foot Transonic Pressure Wind Tunnel. In order to establish the validity of the method prior to design of the HLFC wing, the correlative studies listed in figure 11 were performed to compare the computational results by the present theory with available experimental data.

● Variable sweep wing with NACA 64₂A015 section

● Phoenix wing

● NASA LFC wing

Figure 11

EXPERIMENTAL SETUP FOR TRANSITION MEASUREMENTS ON NASA AMES VARIABLE SWEEP WING

A schematic of the experimental setup used by Boltz⁸ in the NASA Ames Research Center's 12-Foot Pressure Tunnel to determine the transition location on an infinitely swept wing at various sweep angles is shown in figure 12. The sweep angle was varied from 0° to 50° by insertion of wedges, and the wing tips were kept parallel to the free stream with appropriate wing tip extension. The wing section was an NACA 64₂A015 airfoil. The chord of the wing was four feet, and the wing was mounted vertically on the turntable in a semispan manner. In the unswept position the wing had an effective aspect ratio of 5.0. The transition locations were experimentally determined at the various sweep angles and Reynolds numbers using both flow visualization techniques and small microphones located in the model.

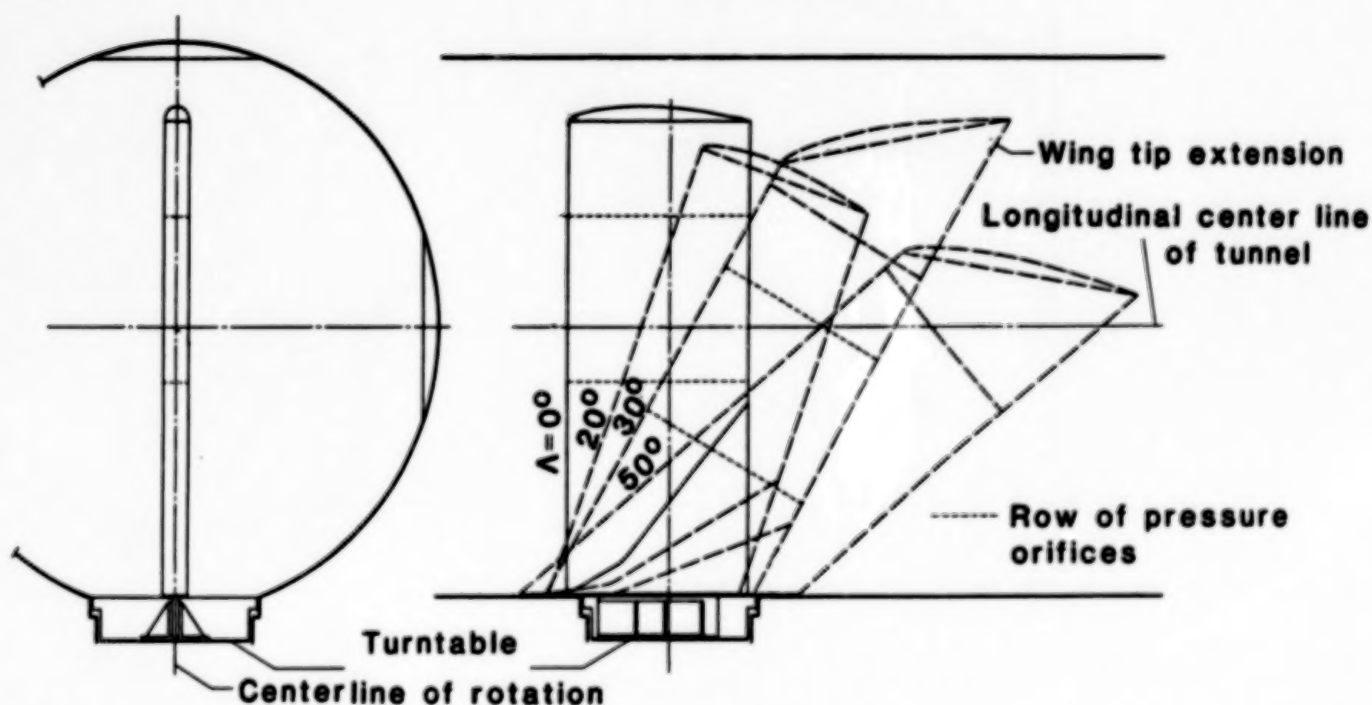


Figure 12

COMPARISON OF PRESSURE DISTRIBUTION FOR NACA 64₂A015 WING WITH 30° SWEEP

The pressure distribution computed by the NASA Multi-Component Airfoil Program (MCARF) for the NACA 64₂A015 section at an angle of attack of 1° and sweep angle of 30° is shown in figure 13. The experimental data shown in this figure were obtained by Boltz at the same free-stream conditions and sweep. The comparison shows excellent agreement between theory and experiment.

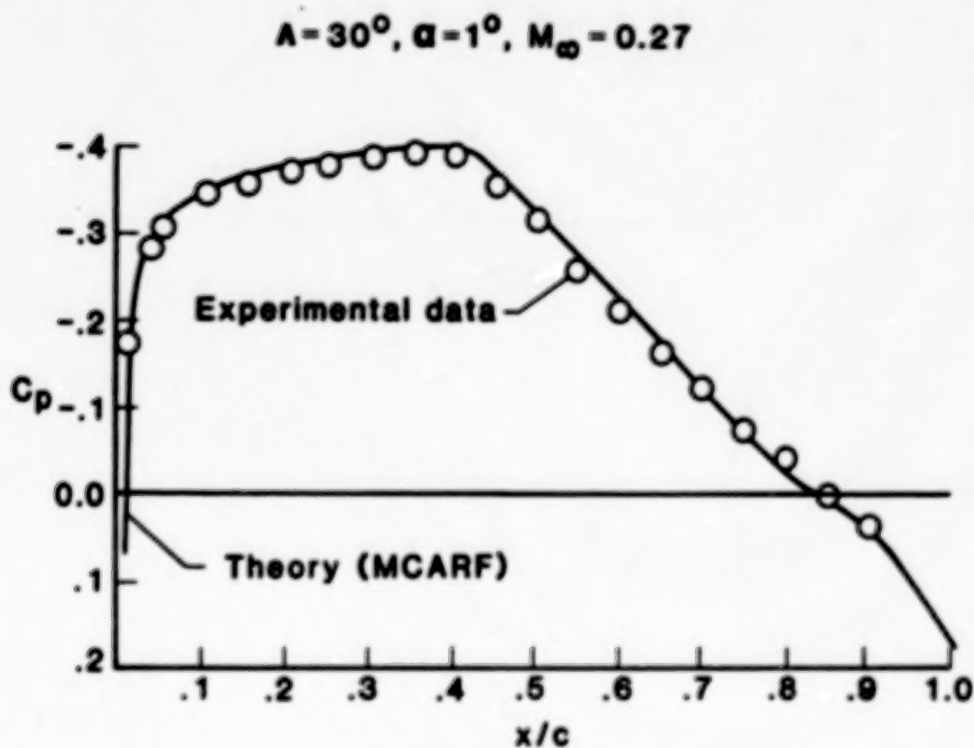


Figure 13

COMPARISON OF PRESSURE DISTRIBUTION FOR NACA 64₂A015 WING WITH 50° SWEEP

The comparison between the theoretically computed pressure distribution and experimental data by Boltz for an angle of attack of 0° and a sweep angle of 50° is shown in figure 14. The computed pressure distribution agrees quite well with the experimental data except in the vicinity of the trailing edge. This discrepancy at the trailing edge can be attributed to turbulent separation due to outboard washout phenomenon which usually occurs at this relatively high sweep angle.

$$\Lambda = 50^\circ, \alpha = 0^\circ, M_\infty = 0.27$$

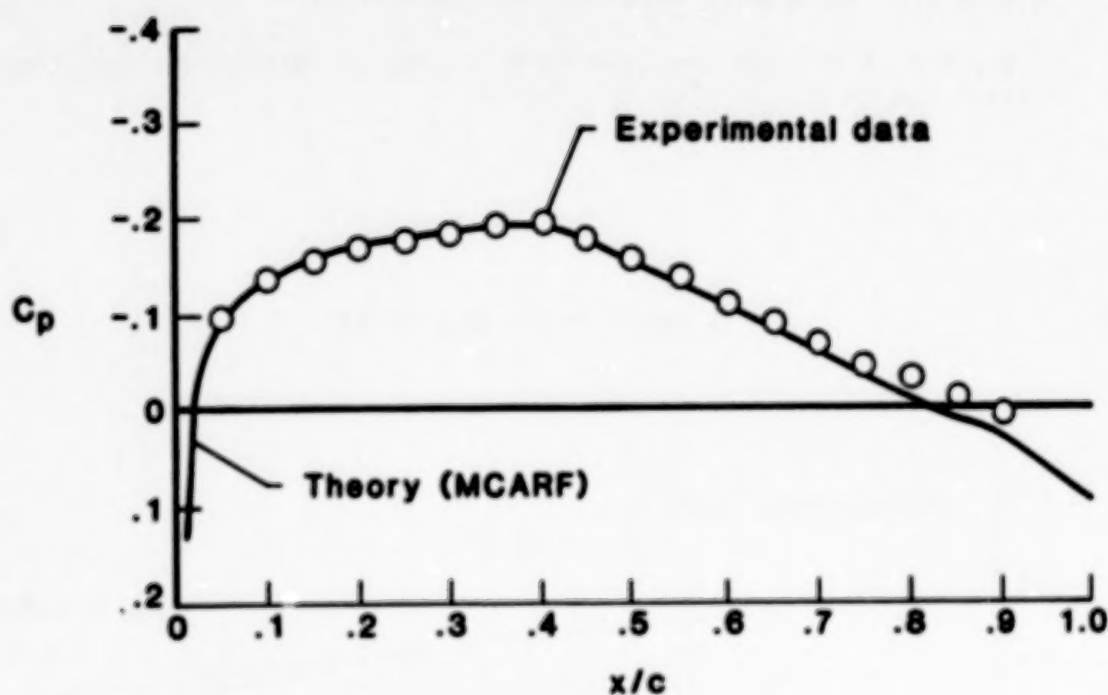


Figure 14

TRANSITION CORRELATION FOR NACA 64₂A015 WING WITH 20° SWEEP

The comparison between predicted and experimentally measured transition locations for the NACA 64₂A015 wing with 20° of sweep is presented in figure 15. The theoretical results are shown as a function of free-stream Reynolds number for transition locations due to 1) Tollmien-Schlichting waves or laminar separation with short bubble turbulent reattachment and 2) transition due to cross flow. Also shown in this figure are the computed x/c locations for Tollmien-Schlichting (T.S.) and cross-flow (C.F.) neutral instabilities as a function of free-stream Reynolds number. The correlation results suggest the following:

- (1) Predicted transition due to T.S. by the present method agrees quite well with experimental data for Reynolds numbers less than 20 million.
- (2) For Reynolds numbers greater than 20 million, the predicted transition due to C.F. occurs upstream of that due to T.S., and the predicted locations due to C.F. agree well with the experimental data.
- (3) For a sweep of 20° and Reynolds numbers greater than 20 million, the transition is due completely to C.F.

$$\Lambda = 20^\circ, \alpha = 0^\circ, M_\infty = 0.27$$

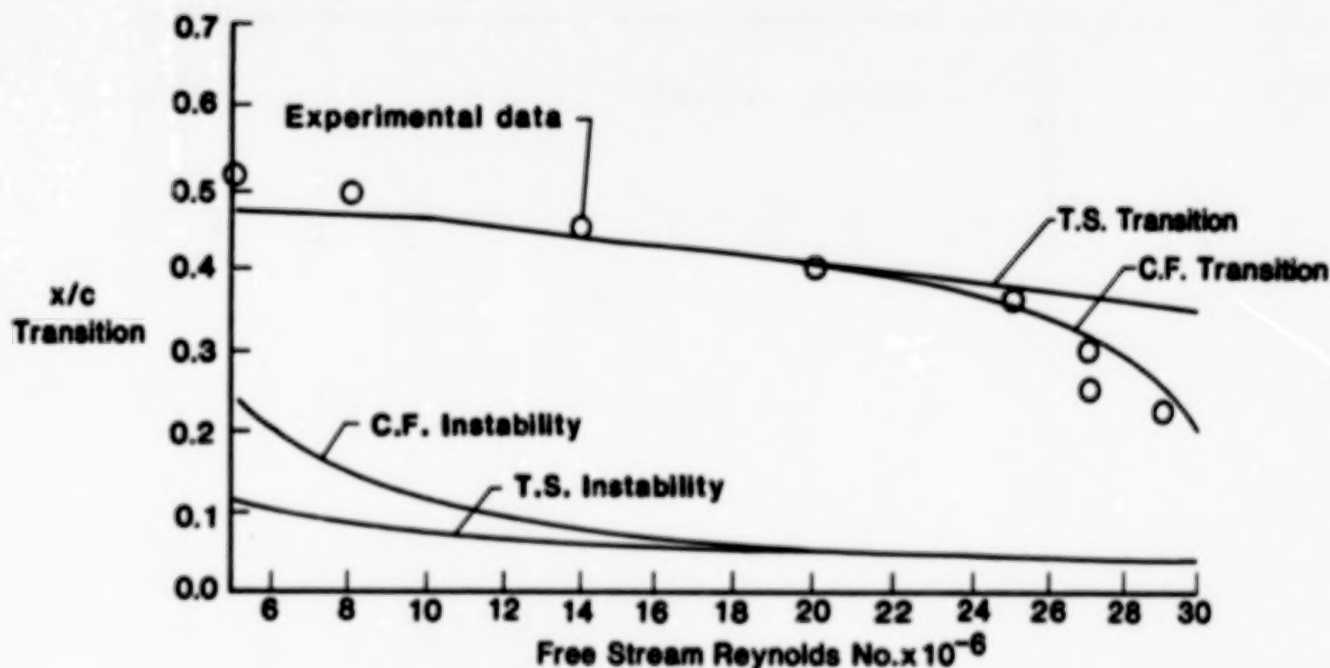


Figure 15

TRANSITION CORRELATION FOR NACA 64₂A015 WITH THE 40° SWEEP

The correlation of results between present method and Boltz's experimental data for the higher sweep angle of 40° is presented in figure 16. The theoretical data presented were computed using the pressure distribution generated by the MCARF program. The following conclusions can be drawn from the correlations presented in this figure:

- (1) Transition locations due to T.S. and C.F. are predicted fairly well.
- (2) For Reynolds numbers greater than 8 million, theoretical computations indicate that C.F. triggers the transition more abruptly and earlier than at the lower sweep angles.
- (3) There is a danger of leading-edge contamination due to C.F. for Reynolds numbers larger than 18 million at a sweep angle of 40°.

$$\Lambda = 40^\circ, \alpha = 0^\circ, M_\infty = 0.27$$

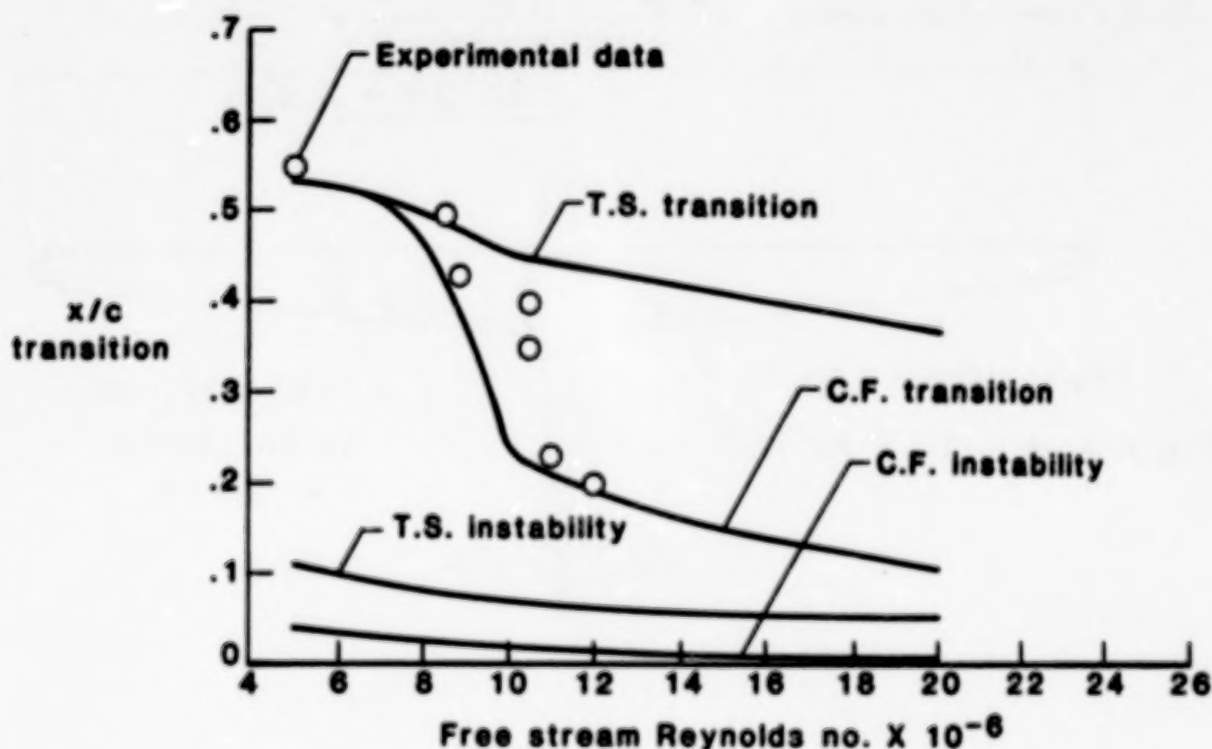


Figure 16

PLANFORM OF PHOENIX SAILPLANE AND AIRFOIL GEOMETRY

The planform of the Phoenix sailplane and the geometry of the airfoil at the test location on the wing are shown in figure 17. The pressure distributions and velocity profiles were measured by Raspets⁹ at several chordwise locations at the test location for several values of lift coefficient. The maximum thickness-to-chord ratio for the test location airfoil is 0.15 and is located at $x/c = 0.35$. The maximum camber is located at $x/c = 0.70$. The aspect ratio of the wing is approximately 18.

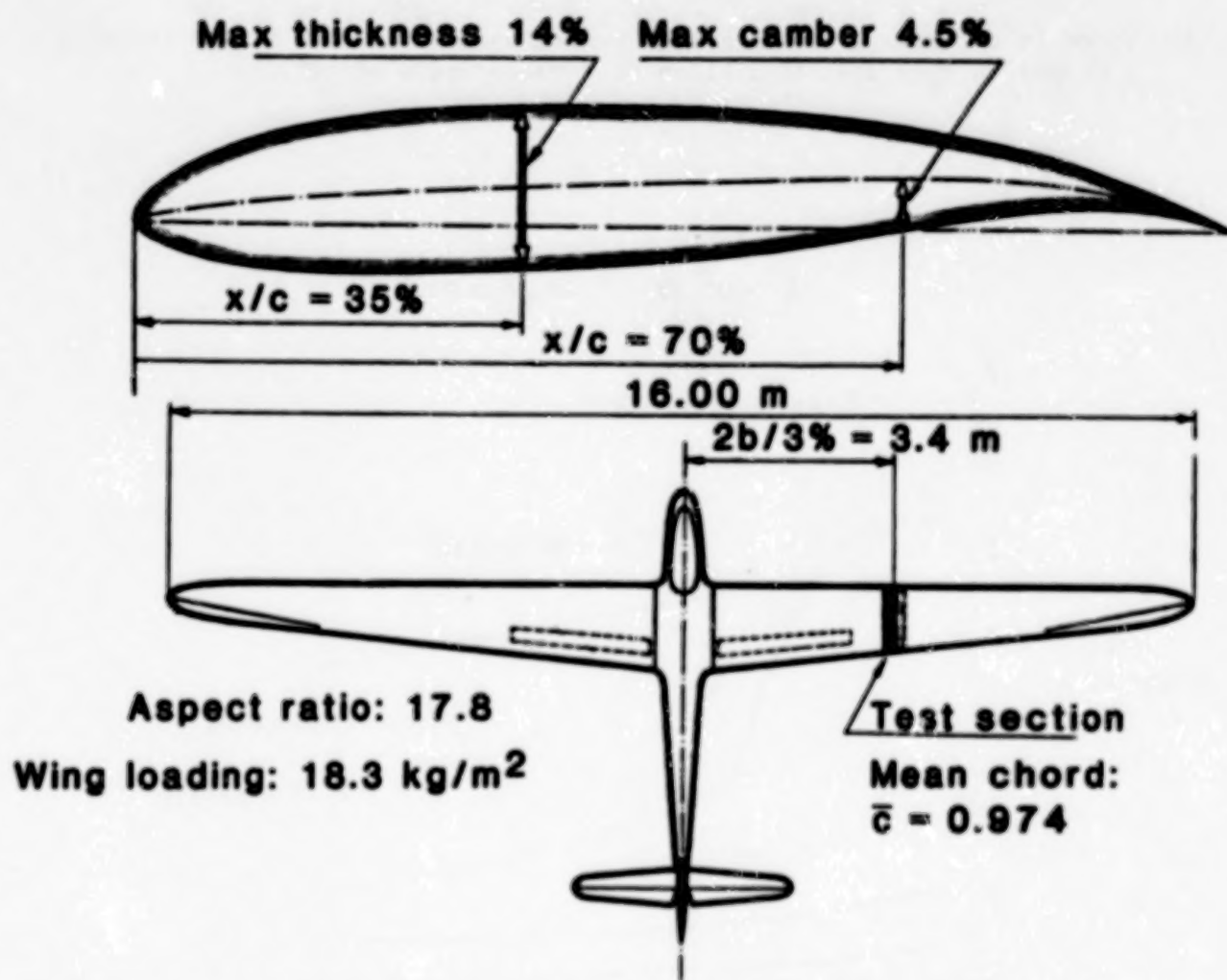


Figure 17

PRESSURE DISTRIBUTION CORRELATION ON PHOENIX WING

$$C_L = 0.76 \text{ AND } R_N = 1.464 \times 10^6$$

The comparison between the theoretical pressure distribution computed by the MCARF program and the experimental data of RASPET for the Phoenix wing at a lift coefficient of 0.76 and a chord Reynolds number of 1.464 million is shown in figure 18. The results plotted in this figure show that the computed pressure distribution agrees quite well with the measured experimental data. These computed and experimental pressure distributions were input as boundary conditions to the integral boundary-layer method used to compute the transition locations presented subsequently.

$$C_L = 0.76, R_N = 1.464 \times 10^6$$

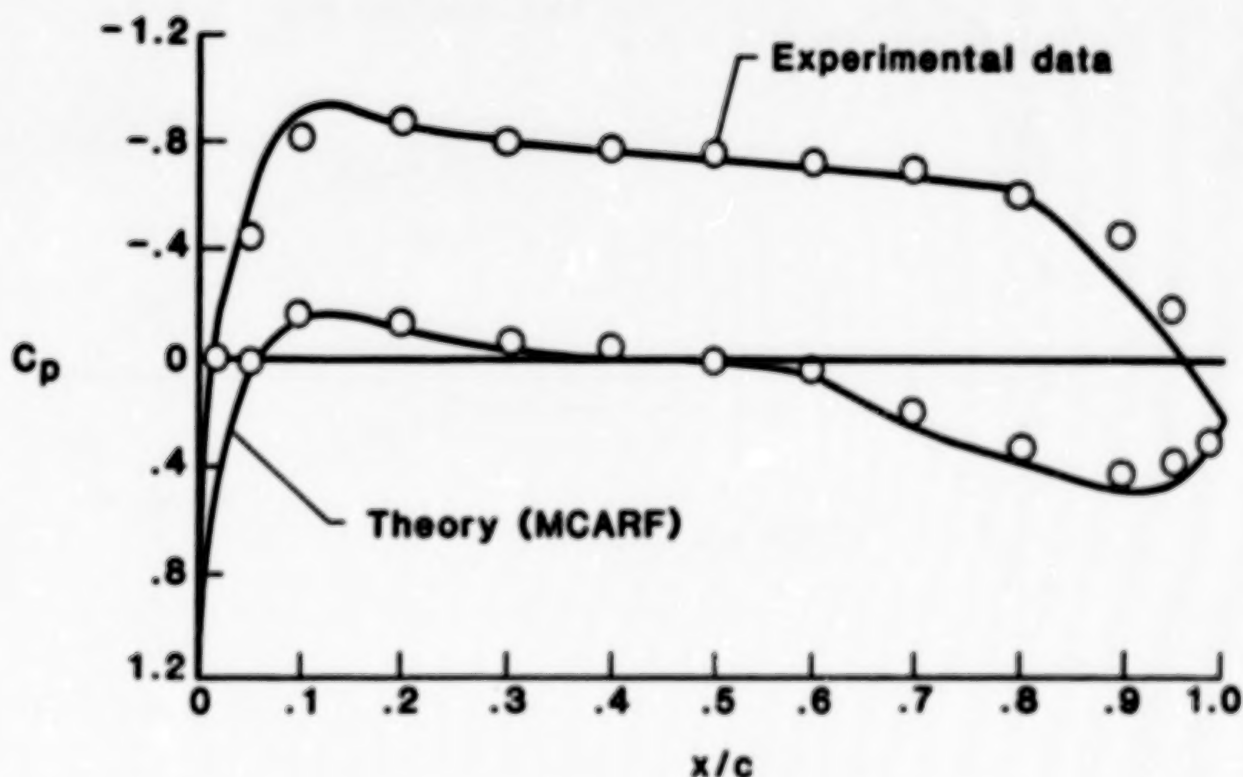


Figure 18

PRESSURE DISTRIBUTION CORRELATION ON PHOENIX WING

$$C_L = 1.14 \text{ AND } R_N = 1.2 \times 10^6$$

The comparison of pressure distribution computed by MCARF and the experimental data for Phoenix wing at lift coefficient of 1.14 and a chord Reynolds number of 1.2 million is presented in figure 19. The computed pressure distribution agrees fairly well with experimental data except near the trailing edge where turbulent boundary-layer separation is present.

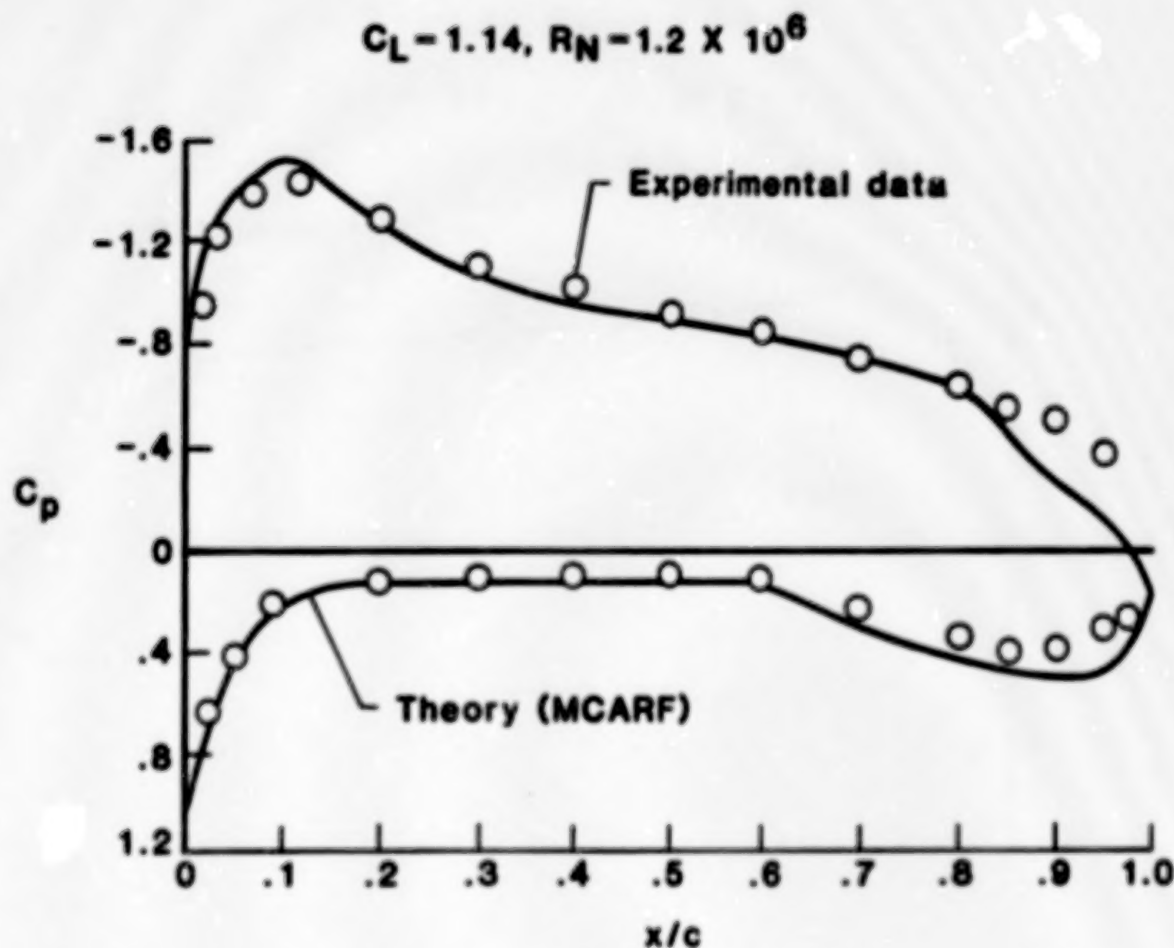


Figure 19

TRANSITION CORRELATION FOR PHOENIX SAILPLANE WING

The correlation for transition and turbulent separation locations on the test location airfoil of the Phoenix wing is presented in figure 20. The results are plotted as a function of lift coefficient. These results indicate that the chordwise location of turbulent separation is predicted fairly well. However, some discrepancy exists between the computed and experimental transition location for lift coefficients in the range of 0.6 to 1.1 when the theoretical pressure distributions were used as input boundary conditions. In order to examine the effect of using different boundary conditions, transition locations were also computed using experimental pressure distributions as input boundary conditions. As seen in figure 20, the difference in the theoretical transition locations using the two different boundary conditions is not significant. It should be emphasized that the author Raspet did not measure the location of transition directly but, instead, inferred the location from the measured velocity profiles; therefore, there may be some discrepancy in the actual measured transition locations.

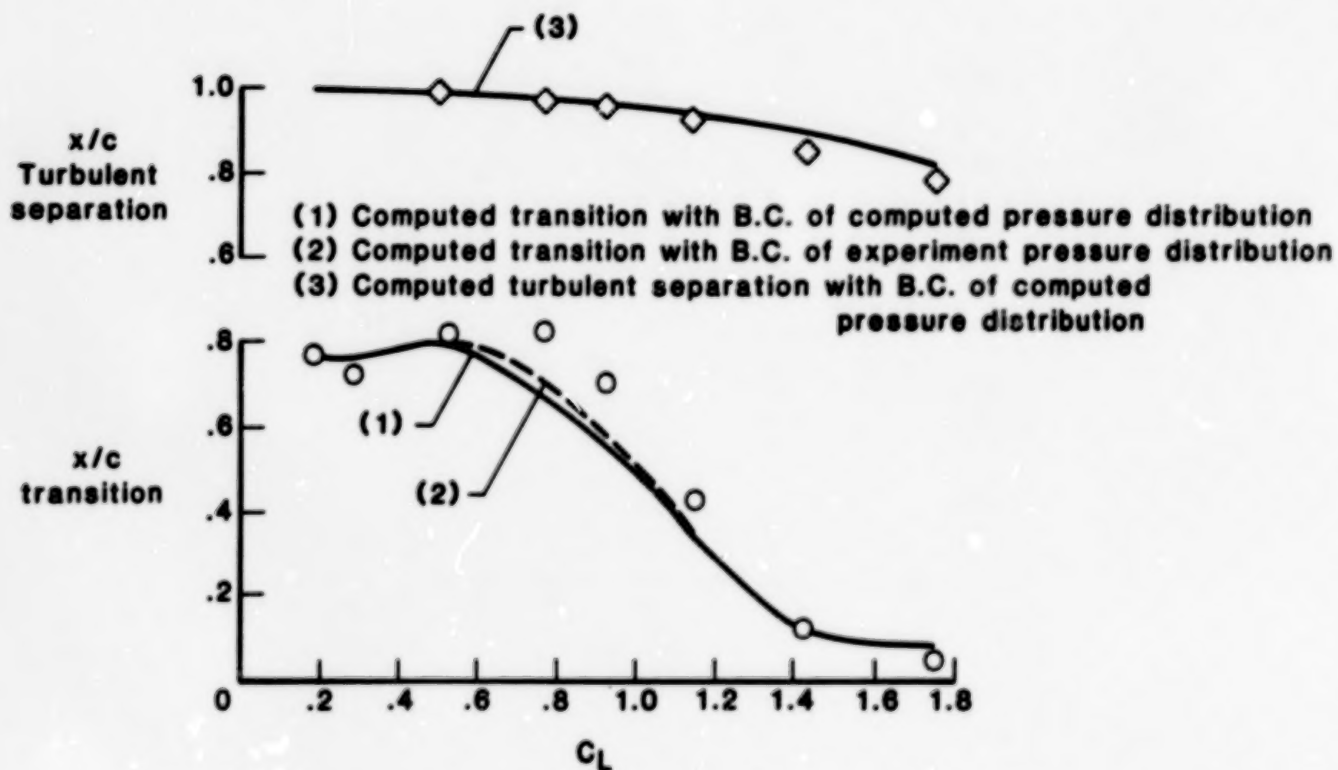


Figure 20

CORRELATION OF TRANSITION DATA FOR LFC WING WITH PARTIAL SUCTION
 $\Lambda = 23^\circ$ AND $M_\infty = 0.826$

The correlation of the transition locations for the NASA Langley LFC wing with partial suction on the upper surface are presented in figure 21. The chordwise location of suction was varied from an x/c of 0.0 to 0.5. The transition measurements were made at a free-stream Mach number of 0.826 and chord Reynolds numbers of 10 to 20 million. Theoretical computations were performed using boundary conditions of experimentally measured suction coefficients as input boundary conditions. The predicted transition locations are in good agreement with the measured transition locations. The results of the three correlation cases presented have demonstrated the validity of the new integral boundary-layer method.

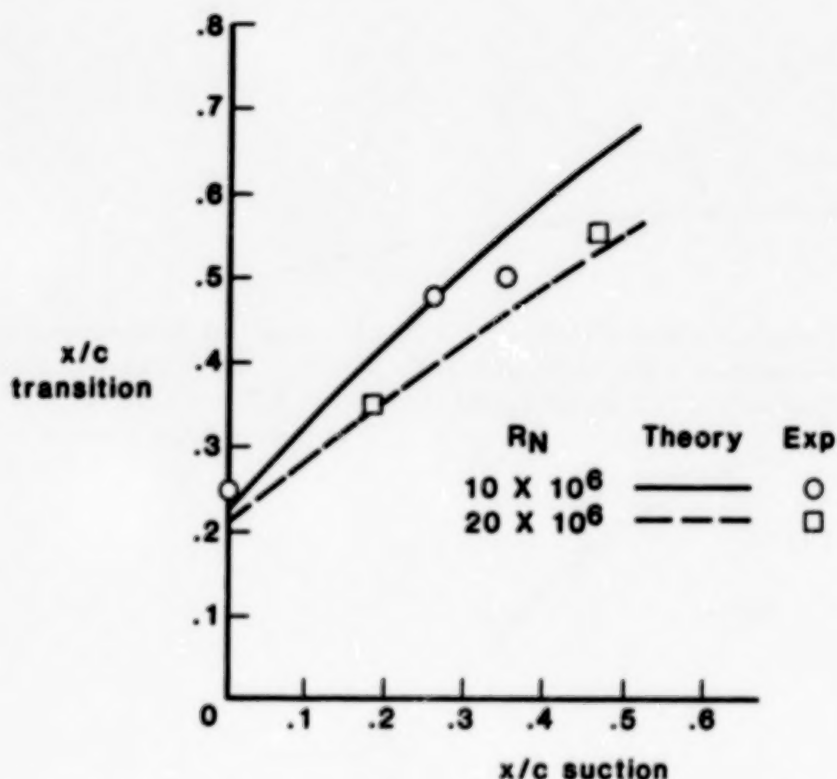


Figure 21

DESIGN CONSTRAINTS OF HYBRID LAMINAR-FLOW CONTROL WING

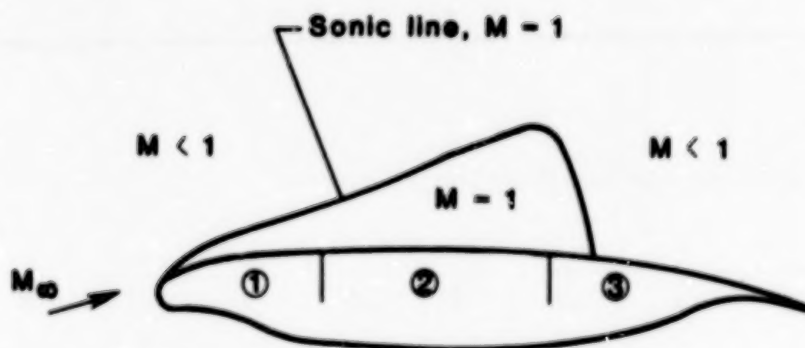
The design constraints and objectives for the Hybrid Laminar Flow Control (HLFC) wing to be tested in the Langley 8-Foot Transonic Pressure Tunnel are illustrated on figure 22. The design constraints and objectives that were laid out by Mr. P. J. Bobbitt, who also directed the HLFC design and optimization studies, are summarized as follows:

Design Constraints

- (1) The geometry of the lower surface of the HLFC wing must be the same as that of the LFC wing.
- (2) The geometry of the upper surface panel #1 of the HLFC wing must be identical to that on the present LFC wing and suction must be applied only through panel #1.
- (3) The sonic bubble height for the HLFC wing must be no greater, and, if possible, smaller than that for the LFC wing.

Design Objectives

- (1) The geometric shape of the upper surface panels #2 and #3 must be derived by the inverse perturbation method of characteristics so that laminar boundary-layer flow is maintained up to $x/c = 0.6$ on the upper surface of HLFC wing for $C_L = 0.45$ and $M_\infty = 0.82$.
- (2) The computed turbulent separation location on the upper surface of the HLFC wing must be aft of $x/c = 0.95$.



- Suction applied to panel 1
- Geometry of panels 2 and 3 altered for:
 - Sonic line height constraint
 - Laminar B.L. flow for $x/c \approx 0.6$
 - Turbulent separation aft of $x/c \approx 0.95$

Figure 22

COMPARISON BETWEEN THEORETICAL AND EXPERIMENTAL PRESSURE DISTRIBUTIONS FOR LFC AND HLFC WINGS

A comparison of pressure distributions between the design HLFC wing and the present LFC wing is presented in figure 23. The application of suction is limited to $0.025 < x/c < 0.26$ on the upper surface of the HLFC wing. The pressure distribution for the HLFC wing (shown by the dotted line) constitutes the boundary condition necessary to achieve the design constraints and objectives outlined on figure 22.

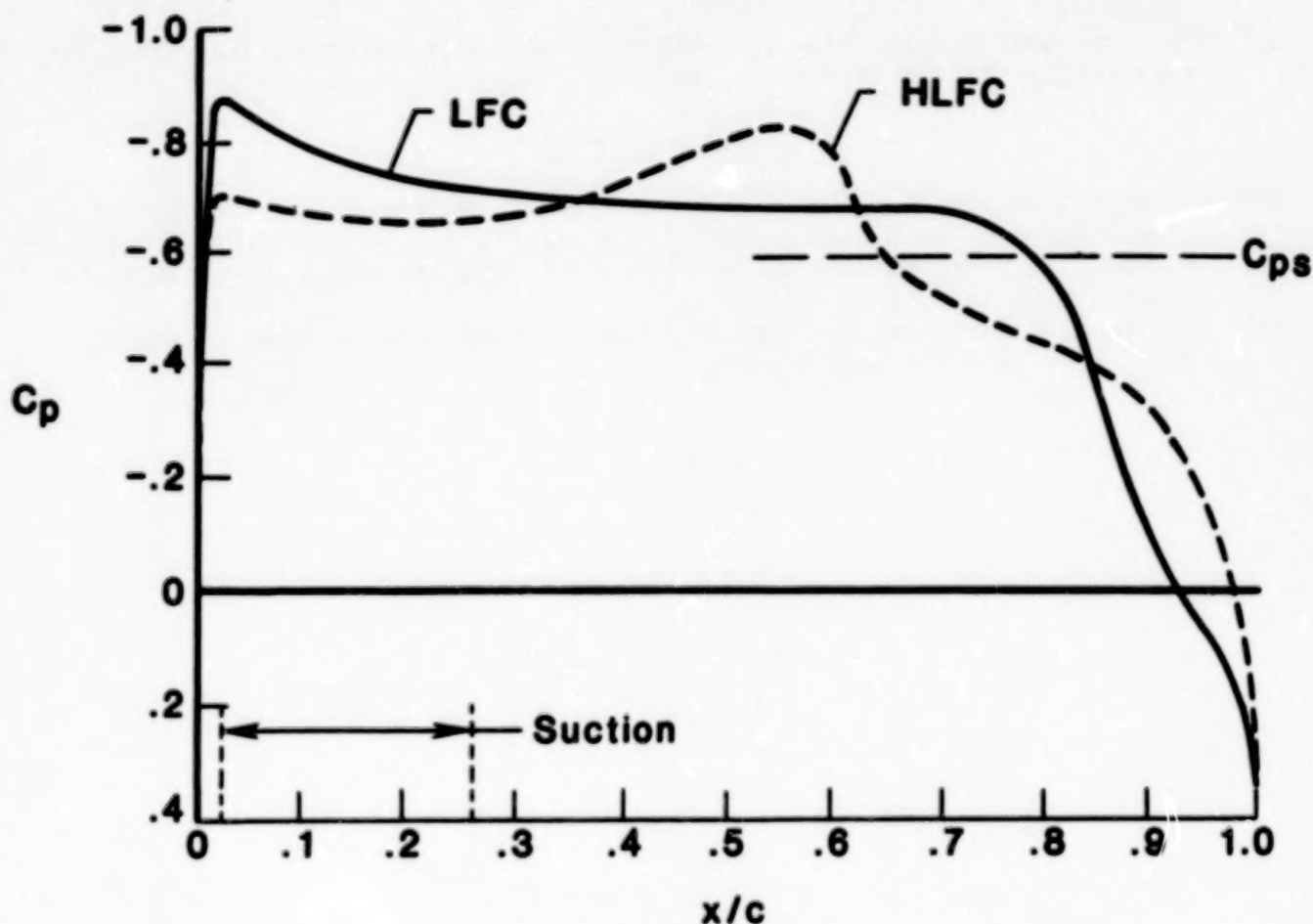


Figure 23

PREDICTED TRANSITION AND TURBULENT SEPARATION LOCATIONS FOR HLFC

The computational results for the predicted transition and turbulent boundary-layer separation locations on the upper surface of the HLFC wing are presented in figure 24. Predicted results are shown for transition due to Tollmien-Schlichting (T.S.) wave amplification, transition due to cross flow (C.F.), and instability due to T.S. and C.F. The chordwise location of computed turbulent separation is also presented. These results are plotted as a function of free-stream Reynolds number and for a wing $C_L = 0.44$ and free-stream $M_\infty = 0.811$.

As shown in figure 24, transition due to T.S. with short bubble reattachment occurs at $x/c = 0.58$ for the range of Reynolds numbers shown. However, transition due to C.F. takes over at a Reynolds number of 15 million. It is assumed with the present theory that the transition occurs on the wing due to whichever phenomena appears first. Thus, cross flow essentially determines the transition location at the higher Reynolds number. In addition, there is a danger of leading-edge contamination due to C.F. instability at Reynolds numbers larger than approximately 20 million. The computed turbulent separation location is downstream of $x/c = 0.95$ for the entire range of Reynolds numbers.

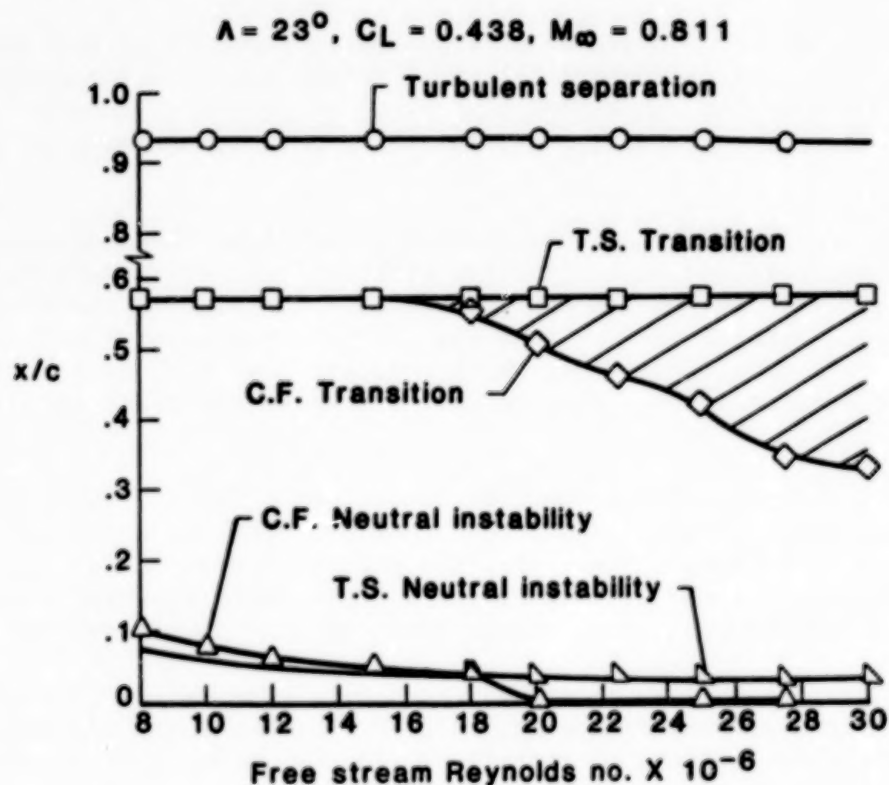


Figure 24

CONCLUSIONS AND RECOMMENDATIONS

The results of the design studies of the HLFC wing using the integral boundary-layer methods of Goradia lead to the following conclusions and recommendations:

- (1) The perturbation method of characteristics was found to be extremely useful for determining the geometric changes needed in the baseline LFC airfoil shape to obtain the desired HLFC pressure distribution.
- (2) The compressible laminar boundary-layer method with suction was found to be quite accurate in predicting the extent of laminar flow for swept wings in the presence of suction. Also with this method the suction requirements can be determined for different local velocity profiles such as those for Blasius, separating laminar, or asymptotic suction velocity distributions.
- (3) The turbulent boundary-layer separation method includes terms to account for the rapid increase in the turbulent fluctuations in the flow near separation; these terms greatly improved the accuracy of the prediction of the location of turbulent separation.
- (4) The integral boundary-layer methods execute very rapidly on the computer making it possible to analyze several hundred configurations in a relatively short period of time.
- (5) The results of the correlative studies generally showed excellent agreement between the theoretical predictions and the experimental data. The results also showed that, for values of Reynolds number and wing sweep of practical interest for commercial and fighter aircraft, cross-flow instabilities were predominant in triggering transition.
- (6) The analysis of the final HLFC design showed that less than one count of suction drag coefficient was required in conjunction with the appropriate pressure distribution to achieve laminar flow on the upper surface of the wing to the 60-percent chord location. This one count of suction drag results in a corresponding 30 to 40 count reduction in the wake drag coefficient which suggests that HLFC is a very lucrative and promising concept for viscous drag reduction at both transonic and supersonic speeds.
- (7) In order to prevent laminar transition due to cross flow at large values of sweep and Reynolds number, it is recommended that both the chordwise and the spanwise pressure gradients be tailored to minimize the growth of the boundary-layer disturbances. With the use of a modified strip theory, arbitrary spanwise pressure gradients can be accounted for when using the present integral boundary-layer methods.

The present integral boundary-layer methods have been extended to compute both laminar and turbulent boundary-layer flow and to predict transition locations at supersonic Mach numbers. The effects of variations in temperature profile and physical flow properties across the boundary layer, suction, wing sweep, wing taper, and wing twist are also accounted for in these methods. These methods are not limited to wings alone, but can also be used for the analysis of fighter aircraft fuselage with suction at supersonic flight conditions. Correlation studies are currently under way to determine the validity of these extended integral boundary-layer methods.

REFERENCES

1. Harvey, William D.; Harris, Charles D.; Brooks, Cyler W. Jr.; Clukey Patricia G.; Bobbitt, Percy J.; and Stack, John P.: Design and Experimental Evaluation of a Swept Supercritical LFC Airfoil. NASA CP-2398, Vol. I, Langley Symposium on Aerodynamics, April 23-25, 1985.
2. Meyer, W. D.; and Jennett, L. A.: In Flight Surface Oil Flow Photographs with Comparison to Pressure Distributions and Boundary-Layer Data. NASA TP 2393, April 1985.
3. Goradia, S. H.: The Method of Characteristics Perturbation Technique as Applied to Airfoil Design. Lockheed-Georgia Company Advanced Design Aerodynamics Memorandum 13-68, March 1968.
4. Bauer, F; Garabedian, P.; and Korn, D.: A Theory of Supercritical Wing Sections, with Computer Programs and Examples. Volume 66 of Lecture Notes in Economics and Mathematical Systems, Springer-Verlag, 1972.
5. Stevens, W. A.; Goradia, S. H.; and Braden, J. A.: Mathematical Model for Two-Dimensional, Multi-Component Airfoils in Viscous Flow. NASA CR-1843, 1971.
6. Goradia, S. H.; and Lyman, V. L.: Laminar Stall Prediction and Estimation of CL_{max} . Journal of Aircraft, Vol. 11, No. 9, pp 528-536, Sept. 1974.
7. Goradia, S. H.; and Morgan, H. L. Jr.: A New, Improved Method for Separating Turbulent Boundary Layer for Aerodynamic Performance Predictions of Trailing Edge Stall Airfoils. AIAA Paper 86-1832-CP, presented at AIAA 4th Applied Aerodynamics Conference, San Diego, California, June 9-11, 1986.
8. Boltz, F. W.; Kenyon, G. C.; and Allen, C. Q.: Effects of Sweep Angle on the Boundary-Layer Stability Characteristics of an Untapered Wing at Low Speeds. NASA TN D-338, 1960.
9. Raspet, A.; Gyorgy-Falvy, D.; and Cornish, J.: Boundary Layer Studies on Phoenix Sailplane. Presented at the VIII Congress of O.S.T.I.V., Koln, Germany, June 1960.

N90-12536

NUMERICAL EXPERIMENTS ON TRANSITION CONTROL

IN WALL-BOUNDED SHEAR FLOWS

S. Biringen and M. J. Caruso
Department of Aerospace Engineering Sciences
University of Colorado
Boulder, Colorado

PRECEDING PAGE BLANK NOT FILMED

[REDACTED]

Results are presented from a numerical simulation of transition control in plane channel and boundary layer flows. Details of the channel flow control are available in reference 1. The analysis is based on a pseudo-spectral/finite-difference semi-implicit solution procedure (ref. 2) employed to numerically integrate the time-dependent, three-dimensional, incompressible Navier-Stokes equations in a doubly periodic domain. In the channel flow, we find the active periodic suction/blowing method to be effective in controlling strongly three-dimensional disturbances. In the boundary layer, our preliminary analysis indicated that in the early stages, passive control by suction is as effective as active control to suppress instabilities. Our current work is focused on a detailed comparison of active and passive control by suction/blowing in the boundary layer.

GOVERNING EQUATIONS

- CONTINUITY EQUATION

$$\frac{\partial u_i}{\partial x_i} = 0$$

- MOMENTUM EQUATION

$$\frac{\partial u_i}{\partial t} + u_j \frac{\partial u_i}{\partial x_j} = -\frac{1}{\rho} \frac{\partial p}{\partial x_i} + \nu \frac{\partial^2 u_i}{\partial x_j \partial x_j}$$

- THERMAL-ENERGY EQUATION

$$\frac{\partial T}{\partial t} + u_i \frac{\partial T}{\partial x_i} = \frac{k}{\rho C_p} \frac{\partial^2 T}{\partial x_j \partial x_j}$$

- CONSTANT PROPERTIES; NO VISCOSITY; TEMPERATURE FIELD UNCOUPLED
- EQUATIONS NONDIMENSIONALIZED BY U_0, h
- FLOW DRIVEN BY A CONSTANT MEAN PRESSURE GRADIENT $2/Re$, $Re = U_0 h/\nu$
- CONVECTIVE TERMS PUT INTO A FORM THAT CONSERVES ENERGY AND MOMENTUM

$$\frac{\partial u_i}{\partial t} + u_j \left(\frac{\partial u_i}{\partial x_j} - \frac{\partial u_j}{\partial x_i} \right) = -\frac{\partial p^*}{\partial x_i} + \frac{2}{Re} \delta_{ij} + \frac{1}{Re} \frac{\partial^2 u_i}{\partial x_j \partial x_j}$$

$$p^* = p/\rho + \frac{1}{2} u_j u_j$$

SOLUTION PROCEDURE

- SAME TECHNIQUE AS THE VELOCITY FIELD
- Non-dimensionalized with $(T-T_0)/(T_w-T_0)$; h and U_0
- Adams-Bashforth 2-step method for the advective terms
- Crank-Nicholson implicit scheme on the diffusive terms.
- Periodicity along allows x_1 and x_3
 - Two-D Fourier transform in the x_1 - x_3 plane
 - The Pseudo spectral method in the x_1, x_3 directions
- Finite differences with variable mesh along the x_2 direction
- Solution in Fourier space as a tridiagonal system
- Back transformed into physical space to obtain temperature field at $(n+1)$

IMPLEMENTATION OF BOUNDARY CONDITIONS

- No-slip B.C.
 $u_1 = u_2 = u_3 = 0$
 p from x_2 -momentum equation
- Suction B.C.
- Flow homogeneous along x_1, x_3
- Incoming mass flow rate must equal to the outgoing mass flow rate

$$\frac{\partial \langle u_2 \rangle}{\partial x_2} = 0$$

$$\langle u_2 \rangle = \text{CONST. or } g(x_1, x_3)$$

- Hence velocity magnitude and direction at one wall must be preserved throughout the flow field to satisfy continuity
- Physically plausible condition is suction-blowing or periodic b. cond.

TRANSITION IN WALL-BOUNDED FLOWS

- . 2-D Tollmien-Schlichting waves.
- . Formation of streamwise vortices.
- . Formation of shear layers away from the wall due to vorticity-induced velocity.
- . Secondary instability (kinks and spikes).
- . Breakdown into smaller scales, formation of wall shear, hairpin eddies.
- . Turbulent spot - horseshoe vortex-turbulence.

MODEL PROBLEMS

- * Periodic plane channel flow
- * Periodic boundary layer.

COMPUTATIONAL DETAILS

Mesh Resolution : $32 \times 32 \times 32$

Channel Flow Reynolds number : $Re = U_\infty h / \nu = 1000$

U_∞ : Centerline velocity
 h : Channel half-thickness

Boundary Layer Reynolds number : $Re = U_\infty \delta^* / \nu = 1000$

U_∞ : Free-stream velocity
 δ^* : momentum thickness (constant)

Initial Conditions

a. Channel Flow

All velocities per cent of channel centerline velocity.
 T_c is the time when control is applied for one time step.

α	β	$\frac{u_{rms}}{u_\infty}$	$\frac{v_{rms}}{u_\infty}$	$\frac{w_{rms}}{u_\infty}$
1	1	3	2	30, 50, 40

b. Boundary Layer

Velocities are per cent of free-stream velocity.

α	β	$\frac{u_{rms}}{u_\infty}$	$\frac{v_{rms}}{u_\infty}$
20%	30%	0.5	0.1

α : Wave number of the 2D fundamental wave.

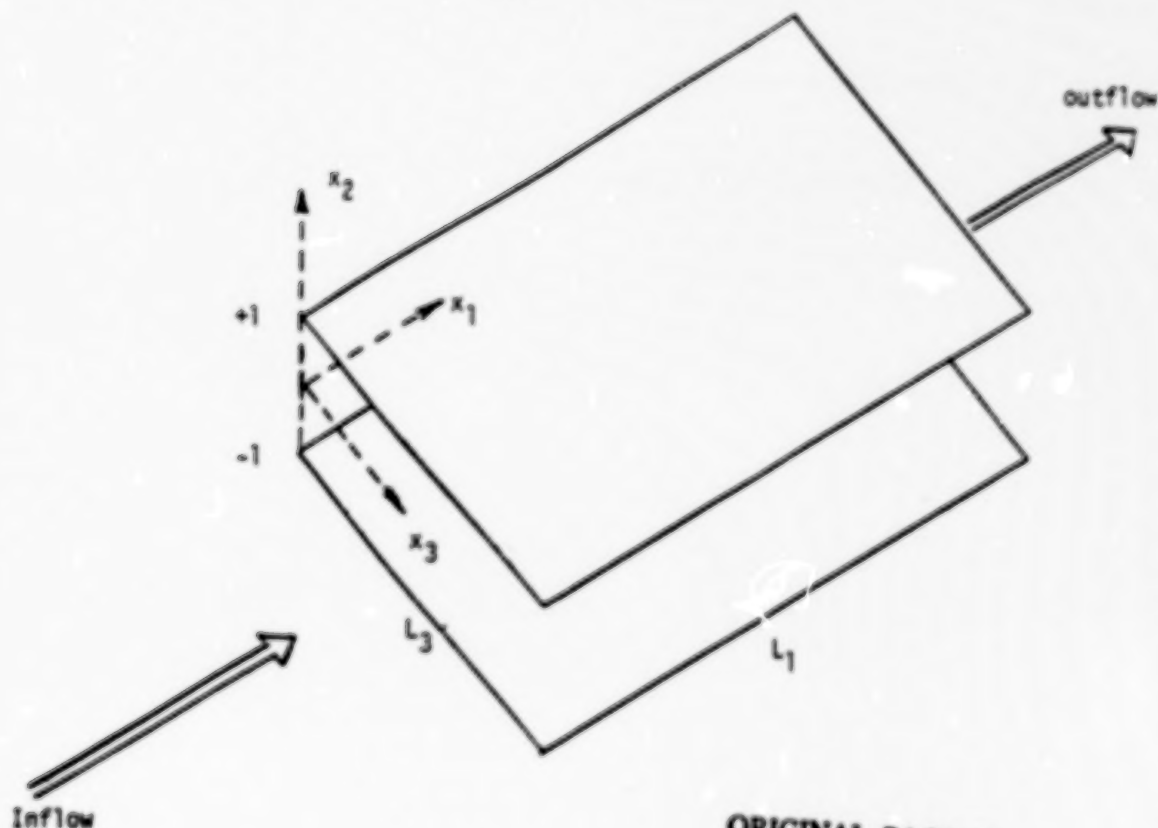
β : Wave number (spanwise) of the oblique wave.

α and β are used to generate the initial conditions from an Orr-Sommerfeld solver.

$(\frac{u_{rms}}{u_\infty})$: Rms amplitude of the initial 2D wave.

$(\frac{v_{rms}}{u_\infty})$: Rms amplitude of the initial 2D wave.

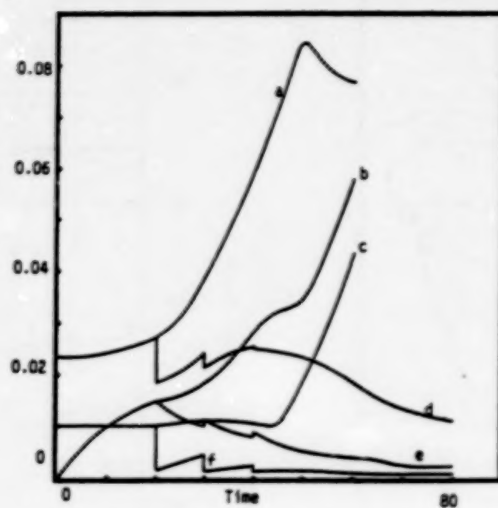
Flow geometry, the computational box



ORIGINAL PAGE IS
 OF POOR QUALITY

MAXIMUM PLANE-AVERAGED RMS VELOCITIES

The temporal development of plane-averaged maximum velocities is presented. These velocities provide comparisons between the controlled flow (three-dimensional control) and no-control cases for the channel flow.

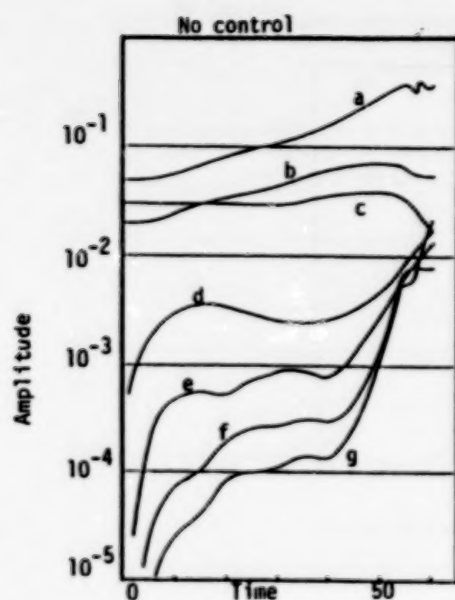


No control		With control	
a.	u_1 RMS	d.	u_1 RMS
b.	u_3 RMS	e.	u_3 RMS
c.	u_2 RMS	f.	u_2 RMS

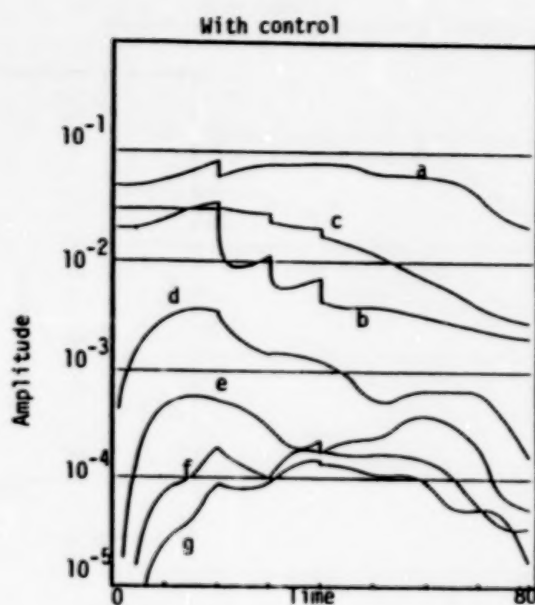
C-4

TEMPORAL DEVELOPMENT OF U-COMPONENT FLUCTUATING VELOCITY AND ITS HARMONICS

The evolution of the various Fourier modes indicated that all amplitudes are significantly reduced, and after the third control wave they all decay rapidly.



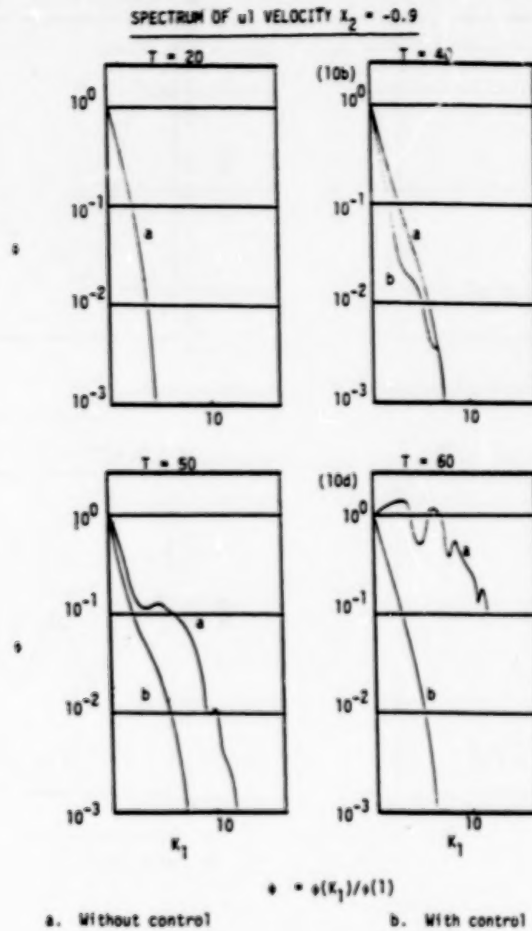
- a. u_1' max
- b. u_1 - 3D primary
- c. u_1 - 2D primary



- d. u_1 - 2D first harmonic
- e. u_1 - 2D second harmonic
- f. u_1 - 2D third harmonic
- g. u_1 - 2D fourth harmonic

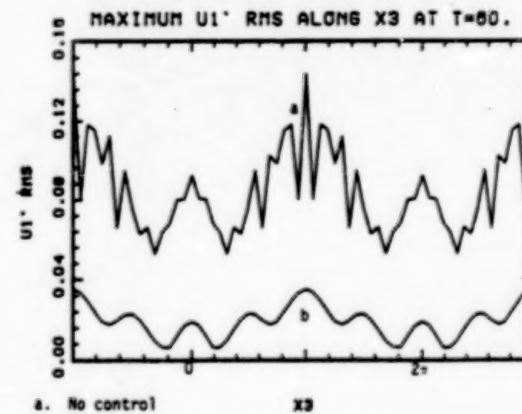
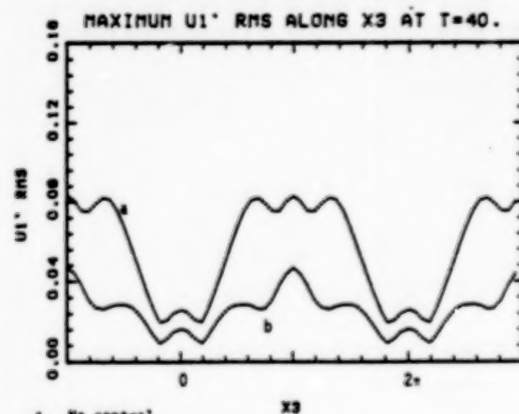
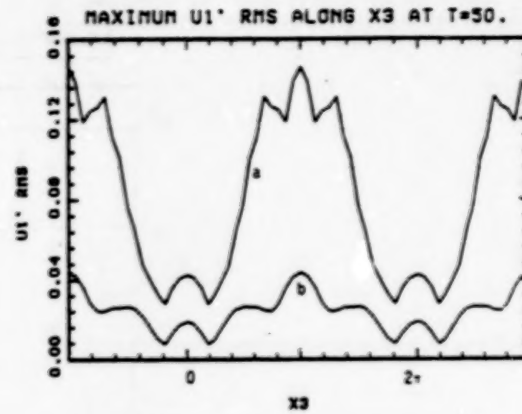
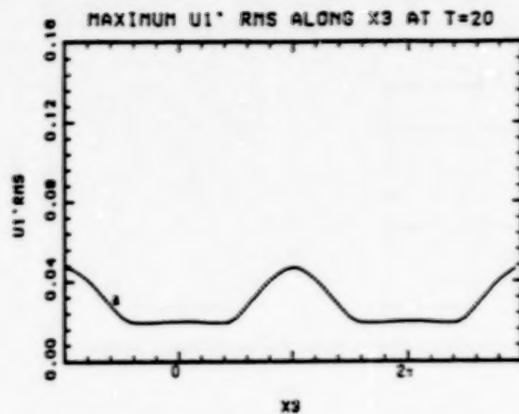
NORMALIZED ONE-DIMENSIONALIZED WAVE SPECTRUM

In the uncontrolled case we observe that energy transfer to the high wave numbers is indicated by a full spectrum. In the controlled case, this does not occur and energy is concentrated in the low wave numbers preventing the development of higher harmonics.



MAXIMUM U-RMS ALONG X_3 (SPANWISE DISTRIBUTION)

In the uncontrolled flow, peak-valley splitting develops. The control wave does not prevent peak-valley splitting, but reduces the amplitudes. The uncontrolled and controlled distributions remain in phase.

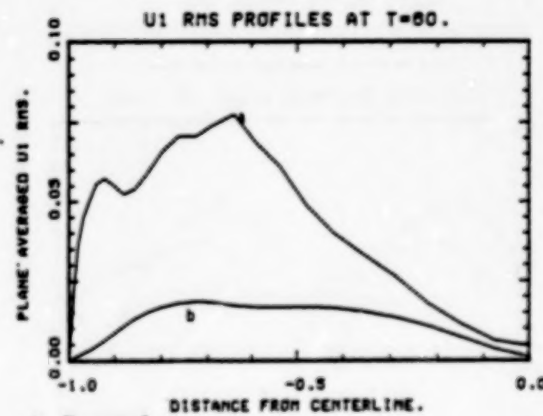
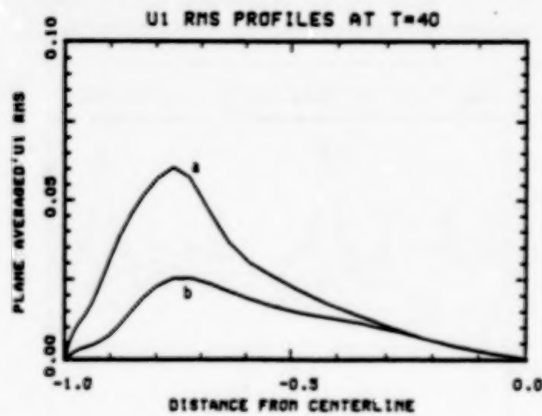
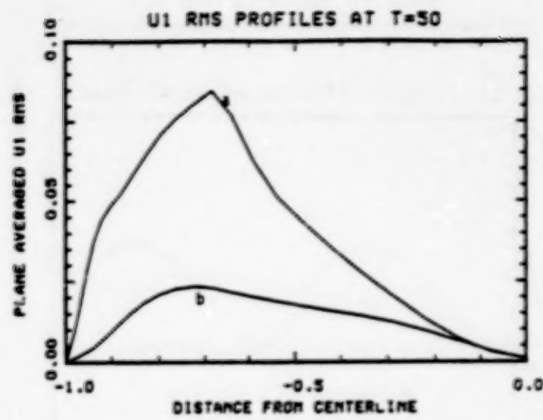
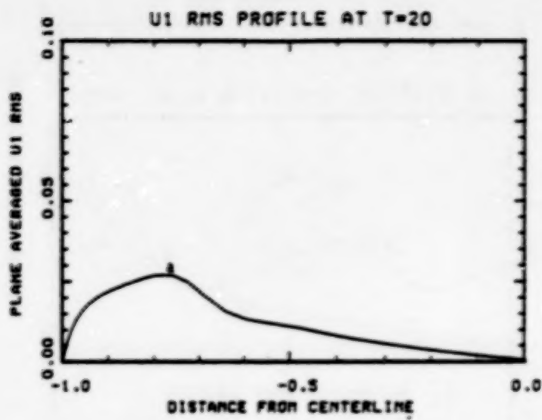


a. No control
b. With control

a. No control
b. With control

U-RMS PROFILE

These figures indicate the amplitude reduction in u-rms distributions due to the imposed control waves.

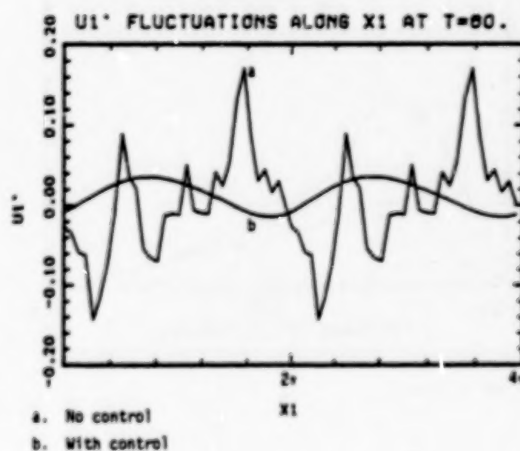
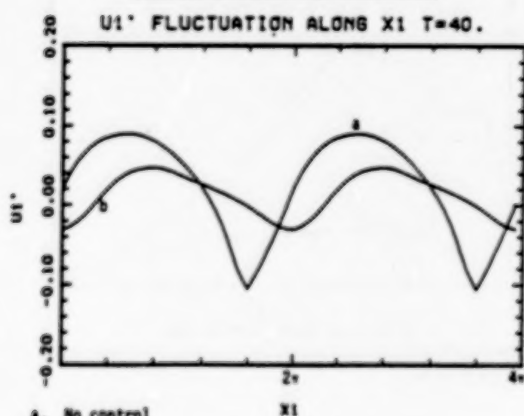
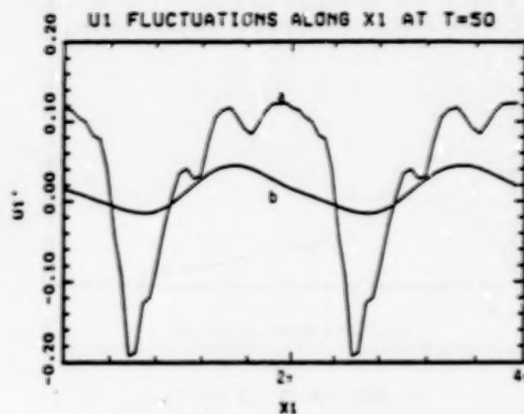
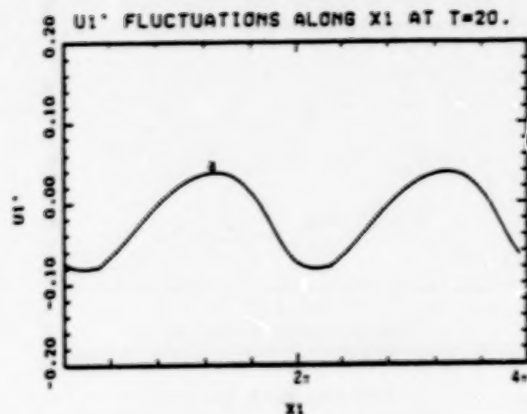


a. No control
b. With control

a. No control
b. With control

U_1 -FLUCTUATIONS ALONG X_1

In the uncontrolled case a strong negative spike develops between $T = 40$ and $T = 50$. No evidence of spike formation and nonlinear distortions is observed in the uncontrolled case. As $T = 60$, the controlled distribution is nearly sinusoidal, whereas the uncontrolled case shows a broad frequency content.

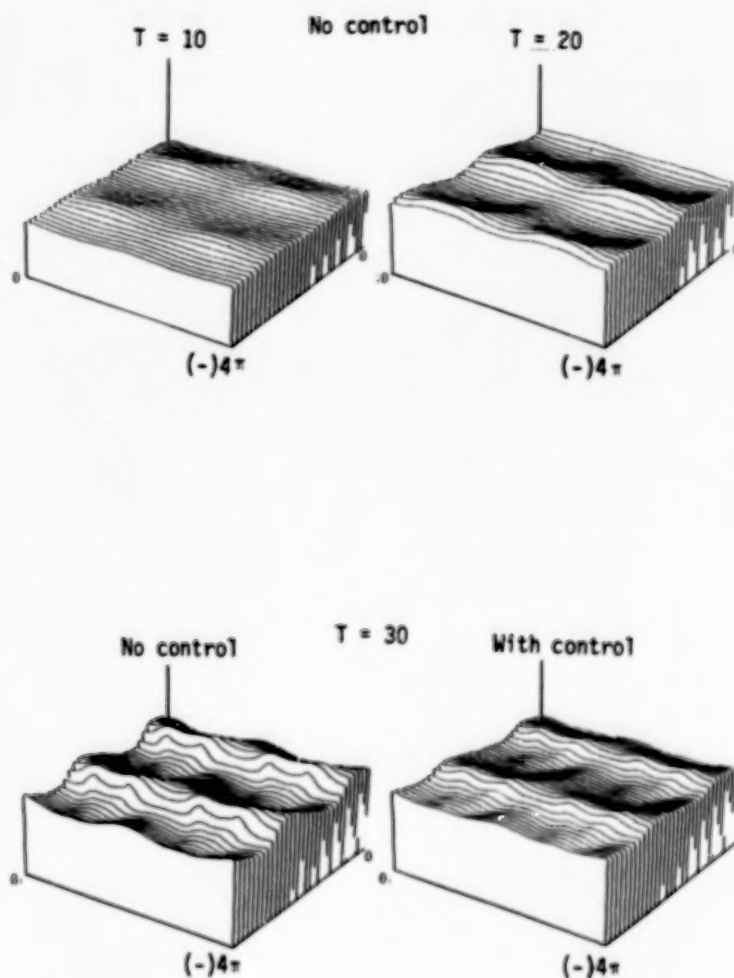


a. No control
b. With control

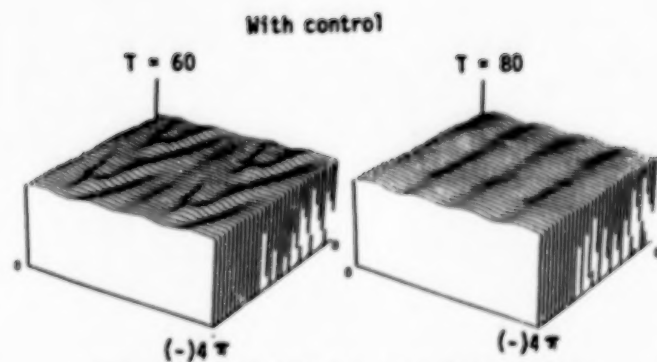
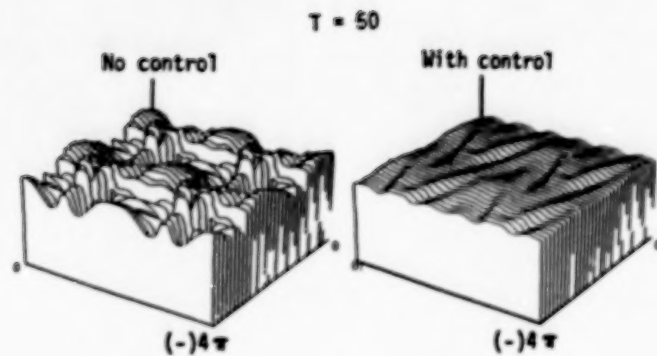
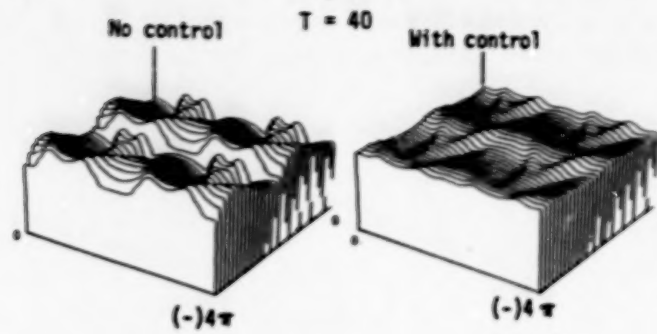
a. No control
b. With control

SURFACES OF CONSTANT TEMPERATURE

In these figures, three-dimensional representations of the temperature field (treated as a passive scalar) are displayed. The uncontrolled flow displays evidence of strong mixing and a highly convoluted temperature surface, while the controlled flow is relatively uniform and indicates local laminarization.



SURFACES OF CONSTANT TEMPERATURE (CONC.)

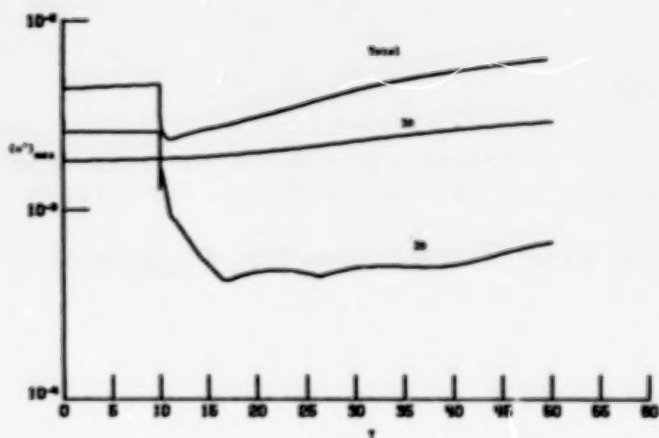


Constant valued temperature surfaces in the computational box between the lower wall and the channel centerline ($y = 0.10$).

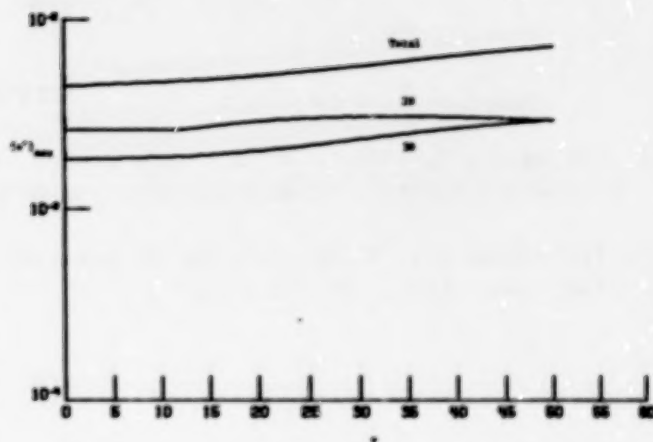
PERIODIC BOUNDARY LAYER

These figures show the time-evolution of the various Fourier components of u-component velocity in response to various control waves.

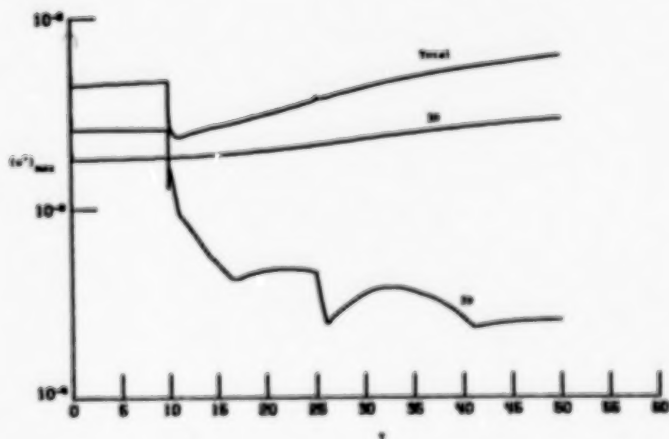
(TS Wave Cancellation ($T = 10 - 32$))



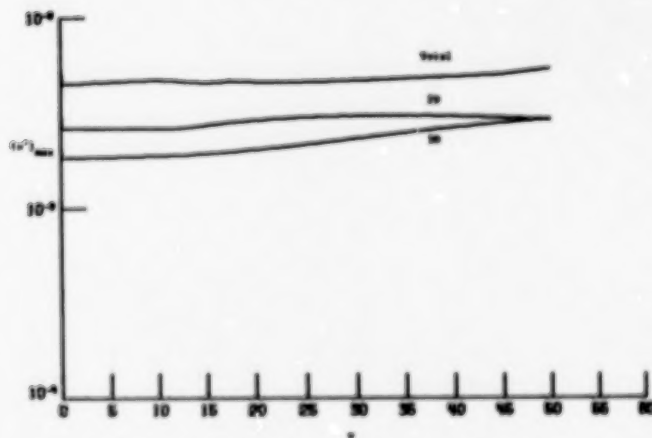
(No Control)



(TS Wave Cancellation ($T = 10 - 13, 25 - 28$))



(Passive Section ($T = 15 - 32.4$))



CONCLUDING REMARKS

- * 2D and 3D wave interaction in channel flow.
- * Preliminary calculations indicate comparable effects of passive and active control in the periodic boundary layer.
- * Passive temperature effective to tag flow dynamics.
- * Need for space-evolving numerical experiments.

REFERENCES

1. Biringen, S., Nutt, W. E., and Ceruso, M. J., "Numerical experiments on transition control by periodic suction/blowing," AIAA Journal, Vol. 25, 1987, pp. 239-244.
2. Biringen, S., "Final stages of transition in plane channel flow," J. Fluid Mech., Vol. 148, 1984, pp. 413-442.

**APPLICATION OF SOUND AND TEMPERATURE
TO CONTROL BOUNDARY-LAYER TRANSITION**

**L. Maestrello
NASA Langley Research Center
Hampton, Virginia**

**P. Parikh
Vigyan Research Associates
Hampton, Virginia**

**A. Bayliss
Northwestern University
Evanston, Illinois**

**L. S. Huang
NRC Research Associate
Langley Research Center
Hampton, Virginia**

**T. D. Bryant
NASA Langley Research Center
Hampton, Virginia**

ABSTRACT

The growth and decay of a wave packet convecting in a boundary layer over a concave-convex surface and its active control by localized surface heating are studied numerically using direct computations of the Navier-Stokes equations. The resulting sound radiations are computed using linearized Euler equations with the pressure from the Navier-Stokes solution as a time-dependent boundary condition. It is shown that on the concave portion the amplitude of the wave packet increases and its bandwidth broadens while on the convex portion some of the components in the packet are stabilized. The pressure field decays exponentially away from the surface and then algebraically, exhibiting a decay characteristic of acoustic waves in two dimensions. The far-field acoustic behavior exhibits a super-directivity type of behavior with a beaming downstream. Active control by surface heating is shown to reduce the growth of the wave packet but have little effect on acoustic far field behavior for the cases considered.

Active control by sound emanating from the surface of an airfoil in the vicinity of the leading edge is experimentally investigated. The purpose is to control the separated region at high angles of attack. The results show that injection of sound at shedding frequency of the flow is effective in an increase of lift and reduction of drag.

OBJECTIVES

The objective is to study the growth and decay of a wave packet developing over a concave-convex surface and the resulting acoustic radiations. An engineering application is the flow through a wind tunnel contraction. The concave portion is known to be potentially unstable to upstream disturbances while the convex portion is stabilizing. This instability can be reduced by active surface heating. The intensity of resulting sound may still be sufficient to trigger instability downstream, for example, on a model leading edge.

The experimental part is concentrated on separation control by sound emanating from the surface of an airfoil at high angle of attack. This reduces the extent of the separated region, thus improving performance.

OBJECTIVES

- Drag reduction by active surface heating
- Separation control by sound emanating from the surface

TOPICS OF DISCUSSION

■ Numerical

- Study of instability over a concave-convex surface
- Active control by surface heating
- Resulting sound radiation

■ Experimental

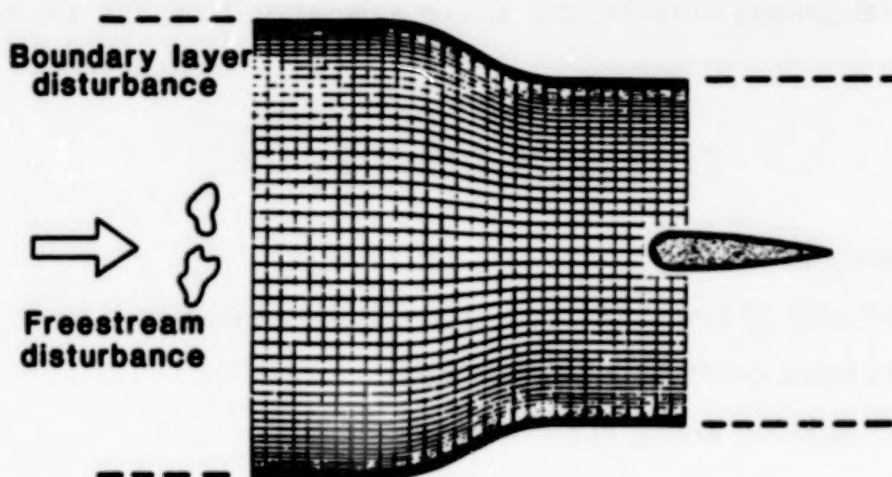
- Control of flow separation over an airfoil

APPLICATION

The geometry considered is typical of a wind tunnel contraction. The disturbances entering a wall boundary layer in a contraction may grow due to the unfavorable pressure gradient, a source of sound radiation, resulting in both standing and downstream propagating waves. In addition, a patch of turbulence (or vorticity) convecting through the pressure gradient created by the contraction geometry undergoes a variable rate of strain, thereby generating sound. The perturbed field from the boundary layer as well as from the sources embedded in the inviscid flow interact with the leading edge of the model is a possible source of transition.

This presentation includes a study over only one wall of the contraction with disturbances externally imposed in the boundary layer.

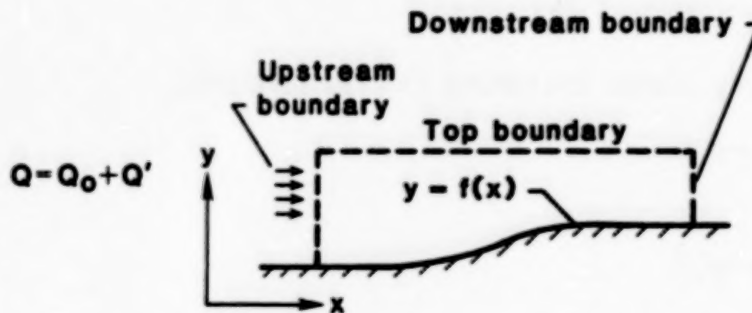
WIND TUNNEL CONTRACTION



COMPUTATIONAL MODEL

The computations are carried out using two-dimensional laminar, compressible Navier-Stokes equations written in conservation form. The finite-difference scheme used is an explicit predictor-corrector method which is second-order accurate in time and fourth order on convective terms in space. Such an accuracy is needed for reducing numerical dispersion in wave propagation problems.

A steady state is first obtained starting with a boundary-layer solution. An unsteady disturbance in the form of the Orr-Sommerfeld solution is then specified at inflow and an unsteady solution is obtained.



- 2-D Navier-Stokes equations: $W_t + F_x + G_y = 0$
 $W = (\rho, \rho u, \rho v, E)^T$
 F & G are standard flux functions
- Predictor-Corrector
- Explicit
- 4th Order accurate on convective terms in space
- 2nd Order accurate in time
- Operator splitting
- Q_0 is steady state
 Q' is Orr-Sommerfeld solution

BOUNDARY CONDITIONS

For a complete description, certain boundary conditions must be imposed. At inflow, characteristic boundary conditions are used. Three incoming characteristic variables are obtained from known solutions. In addition, one outgoing characteristic is extrapolated from the interior.

At the top and downstream, radiation boundary conditions are used. This accelerates convergence to steady state and facilitates the upper boundary to be brought closer to the surface.

At the surface, velocities and temperature are specified while the pressure is obtained from normal momentum equation.

● Inflow

■ Specify three incoming characteristics

$$\bullet p + \rho c u$$

$$\bullet v$$

$$\bullet p - \rho c^2$$

■ Extrapolate outgoing characteristic

$$\bullet p - \rho c u$$

● At top and outer boundaries

■ Radiation condition

$$\bullet p_t - \rho c u_t = 0 \text{ downstream}$$

$$\bullet p_t - \rho c v_t = 0 \text{ top}$$

● At the wall specify u, v and T

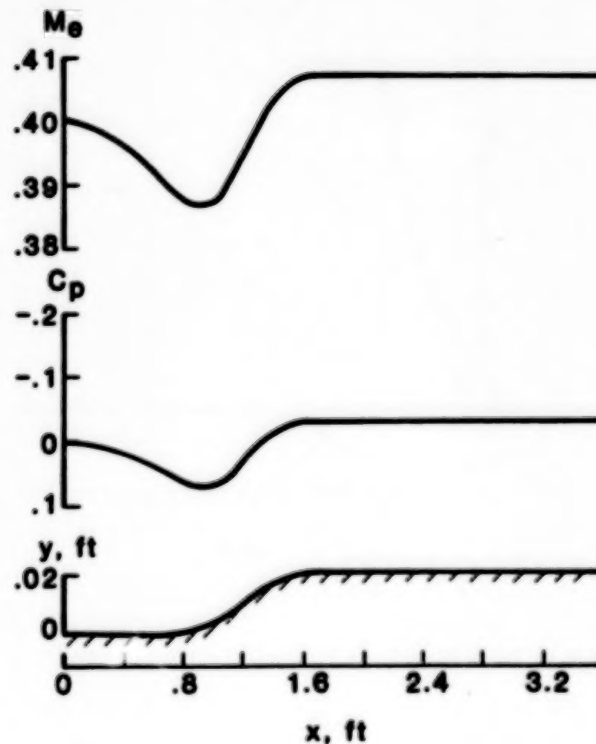
Pressure from normal momentum equation

MEAN FLOW

The surface has portions of both concave and convex curvatures. The algebraic equation describing the curve is a seventh-degree polynomial with first three derivatives zero at both ends. This curved surface is accompanied by flat portions both up and downstream. The curve rises to 0.02 ft. in a 1.2-ft. distance. The total length in the streamwise direction is 3.6 ft.

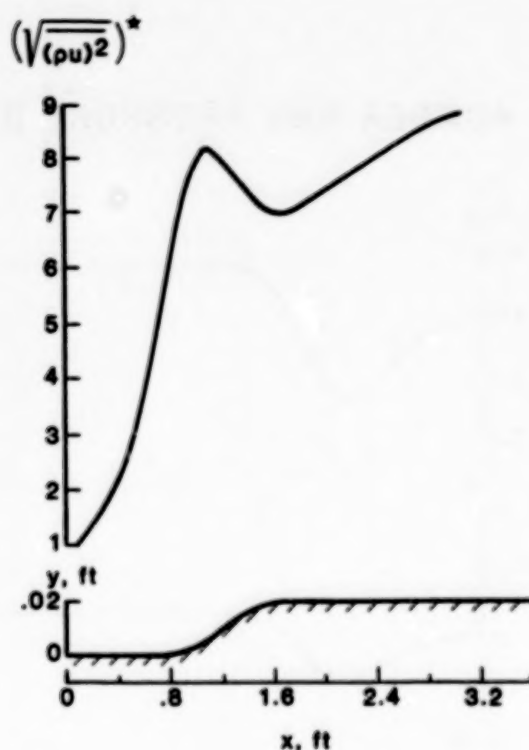
The results presented are for an inflow Mach number of 0.4 and a unit Reynolds number, based on freestream values, of 3.0×10^5 . The mean Mach number and pressure distribution are shown. The pressure gradient induced by the surface curvature decelerates the flow at first and then accelerates to a maximum Mach number of about 0.41.

MEAN MACH NUMBER AND PRESSURE DISTRIBUTION



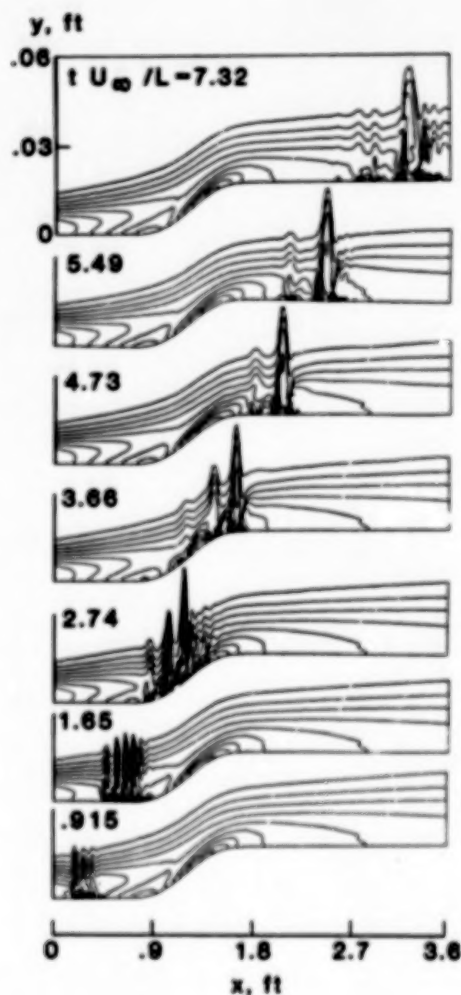
UNSTEADY FLOW - GROWTH OF DISTURBANCES

The unsteady flow is obtained by introducing disturbances (in the form of a wave packet obtained from the Orr-Sommerfeld solution) on the mean flow. The growth of the disturbances is shown in terms of the root mean square (rms) of the massflux integrated across the boundary layer. The value at each station is normalized by the inflow value. The disturbance is initially amplified on the flat portion. Additional amplification comes on the concave curvature due to the unfavorable pressure gradient. Farther downstream, the favorable pressure gradient results in a reduction of growth, followed by an exponential-like growth on the flat portion.



UNSTEADY FLOW - INSTANTANEOUS TOTAL VORTICITY

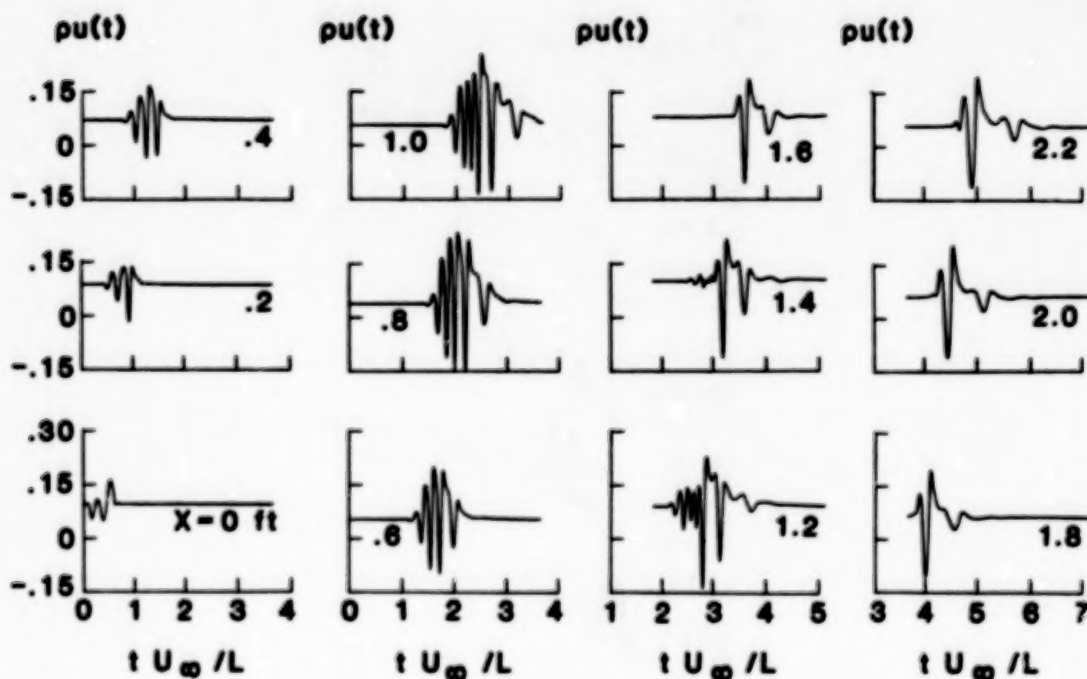
The instantaneous total vorticity is shown at successive times as the wave packet passes over the surface. The same range of vorticity is plotted for all the frames. The figure distinctively shows that as the disturbance passes over the concave portion, it changes in amplitude and broadens in bandwidth. Further, on the convex portion, drastic changes occur in the bandwidth showing that the favorable pressure gradient stabilizes certain components, as if the flow has passed through a bandpass filter. The phenomenon is strongly dependent upon the geometry of the curvature inducing the pressure gradient.



UNSTEADY FLOW - MASS FLUX ALONG THE SURFACE

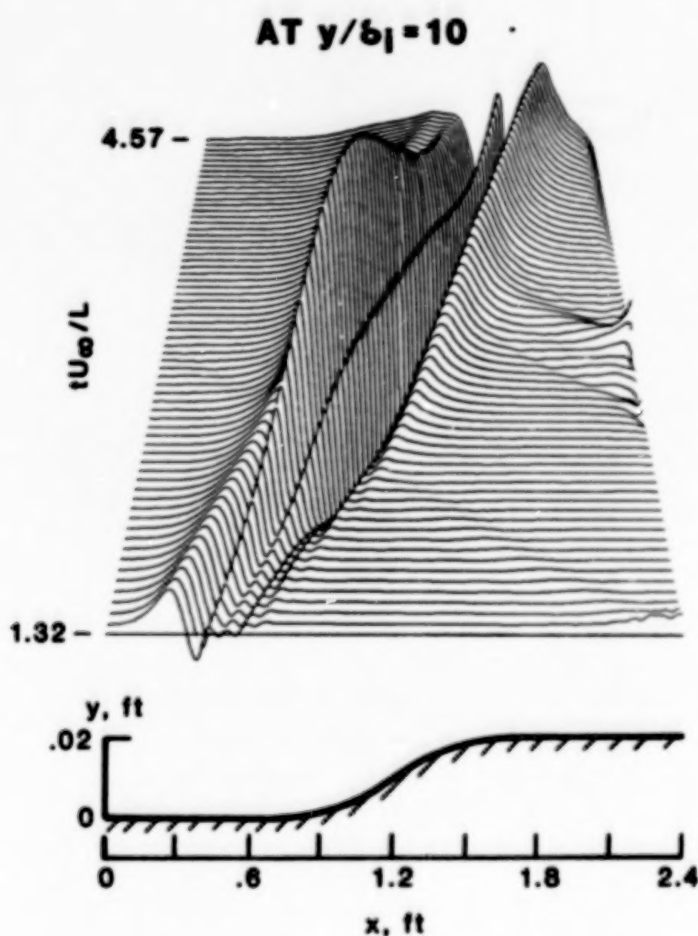
Further details of the unsteady flow are shown in terms of the mass flux variation with time at several locations along the surface for a fixed distance away from the wall in the boundary layer. It is clear that the initial packet grows both in amplitude and bandwidth over the initial portion and reaches a maximum at $x = 1.0$ feet, just downstream of the concave portion, thus showing a strong non-linear behavior. This is followed by a significant decay in the favorable pressure gradient portion of the curvature and a growth again on the flat portion downstream.

$$y/b_1 = .062, L = 1$$



SPACE-TIME GROWTH OF PERTURBATION PRESSURE

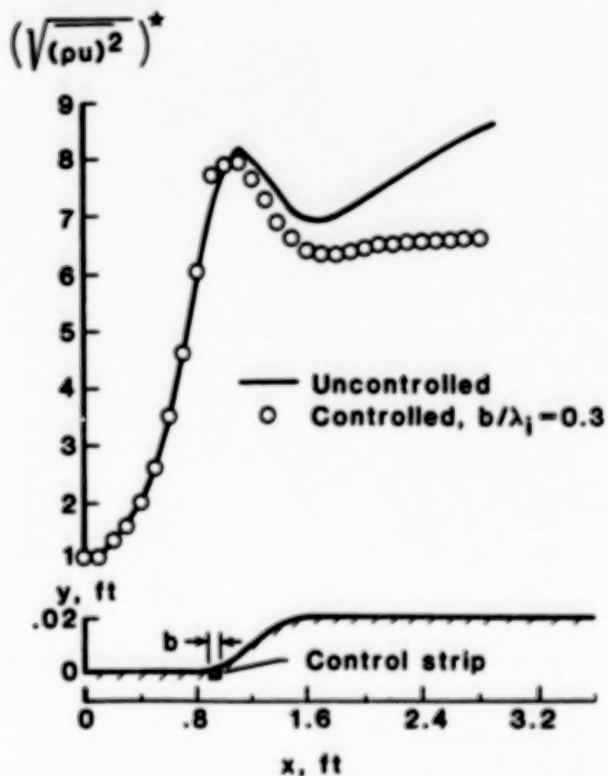
This figure shows the space-time variation of the perturbation pressure at a fixed distance away from the wall. The additional information provided by this picture is that the crests of different waves reach their maximum at different positions on the surface indicating stability for some while continuous growth for others. The time rate of change of pressure is responsible for acoustic radiations. A larger height of the surface may further reduce the growth of the disturbances, but a resulting sound field could be larger. In this context, the resulting sound can be viewed as a source of instability.



ACTIVE CONTROL - EFFECT ON DISTURBANCE GROWTH

Active control by surface heating is modeled by modifying the temperature boundary condition over a small portion of the surface. The control temperature is applied for a finite time interval coinciding with the passage of the wave packet over the control strip location. The control strip is located in the region of unfavorable pressure gradient at $x = 0.9$ feet. This location was selected because it is a region of large growth and also because the coupling of the control with the flow is favorable.

The control is not optimized. Larger reductions in growth can be achieved by optimizing amplitude and phase as well as using multiple control strips.



DETERMINATION OF ACOUSTIC FIELD

Due to the vastly different length scales between the acoustic far field and the boundary layer, it is not feasible to compute the acoustic far field concurrently with the Navier-Stokes simulation. The acoustic analogy introduced by Lighthill (ref. 1) provides a formalism to couple wave equations in order to determine the acoustic far field with the near field behavior of the viscous flow. The unsteady near field (generally including turbulent fluctuations) is used as a source term for a convective wave equation describing the far-field acoustic behavior. Our approach is to solve the linearized Euler equations using the pressure computed from the Navier-Stokes solution as a time-dependent boundary condition. We ignore the curvature of the surface because it is considered negligible on the acoustic length scale.

- Due to vastly different length scales between the acoustic far-field and the boundary layer, it is not feasible to compute acoustics from the Navier-Stokes solution
- The acoustic field is evaluated by solving linearized Euler equations using pressure from the N-S as time dependent boundary condition
- This approach is an exact instance of the Lighthill's acoustic analogy

$$p_t + p_x + \frac{(u_x + v_y)}{M^2} = 0$$

$$u_t + u_x + p_x = 0$$

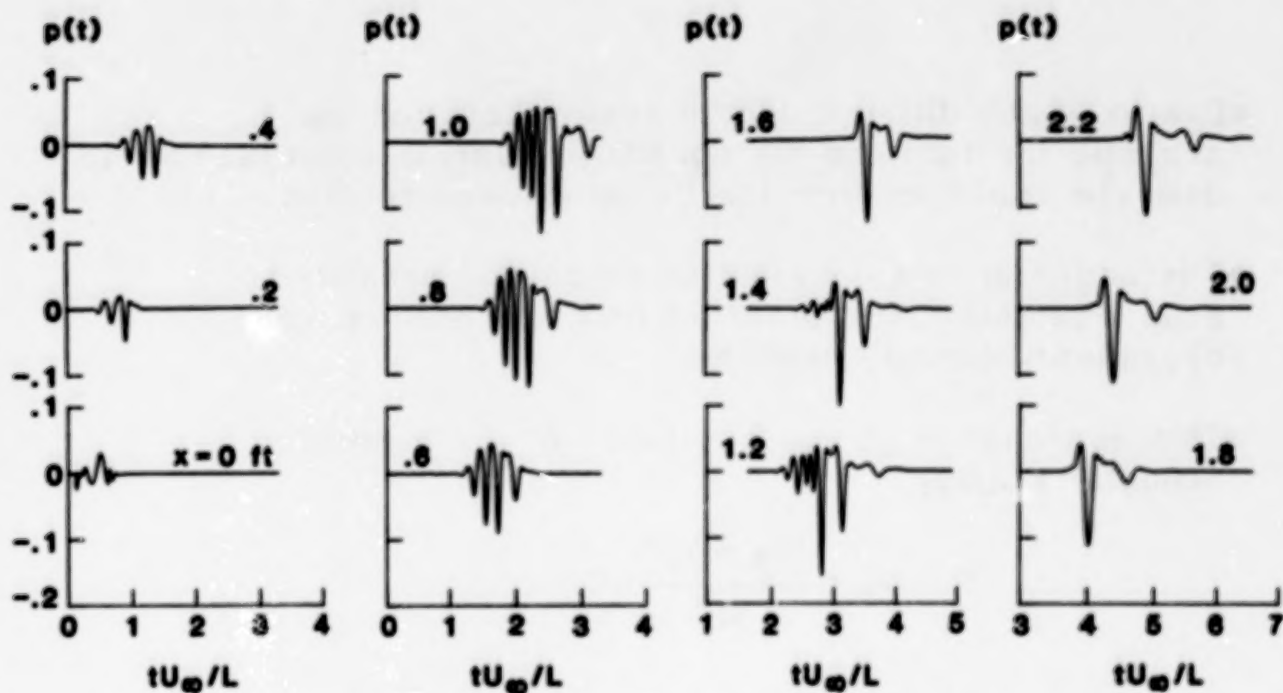
$$v_t + v_x + p_y = 0$$

B.C. $p(x,0,t) \rightarrow$ known from the N-S solution

WALL PRESSURE PERTURBATION ALONG THE SURFACE

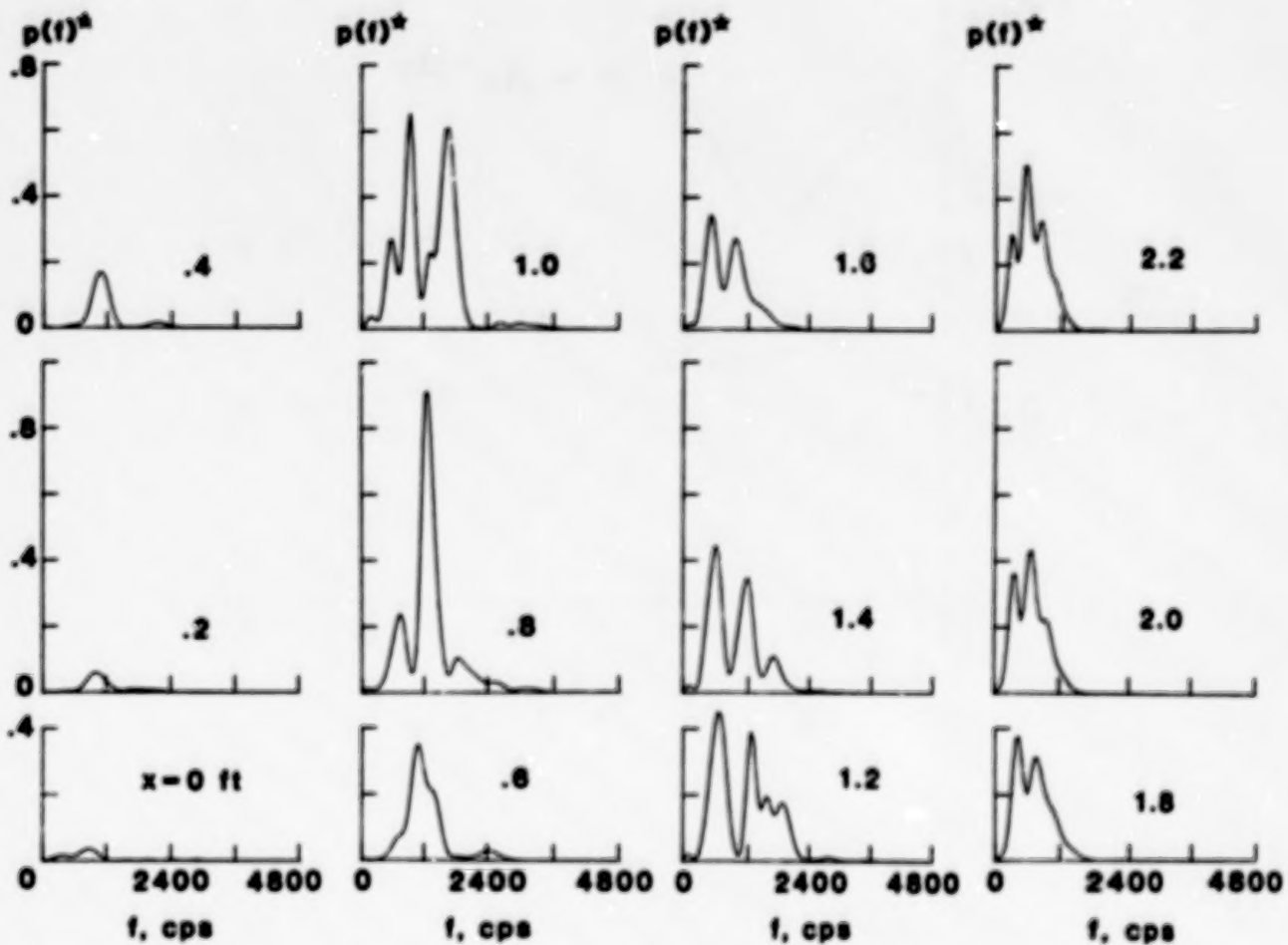
The acoustic radiations, which depend on the time rate of changes within the flow, are present even when the flow is being stabilized. In addition, acoustic radiations are known to produce instability leading to transition. Therefore, it is important to study not only the flow instability but the acoustic radiations as well.

The pressure perturbation versus time is shown at different stations along the wall. This is used as an input to the linearized Euler equations to calculate the acoustic field. It may be noticed that the maximum amplitude and bandwidth are around $x = 1.0$ ft., which is on a location corresponding to maximum growth.



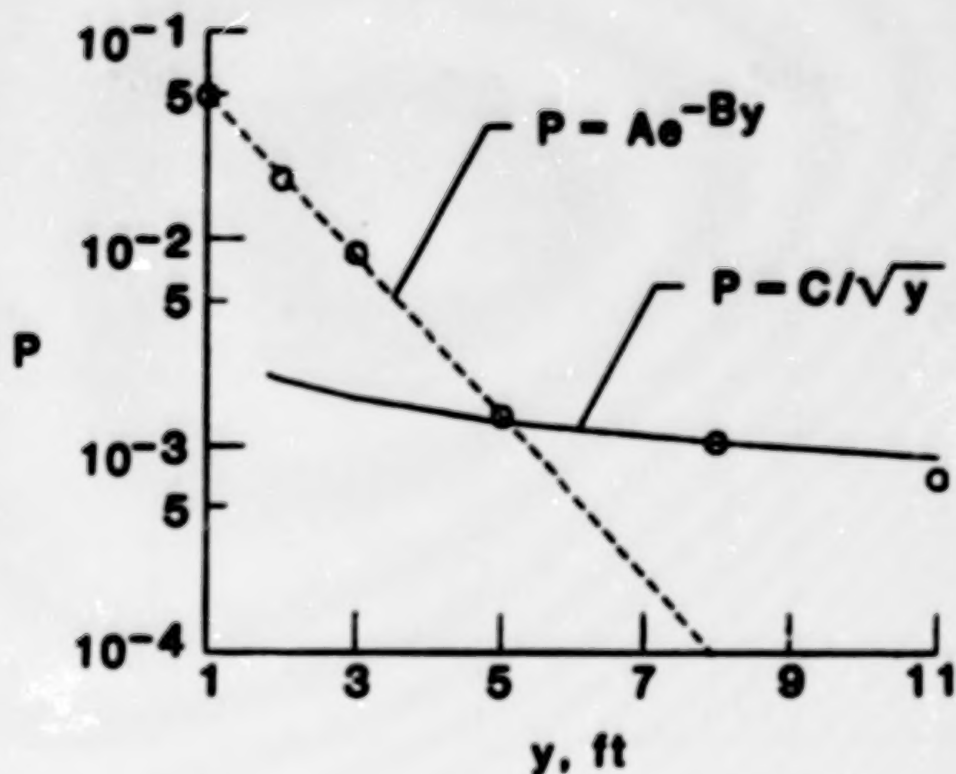
POWER SPECTRA OF WALL PRESSURE PERTURBATIONS

The power spectral density of the wall pressure shows that in addition to the two input frequencies comprising the wave packet, two other frequencies appear between $x = 0.8$ ft. and 1.2 ft. carrying most of the energy. This is a result of the instability produced by the concave surface. In the convex region and the flat region that follows, the energy content of these two additional modes is reduced drastically and the two original frequencies reappear at $x = 1.6$ ft.



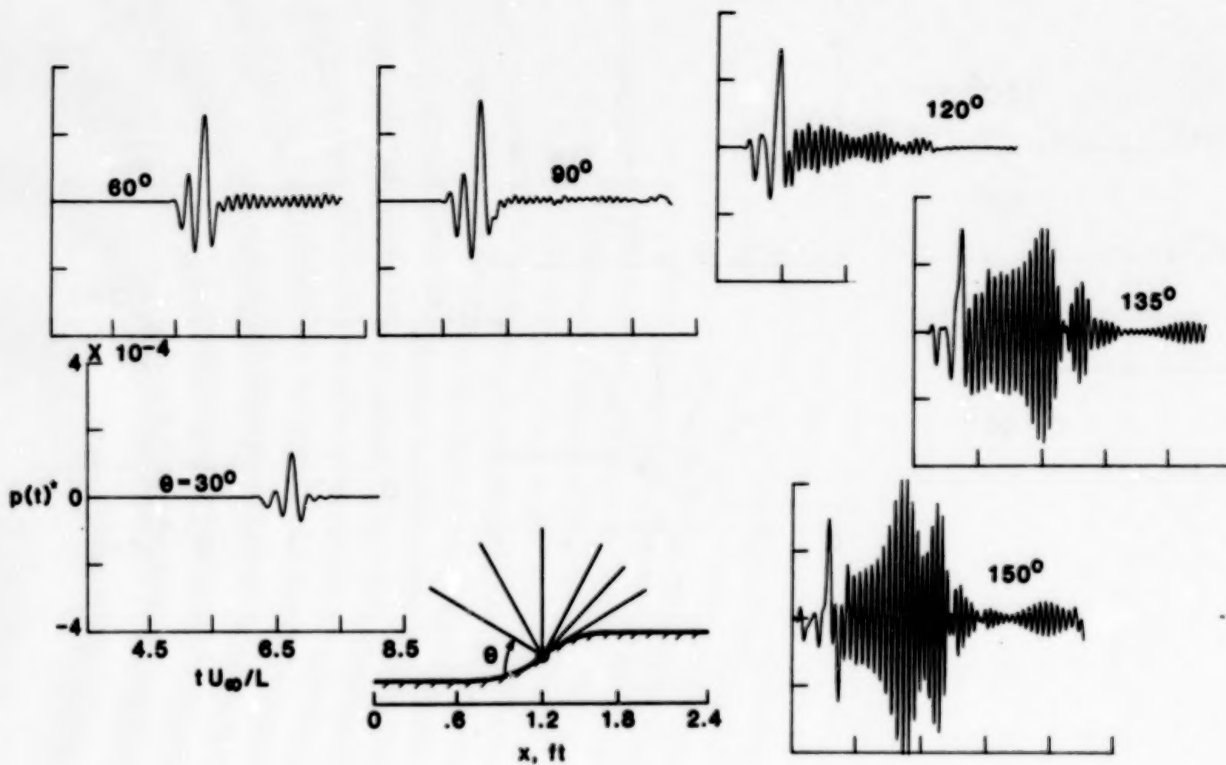
DECAY OF TOTAL POWER WITH DISTANCE FROM THE SURFACE

In order to establish the near- and the far-field behavior, total acoustic power is plotted against the distance from the wall. Two distinct regions can be identified, one close to the boundary ($y \sim 5$ ft.) where the decay is exponential and the other farther away with an algebraic decay, the acoustic far field.



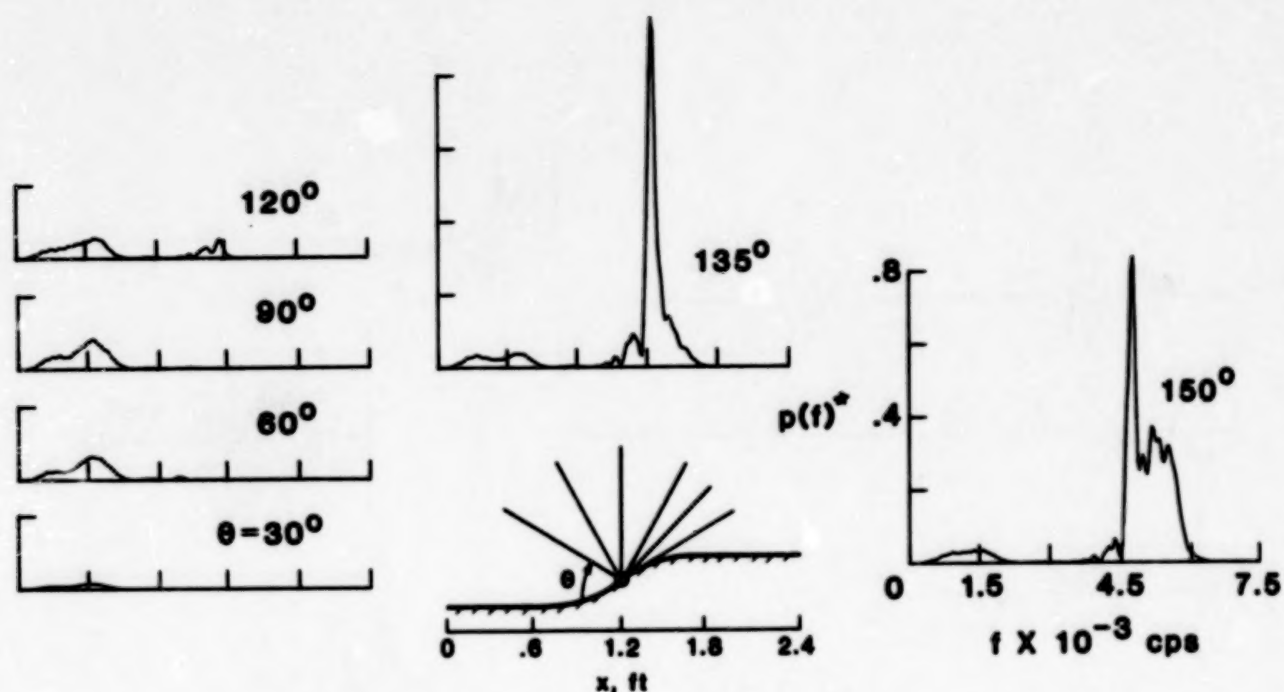
ACOUSTIC PRESSURE AT 11 FT. RADIUS

The acoustic pressure at a radius of 11.0 ft. from the surface is shown at various angular positions between 30° and 150°. Two distinct features are noticeable. One is the sound resulting from the input instability. This reaches the far field at different times due to convection. The other is the sound radiated due to the growth and decay of the wave packet. This component has strong beaming characteristics in the downstream direction. In addition, the modulation resulting from the passage of the wave packet on the curved surface can be clearly seen. Such strong amplitude and directivity have special significance when originating from a wind tunnel contraction since they may trip instability at the model's leading edge.



PSD OF ACOUSTIC PRESSURE AT 11 FT. RADIUS

The power spectral density (PSD) of the radiated acoustic field is shown at 11.0 ft. from the surface at various angular positions. Most of the sound is directed downstream with a widening in bandwidth near $\theta = 150^\circ$. The predominant radiation frequencies are those resulting from the growth and decay of the wave packet.

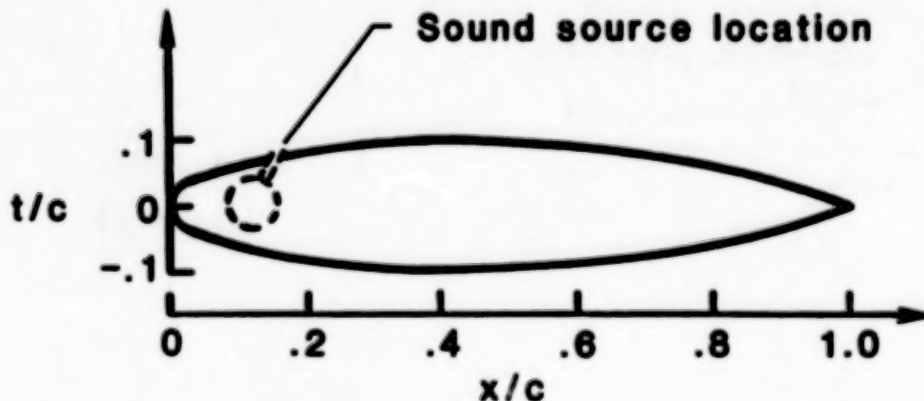


SEPARATION CONTROL BY SOUND OVER AN AIRFOIL

This section concerns an experiment designed to study the effect of sound emanating from the surface of an airfoil on the separated flow at higher angles of attack. At high angles of attack the free shear layer, which sheds from the point of separation, displays the characteristic instability, whereby a sequence of discrete vortex forms. The aim is to study the coupling between the sound and the flow and its effect on separation. This coupling is utilized to increase circulation, stall angle, as well as to reduce the drag of an airfoil.

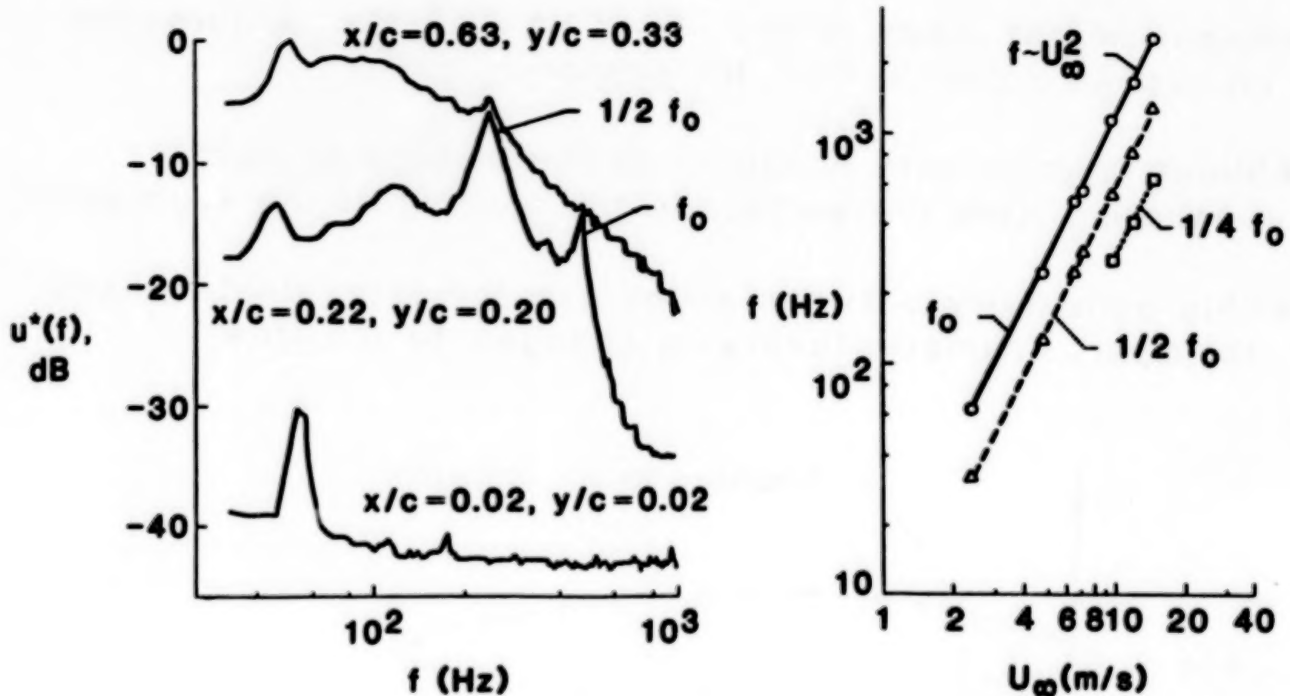
The experiment was conducted in the 2- by 6-inch wind tunnel at low Reynolds number. Smoke visualization and a hot wire were used to study the flow.

- Experimental study of the effect of acoustic perturbation on pressure distribution, lift and drag
- Shear layer is very sensitive to the excitation field emanating from the surface in the vicinity of the separation
- This sensitivity between sound and the local field is used to impart dramatic favorable changes to the flow



RESULTS - BEHAVIOR OF THE SHEAR LAYER

At high angles, $\alpha = 15$ and 20 degrees, the flow separates over most of the upper surface. Typical velocity power spectra at different locations over the upper surface of the airfoil are shown (left). At $x/c = 0.02$, only a low-frequency peak is observed. This peak frequency is approximately 50 Hz and corresponds to the "shedding" frequency of the wake region. Further downstream from the leading edge, $x/c = 0.22$, other peaks appear with frequencies of 125 , 250 , and 500 Hz. This observation suggests that the separated shear layer forms and develops with a fundamental frequency of about 500 Hz at a distance away from the leading edge. We notice also that the predominant frequencies in the shear layer vary with the second power of freestream velocity (right figure).



ORIGINAL PAGE
BLACK AND WHITE PHOTOGRAPH

RESULTS - SMOKE VISUALIZATION

A smoke visualization technique is used to see the effectiveness of control by sound. For the uncontrolled case, a large region of separation can be seen on the upper surface. Separation control is achieved by sound injected from a narrow slot located at $x/c = 0.15$ on the upper surface. When forced excitation at one of the subharmonic frequencies is applied, the separated region becomes drastically reduced. The figure shows the controlled and the uncontrolled pictures.

It is remarkable that a single injection gap can induce such a dramatic change in reducing the area of separation in contrast to the relatively modest control that is achieved at small angles of attack.

$$Re_c = 3.5 \times 10^4, f = 100 \text{ Hz}$$

UNCONTROLLED



$\alpha = 15^\circ$

CONTROLLED



$\alpha = 20^\circ$



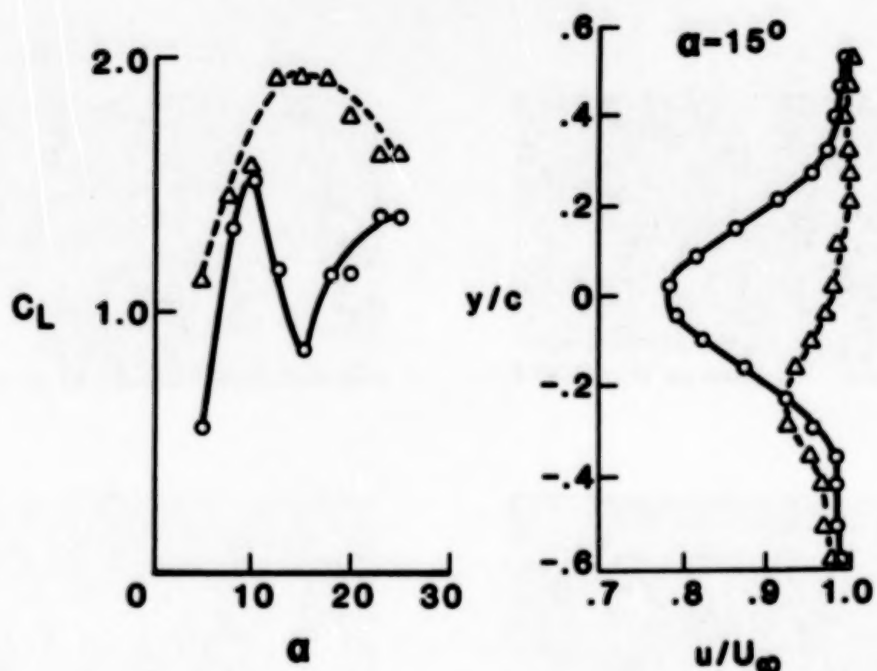
~~ORIGINAL PAGE IS~~
~~OF POOR QUALITY~~

CONTROL OF LIFT AND WAKE PROFILES

The effectiveness of control is plotted in terms of the lift coefficient versus the angle of attack and a typical wake profile at one angle of attack. The gain in lift over the whole range of angle of attack is apparent. Similarly, the defect in the wake profile becomes much smaller, indicating a reduction in drag.

$$Re_c = 3.5 \times 10^4$$

△ Controlled
○ Uncontrolled



CONCLUDING REMARKS

- Flow control using active surface heating and sound is a powerful and effective technique

BENEFITS

- Development of low drag configurations by control for laminar and turbulent flows
- Optimization of control technique for flows with periodic and random behavior

FUTURE DIRECTIONS

- Extension to turbulent and high speed flows
- Application to realistic aircraft configurations
- Design of wind tunnel contractions with minimum flow and acoustic interference

REFERENCE

1. Lighthill, M. J.: On Sound Generated Aerodynamically. I. General Theory, Proc. Roy Soc. A., 211, 1952, pp. 564-587.

**NEAR-FIELD NOISE PREDICTIONS
OF AN AIRCRAFT IN CRUISE**

**John W. Rawls, Jr.
PRC Kentron, Inc.
Hampton, Virginia**

INTRODUCTION

The application of laminar-flow wing designs will offer significant drag reduction and fuel savings on large commercial transports. Traditionally, surface contamination, surface defects, vibration and turbulence have prevented practical application on commercial aircraft. These concerns are being overcome through innovative research.

Noise generated by the aircraft is now being investigated as a cause of premature transition of a laminar boundary layer. An acoustic disturbance with the correct frequency and intensity is known to cause transition of a laminar boundary layer under laboratory conditions. It is speculated that aerodynamic noise sources may have the correct characteristics to cause boundary-layer transition under flight conditions.

One important element in determining whether a laminar boundary layer will transition (due to the presence of an acoustic source) is an accurate prediction of the noise source and its characteristics. Predictions yield not only the total noise level, which can be verified by measurements, but also information concerning the characteristics of the individual noise sources. The prediction of the near-field noise environment of an aircraft in cruise has become an important element in the research and development of wing designs that can maintain laminar flow at a cruise speed of Mach 0.8.

CAUSES OF TRANSITION

- **Surface Contamination**

 - Insect Residue**

 - Ice Crystals**

- **Surface Defects**

- **Vibration**

- **Turbulence**

- **Noise**

LOCKHEED NEAR-FIELD NOISE PREDICTION PROGRAM

A computer program was developed by Lockheed-Georgia Company for the purpose of predicting the near-field acoustic environment of an aircraft in cruise (Refs. 1, 2, 3). This program is designed to compute the 1/3 octave band spectra and Overall Sound Pressure Level (OASPL) at a point on an aircraft operating at high altitude and high-speed conditions.

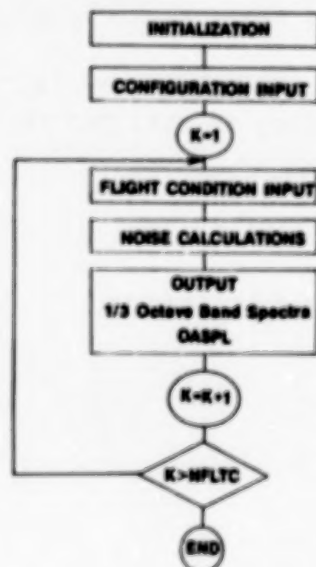
Noise sources predicted by the code can be divided into two categories: propulsion sources and airframe sources. The propulsion system of the aircraft is assumed to be a turbojet or turbofan engine. The components of the engine which produce noise are fan/compressor, combustor, turbine and jet. Acoustic suppression material may be used in the engine and is accounted for in the prediction procedure.

The airframe itself is also a producer of noise. The two airframe sources predicted by the code are trailing-edge noise and turbulent boundary-layer noise.

The noise source algorithms are based on empirical formulations derived from data at near sea level conditions with relatively low or no forward speed effects. Since the noise predictions are for high speed and high altitude, corrections for forward speed and altitude are required.

A forward speed correction is required to determine the correct emission angle and propagation distance at the time the sound is emitted. The correction is a function of the observed angle and distance at the time the sound is received. Forward speed corrections are also made to the OASPL to account for convective and dynamic amplifications. (A detailed discussion of these forward speed corrections can be found in Ref. 1.)

An altitude correction is made by adjusting the acoustic impedance to correspond to the ambient conditions at altitude. Other altitude corrections such as atmospheric attenuation and atmospheric absorption are assumed to be small in the near field.



NEAR-FIELD NOISE SOURCES

For the purpose of this report, the propulsion system will be a high-bypass turbofan engine. This propulsion system is widely used in large commercial transports where laminar-flow wing designs would be most beneficial. Noise prediction procedures are provided for the four basic jet engine components i.e., the fan/compressor, combustor, turbine and jet. With these basic components the noise generated by a high bypass turbofan can be modeled.

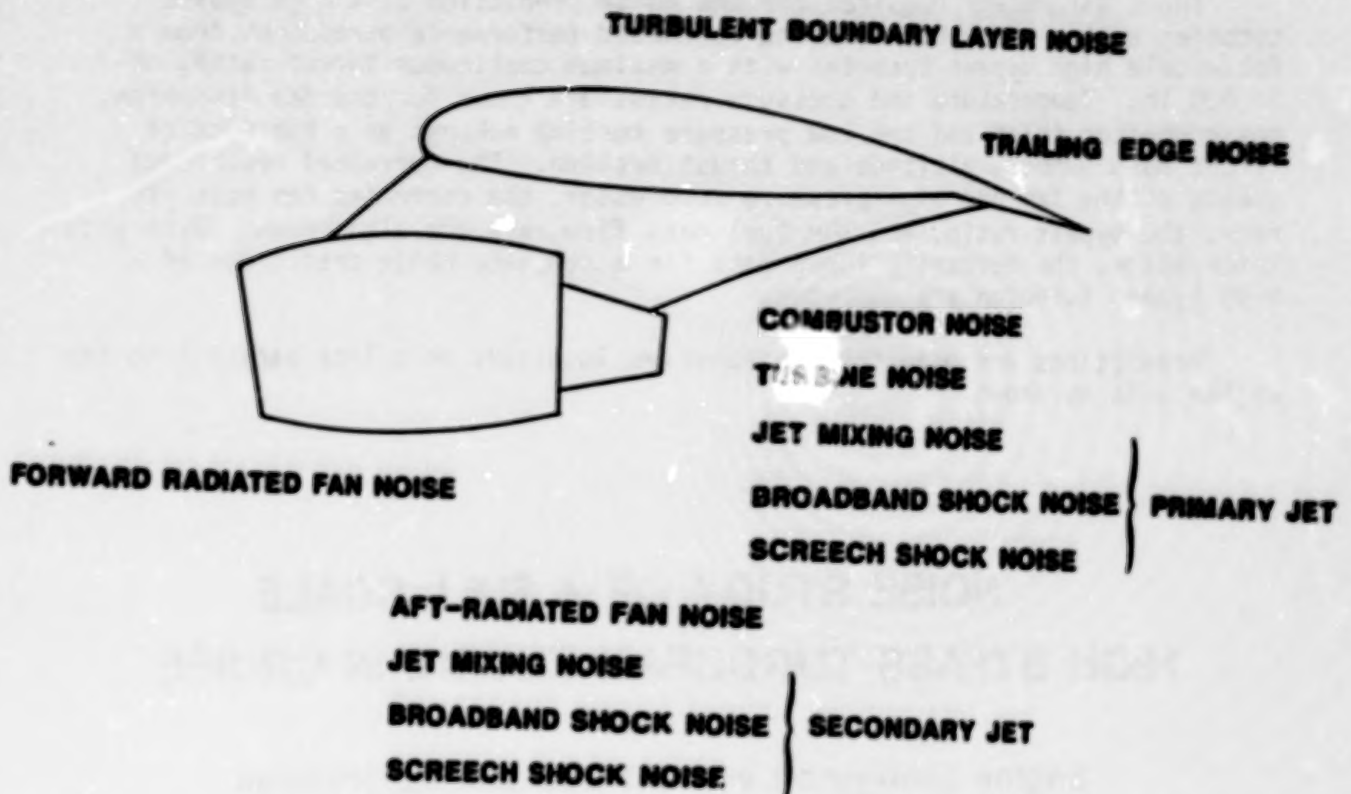
Fan noise is generated by the fan blade interacting with the incoming flow. Noise from the fan can radiate forward through the inlet and aft through the secondary jet nozzle. In addition to the broadband component of the noise spectra, discrete tones occur at the blade passing frequency and its harmonics. If the tip speed of the fan blade is supersonic, subharmonics of the blade passing frequency are also generated which only propagate forward. Compressor noise is predicted by the same method used to predict fan noise. However fan noise usually dominates compressor noise and is not considered in this report.

Combustor noise and turbine noise both propagate through the primary nozzle. Combustor noise is a low-frequency source while turbine noise is a high-frequency source. Like fan noise, turbine noise is composed of a broadband spectra and discrete tones occurring at the blade passing frequency and higher harmonics. Typically, the blade passing frequency of the turbine is so high that only the fundamental tone is included in the spectra.

Jet noise, which is made up of three components, propagates from both the primary nozzle and the secondary nozzle. The first component of jet noise is mixing noise. Mixing noise is always present in a jet and is the result of the jet interacting with the ambient air. The second and third components of jet noise are broadband shock and screech shock noise. Both broadband shock and screech shock occur only when the jet velocity exceeds the local speed of sound in the jet. The onset of broadband shock noise is predicted as soon as the jet flow conditions are supersonic. The onset of screech shock noise is not well defined and can usually be controlled with an appropriate nozzle design. Consequently screech shock noise is not considered in this report.

The two airframe sources, turbulent boundary-layer noise and trailing-edge noise are also included for study in this report.

NEAR-FIELD NOISE SOURCES



HIGH BYPASS TURBOFAN MODEL DESCRIPTION

Input parameters required for the noise prediction of a high bypass turbofan engine are obtained using estimated performance parameters from a full-scale high bypass turbofan with a maximum continuous thrust rating of 38,000 lb. Temperature and pressure ratios are known for the fan discharge, the combustor inlet and the low pressure turbine exhaust as a function of flight Mach number, altitude and thrust setting. The corrected rotational speeds of the fan and high pressure compressor, the corrected fan mass flow rate, the bypass ratio, and the fuel mass flow rate are also known. With this information, the necessary input data for a complete noise prediction of a high bypass turbofan are computed.

Predictions are made for two observer locations on a line parallel to the engine axis as shown.

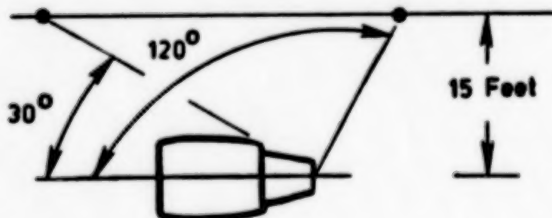
NOISE STUDY OF A FULL SCALE HIGH BYPASS TURBOFAN ENGINE IN CRUISE

Engine configured without acoustic suppression

Engine performance data given as a function of

- Altitude
- % Thrust
- Flight Mach No.

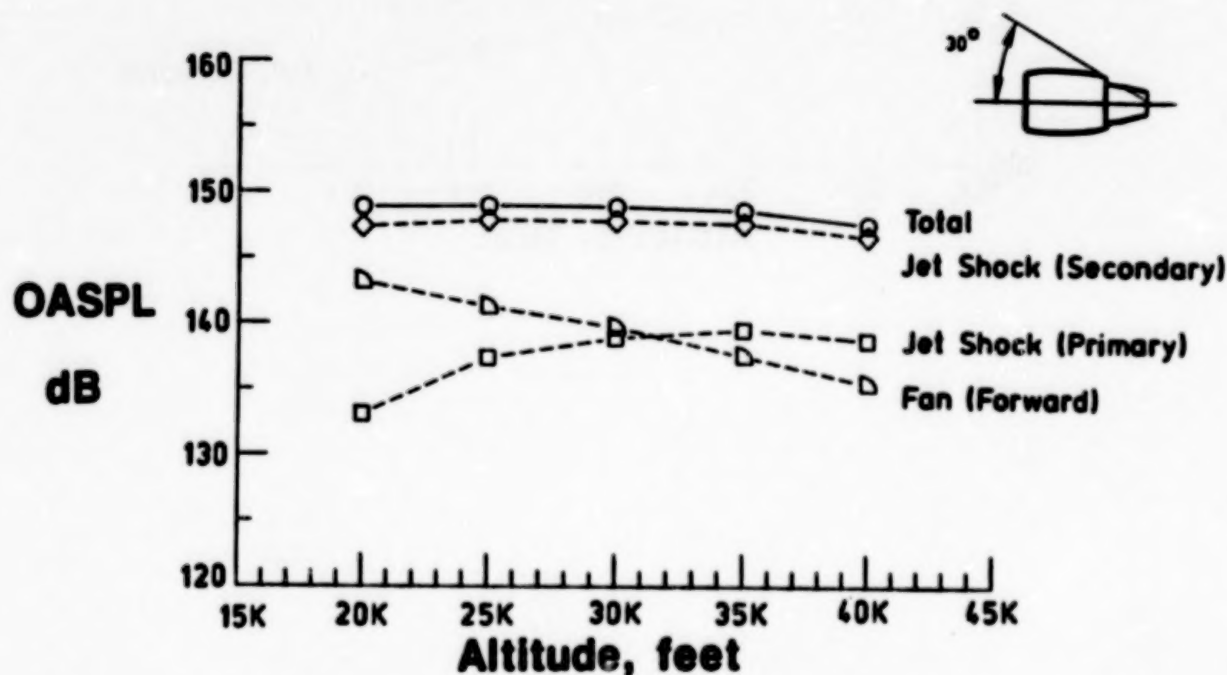
OBSERVER LOCATION



ALTITUDE VARIATION

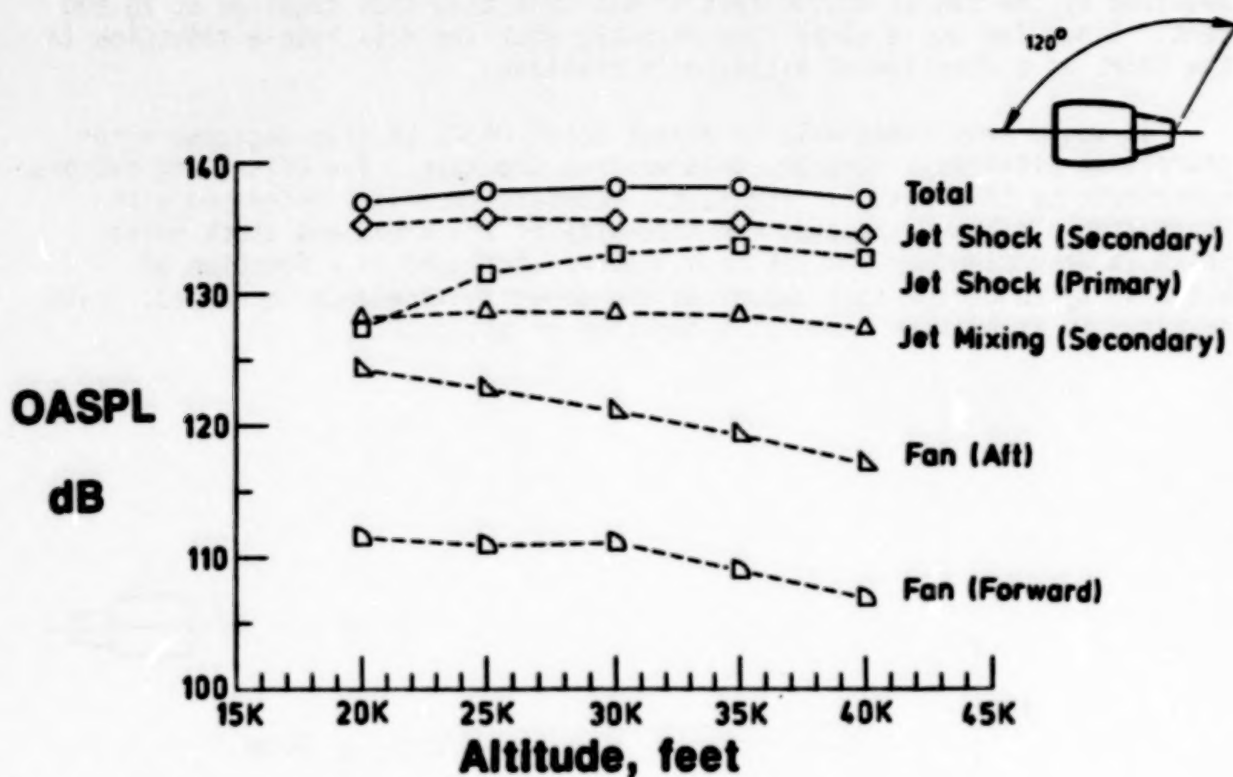
Noise levels are investigated by varying the altitude from 20,000 feet to 40,000 feet while operating at maximum continuous thrust and a flight Mach number of 0.8. Parameters relevant to noise predictions and engine performance vary significantly with altitude. For example the mass flow rate required by the fan at 40,000 feet is 46% less than that required at 20,000 feet. Since fan noise correlates directly with the mass rate a reduction in the OASPL as a function of altitude is realized.

It would seem reasonable to expect total OASPL to also decrease with increasing altitude. However, this was not the case. Two offsetting factors contribute to this result. First, the acoustic impedance decreased with increasing altitude. Second, the intensity of the broadband shock noise, which is determined by the jet Mach number, increased as a function of altitude by about the same amount as the acoustic impedance decreased. This resulted in a constant OASPL as a function of altitude.



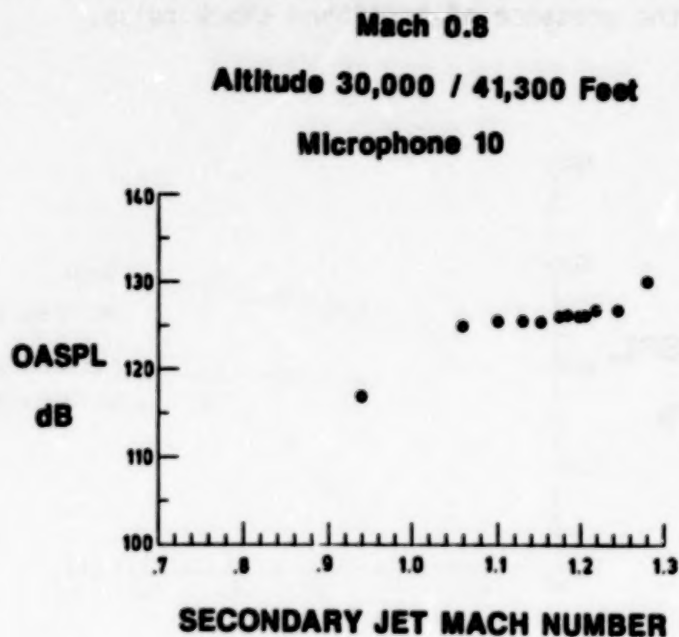
ALTITUDE VARIATION

Mach 0.8
100% Maximum Continuous Thrust

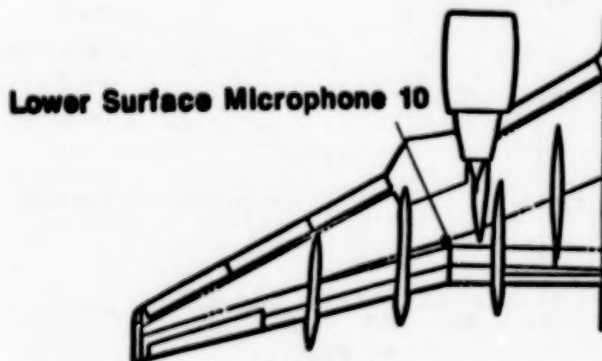


BOEING 757 GLOVE TEST DATA

During the Boeing 757 glove test, data were obtained over an altitude range of 30,000 feet to 41,300 feet. The OASPL is plotted as a function of the secondary jet Mach number as shown. In this figure, the OASPL maintains a level of 126 dB for secondary jet Mach numbers between 1.0 and 1.28. When the jet Mach number exceeds 1.0, broadband shock noise is present and follows the trend of constant noise level as a function of altitude. When the jet Mach number is less than 1.0, the noise level is reduced as would be expected since broadband shock noise is not present in the secondary jet.

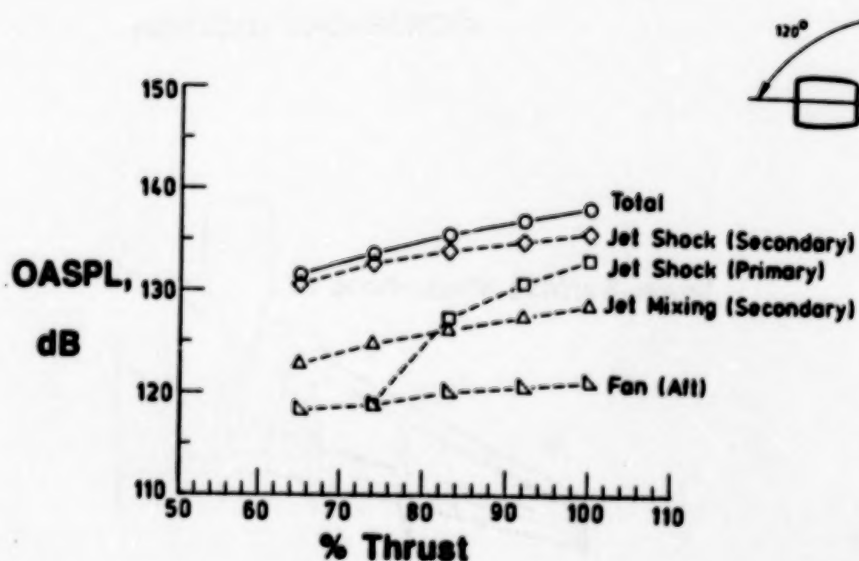
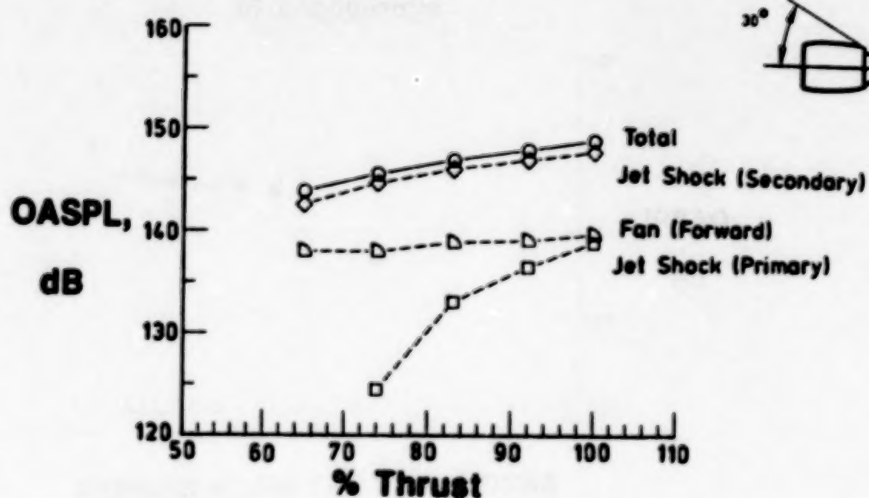


MICROPHONE LOCATION



THRUST VARIATION

Noise levels are also investigated by varying the thrust of the jet while operating at a flight Mach number of 0.8 and an altitude of 30,000 feet. As expected the total OASPL increases with increasing thrust. However the increase is not as great as might be expected. A reduction of 64% in thrust results in only a 5 dB decrease at 30° and 6 dB at 120°. The dominate noise source is again broadband shock noise from the secondary jet. In fact the remaining propulsion noise sources contribute very little to the total OASPL. Examination of the jet conditions indicates that additional thrust is generated by the primary jet with the jet Mach number increasing from .96 at 64% thrust to 1.17 at 100% thrust. The secondary jet conditions on the other hand increase from 1.11 at 64% thrust to 1.18 at 100% thrust. It is worth noting that the secondary jet conditions are supersonic even at low thrust accounting for the presence of broadband shock noise.



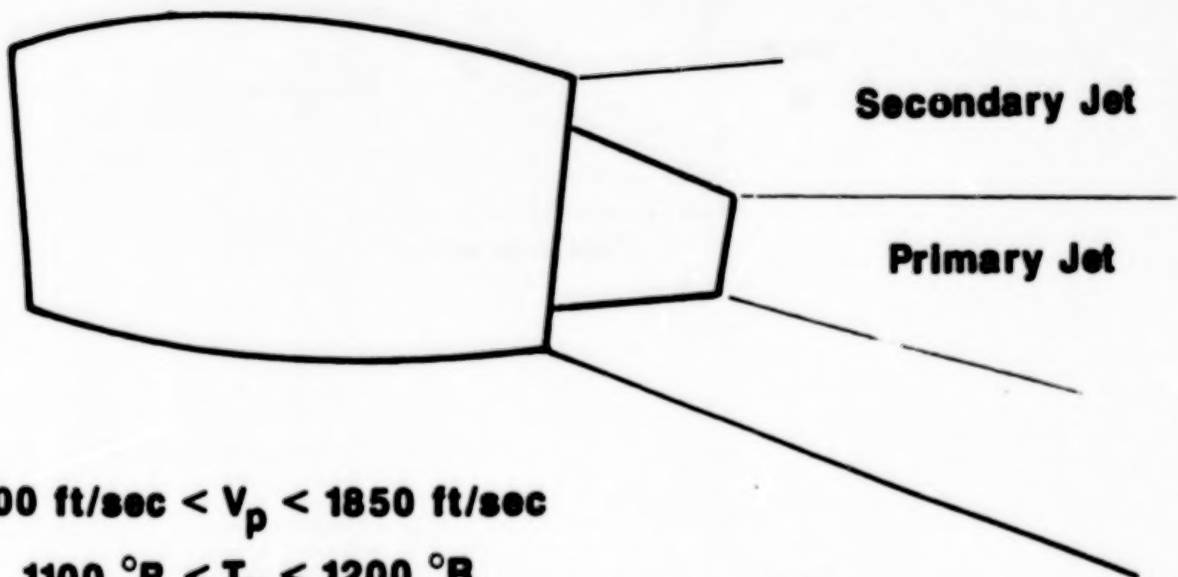
TYPICAL JET CONDITIONS DURING CRUISE

Broadband shock noise from the secondary jet has emerged as a very important noise source during cruise. Even though the secondary jet velocity at total temperatures is much lower than the primary jet, the Mach number in the secondary jet is typically supersonic when varying altitude and thrust. The supersonic conditions in the secondary jet are primarily the result of the low total temperature in the jet. Not only is broadband shock noise typically present in the secondary jet but the secondary flow acts as a shield to reduce the effect of the noise levels produced by the primary jet.

$$1000 \text{ ft/sec} < V_s < 1200 \text{ ft/sec}$$

$$500 \text{ }^\circ\text{R} < T_s < 575 \text{ }^\circ\text{R}$$

$$1.00 < M_{js} < 1.15$$



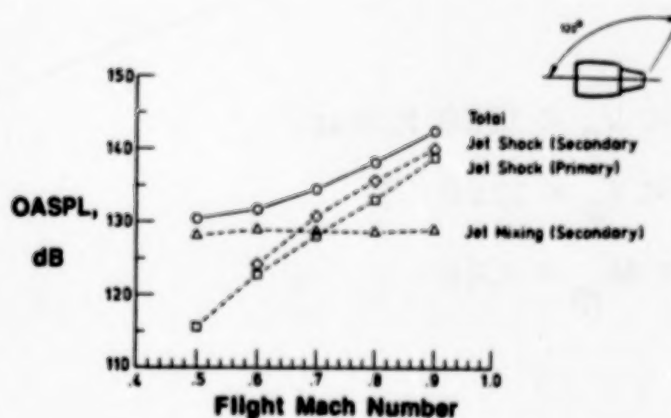
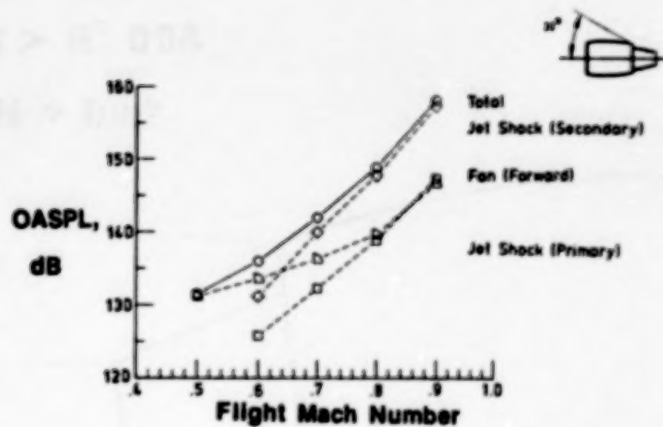
$$1400 \text{ ft/sec} < V_p < 1850 \text{ ft/sec}$$

$$1100 \text{ }^\circ\text{R} < T_p < 1200 \text{ }^\circ\text{R}$$

$$0.93 < M_{jp} < 1.25$$

FLIGHT MACH NUMBER VARIATION

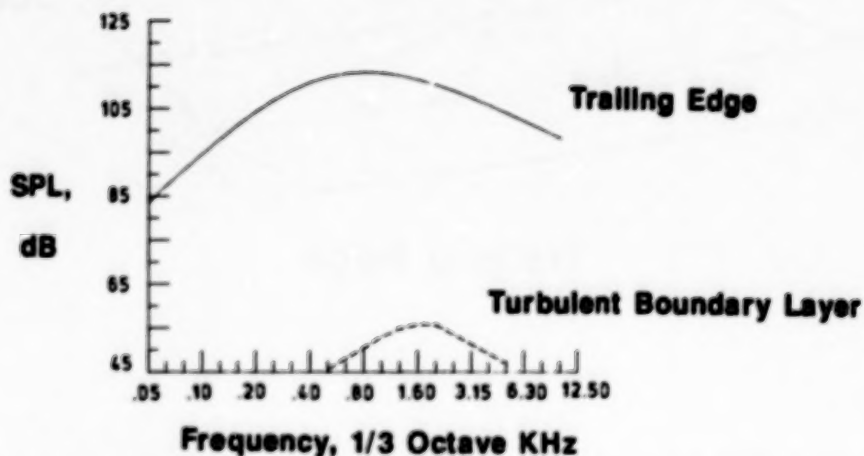
Finally noise levels are examined by varying the flight Mach number from 0.5 to 0.9 in 0.1 increments. Thrust and altitude are maintained at 100% and 30,000 feet, respectively. At a flight Mach number of 0.5, broadband shock noise is absent from both the primary and secondary jets. An increase in the flight Mach number to 0.9 dramatically increases the total OASPL at both observer locations. An increase of 26 dB is observed at 30° and an increase of 12 dB is observed at 120°. This increase in noise is the result of several factors. One factor is that the engine performance parameters are at higher levels as the flight Mach number increases; another is that the forward speed correction for the noise sources is larger as the flight Mach number increases.



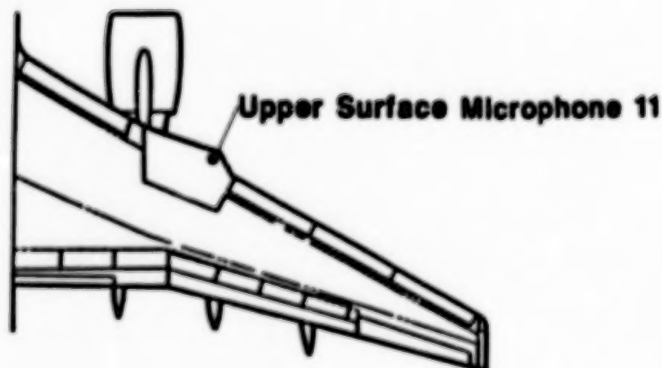
AIRFRAME NOISE SOURCE SPECTRA

Airframe sources are important in determining the total OASPL especially in cases where a surface is shielded from the propulsion system. Recent measurements on the wing of a Boeing 757 showed that noise levels on the upper surface were unaffected by increases in the engine RPM which is mounted by a pylon from the wing lower surface. This spectrum shows the contributions of turbulent boundary-layer noise and trailing-edge noise at an upper surface point near the leading edge of a Boeing 757 wing. The turbulent boundary-layer noise levels predicted by this code are typically 10 to 15 dB lower than the trailing-edge noise levels as shown. Therefore turbulent boundary-layer noise does not contribute to the total OASPL.

Altitude 40,000 Feet; Mach 0.8; Mic 11



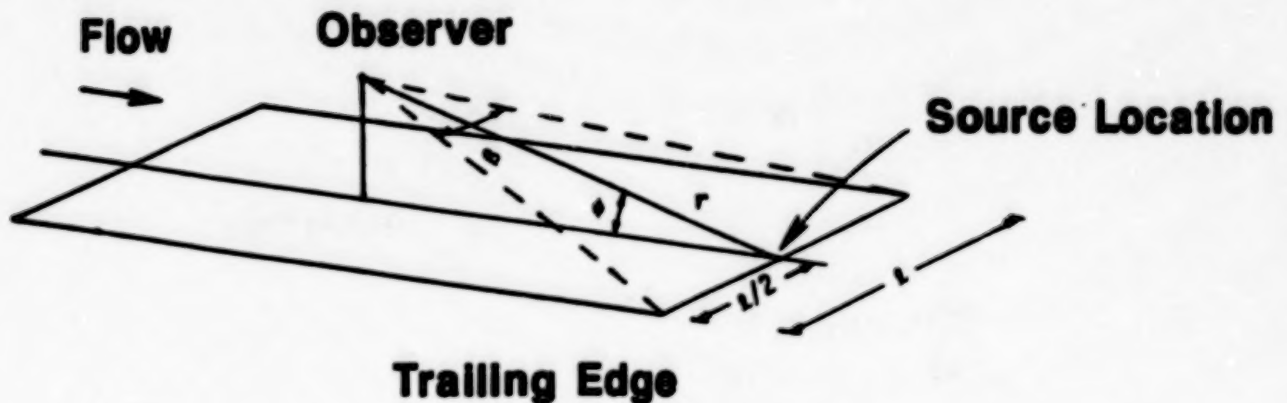
MICROPHONE LOCATION



TRAILING-EDGE NOISE

Trailing-edge noise is the result of a sudden change in the pressure as a boundary layer is convected past a surface trailing edge. As the boundary layer approaches the trailing edge, the pressure differential between the upper and lower surface is forced to zero to satisfy the Kutta condition. This, in turn, results in an induced pressure field which propagates away from the trailing-edge region (Ref. 4).

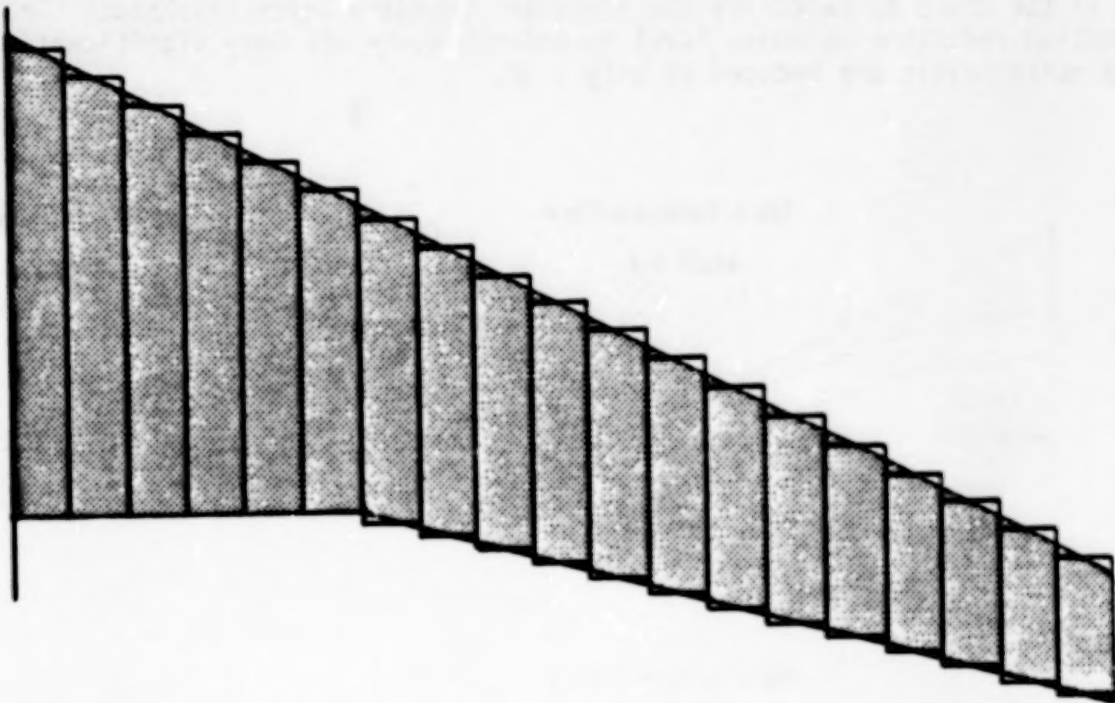
The algorithm for the prediction of trailing-edge noise is based on a flat plate analysis. The observer is restricted to be on the centerline of the plate and the flow must leave perpendicular to the trailing edge.



Source/Observer geometry for trailing edge noise

TRAILING-EDGE NOISE

Trailing-edge noise is a distributed source and not conducive to point source analysis. The wing of a Boeing 757 therefore is approximated as a series of adjacent flat plates. Contour levels are generated on a grid of 121 chordwise and 201 spanwise stations. This corresponds to a point every 3 inches in both the spanwise and chordwise directions and gives sufficient resolution for smooth contour levels.

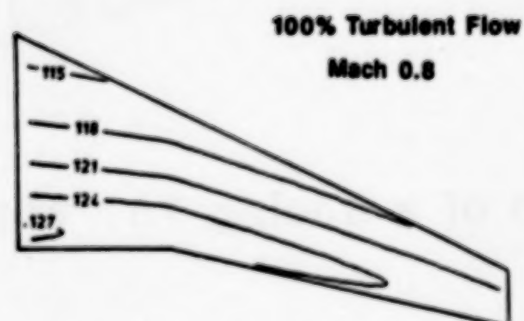
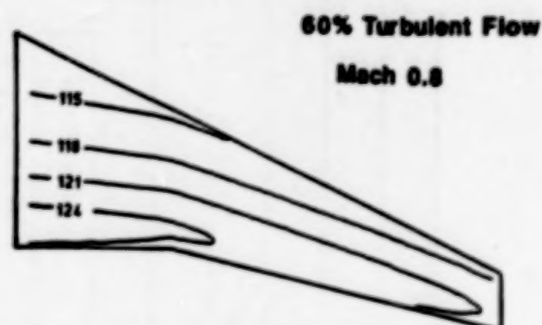
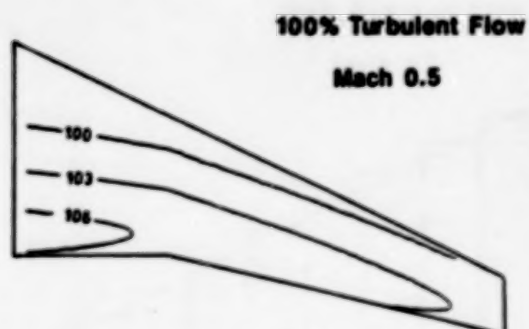


Flat plate approximation of a Boeing 757 wing

TRAILING-EDGE NOISE

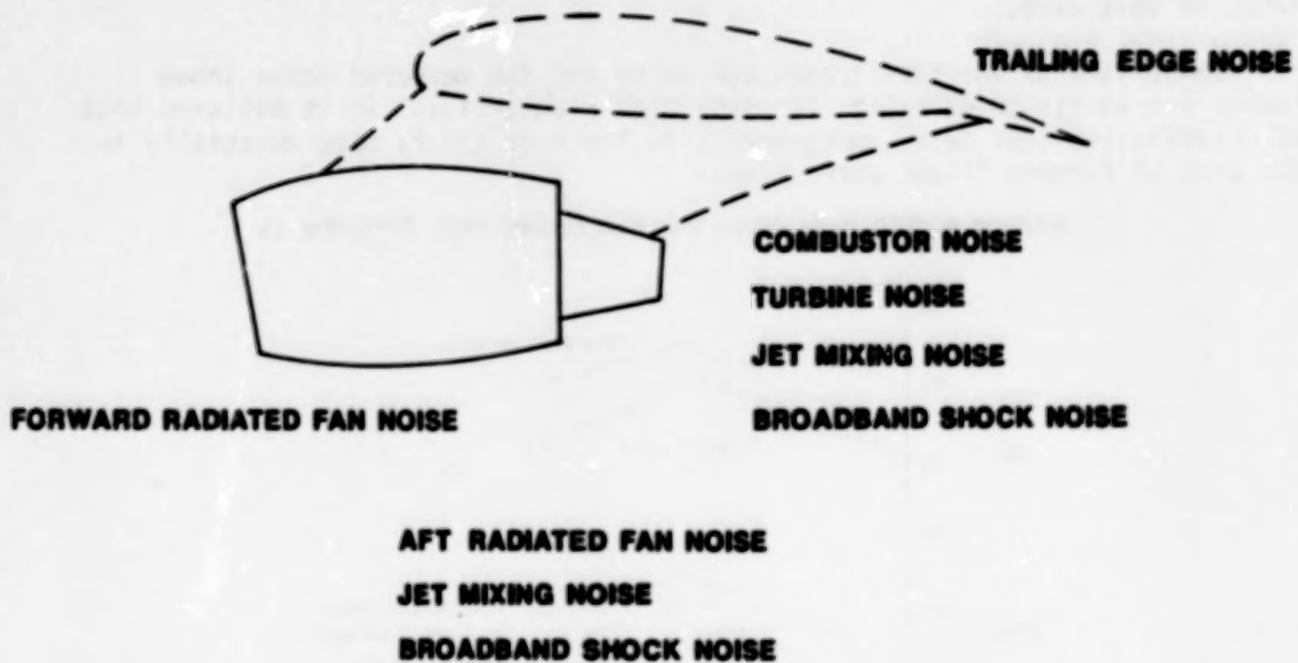
Trailing-edge noise is a function of primarily two factors, the flight Mach number and the thickness of the turbulent boundary-layer at the trailing-edge. An increase in the flight Mach number significantly increases the noise levels. An increase in the flight Mach number from 0.5 to 0.8 for example will increase the peak Overall Sound Pressure Level by 21 dB.

The effect of varying the turbulent boundary-layer thickness is perhaps of greater interest to laminar-flow studies, since a laminar boundary layer on the leading-edge portion of the wing will reduce the thickness of the turbulent boundary-layer thickness at the trailing edge. A laminar boundary layer is simulated over the first 40% of the wing by using a length scale of 60% of the chord to calculate the turbulent boundary-layer thickness. The resulting reduction in noise level is unfortunately not very significant. Peak noise levels are reduced by only 3 dB.



MODELING THE ACOUSTIC FIELD

The total noise at a point on the surface of the aircraft is computed by summing the contribution of the propulsion and airframe sources. In the case of the propulsion sources, the predictions are free-field so that the presence of a wing surface is not accounted for. The effect of shielding by a surface is also not predicted but can be simulated by judiciously choosing the noise sources to be predicted.

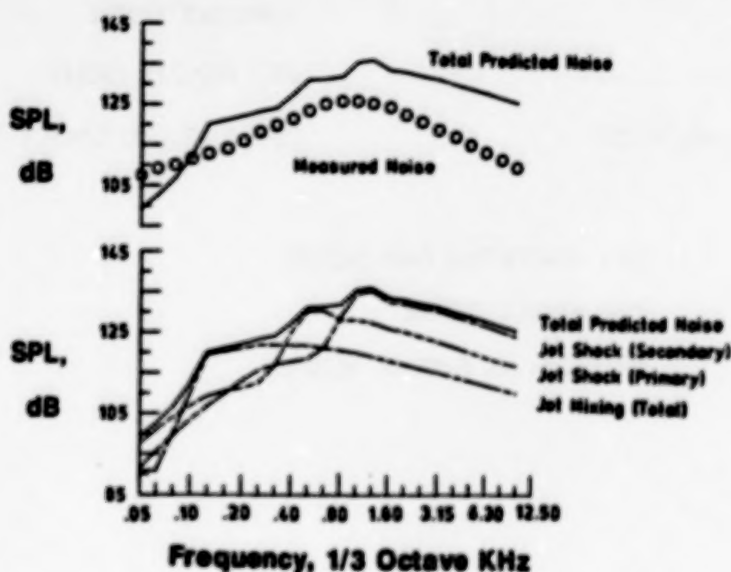


COMPARISON OF MEASURED VERSUS PREDICTED NOISE

A noise prediction is made and compared with test data obtained on the wing of a Boeing 757 aircraft. The microphone is located on the lower surface of the wing near the leading edge of a test section designed for laminar flow. Three sources contribute to the total OASPL. They are jet mixing noise and broadband shock noise from the primary and secondary jets. In the low frequency range, .05 to .4 KHz, jet mixing noise is the dominate source. At higher frequencies, the spectra are dominated by broadband shock noise from the primary and secondary jets. Fan, combustor, turbine, and trailing-edge noise were included in the noise prediction but did not contribute to the total OASPL in this case.

Comparison of the total predicted noise and the measured noise shows levels are within 10 dB except for very high frequencies. It is believed that with sufficient test data, improvements to the code can be made especially in the area of forward flight corrections.

Altitude 40,000 Feet; Mach 0.8; Fan Speed 4100 RPM; Mic 13



MICROPHONE LOCATION



CONCLUSIONS

The physics of the coupling of sound waves with the boundary layer is not yet well understood. It is believed; however, that for effective coupling of the sound waves and instability waves in the boundary layer, a matching of both frequency and wave number must occur (Ref. 5). This requires that the sound field to be accurately defined in both space and time. Currently analytical prediction methods lack sufficient accuracy to predict the noise levels from components of a turbofan engine. Although empirical methods do not yield the detail required for an analysis of the receptivity of sound by a boundary layer, valuable insight can be gained as to the changes in noise levels that might be expected under various operating conditions and aircraft configurations.

Predictions

Noise levels remained unchanged with increasing altitude when flight Mach number and thrust are held constant at 0.8 and 100% respectively

Noise levels increase significantly with increasing flight Mach number

Noise levels increase moderately with increasing thrust

Flight Data

Limited flight data tend to support these conclusions although noise prediction program tends to over predict the total noise level

Significant noise sources

	Broadband Shock	Primary Jet
		Secondary Jet
• Jet Noise		Primary Jet
	Jet Mixing	Secondary Jet
• Forward Radiated Fan Noise		
• Trailing Edge Noise		

Dominant noise sources dependent on flight Mach number

Under normal cruise conditions broadband shock noise can be expected to be present in the secondary jet

REFERENCES

1. Swift, G. and Mungur P.: A Study of the Prediction of Cruise Noise and Laminar Flow Control Noise Criteria for Subsonic Air Transports. NASA Contractor Report 159104, August 1979.
2. Tibbetts, J. G.: A Computer Program for the Prediction of Near-Field Noise of Aircraft in Cruising Flight-User's Guide. NASA Contractor Report 159274, June 1980.
3. Tibbetts, J. G.: Near-Field Noise Prediction for Aircraft in Cruising Flight-Methods Manual. NASA Contractor Report 159105, August 1979.
4. Schlinker, R. H. and Amiet, R. K.: Helicopter Rotor Trailing Edge Noise, NASA CR-3470, 1981.
5. Tam, C. K. W.: Excitation of Instability Waves by Sound - A Physical Interpretation. Journal of Sound and Vibration, 105, 169-172, 1986.



Report Documentation Page

1. Report No. NASA CP-2487, Part 2		2. Government Accession No.		3. Recipient's Catalog No.	
4. Title and Subtitle Research in Natural Laminar Flow and Laminar-Flow Control				5. Report Date December 1987	
				6. Performing Organization Code	
7. Author(s) Jerry N. Hefner and Frances E. Saho, Compilers				8. Performing Organization Report No. L-16350	
				10. Work Unit No. 505-60-31-06	
9. Performing Organization Name and Address NASA Langley Research Center Hampton, VA 23665-5225				11. Contract or Grant No.	
				13. Type of Report and Period Covered Conference Publication	
12. Sponsoring Agency Name and Address National Aeronautics and Space Administration Washington, DC 20546-0001				14. Sponsoring Agency Code	
15. Supplementary Notes					
16. Abstract <p>Since the mid 1970's, NASA, industry, and universities have worked together to conduct important research focused at developing laminar-flow technology that could reduce fuel consumption for general aviation, commuter, and transport aircraft by as much as 40 to 50 percent. This research, which was initiated under the NASA Aircraft Energy Efficiency Program and continued through the Research and Technology Base Program, has proved very successful with many very significant and impressive results having been obtained.</p> <p>This symposium was planned in view of the recent accomplishments within the areas of laminar-flow control and natural laminar flow, and the potential benefits of laminar-flow technology to the civil and military aircraft communities in the United States. The symposium included technical sessions on advanced theory and design tool development, wind tunnel and flight research, transition measurement and detection techniques, low and high Reynolds number research, and subsonic and supersonic research.</p>					
17. Key Words (Suggested by Author(s)) Laminar flow Natural laminar flow Aerodynamics				18. Distribution Statement Subject Category 02	
19. Security Classif. (of this report) Unclassified		20. Security Classif. (of this page) Unclassified		21. No. of pages 334	
				22. Price	

END

DATE

FILMED

FEB 20 1990